Durham E-Theses

A study of the characteristics of high energy nuclear active particles in extensive air showers

Nasri, A.

How to cite:

Nasri, A. (1977) *A study of the characteristics of high energy nuclear active particles in extensive air showers*, Durham theses, Durham University. Available at Durham E-Theses Online: http://etheses.dur.ac.uk/8377/

Use policy

The full-text may be used and/or reproduced, and given to third parties in any format or medium, without prior permission or charge, for personal research or study, educational, or not-for-profit purposes provided that:

- a full bibliographic reference is made to the original source
- a link is made to the metadata record in Durham E-Theses
- the full-text is not changed in any way

The full-text must not be sold in any format or medium without the formal permission of the copyright holders.

Please consult the full Durham E-Theses policy for further details.

Academic Support Office, The Palatine Centre, Durham University, Stockton Road, Durham, DH1 3LE
e-mail: e-theses.admin@durham.ac.uk Tel: +44 0191 334 6107
http://etheses.dur.ac.uk


E 5 5

PLATE 1

FRONT VIEW OF THE FLASH TUBE CHAMBER

A STUDY OF THE CHARACTERISTICS
OF HIGH ENERGY NUCLEAR ACTIVE
PARTICLES IN EXTENSIVE AIR SHOWERS

by

A. Nasri B.Sc. (Tehran)

The copyright of this thesis rests with the author. No quotation from it should be published without his prior written consent and information derived from it should be acknowledged.

A thesis submitted to the
University of Durham
for the degree of Doctor of Philosophy

May, 1977

31 MAY 1977
LIBRARY

"Cosmic ray research has advanced our understanding of fundamental problems in physics, when concepts previously used are shown to have a limited range of applicability. Since Cosmic rays contain information on the behaviour of matter in the smallest (elementary particles) and largest dimensions (the universe), they have been particularly valuable in testing the concepts of daily life in relation to their meaning in physics and in leading physicists to find new ones."

by

W. Heisenberg

At the opening of the 14th International Cosmic Ray Conference in Munich (1975)

CONTENTS

Page

ABSTRACT

The characteristics of hadrons of energy > 300 Gev in extensive air showers of size $5.10^4 - 1.6.10^6$ particles at sea level has been investigated using a neon flash tube chamber as a hadron detector operated in conjunction with part of the Durham air shower array.

The lateral distribution of hadrons tends to flatten as the shower size increases. The energy spectrum in the range 300 - 1000 Gev can be represented as a power law with exponent 1.0 ± 0.1 beyond this energy the spectrum gradually steepens.

The energy and shower size dependence, of the quantity $E_h.r$ (reflecting the transverse momenta of hadrons, where E_h is the hadron energy and r, is the distance between the hadron and shower core) has been determined. The results are in agreement with the hypothesis of an increasing transverse momentum of produced particles in ultra-high energy collisions.

A measurement of the energy spectrum of hadrons either accompanied or not has been performed. In the energy range 400 Gev up to about 8 Tev the measured differential energy spectrum shows a constant slope of 2.74 ± 0.16.

A search for magnetic monopoles has been carried out. Eleven anomolous events that could be attributed to high Z -particles ($Z \sim 20$) have been observed.

To estimate the energy of hadrons interacting in a thick (15cms) lead or iron (15cms) absorbers, the burst size was detected by scintillators placed under the lead and the iron. A calculation has been carried out to relate the burst size and the hadron energy.

PREFACE

This thesis describes the work performed by the author in the Physics Department of the University of Durham while he was a research student under the supervision of Dr. F. Ashton.

A study of high energy nuclear active particles in extensive air showers has been carried out using a large flash tube chamber.

The energy spectrum of unaccompanied hadrons was also measured.

A search for magnetic monopoles was carried out. Eleven possible high Z particles ~~has~~ have been observed.

The author has shared with his colleagues in the construction of the experiment. The running of the Chamber, the collection of data, analysis and interpretation of the data was the sole responsibility of the author.

The result concerning the observation of high transverse momentum was presented at the 5th European Cosmic Ray Symposium in Leeds by the Author (1976).

CHAPTER 1

INTRODUCTION

1.1 General

Towards the earth from all directions and at all times a continuous stream of various kinds of particles of extremely high energy are incident on the top of the atmosphere. According to our present knowledge most of these particles are protons. Heavier nuclei, electrons, positrons and X-rays have also been detected.

In traversing the atmosphere the primary radiation (the particles which have still not entered the atmosphere) interact with air atomic nuclei and generate new particles. The group of generated particles are known as secondary particles and proceed towards the earth. Mesons are the most abundant particles amongst the secondaries, that are produced by conversion of Kinetic energy of the primary to matter.

In spite of the low level flux of the primary particles at high energy, it is possible to investigate new kinds of nuclear processes which can not be done in any other way. A detailed study of these new processes is important in contributing to the solution of particle physics problems. The main problem that one can hope to examine is the nature and the origin of the forces responsible for binding the partons which constitute protons and neutrons in the atomic nucleus. So cosmic rays can lead us to the discovery of phenomena which are of fundamental importance for the understanding of interactions in the region of cosmic ray energies.

1.2 Historical review

After the discovery of X-rays in 1895 and radioactivity shortly after, one phenomenon remained unknown for a long time. The fact was

DURHAM UNIVERSITY SCIENCE 31 MAY 1977 SECTION LIBRARY

that whatever attempts were made to maintain the leaves of the ordinary electroscope apart. After charging electrically, they fell some time after, as their charge gradually leaked away.

A speculation arose whether the electroscope was effected by some other, still unknown radiation. Although the electroscope was shielded from X-rays and ~~radiative~~ radioactive radiation, nothing could stop this mysterious radiation. It was thought that presumably this radiation was emitted by some sort of radioactive substances still unknown in the earth's crust. On the basis of this hypothesis the intensity of this radiation has to naturally decrease with increasing height above the surface of the earth. To examine this postulation the German physicist V. Hess and two other people in 1912 began to launch balloons carrying recording apparatus to an altitude of 5000 metres. It was surprising that the intensity decreased for some altitudes, then increased. It was not clear where this ionising radiation is coming from. Some argued that this could be due to radioactive gases high in the atmosphere or might be the effect of thunderstorms. To know more about this unknown radiation Millikan and his collaborators carried out a series of remarkable experiments between the years 1923 to 1926. Millikan's experiments showed that the radiation discovered by Hess, come beyond the earth's atmosphere and was given the name cosmic rays.

At that time the only kind of radiations known were, α , β and γ . From these three types of radiations γ -ray could traverse the whole atmosphere and reach the earth. So the cosmic rays assumed to be photons. But some geomagnetic effects proved that this radiation is composed of charged particles. More experiments showed that the primary radiations are mainly positive particles, presumably hydrogen nuclei (protons).

The discovery of positrons came about after the observation of the electron-photon cascade by Rossi, that postulated by Dirac. Neddermeyer and Anderson discovered muons in 1937. The mass of muons was found to be approximately 200 electron masses and it was found that they occur almost in equal numbers as positive and negative. The ratio of the positive to negative implied that muons are secondaries and the interaction of primary charged particles to produce secondaries was proved.

1.3 Cosmic rays and particle physics

The study of Cosmic radiation has two main features. It deals with both the large scale universe and the tiniest particles. In other words there are two important aspects to Cosmic ray studies -the astrophysical and the nuclear physical.

Cosmic radiation is one of the most powerful means of carrying astrophysical information from otherwise inaccessible regions of space. The various high-energy particles including high energy photons (x and γ rays) are sources and carriers of astronomical information. Energies orders of magnitude greater than those attainable by present accelerators enable the Cosmic ray physicist to probe deeper than anyone else into the structure of matter.

The energy of particles produced in accelerator machines has reached about 2.10^{3} Gev (I.S.R.). The Cosmic ray energy spectrum, however, extends to at least 10^{20} ev and no indication of a cut-off has been found, so far. Figure 1.1 shows the primary Cosmic ray energy spectra measured by different methods.

It was at these ultra-high energies that Cosmic ray people discovered the existence of many stable particles, for instance, the discovery of π and μ mesons, ~~and~~ Kaons and the "strange" particles. It was at Cosmic ray

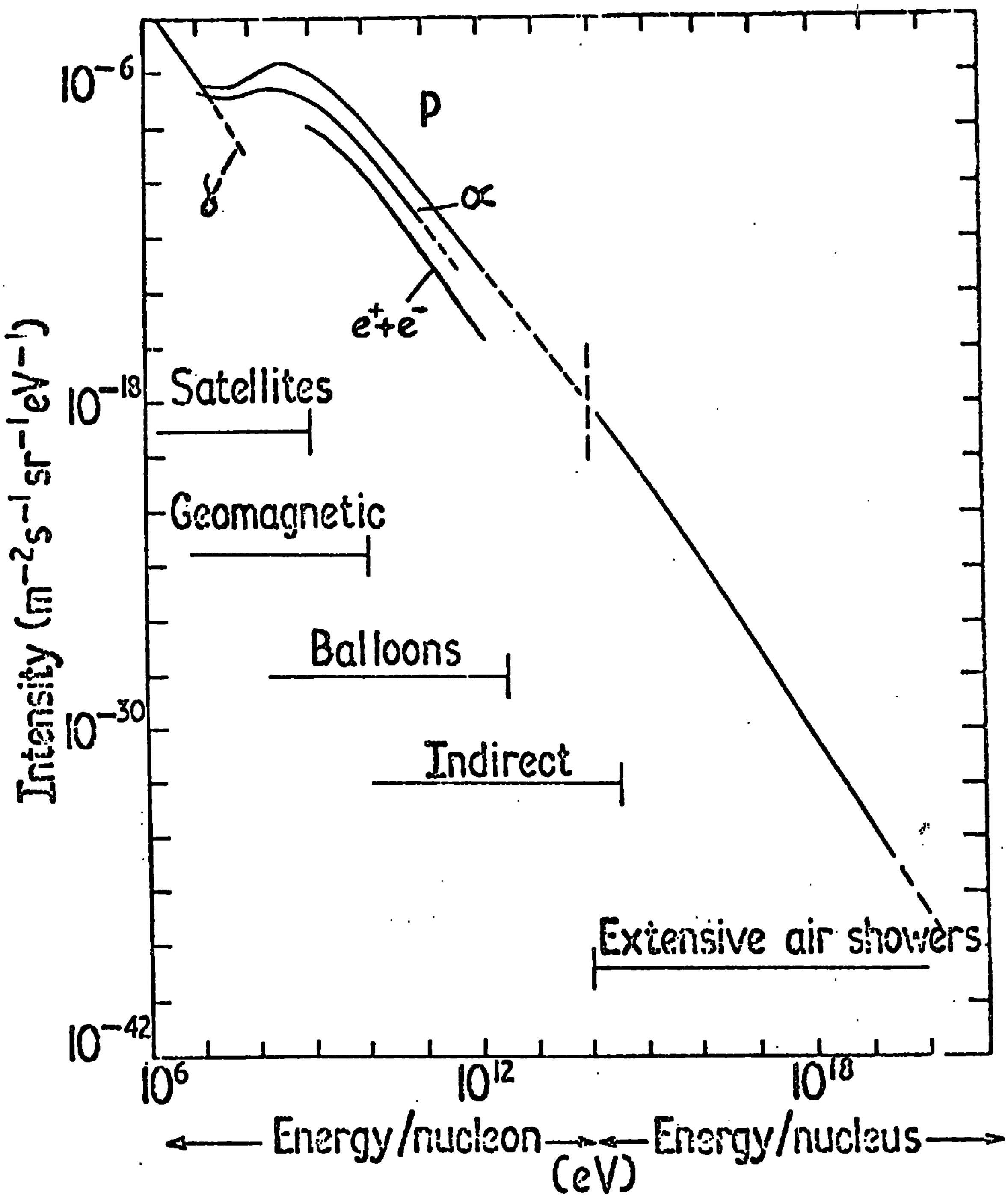

Figure 1.1. Primary cosmic ray spectra. (After Wolfendale, 1973)

energies that led investigators to the discovery of secondary particles of very high transverse momentum and several other fundamental phenomena such as the increase in $N - \bar{N}$ production, the rising of p - p cross-section and the change in the multiplicity of secondaries with energy.

It should be pointed out, as the energy of the particles goes up the study of Cosmic rays becomes more difficult, since the intensity of the high energy particles is weak. As a result, the uncertainties in the study of nuclear interaction increases.

The study of various Cosmic ray spectra at different observation levels in the atmosphere makes it possible to study the propagation of nucleons through the atmosphere.

The best region for investigating phenomena revealed in high energy interactions is the core of extensive air showers, which are produced by the interaction of a very high energy primary particle with the air nuclei, producing a large number of different kinds of secondary particles.

Recently much effort has been made to obtain more information on the structure of air shower cores. This region of an air shower is important since it contains the most energetic nuclear active particles useful for different measurements. Most important, the core structure can give information regarding the composition of the primary radiation or the distribution of high transverse momentum. Therefore from air shower studies information about the characteristics of high energy interactions can be obtained.

It should be mentioned that the information obtained from air shower experiments is the result of the superposition of numerous processes taking place along the axis of the shower from the first interaction of the primary to the level of observation which is several interaction lengths away from the point of initiation. For this reason it is difficult to identify accurately the various shower processes from the information obtained in the experiments.

A possible approach to tackle the problem is by Computer simulation of air showers, though this way of approach does not remove the whole problem. This method is based on the construction of a shower model, including various interaction parameters, in the form of a Computer program.

Because of ~~a~~ The lack of a detailed knowledge on the processes involved, construction of a real interaction model without any uncertainty is difficult. Therefore the air shower simulations are rough approximations of the actual physical processes.

1.4 The nature of primary Cosmic radiation

It is believed that the primary Cosmic ray composition consists of about 80% protons (hydrogen nuclei), 10% alpha particles (helium nuclei) and about 1% of nuclei with atomic number Z more than 2 up to a few Gev per nucleon. The measurement of nuclei in primary Cosmic rays now extends up to 10^{20} ev. In figure 1.2 the Cosmic ray spectra of different primary component calculated and summarised by ~~Jullison~~ Juliusson (1975) is shown. In figure 1.3 a possible interpretation on the basis of this calculation is seen. This calculation has carried out relating to the composition of Cosmic rays at 10^{10} to 10^{13} ev/nucleus. Some of the results of the relative composition of the different charge group is recorded in table 1, normalised as a percentage of the total. It can be concluded that at higher energies iron is as abundant as hydrogen nuclei in the primary Cosmic rays. Iron is possibly the most abundant component of the Cosmic radiation at energies 10^{13} ev.

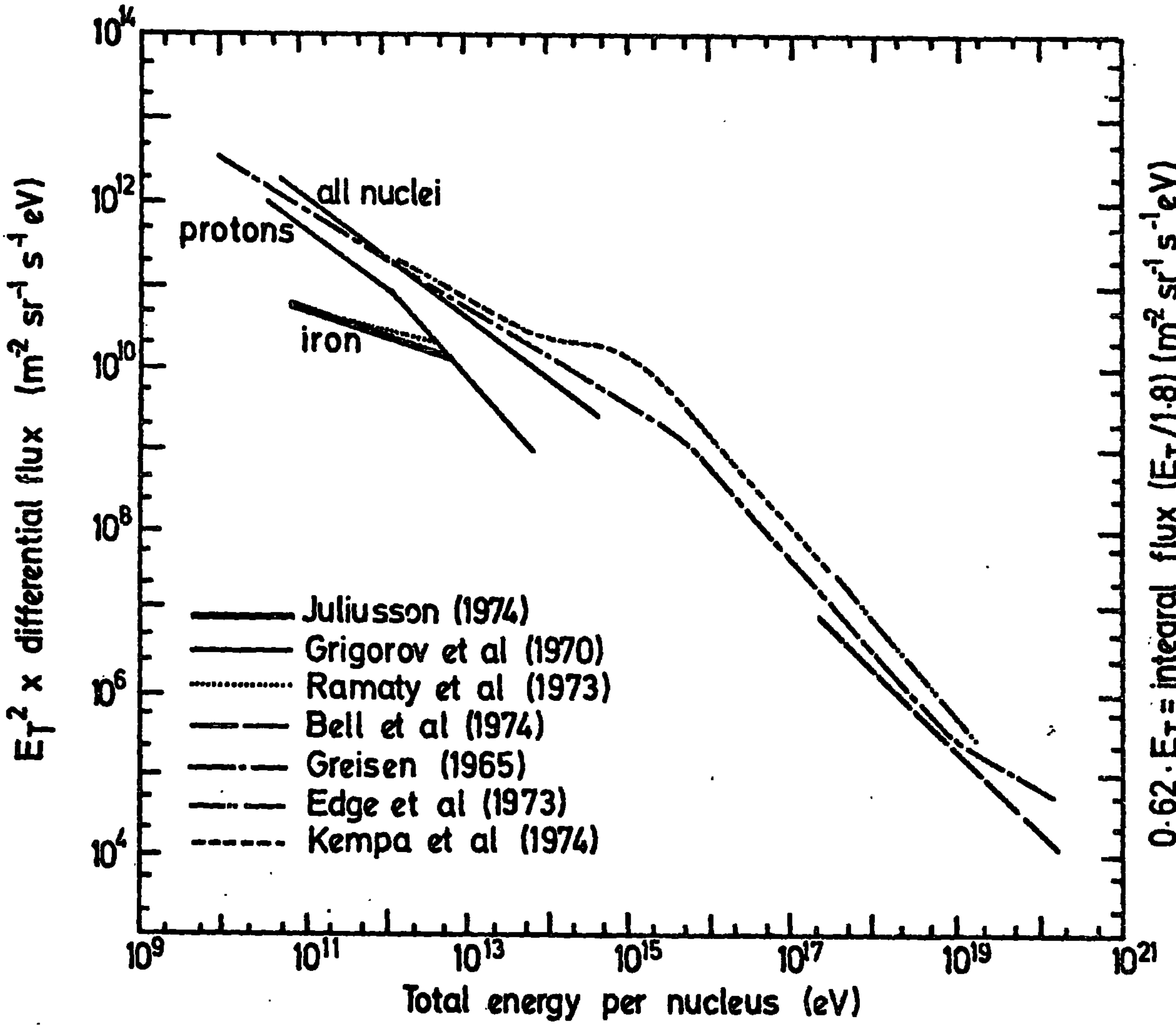

Figure 1.2 . Energy per nucleus spectra of cosmic rays
(After Juliusson 1975)

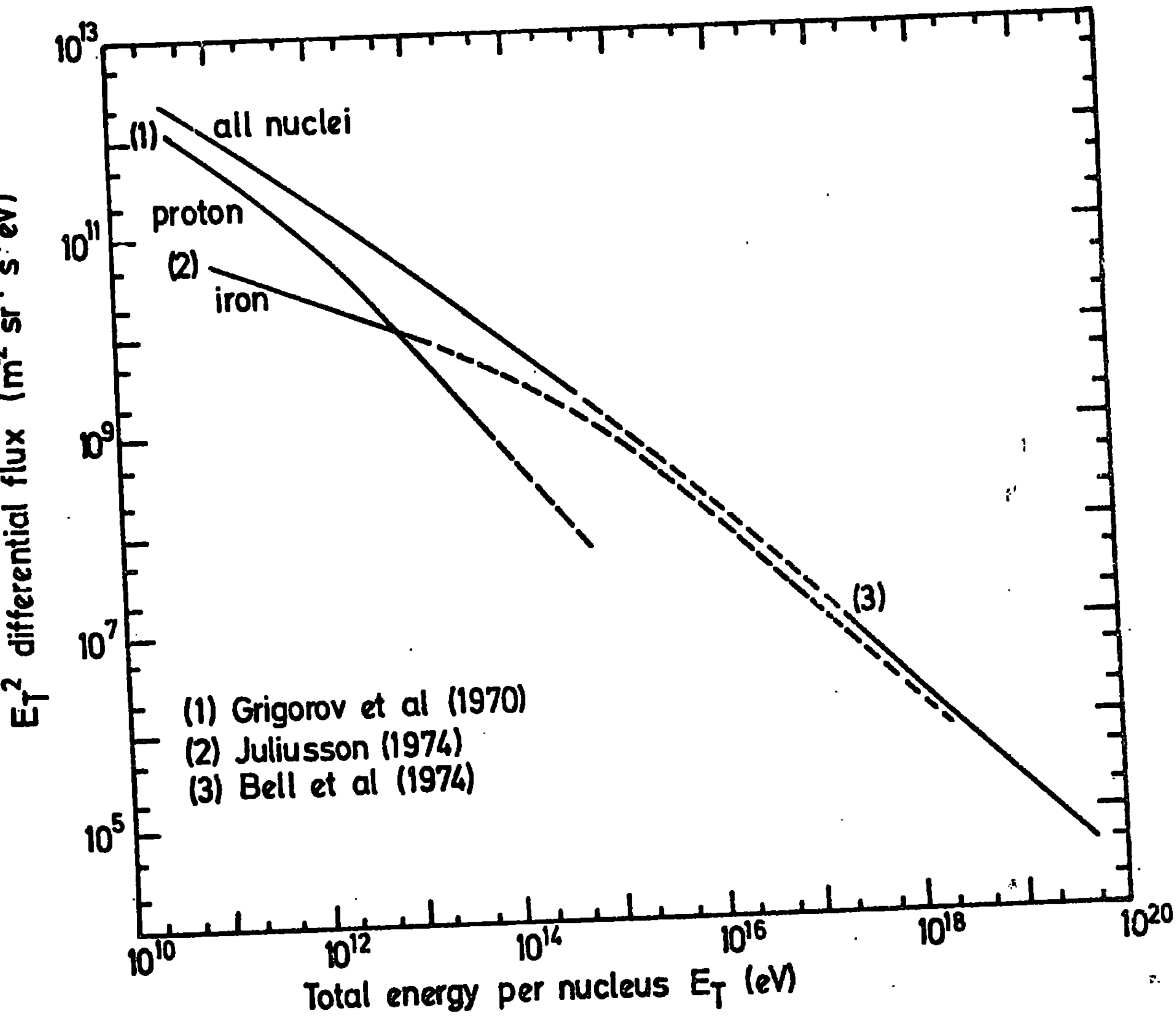

Figure 1.3 A possible interpretation of cosmic rays spectra
(After Juliusson, 1975)

TABLE 1 - COMPOSITION OF COSMIC RAYS AT HIGH ENERGIES

		KINETIC ENERGY PER NUCLEUS (eV)			
Z	ELEMENTS	10^{10}	10^{11}	10^{12}	10^{13}
1	Hydrogen	58 ± 5	47 ± 4	42 ± 6	24 ± 6
2	Helium	28 ± 3	25 ± 3	20 ± 3	15 ± 5
3 - 5	Light-nuclei	1.2 ± 0.1	1.1 ± 0.1	0.6 ± 0.2	
6 - 8	Medium-nuclei	7.1 ± 0.4	12.2± 0.8	14 ± 2	
10 -14	Heavy-nuclei	2.8 ± 0.2	6.7 ± 0.5	10 ± 1	
16 -24	Very heavy-nuclei	1.2 ± 0.2	3.6 ± 0.4	4 ± 1	
26 -28	Iron group nuclei	1.2 ± 0.2	4.5 ± 0.5	10 ± 2	24 ± 7
30	Very very heavy-nuclei		.007 ± .004		

1.5 <u>The origin of cosmic rays</u>

After extraordinary achievement in this subject through the passage of nearly 65 years since the discovery of the Cosmic radiation, still, the origin and the way of acquiring their tremendous energies is in doubt. At first it was believed that the sun is the only source of Cosmic particles, but, the suspicion arose to this idea after the indication of the uniformity of its intensity.

Cosmic rays come not only from the sun but from everywhere in the Universe. At the present time Cosmic ray people believe that sun, stars, our galaxy and other galaxies together are the sources of Cosmic rays and their magnetic fields are responsible for accelerating them. In fact the doubt about the origin of all Cosmic particles has not completely been removed. Some people believe that the bulk of the radiation comes from Galactic sources, such as, supernovae. Some find rather good reasons for supposing that the radiation is extra-galactic sources and an intermediate group that believe Cosmic rays come from both sources.

1.6 Secondary particles

On passing through the atmosphere, the primary Cosmic rays collide with the air nuclei and produce a variety of secondary particles. Among these secondaries π - mesons are the most abundant. A significant number of secondaries are nucleons (protons and neutrons) and K - mesons. Most of the particles cannot survive down to sea level, μ - mesons make a significant contribution to the intensity of Cosmic rays at sea level. The remaining charged particles at sea level are electrons protons, neutrons and pions and a small number of as yet undetected K mesons, antiprotons etc.

1.7 Nuclear active particles in extensive air showers

The most valuable contribution that Cosmic rays can make to the understanding of matter is to use it as a high energy beam and let it to collide with matter. This is not so easy, however, since as was mentioned earlier the intensity of ultra-high energy particles in Cosmic rays is extremely weak and as the dimensions of the detectors are limited this investigation cannot be achieved directly, therefore an indirect method must be selected, namely studying extensive air showers.

It is possible to obtain valuable information in extensive air showers at any observation level. The most important information can be deduced by a close investigation of the core of the extensive air showers. In this region the most energetic nuclear active particles are concentrated. The aim of the present experiment is to study the hadromic component of this region.

In chapter two of this thesis the features of high energy interaction are described. In this chapter a brief account of the energy dependence of various interaction parameters with the present status of important problems is presented.

In chapter 3 a summary of measurements of nuclear active particles in extensive air shower is given.

Chapter 4 describes the construction of one of the three scintillators built for inclusion in the Durham Extensive Air Shower array.

Chapter 5 deals with the theory of burst production in lead and iron absorbers, calculations have been done to obtain the relation between burst size and hadron energy.

In chapter 6 the flash-tube chamber and the arrangement for the study of hadrons in extensive air showers is described. In this chapter the method of E.A.S. core location is also explained.

In chapter 7 the results of the present experiment, the lateral distribution and energy spectrum of hadrons in E.A.S., is presented.

Chapter 8 deals with the investigation of the dependence of mean transverse momentum on hadron energy and shower size.

In chapter 9 the results of the measurement of the single hadron energy spectrum is given.

Chapter 10 gives an account of eleven possible highly ionizing particles detected by the chamber in the course of the experiment.

Chapter 11 summarises the results of the present experiment.

CHAPTER 2

HIGH ENERGY NUCLEAR INTERACTIONS AND THE STUDY OF EXTENSIVE AIR SHOWERS

2.1 Introduction

One of the aims of the study of the nuclear interactions due to high energy Cosmic radiation is to investigate the characteristics and the structure of fundamental units of matter. As the energy of the colliding particle increases valuable information concerning the properties of matter becomes accessible. To obtain knowledge of this kind, one has to turn to the experimental data.

At present time considerable effort is being made to study the behaviour of high energy nuclear interactions using both accelerators and Cosmic radiation. It has now become feasible to extend investigations on the behaviour of proton-proton interactions up to energies of some 2000 Gev.

Since the discovery of multiple production of hadrons at Cosmic ray energies was achieved, particular interest arose in understanding the laws governing the strong nuclear interactions, in order to interprete the Cosmic ray phenomena at higher energies as well as to verify the asymptotic validity of scale invariance theories.

The energy region covered by the studies on multiple particle production extends from a few Gev to the highest energies available in the Cosmic radiation.

The study of individual events is possible by means of large photo emulsion stacks where the tracks of charged particles can be seen.

Since the flux of high energy Cosmic rays is low, the behaviour of nuclear interactions at high energies is studied by an indirect method, namely through the study of extensive air showers (E.A.S.)

The extensive air shower phenomena are caused by interactions of primary Cosmic rays with the nuclei of air atoms. The product of these high energy collisions are particles, most of which are pions. Figure 2.1 shows the development of a high energy shower through the atmosphere. This indirect method of investigation compensates for the weak flux of Cosmic radiation, making it possible to cover a vast area by say, scintillation detectors.

What one usually would like to know about the characteristics of high energy nuclear collisions and their dependence on the primary energy are as follows:

(a) The multiplicity of different kinds of particles created in the collision.

(b) The angular distribution of the secondary particles .

(c) The fraction of energy of the incident particles radiated in the collision and the distribution of this quantity among the secondaries, termed inelasticity.

(d) The interaction cross-section.

(e) The nature of the created particles.

A survey of the important nuclear interaction parameters will clarify the present situation of ultra-high energy characteristics.

2.2 Variation of mean multiplicity $\langle n_s \rangle$ with energy.

Figure 2.2 shows a survey of the measurements of the multiplicity of produced charged particles with various primary energies. On the basis of experimental data different multiplicity laws have been proposed such as:

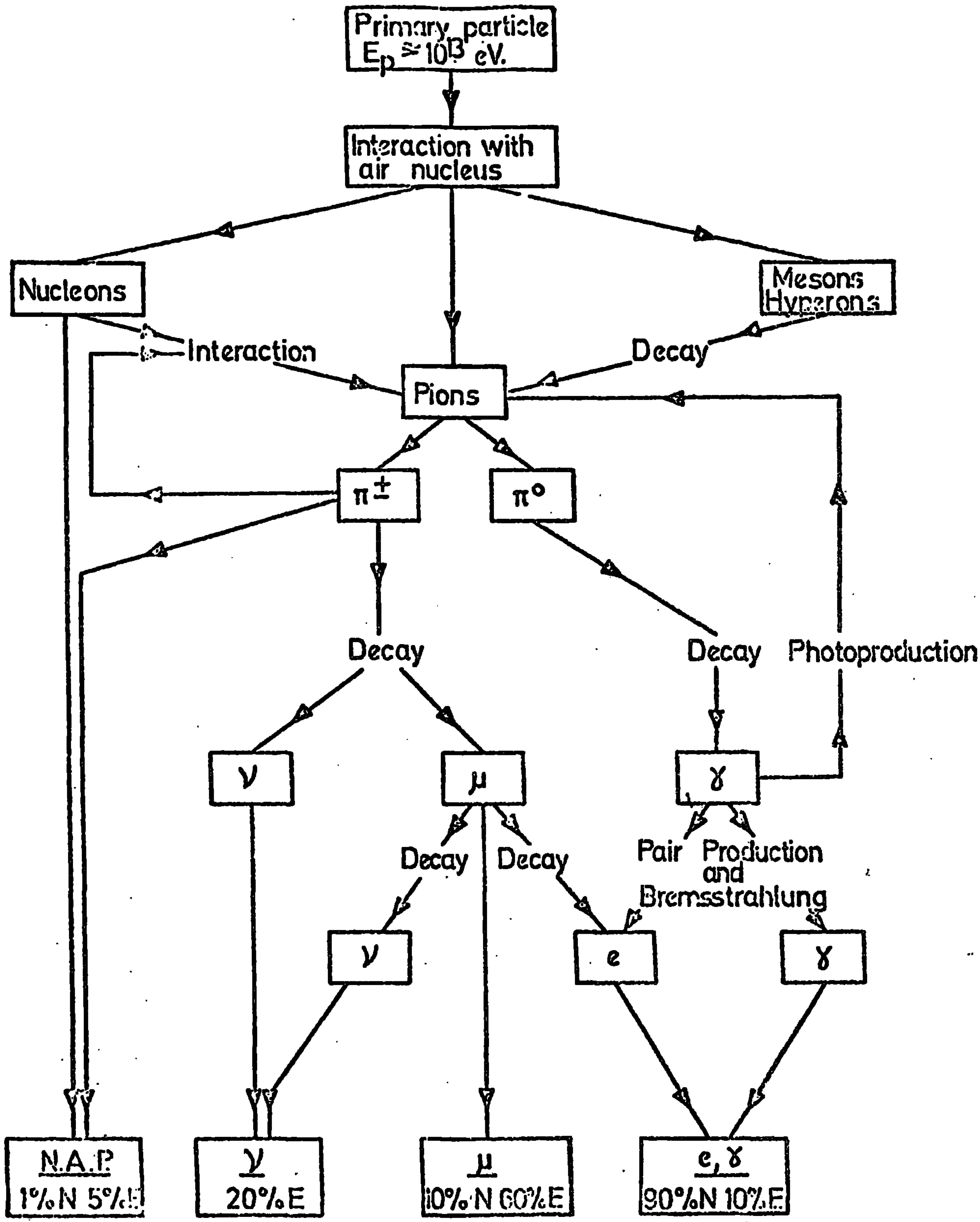

Figure 2.1 The development of a high energy shower, E is total energy of a shower containing N particles at ground level, (After Smith, 1976)

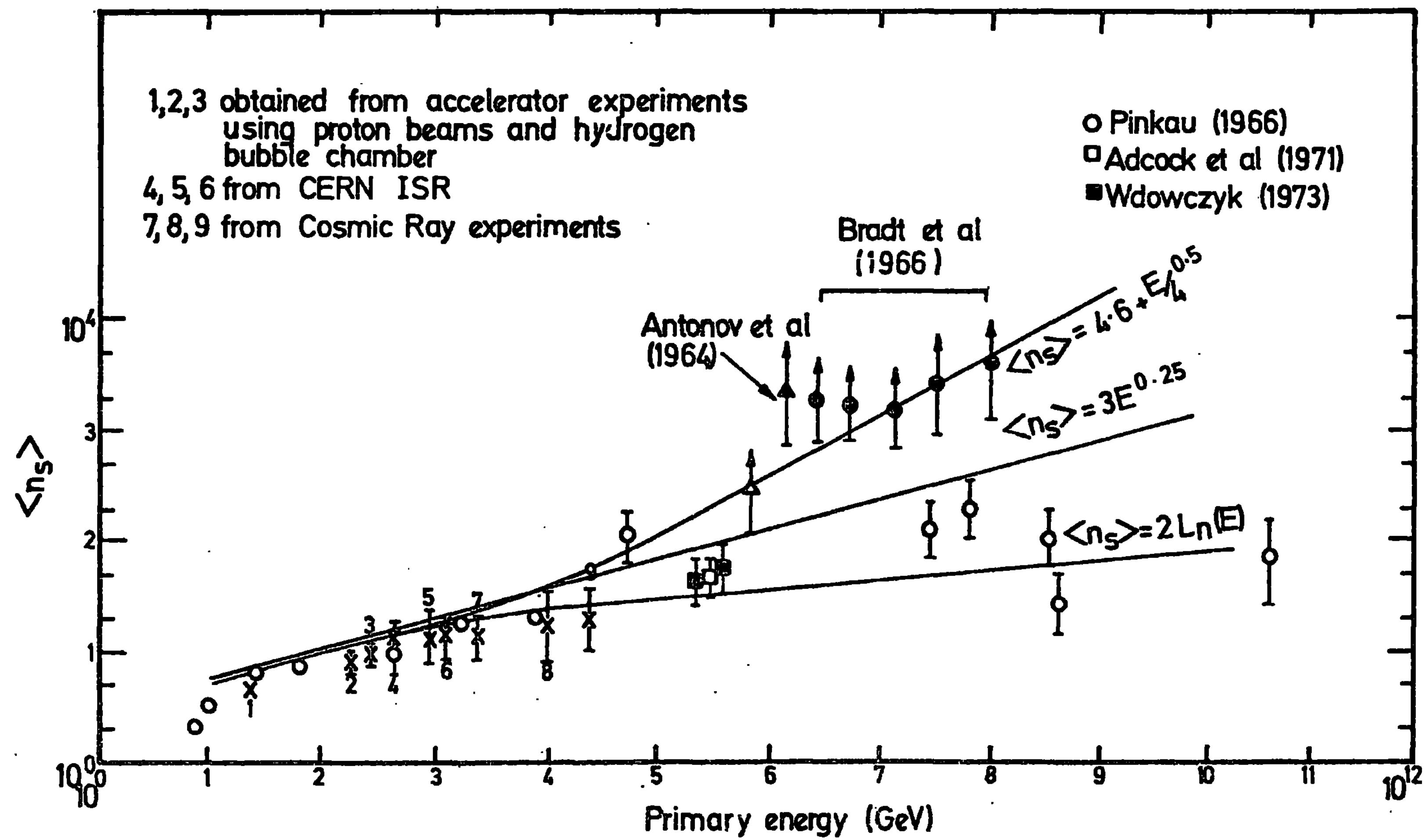

Figure 2.2 Variation in mean multiplicity of charged particles at different energies

(a) $$N_s = 3E^{\frac{1}{4}}$$

Where E is the primary energy in Gev, proposed by Fermi (1950)

(b) $$N_s = 4.64 + \frac{E^{\frac{1}{2}}}{4}$$

suggested by Yash Pal and Peters (1964)

(c) $$N_s = 2 \ln (E)$$

proposed by Frautschi (1963), assuming that fireballs are produced with multiplicity according to a logarithmic law and that each fireball produces about 6 pions.

It is clear from the figure that up to an energy of about 10^5 Gev all these multiplicity laws agree with each other, but beyond this energy the experimental data are quite different, sufficient information should be collected to fit the data to a reasonable law ~~by~~ beyond this energy. Pinkau (1966) has concluded from an interpretation of the variation of the height of the maximum of shower development with primary energy that a logarithmic law is most probable up to primary energy about 10^{10} Gev, however, the errors are too large to support this multiplicity law accurately.

2.3 Transverse momentum

Collimation of the created secondary particles is one of the most characteristics features of the interactions from the view point of particle physics. Transverse momenta reflects the angular distribution of the secondary particles of the product of the collisons.

At very high energies the measurement of transverse momenta is a very difficult task and can only be measured from the E.A.S. analysis.

Accelerator and Cosmic ray experiments have proved that the mean transverse momenta of secondaries is rather small, $\langle P_T \rangle \sim 0.3 - 0.5$ Gev/c for low energy collisions and slowly increases with primary energy.

Figure 2.3 shows a summary of the measured mean transverse momenta.

Various analytical expressions for the distribution in transverse momentum (P_T) have been given by different people, having very similar mean values. Some of these expressions are as follows:

(a) $$F(P_T)\, dP_T = \frac{P_T}{Po^2} \exp\left(-\frac{P_T}{Po}\right) dP_T$$

Where $\langle P_T \rangle = 2Po$ Gev/c by Cocconi, Koester and Perkins (1961).

(b) $$F(P_T)\, dP_T = \frac{2P_T}{Po} \exp\left(-\frac{P_T^{\,2}}{Po}\right) dP_T$$

Where $Po = 2(P_T \text{ max.})^2$ Gev/c by Aly, et al. (1964).

(c) $$F(P_T)\, dP_T = \frac{P_T^{\,2}}{2Po^3} \exp\left(-\frac{P_T}{Po}\right) dP_T$$

Where $\langle P_T \rangle = 3Po$ Gev/c by Nikolskii (1963).

(d) $$F(P_T)\, dP_T = \frac{1}{1.33Po} \left(\frac{P_T}{Po}\right)^{3/2} \exp\left(\frac{-P_T}{Po}\right) dP_T$$

Where $\langle P_T \rangle = 2.5Po$ Gev/c suggested by Elbert et al. (1968)

The idea of a slow increase in mean transverse momentum might not be true beyond the primary energy 5.10^4 Gev, there is evidence that it increases drastically beyond this energy.

In chapter 8 of this thesis further evidence is presented.

2.4 Inelasticity Coefficient

The inelasticity of a nuclear collision is defined as the ratio of the sum of the energies going into the production of the secondary particles to the energy of the colliding particle.

$$K_L = \frac{\sum Esec.}{Epri.}$$

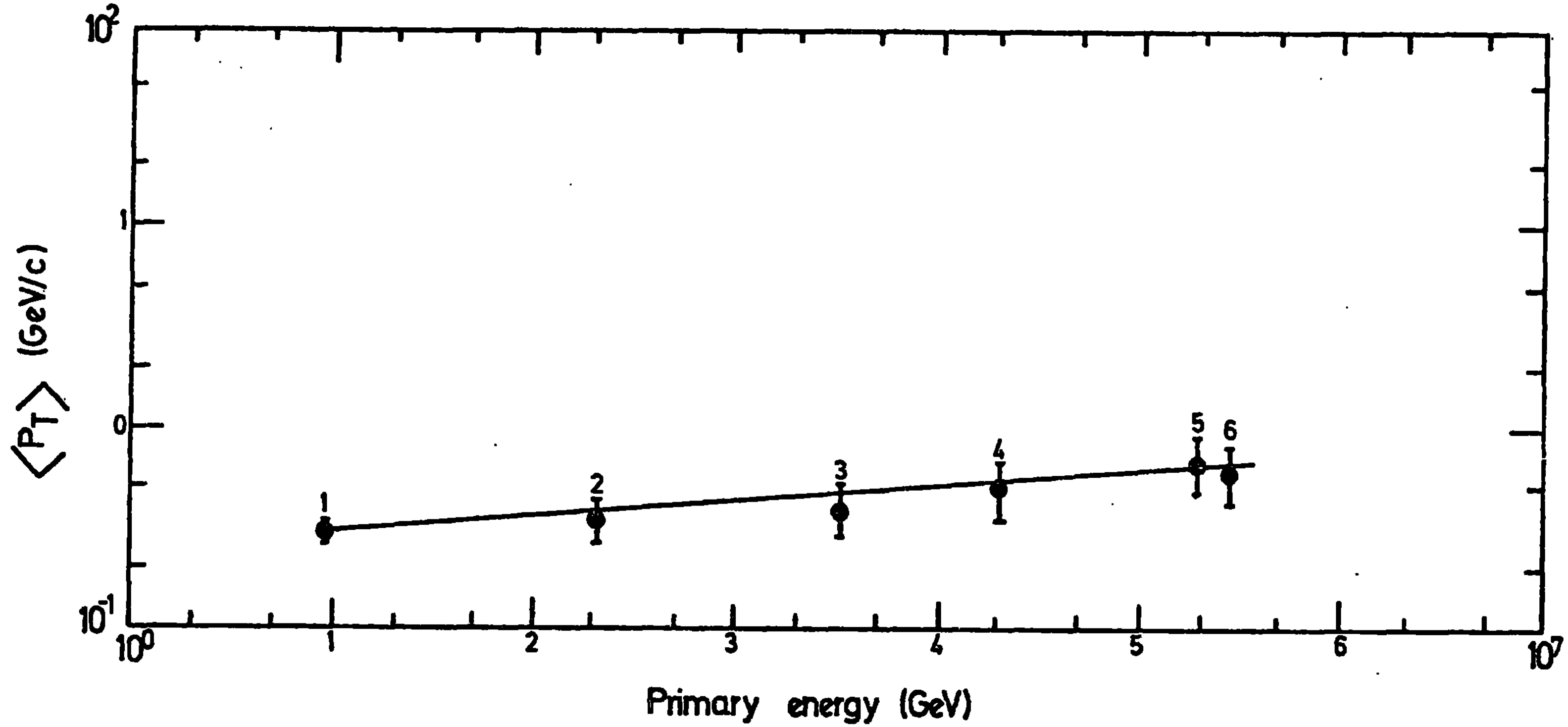

Figure 2.3 Mean transverse momentum P_T as a function of primary energy.

Each point is the average transverse momentum measured by the authors indicated below.

1. Femino et al. (1964); Bigi et al. (1964); Godksack et al. (1962)
2. Fujioka et al. (1961; Edwards and Pinkau (1958); Brisbout and McCusker (1961)
3. Schein and Naskin (1959); Debenedetti and Carelli (1956); Minakawa et al. (1959); Edwards and Pinkau (1958)
4. Nishikawa (1959); Awunor-Renner et al (1960); Malhotra et al (1965)
5. Adcock et al. (1970)
6. Hasegawa (1959); Kazuno (1962); Ciok et al. (1957)

Where $\sum E_{sec}$ indicates the total sum of the energy transferred into the secondary particles from the primary particle. Imaeda (1962) has reported the variation of the total inelasticity Coefficient (K_T) with primary nuclear energy (E_o) in the form:

$$K_T \propto E_o^{-0.5}$$

A survey of Abraham, et al. (1967), Gierula, Krzywd - Zinski (1968), Yameda and Koshiba (1968) yields that K_T is independent of the primary energy and gives the values ranging from 0.3 to 0.6. This important characteristic of the Collision has rather a broad distribution.

The value of $\langle K_T \rangle = 0.5$ used, by many authors is probably the best estimate of the total inelasticity coefficient. In the case of π - N Collision, the inelasticity is usually taken to be 1.0. This value has been supported by measurements of the attenuation length of the hadrons in E.A.S.

2.5 Variation of hadronic cross-section with energy

The inelastic cross-section at high energies is measured by Cosmic rays. This measurement is made by observation of the attenuation of the hadrons in E.A.S. and also from the variation of the position of the shower maximum with primary energy.

An E.A.S. is produced by, say, the interaction of a proton high in the atmosphere. The first generation can make further interactions, therefore, at the level of observation one can observe an energetic proton and an accompanying shower. At any observation level there is a possibility to detect a proton not interacted in traversing the atmosphere above the detector. Clearly this probability is dependent on the cross-section for interaction of the primary proton of a certain energy. The number of protons which suffer no interaction will vary, if the cross-section varies with energy.

The cross-section, measured by Cosmic rays is inelastic cross-section and up to now there is no hope to measure the elastic cross-section at ultra high energies. Yodh, Yash Pal and Trefil (1972) obtained the results shown in Figure 2.4 from Cosmic ray analysis. This figure includes values of the cross-section measured at 10, 70 and 300 Gev, using protons incident on hydrogen in bubble chambers and a point at equivalent energy 2000 Gev from the CERN I.S.R.

2.6 Relation of nuclear-nucleus and nucleon-nucleon cross-section

The nucleon-nucleon cross-section measurement is made directly by the accelerators up to the energy produced by these machines. Beyond this energy this value is measured using Cosmic radiation. In such experiments generally one does not have nucleon targets. The absorbers are composed of different heavier elements such as iron or carbon, therefore what one measures is the hadron nucleus cross-section.

At high energies the collision can be assumed to occur between the colliding particle and the individual nucleons of the nucleus.

The probability of the occurence of an interaction between the incident particle and one of the nucleons depends on the cross section (σ) for incident particle-nucleon collision. As the particle passes at a distance, b from the centre of the nucleus of radius, r, the volume swept out by its cross-section Ω, depends on the impact parameter b, the radius r, and the cross section σ .

According to poissonian statistics the probability in volume V no nucleons are present is given by: $\exp\left(-\frac{\Omega A}{V}\right)$, where A is the atomic weight and V the volume of the nucleus. The total inelastic cross-section

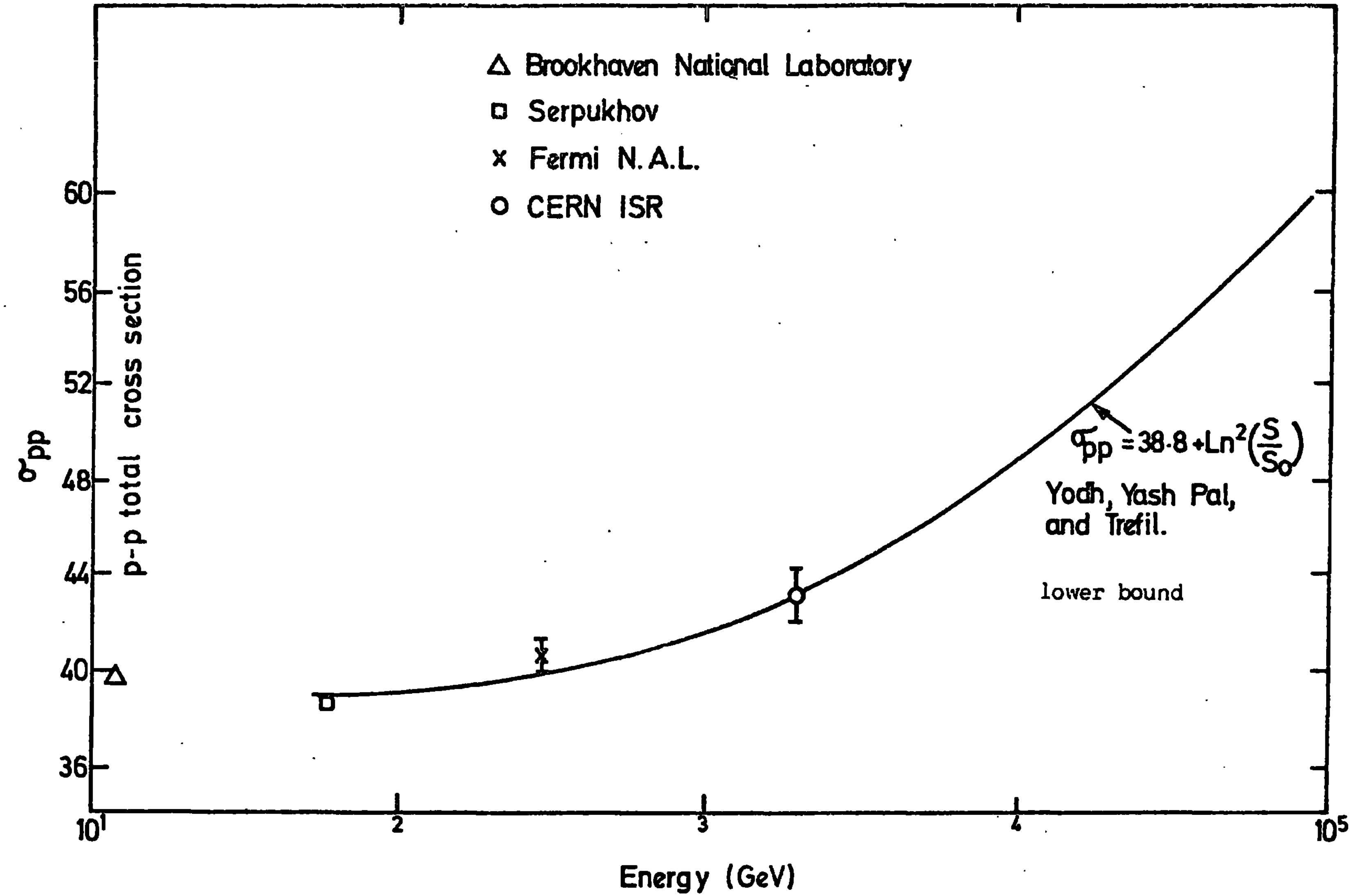

Figure 2.4 Proton-proton total interaction cross section, σ pp, as a function of primary energy. (After McCusker 1975)

of the hadron-nucleus interaction is:

$$\sigma = \int_0^{r+r_1} 2\pi \left[1 - \exp\left(-\frac{\Omega A}{V}\right)\right] bdb$$

Where r_1 is the radius of the collision of the particle given by $\pi r^2 = \sigma$ and $\left[1- \exp(-\frac{\Omega A}{V})\right]$ is the probability of the occurrence of the collision and b is the impact parameter.

Wiliams (1960) has evaluated the nucleon-nucleus cross-section as a function of σ, using the charge distributions for different nuclei obtained by Abashian et al. (1956) and Bremer, et al. (1957). This evaluation was also made by Brenner et al. (1957), Bozoki et al. (1961), Alexander et al. (1961) for different materials. Figure 2.5 shows the average air nucleus cross-section as a function of the nucleon-nucleon interaction cross-section. A reasonable estimate of the inelastic cross-section of nucleon-nucleon interaction at the energies greater than 1 Gev is 30 mb. The above argument gives the relationship between the nucleon-nucleon cross-section and the nucleon-nucleus cross-section, therefore by knowing a reasonable estimate of nucleon-nucleon cross-section, it is possible to evaluate the nucleon-nucleus interaction lengths in different materials.

The interaction length λ can be estimated by the expression $\lambda = A/_{N\sigma}$ where A is the atomic weight of the material, N is the Avagadro's number and σ the inelastic cross-section in a given material.

$$\text{For air } \lambda = \frac{14.4}{6.10^{23}\sigma_{air}} = \frac{2.4.10^{-23}}{\sigma_{air}}$$

This relation gives λ in air as a function of the elementary nucleon-nucleon cross-section. Figure 2.6 shows this relationship. The result of different calculation is also presented. An elementary nucleon-nucleon cross-section of 30 mb corresponds to a nucleon interaction length in air target of 96 gm/cm^2

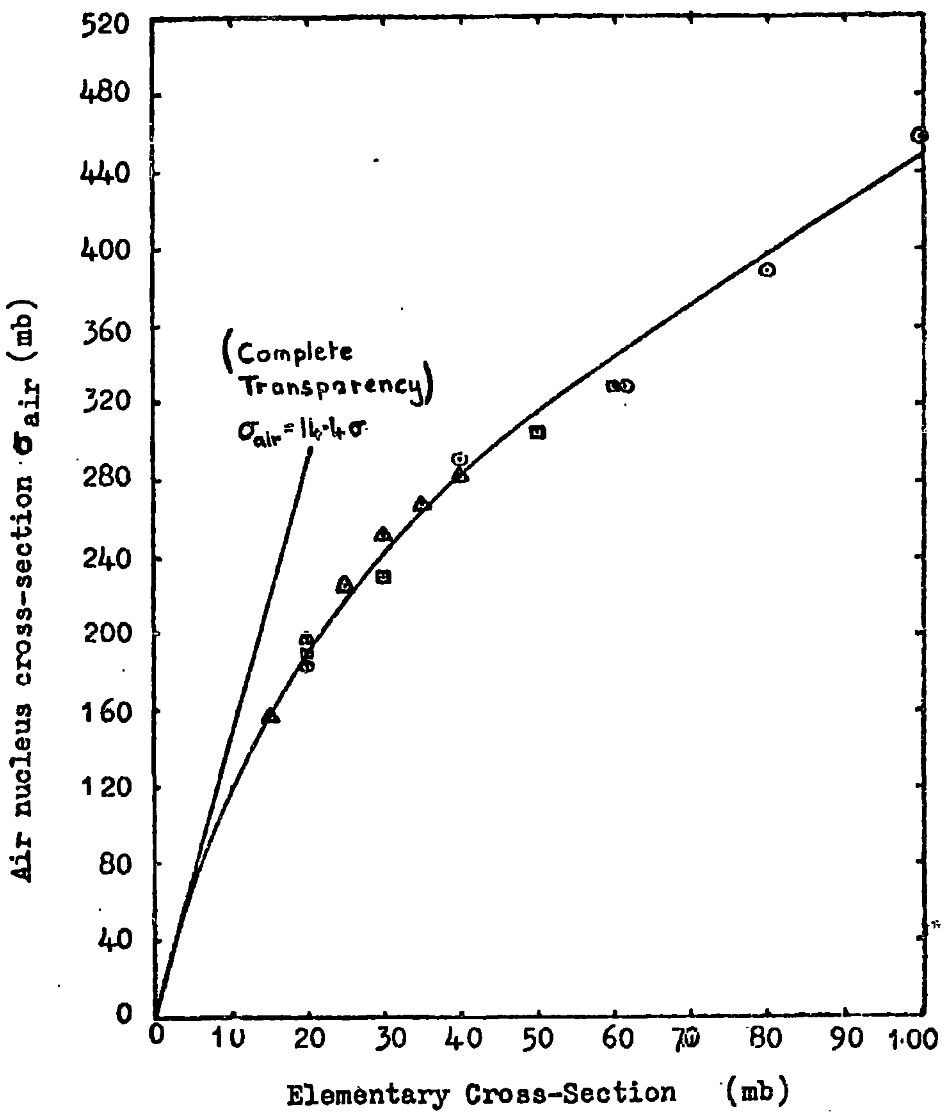

Figure 2.5 Average air nucleus cross-section as a function of the elementary cross-section.

- ⊠ Alexander et al (1961).
- △ Williams (1960).
- ⊙ Constant density spheres, $r=1.38.10^{-13}A^{\frac{1}{3}}$ cm. (After Smith, 1969)

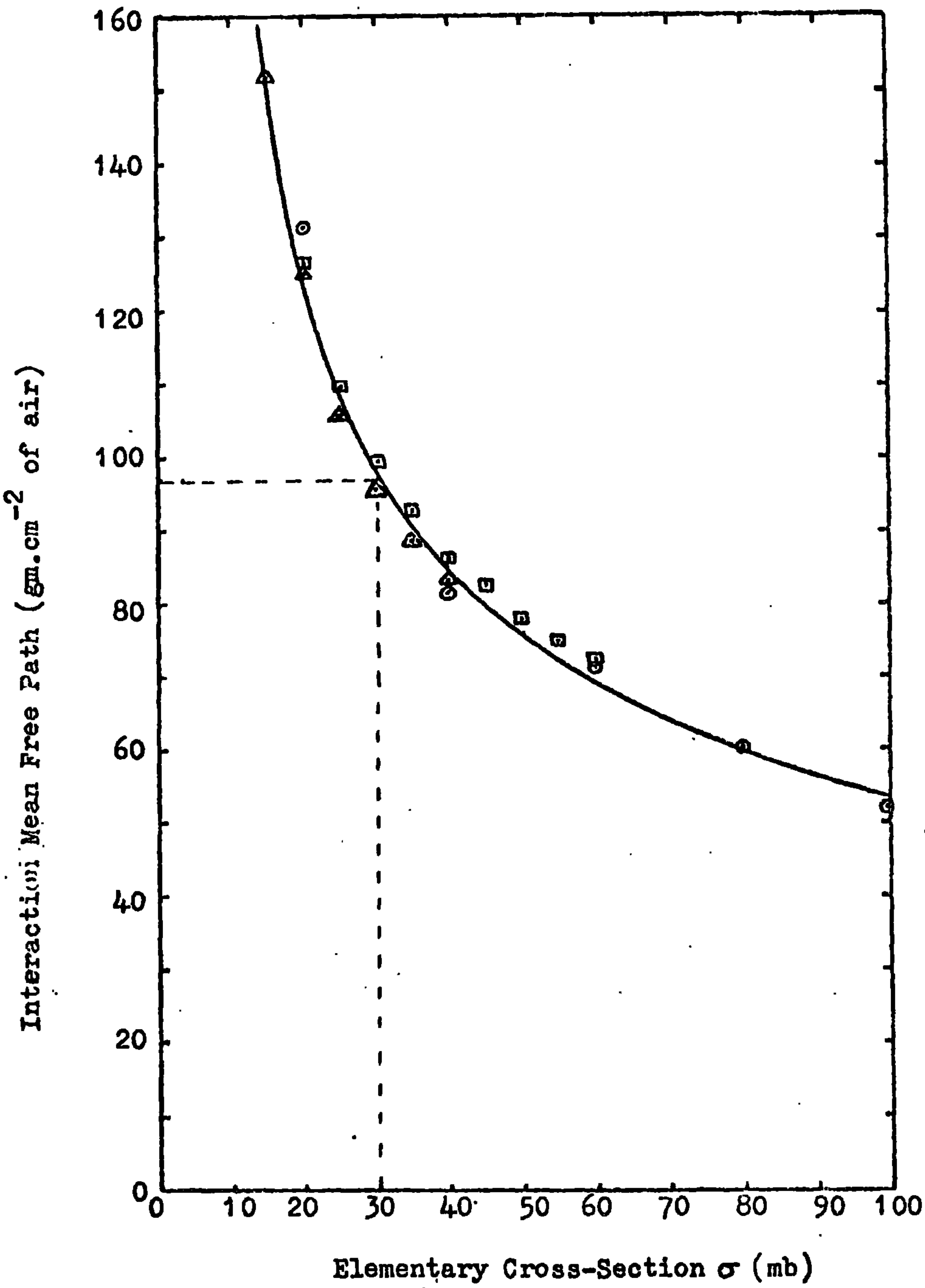

Figure 2.6 Interaction Mean Free Path in air as a function of the Elementary Cross-Section.

- ⊡ Alexander et al (1961).
- △ Williams (1960).
- ⊙ Constant density spheres, $r=1.38.10^{-13}A^{\frac{1}{3}}$ cm.

(After Smith, 1969)

2.7 Conclusion

The review of the present experimental knowledge concerning the ultra-high energy interaction parameters indicates that very little is known about the characteristics of nuclear interactionsin this energy region, that is beyond the energy about 10^4 Gev.

On the basis of the present experimental knowledge it can be concluded that:

(a) The mean multiplicity $\langle n_s \rangle$ of the secondary particles is still unknown for primary energies greater than 10^4 Gev. Below this energy $\langle n_s \rangle$ seems to increase slowly with incident energy.

There is considerable evidence that at high energies new processes occur leading to very high multiplicities.

(b) The mean transverse momentum $\langle P_T \rangle$ increases slowly with primary energy up to about 10^4 Gev. From this energy there is evidence for a drastic increase in mean transverse momentum (see chapter 8)

(c) The inelastic nucleon interaction cross-section rises with energy but much more accurate measurements are needed to understand it.

In connection with the discovered discrepancy between the experimental data and the scaling model, there arise new problems, these necessitate to determine more accurately at what primary energy the scaling violation begins and what does this violation mean?

Apart from the above considerations new particles are possibly created in these high energy collisions such as: quarks, monopoles and tachyons that makes such studies remarkable.

So far, these studies in the high energy region are possible only by E.A.S. investigation. The study of E.A.S. might also solve the problem of the primary Cosmic ray Composition at ultra-high energies, the origin and the mechanism of the acceleration.

CHAPTER 3

A SURVEY OF MEASUREMENTS OF HADRON CHARACTERISTICS IN EXTENSIVE AIR SHOWERS

3.1 Introduction

In this chapter a summary of the measurements of the properties of hadrons in E.A.S., made by different experimenters at different altitudes is presented.

In this survey a variety of hadron detectors, mostly cloud chamber, ionization calorimeter and burst producing techniques are employed to detect and measure the energy of nuclear active particles.

The E.A.S. core location and shower parameters are usually obtained by means of scintillation detectors, distributed around the hadron detector.

3.2 Miyake et al. (1969)

The high energy hadrons ($\gg$ 200 Gev) in the core region of extensive air showers of size $3.10^5 - 10^6$ particles have been studied, using a multiplate cloud chamber of 1.3x2.0x0.7 m^3 with 21 lead plates (each 1 cm thick) and scintillation detectors covering 12 m^2 above and below a water tank.

The experimental arrangement used, consists of 26 scintillators distributed within a range of 100m from the centre. Within an area of 12 m^2 located horizontally 48 scintillators each of size 50x50 cm^2 above and below a water tank of depth 2m.

To study the behaviour of the nuclear active particles in detail a multiplate cloud chamber of 1.3x2.0x0.7 m^3 with 21 lead plates (each 1 cm thick) was used.

The observed lateral distribution of hadrons for core distances $<$ 10m is expressed as: A $\exp(^{-r}/r_o)$. The dependence of r_o (characteristic length) and the amplitude A, on hadron energy is expressed as:

$$r_o \backsim E_N^{-0.33} \qquad A \backsim E_N^{-1.0}$$

This dependence is shown in figure 3.1a. The dependence of A, on hadron energy, expressed above, is correct for energies beyond 500 Gev. For energies less than 500 Gev the curve, A as a function of E_N, becomes flatter.

The energy spectrum of hadrons in the showers of size 3.10^5-10^6 is expressed as: $E_N^{-1.0}$ for energies less than 500 Gev and $E_N^{-1.8}$ for energies more than 500 Gev. They also found the same slope by integrating the lateral density distribution. No significant change in the exponent of the energy spectrum with the size of air showers and age parameter, s, has been observed. Figure 3.1b shows the observed energy spectrum.

The observed dependence of the lateral distribution of hadrons on shower size is shown in figure 3.1c. The dependence of A and r_o on the shower size is expressed as:

$$r_o \backsim N_e^{0.16} \quad , \qquad A \backsim N_e^{0.40}$$

In figure 3.1d the total number of hadrons (> 500 Gev) as a function of shower size with an exponent 0 .73 is shown.

3.3 Hinotani (1961)

A study of nuclear active component in extensive air showers was made at altitude 2770 m above sea level. Using a large multiplate cloud chamber and two standard neutron monitors which were installed in E.A.S. array of 16 ~~election~~ electron density measuring detectors.

High energy hadrons (> 10 Gev) were investigated, using a multiplate cloud chamber. Hadrons of energy (> 200 Mev) were observed separately by means of a neutron monitor.

The integral energy spectra of hadrons are expressed by: $E^{-0.7\pm0.1}$, $E^{-1.1\pm0.2}$ and $E^{-1.5\pm0.2}$ for the events observed at distances 0-5 m, 5-10 m and more than 10 m from the shower axis respectively. The integral energy spectrum of the total hadrons is expressed by : $E^{-1.0\pm0.1}$.

The lateral distribution of hadrons above 10 Gev is obtained as: $r^{-1.4\pm0.2}$ within 25 m from the axis. The lateral distribution of low energy hadrons is expressed by, $r^{-1.0\pm0.2}$ for the distances 5-30 m. The distribution becomes flatter within 5 m. The lateral distribution for each energy region is well fitted with an exponential function, $\exp(-r/r_o)$. The characteristic length, r_o, is measured as 20 m, 7m and 1.2m for the energies $\geqslant 10^8$ev, $\geqslant 10^{10}$ev and $\geqslant 10^{11}$ev, respectively. The lateral structure of energy flow carried by low energy hadrons is expressed as: $r^{-1.8\pm0.2}$. The larger air shower has slightly steeper structure for the energy flow. The total number of hadrons of energy $>$ 200 Mev varies with the shower size (N_e) such:

$$N_N \propto N_e^{1.0\pm0.1} \qquad (10^5 < Ne \leqslant 3.10^6)$$

$$N_N \propto N_e^{0.6\pm0.1} \qquad (N_e > 3.10^6)$$

3.4 Kameda et al. (1962)

A study of hadronic component in energy range 10-500 Gev has been made near sea level using a multiplate cloud chamber with illuminated region of 120 cm width, 50 cm depth and 100 cm height at the centre. The absorbers used, were 7 plates of 8 mm thickness of lead lined with 5 mm thickness of iron and 8 plates of 18 mm thickness of lead lined with 5 mm thickness of iron.

Figure 3.2a shows the lateral distribution of the nuclear active particles producing π^o - mesons of total energy $>$ 10 Gev. It is well expressed as: $\exp(-r/r_o)$, where r is the core distance of the E.A.S.

For showers of size ranging from $10^4 - 3.10^4$, r_o is about 1 m, for $3.10^4 - 3.10^5$, r_o is about 2 m and for showers of size $3.10^5 - 10^6$, $r_o = 3$, therefore r_o increases as the shower size increases.

Figure 3.2c shows the integral energy spectra of high energy nuclear active particles for different bands of distances from the shower axis. Assuming a power law of the form E^{-n} for the energy spectra, n, is dependent on the shower core distance as shown in figure 3.2b. The exponent n, changes from 0.5 to 1.5, dependent on the lateral distribution and energy spectra in three different bands of distances. The energy spectrum of the total number of high energy hadrons in a shower is shown in figure 3.2c. The energy spectrum obeys a power law of the form $E^{-(1.0 \pm 0.15)}$ in the energy range 10 - 500 Gev.

Figure 3.2d shows the total number of hadrons of energy $\geqslant$ 10 Gev as a function of shower size. This relation is expressed by:

$$N_n = (13 \pm 4) \quad \left(\frac{N_e}{10^5} \right)$$

The ratio of charged to neutral hadrons was measured as 5:1, implying that about 70% of hadrons seem to be π - mesons. In a similar way the energy spectrum of hadrons producing π^o - mesons of total energy ranging from 1 - 10 Gev is obtained and expressed as: $E^{-(.4 \pm .15)}$.

3.5 <u>Kameda et al. (1965)</u>

A study of nuclear active particles of energy $\geqslant$100 Gev in E.A.S. of size 4.10^4-4.10^6 particle, using a multiplate cloud chamber has been performed by this group near sea level (1000 gr/m^2), for a running time of 4300 hours.

The total number of photographs analysed have been 10,000, among which 250 hadrons of energy $\geqslant$ 100 Gev have been analysed.

The ratio of the charged to neutral has been measured and obtained

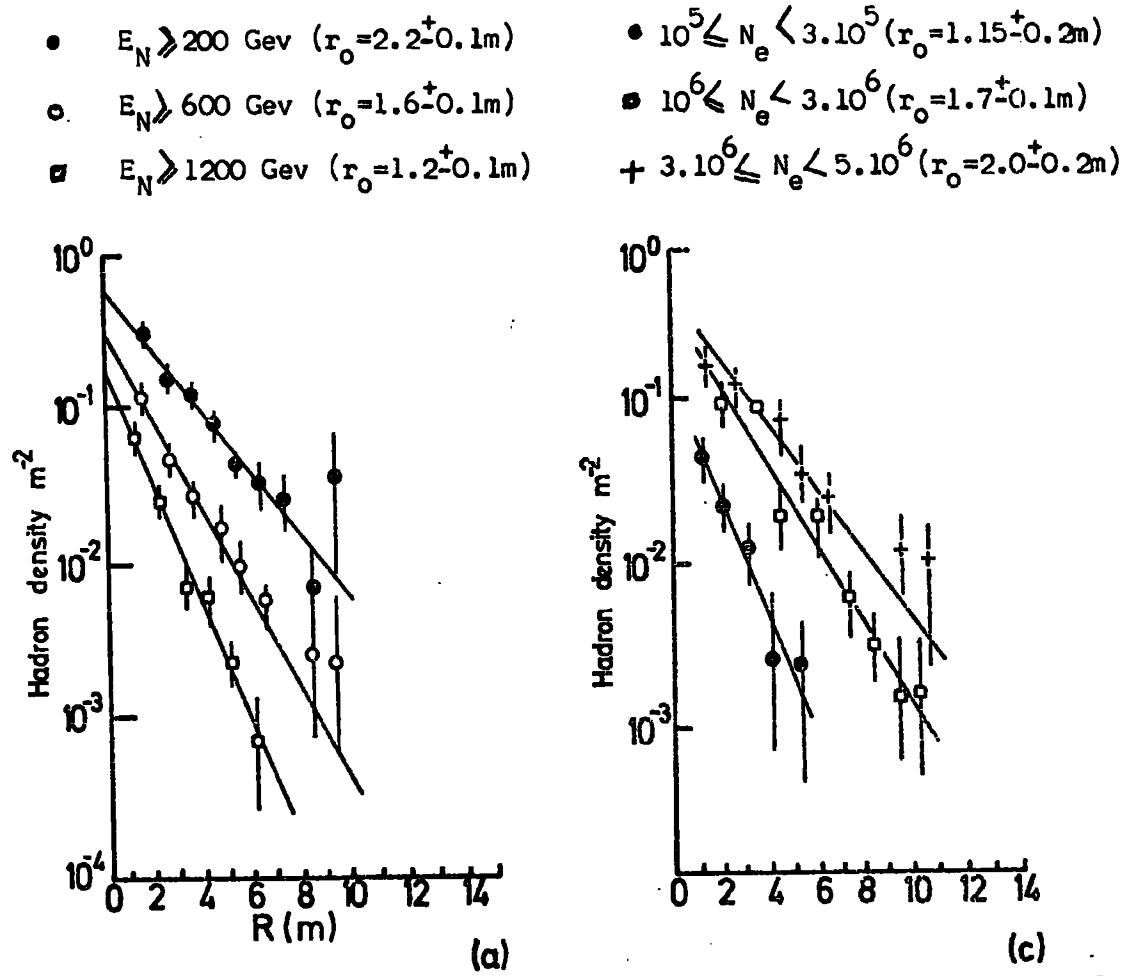

The lateral density distribution of hadrons for different energy

The lateral distribution of hadrons >500 Gev for different shower size

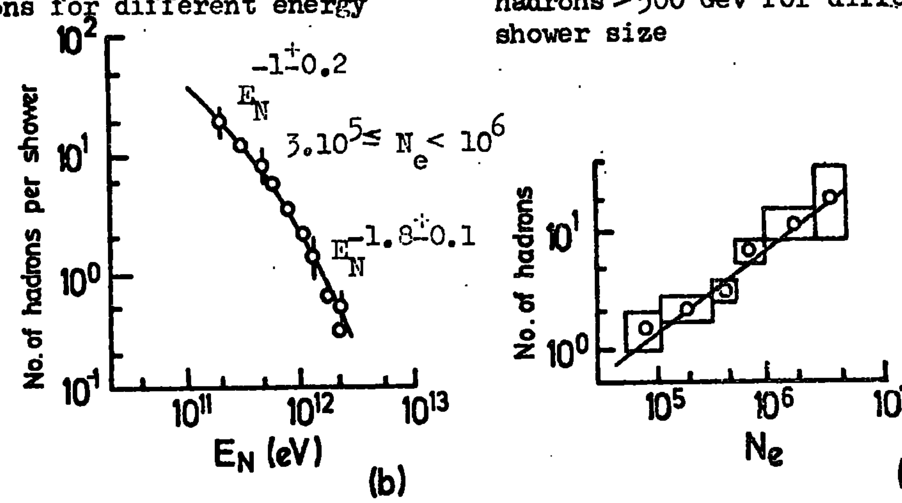

The energy spectrum of high energy hadrons

The total number of hadrons as a function of shower size

Figure 3.1 Summary of the data of Miyake et al (1969)

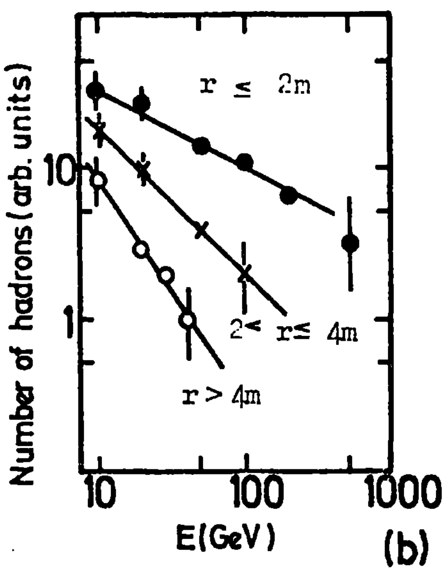

The Integral energy spectra of hadron for various distances.

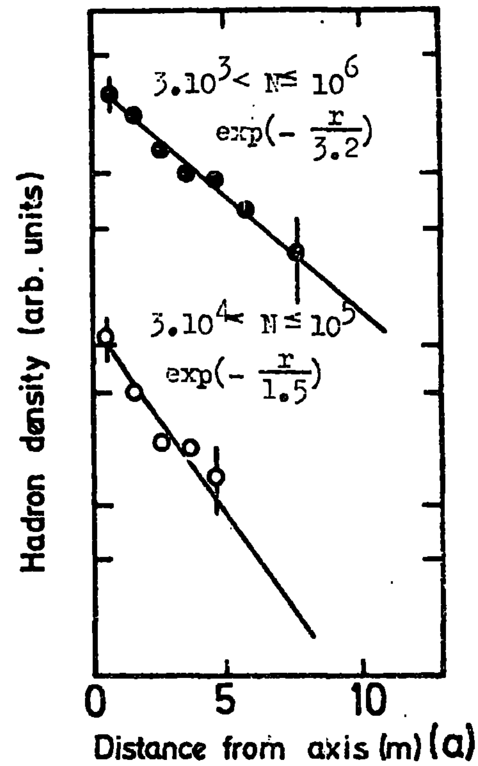

The lateral distribution of hadrons with $E_{\pi^o} \gg 10$ Bev

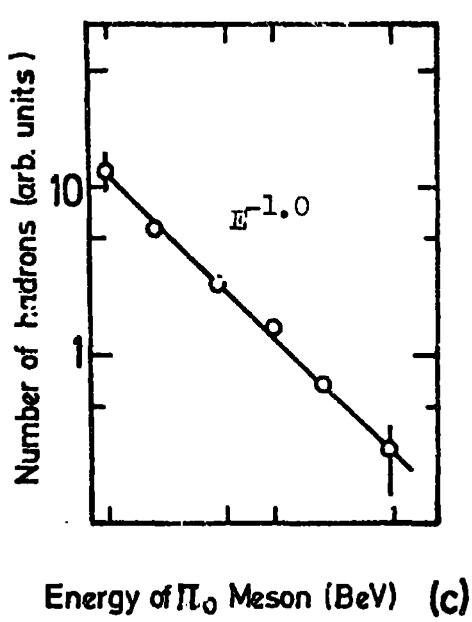

The Integral energy spectrum of hadrons

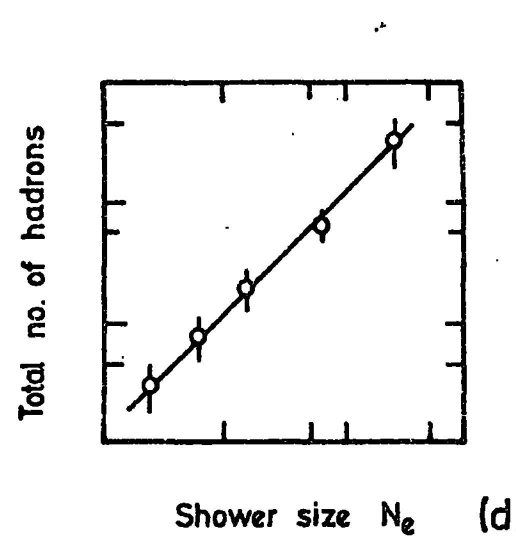

The variation of total number of hadrons with shower size ($E_{\pi^o} \gg 10$ Bev)

Figure 3.2 Summary of the data of Kameda et al (1962) to be 4.5±0.5. No shower size dependence has been found. The zenith angle distribution of hadrons are well represented by $\cos^n\theta$ where $n = 12 \pm 2$.

The attenuation length was measured, the value 85^{+15}_{-10} g/cm^2 was obtained.

The lateral distribution of hadrons is fairly well represented by the expression, $\exp(-r/r_o)$. It is understood that r_o increases with shower size and decreases with increasing energy of hadrons. Figure 3.3a and 3.3b show these dependences. The brackets around r_o indicate the average from all hadrons of energy $\geq$ to 100 Gev. Figure 3.3c shows $r_o = N^{-\alpha}$ where $\alpha = .32 \pm .01$. The dependence of r_o on hadron energy can be expressed as: $r_o = E^{-\beta}$ where $\beta = .25 \pm .05$. Therefore

$$r_o = A \left(\frac{N}{10^5}\right)^{.32} \left(\frac{E}{100}\right)^{-.25}$$

A, has been found form $\langle r_o \rangle$ and energy spectrum to be $2.4 \pm .3$. The total number of nuclear active particles is calculated from, $n_T = 2\pi \langle r_o \rangle^2 B$ where B is the hadron density at shower core. Figure 3.3d shows the relation of the total number of hadrons of energy $\geq$ 100 Gev with shower size. In figure 3.3e the integral energy spectrum is shown. No shower size dependence is observed. The spectrum is represented by $E^{-0.75 \pm .10}$ in the energy range 10^2 - 10^3 Gev. Figure 3.3f shows the relation of shower size with B. The absolute density of hadrons in the energy range (E, E+dE) at a distance (r, r+dr) from the axis of a shower of size in unit 10^5 particles is expressed as:

$$n(E, r, N)dE\, dr = 0.35 \left(\frac{N}{10^5}\right)^{.35} \left(\frac{E}{100}\right)^{-1.2} \exp\left(-\frac{r}{r_o}\right) d\left(\frac{E}{100}\right)^{dr}$$

where $r_o = 2.4\, (N/10^5)^{.32}\, (E/100)^{-.25}$

Figure 3.3a

The dependence of the lateral distribution of nuclear active particles of energy $\geq$ 100 Gev on the shower size. The lateral distribution function is expressed in the form: exp $(^{-r}/r_o)$.

Figure 3.3b

The dependence of the lateral distribution of nuclear active particles on energy r_o decreases with increasing energy.

Figure 3.3c

The relation between shower size N and $< r_o >$. $< r_o >$ is proportional to $N^{0.32}$. $\ddagger$ is the value obtained from high energy electron components.

Figure 3.3d

The total number of nuclear active particles in a shower as a function of shower size. It is represented as $N^{1.0}$.

Figure 3.3e

The integral energy spectrum of nuclear active particles in a shower. The spectrum is represented by $E^{-0.75}$ at energy less than 10^3 Gev; at higher energy the power of E increases.

Figure 3.3f

B against shower size. B is the constant which appears when the lateral distribution is expressed as B $\exp(-^{r}/r_o)$, and proportional to $N^{0.35}$.

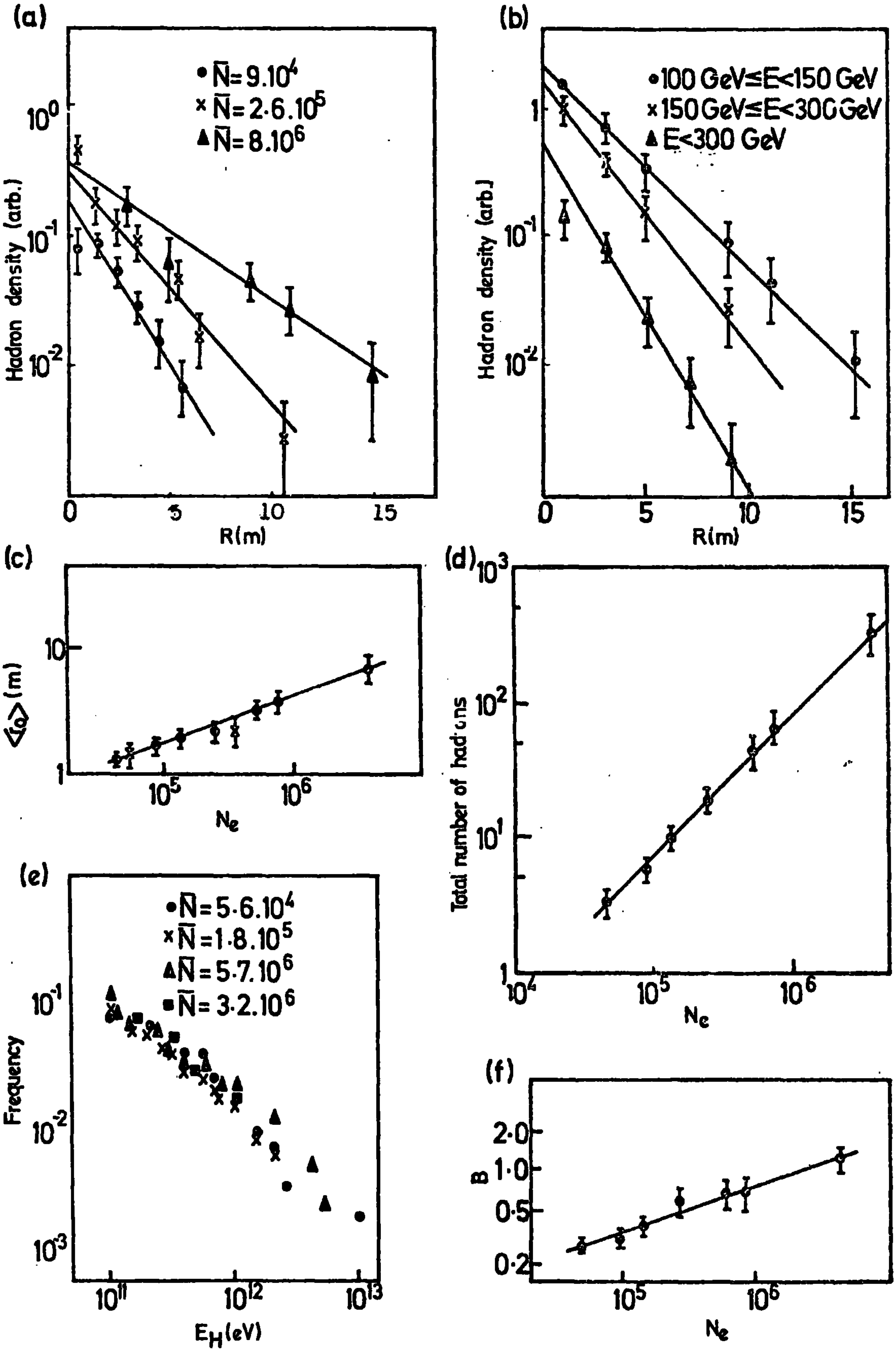

Figure 3.3 Summary of the data of Kameda et al (1965)

3.6 Chatterjee et al. (1967)

This group has studied the nuclear active particles of energy $\geqslant 50$ Gev in E.A.S. of size 3.10^4–3.10^6 particles at the altitude $800 g/cm^2$, using a total absorption spectrometer. Showers with core distance < 10 m from the centre, at zenith angles $< 20^{\circ}$ are accepted. The uncertainty in the energy estimate is $\leqslant$ 40%. The error in core position is 1–2 m in individual showers.

The lateral distributions are well represented by an exponential function defined by:

$$\rho_n(N_e, r, > E) = A \exp(-r/r_o),$$

where A, the density in the core, is given by

$$A = 8.2\ (N_e/2 \times 10^7)^{0.097E^{0.28}}$$

r_o is given by:

$$r_o = 13.3\ (Ne/2 \times 10^7)^{0.39-0.049E^{0.28}} \times (E/50)^{-0.55}$$

for $0 \leqslant r \leqslant 15$m , $50 \leqslant E \leqslant 1\,600$ Gev and $3 \times 10^4 \leqslant N_e \leqslant 3 \times 10^6$

The dependence of the lateral distribution on shower size can be seen in figure 3.4a. It is clear that as the ~~energy threshold~~ shower size increases ~~this dependence weakens~~ The lateral distribution flattens. Figure 3.4b shows r_o as a function of shower size. The energy dependence of the lateral distribution is seen in figure 3.4c. For a given size group, the lateral distributions steepens with increasing energy threshold. The total number of N-Component of a given energy threshold in a shower of size N_e is expressed by:

$$N_n(> E, N_e) = 1.75\ N_e^{0.78}\ E^{-1.1}$$

This relation is shown in figure 3.5d.

For each energy threshold the integral energy spectrum was obtained by integrating the fitted lateral distribution.

They have found that the integral energy spectrum for all hadrons

Figure 3.4a

The lateral density distribution of nuclear active component of energy $>$ 50 Gev for different shower sizes. For shower size range 5.6 - 100×10^4, $r_o = 3.62 \pm .20$, for 3.2-5.6×10^5, $r_o = 6.08 \pm 2.9$, and for 1.8-3.2×10^6, $r_o = 8.0 \pm 0.87$

Figure 3.4b

The variation of r_o with shower size, N_e, for two different thresholds $E > 50$ Gev and $E > 100$ Gev. For $E > 50$ Gev the slope is $0.23 \pm .02$ and for $E > 100$ Gev, 0.18 ± 0.2.

Figure 3.4c

The lateral structure of nuclear active component for different energy threshold. It can be seen that for $E \gg 50$ Gev, $r_o = 5.36 \pm 0.21$ - $E \gg 200$ Gev, $r_o = 3.19 \pm 0.17$ - $E \gg 800$ Gev, $r_o = 1.87 \pm 0.17$.

~~The lateral distribution can be represented as:~~

$$\Delta_N(r) = \Delta_N(0) \exp(^{-r}/r_o)$$

Figure 3.4d

The total number of hadrons of a given energy threshold as a function of shower size.

The integral energy spectrum of hadrons for various shower sizes.

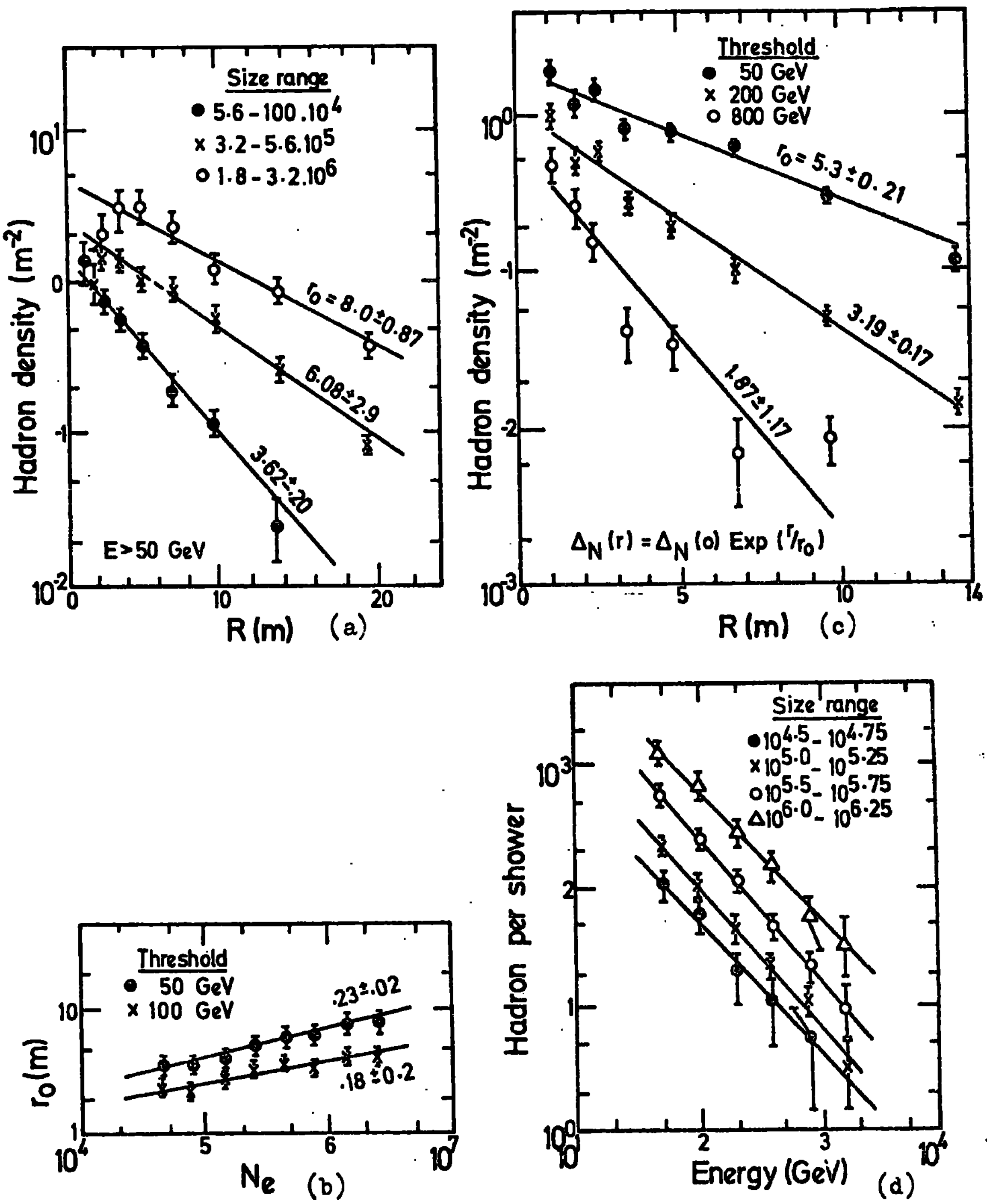

Figure 3.4 Summary of the data of Chatterjee et al (1967)

in a shower can be fitted to a negative power law of the same exponent independent of size. On the basis of their results they concluded that the observed increase r_o with N_e cannot be explained by models in which P_T distributions and ~~ineluesticity~~ inelasticity are invariant (Murthy et al. 1967); nor can this be explained by any conceivable change in primary composition with energy.

To understand the flattening of the lateral distribution with shower size a preliminary calculation based on a model with some changes in collision behaviour above 10^5 Gev was tried (Murthy 1976), these changes are:

(i) Increase in inelasticity,

(ii) Increase in average transverse momentum of produced particles,

(iii) A faster increase in multiplicity of created particles.

They argue that, the behaviour of the lateral distribution can also be due to an increase in P_T of only the surviving particles with increasing primary energy. Of course in this case they noted that the energy spectra, the size variation and the number of different components as obtained from the usual models will remain unaffected.

Another possibility which has to be tried quantitatively as far as they are concerned is the passive baryon hypothesis (Smorodin 1967). In this model the effective interaction mean free path would increase with energy and hence the effective production height of hadrons of a given energy threshold at a given level increases with primary energy.

3.7 Vatcha and Sreekantan (1972)

The characteristics of high energy nuclear active particles of energy 25 Gev to 10^4 Gev in air showers of size 5.10^4 - 3.10^6 particles at 800 g/cm^2 have been studied using a $2m^2$ multiplate cloud chamber of dimensions 2m x 1.5m x 1m with 21 iron plates inside, each of 2cm thickness, corresponding to a radiation length, and the whole plate assembly corresponds to about 2.2 interaction mean free paths. The chamber was shielded on the top by an absorber equivalent to about 5.5 radiation lengths of iron and lead.

They calculated the hadron density by the following formula,

$$\Delta\,(N_e, r, > E_H) = \frac{H(N_e, r, \; E_H)}{N(N_e, r)}\, F$$

where H is the observed number of hadrons in the bin of average size N_e, average distance r and hadron energy greater than E_H; N is the observed number of showers in the same bin and F is the geometrical factor of the cloud chamber. Some typical cases are shown in figure 3.6a for hadron energies greater than 50 Gev for two size regions. In this experiment they have observed a tendency for the lateral distribution of high energy hadrons to flatten with increasing shower size.

The variation of the number of hadrons per shower as a function of shower size has been determined for different threshold energies of hadrons, they have expressed it in the form of

$$N_n(>E) = A\, N_e^{\alpha(E)}$$

It has been observed that $\alpha(E)$ decreases from about 0.8 at $E > 50$ Gev to $\sim$ 0.4 for $E > 400$ Gev. The result is shown in figure 3.6b. The energy spectrum of hadrons in the energy range 50 - 800 Gev may be expressed as a power law of the form:

$$N_n(>E) = B\, E^{-\gamma(N_e)}$$

Where γ increases from 1.4 at 5.10^4 to 2.2 at $N_e \sim 4.10^5$ and remains at this high value up to 3.10^6 particles. The integral energy spectrum is shown in figure 3.6c.

The charge to neutral ratio has been determined for hadrons of different energy and at various core distances for showers of different sizes.

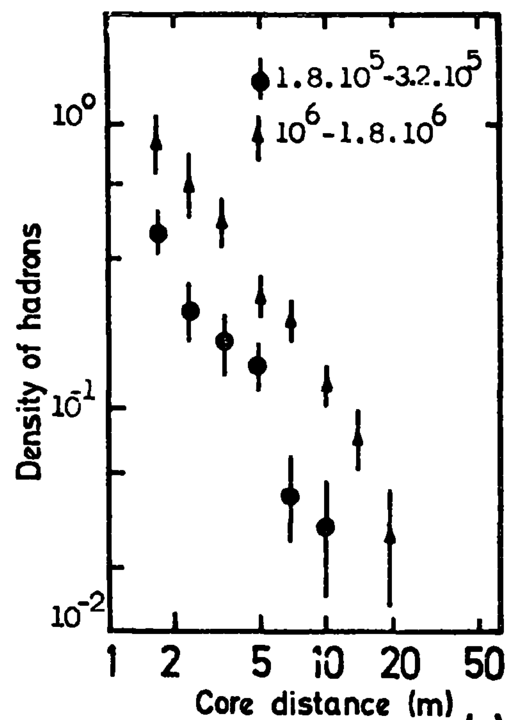

The lateral distribution of hadrons (> 50 Gev) associated with E.A.S. in two typical size groups.

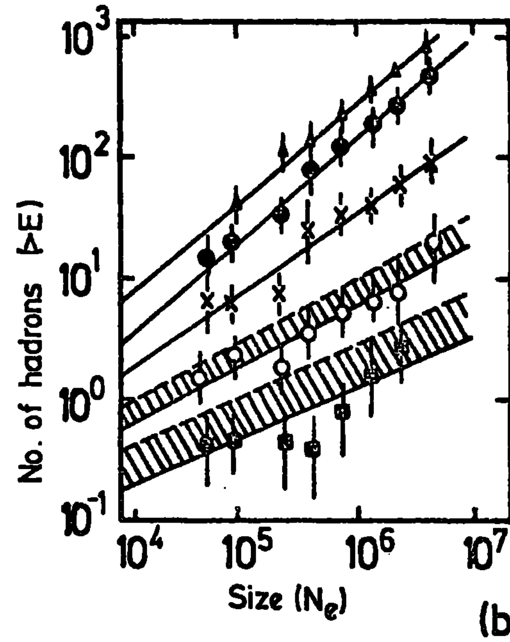

The variation of the number of hadrons of different energy threshold with shower size. Values of E(Gev) are 25; 50; 100; 200; 400. The straight lines are the least square fits. The hatched regions pertaining to hadrons of energies > 200 Gev and > 400 Gev.

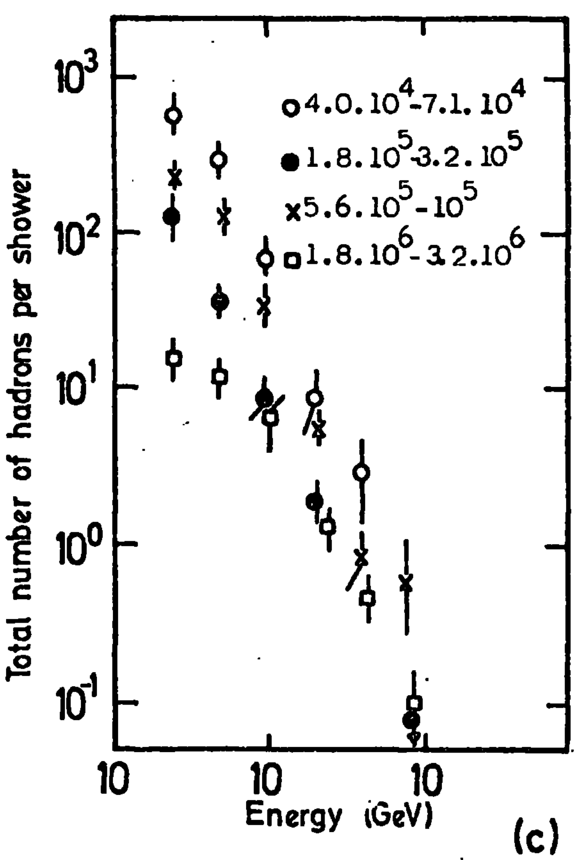

The integral energy spectrum of hadrons of energies ~~from~~ greater than 25 Gev to ~~greater~~ 800 Gev associated with E.A.S. of sizes ranging from 4.10^4 to $3.2.10^6$.

Figure 3.6 Summary of the data of Vatcha and Sreekantan (1972)

3.8 Matano et al 1973

A study of hadrons of energy $\geqslant$ 770 Gev in air showers of size 10^4 to 10^7 at sea level and Norikura (2770 m) with an identical hadron detector has been carried out.

The experimental arrangement used was a hadron detector with a total area 6 m^2 and consisted of 24 units of the scintillators of 0.25 m^2 combined with the same area emulsion chamber installed below the 20 m^2 spark chamber of the air shower array. The energy of hadrons is estimated by the darkness of spots on the x-ray film of the cascade shower produced by a hadron in the emulsion chamber. The energy is also determined from the burst size detected with the scintillators.

The observed energy spectrum are shown in figure 3.7a. The points enclosed with an open circle represent the number of hadrons determined by the emulsion chamber. The slope of the energy spectrum is 1.7 for energy above 770 Gev in showers of size 10^6 and 1.8 in the energy interval 770 Gev to 1 Tev, and 2.6 for energy above 2 Tev for the sizes 10^4 to 10^5 particles the spectra at 735 g/cm^2 have also similar slope.

The observed energy spectra at sea level are compared with the cloud chamber data obtained by Kameda et al, the result is shown in figure 3.7b it can be seen that both results are compatible within the statistical errors.

For a shower size 10^5 particles the number of hadrons with energy above 1.5 Tev at sea level is 0.35 ± 0.20.

The variation of hadrons with shower size is shown in figure 3.7c for various energy regions of hadrons. The slope is about 1.0 for all groups. In figure 3.7d the total number of hadrons per shower as a function of shower size is plotted.

3.9 Conclusion

From the summary presented in this chapter one can conclude that:

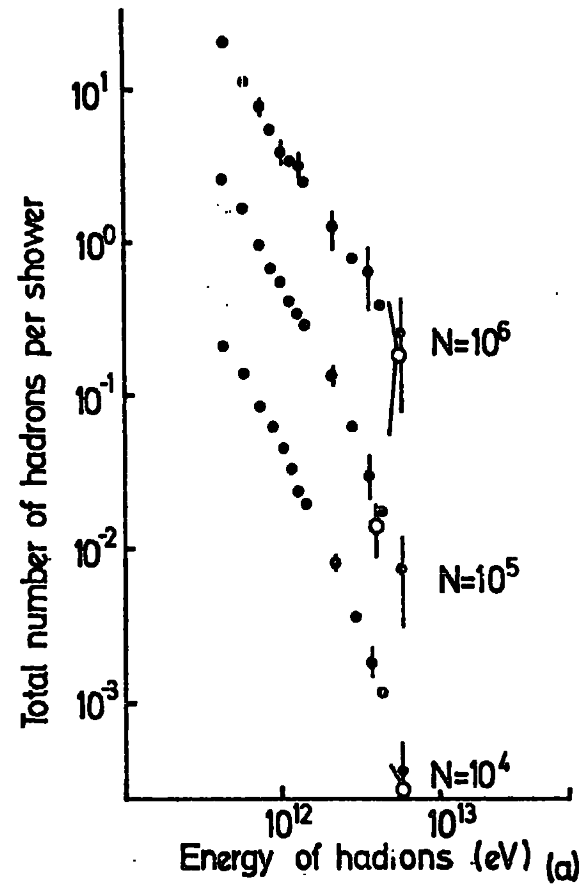

The energy spectra of hadrons in showers of different sizes.

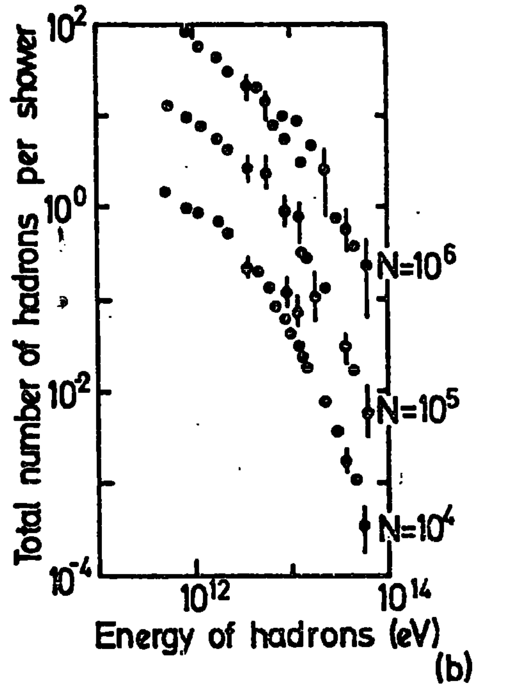

The Comparison of energy spectra of hadrons with the cloud chamber data at sea level.

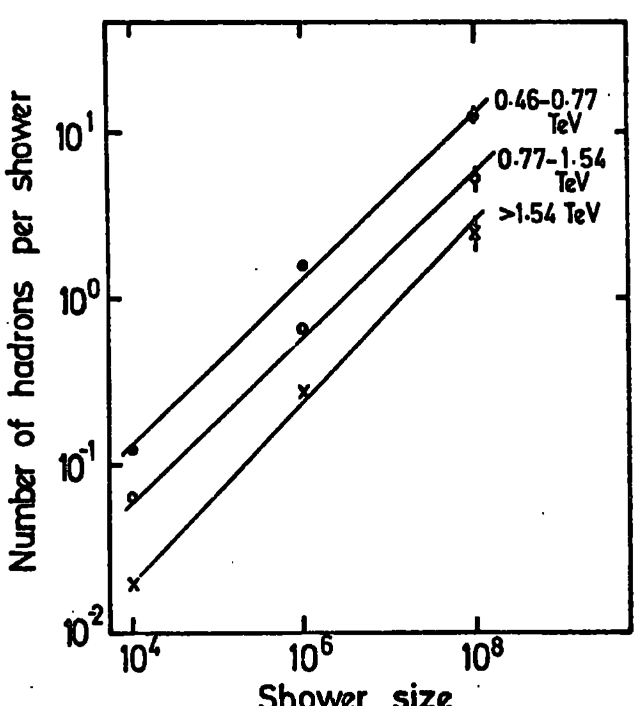

The variation of hadrons with shower size for various region of hadron energy

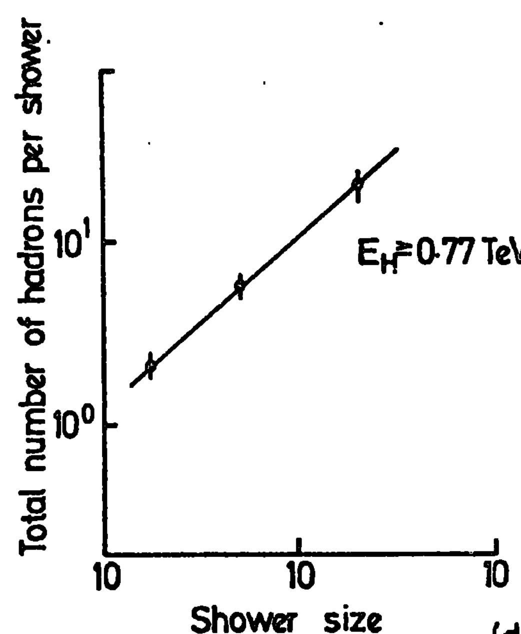

The total number of hadrons per shower as a function of shower size.

Figure 3.7 Summary of the data of Matano et al (1973)

1. The integral energy spectrum of nuclear active particles can be expressed as a power law with exponent, $\gamma \approx 1$ which increases as the hadron energy increases.
2. The lateral density distribution of hadrons becomes steeper for particles of higher threshold energies.
3. The lateral distribution becomes flatter with increasing shower size.
4. There is a linear relationship between shower size and the number of nuclear active particles associated with the showers. The slope of this line varies with hadron energy threshold.

CHAPTER 4

AIR SHOWER ARRAY

4.1 Introduction

In conjunction with two major Cosmic ray detectors, the neon flash tube chamber and muon spectrograph, the MARS group started to build an air shower array.

At the early stage of the work the author was appointed to help in the construction of some of the scintillators. The contribution to this work ended by constructing three 2 m^2 detectors. In this chapter one of these detectors is described.

4.2 The 2 m^2 scintillation detectors.

Among the air shower array there are six 2 m^2 scintillators which sample the electron density of the air shower and also give information on the arrival time of shower front for the determination of the direction of the shower axis. This type of detector measures 2m x 1m x 2.5cm slab of NE 110 plastic scintillator. The phosphor is viewed by four 5" diameter EMI 9579 B photomultiplier tubes for electron density measurement and a 2" diameter philips 56AVP photomultiplier tube for fast timing. Plate 4.1 shows the features of this type of detector. The 5" photomultipliers view the long edges of the phosphor without light guide. The 2" diameter photo tube (fast) is attached with NE 580 optical cement to one of the long edges of the phosphor. The head amplifier and the E.H.T. distribution unit are attached to the wall of the detector box. The box of the scintillator is made of wood and is weather proofed with bitumen paint and aluminium foil. The detector box rests on an angle iron bed to lift the detector up from the surface of the ground to prevent damp and let the air circulate all around the box. The detector is housed in a weather proofed hut.

PLATE 4.1

A TYPICAL 2 m^2 SCINTILLATION DETECTOR

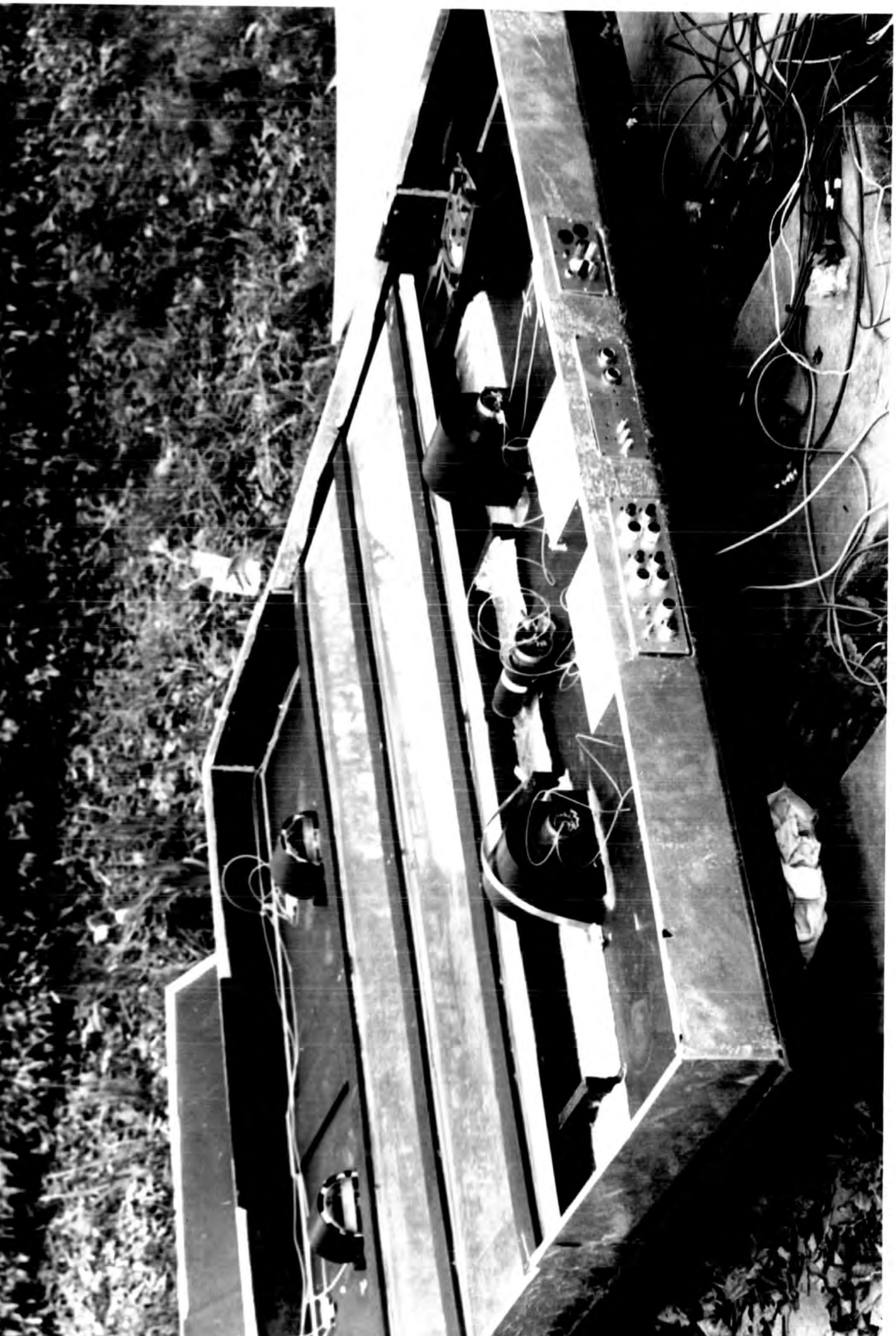

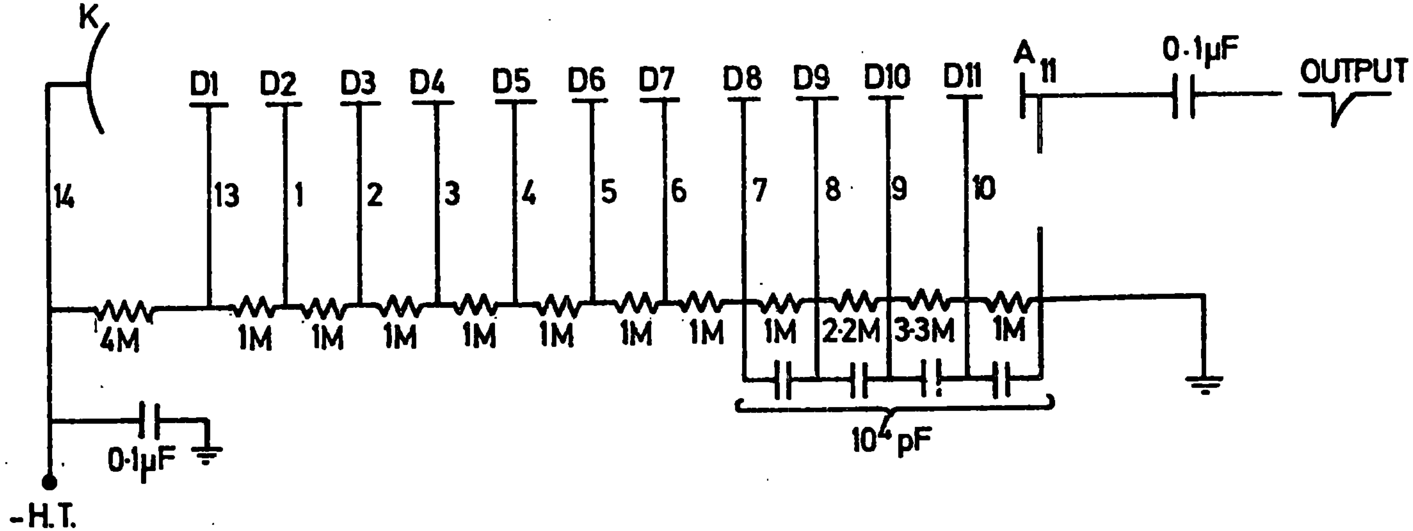

Base circuit for EMI 9579B P.M.I.

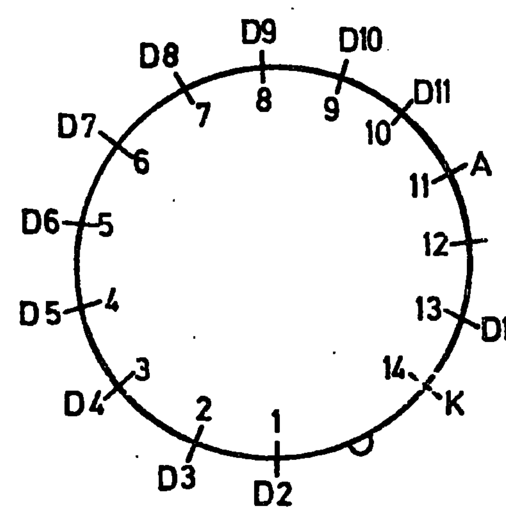

Figure 4.1 Base: 14 pin Mullard FE1001 EMI B14A viewed from beneath. (After Smith 1976)

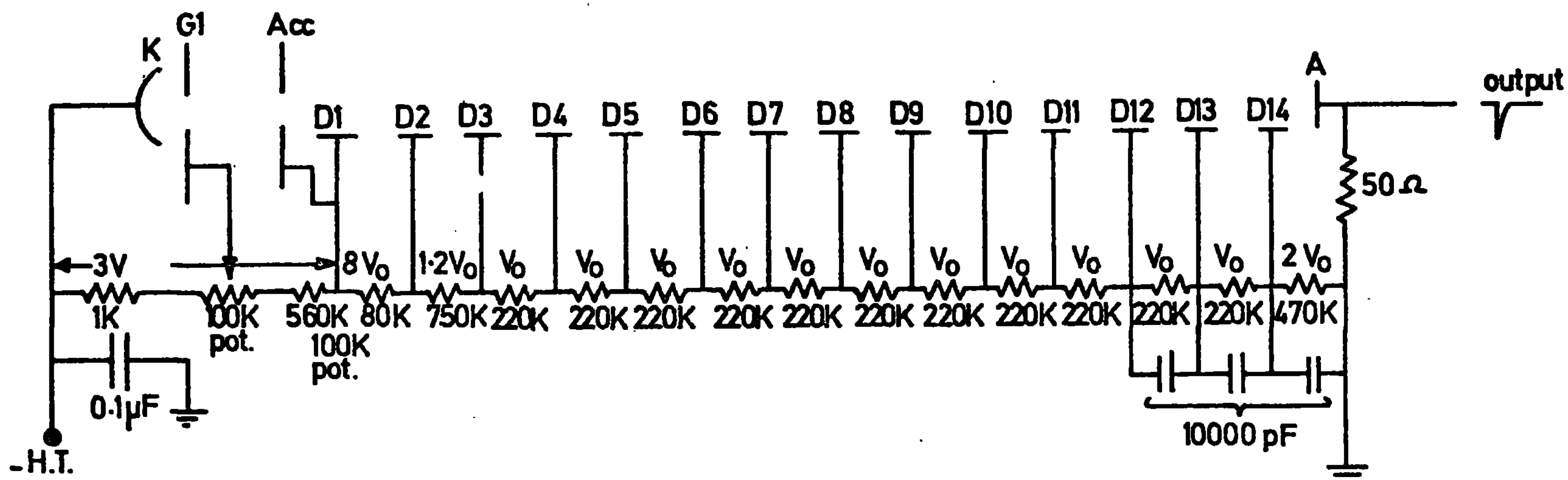

Base circuit for PHILIPS 56 AVP P.M.T.

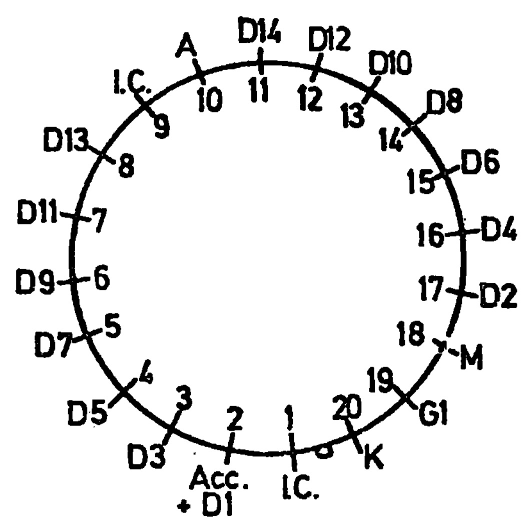

Figure 4.2 Base: 20 pin Mullard FE1003 viewed from beneath. (After Smith, 1976)

The high voltage to the two types of photomultipliers is supplied by two E.H.T. units. The 'slow' tubes operate on an ortec 456, located in the laboratory. The fast photomultiplier operates with an NE 4646 E.H.T. unit. The high voltage is connected to a resistor chain through a co-axial cable. Since the tubes are not exactly similar the E.H.T. distributer enables each tube's voltage to be adjusted independently. Figures 4.1 and 4.2 show the base circuit for the slow and fast phototubes respectively. The slow tubes operate on a negative E.H.T. supply giving a negative out put pulse with an exponential decay time with a constant of 20 microseconds.

4.3 The response of P.M.T. for various light inputs

Since the phototubes are used to convert the light output of the scintillators into electrical pulses, it is necessary to know the response of this device for various light inputs. To examine this characteristics three different light emitting devices were used; an 241 Am alpha-source in NE 110 plastic scintillator, a neon tube and a pulsed light emitting diode. The variation of the light was made by two crossed polarised filters. In using the 241 Am alpha source in spite of producing fast rise time pulses (similar to the actual pulses from the scintillators) the intensity of its light output was too weak. In the case of the neon tube the rise time of the pulse was too slow, different to the actual pulses produced by the scintillation counters. In this case the phototube pulse rise time was affected by the light output rise time of the neon tube. The light emitting diode (L.E.D.) was used satisfactorily. In figure 4.3 the variation of the angle, θ between the crossed polariser and the output after photomultiplier is seen at an operating voltage of 1.8K.v. Figure 4.4 shows the variation of $\cos^2\theta$ as a function of photomultiplier

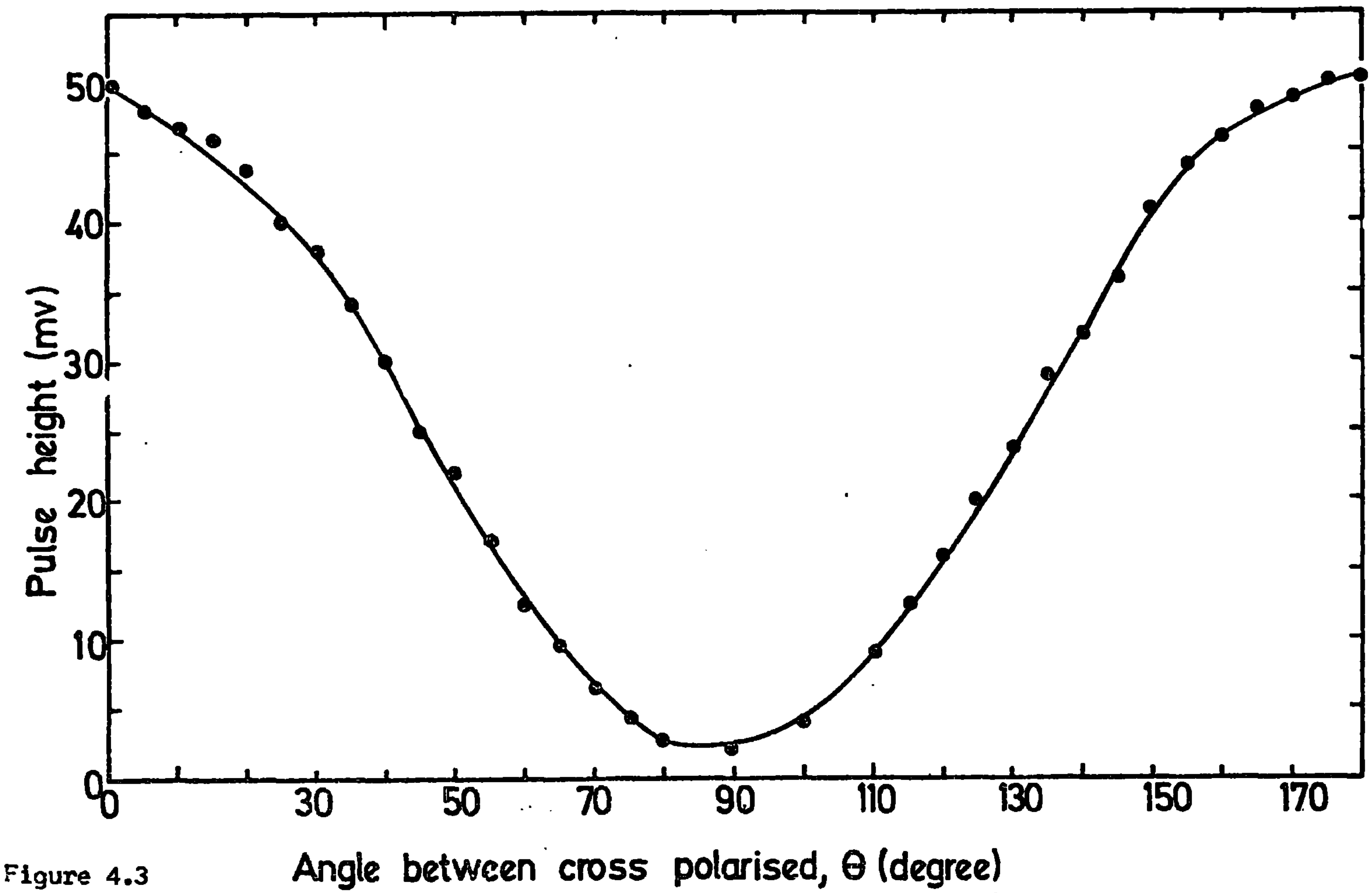

Figure 4.3

The variation of the pulse height with light intensity, E.H.T. 1.8 K.V., light emitter : L.E.D., P.M.T. 9579B

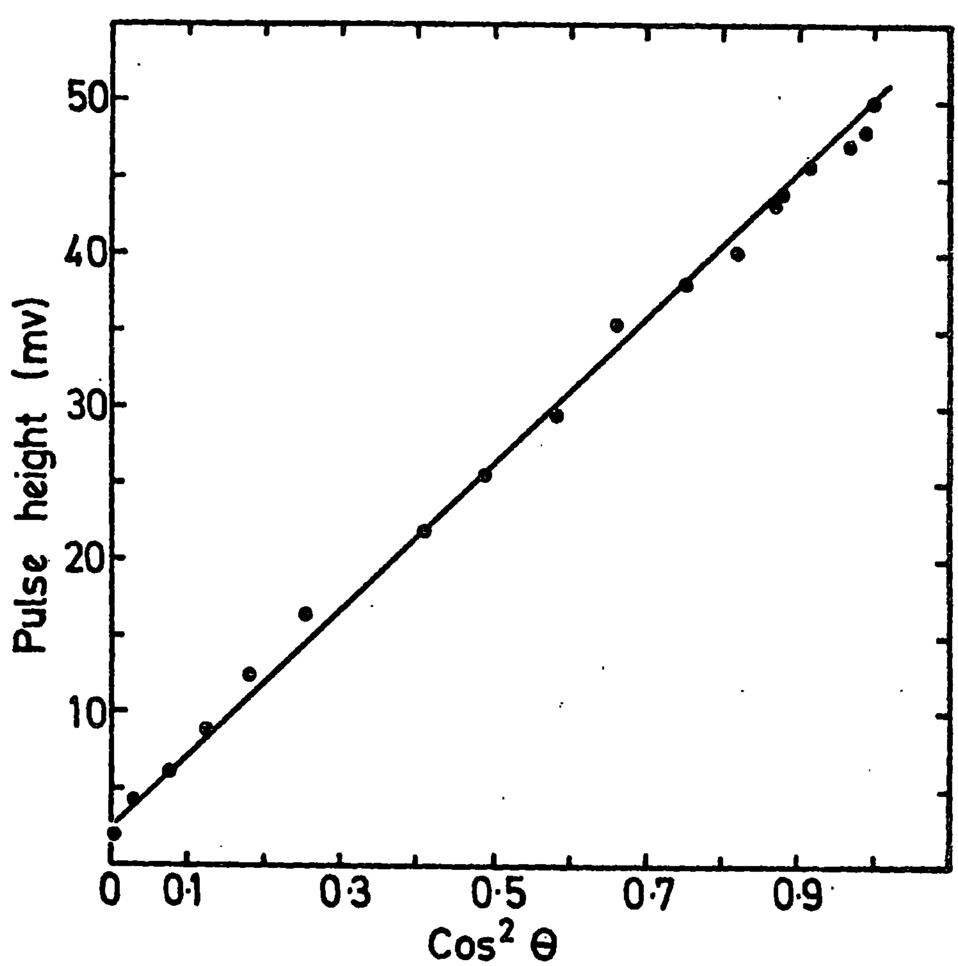

Figure 4.4 The variation of the output pulse with $\cos^2\theta$, where θ is the angle between crossed polariser, E.H.T. = 1.8 K.V, light pulser, L.E.D., P.H.T. 9579B

output. To produce this plot the output of the photomultiplier tube was connected to a 512 channel pulse height analyser, after producing a distribution the mean was worked out and related to the angle θ, of the crossed polarising device. This investigation was made for different tubes. It was found that the linearity of the photomultipliers is satisfactory.

4.4 The linearity of the pulse height analyser.

Before using the pulse height analyser it was necessary to examine its linearity, for this purpose a reliable pulse generator was used and the response of the P.H.A. was investigated. Figure 4.5 shows the result of this investigation.

4.5 The response of the photomultiplier to the E.H.T. supply

Another important characteristics of the photomultiplier tubes to be known is their response to the high voltage power supply. For this investigation the power supply voltage was altered for a fixed θ, (the angle between crossed polariser. The out put voltage of the phototube for each value of the high voltage was found. The result is shown in figure 4.6.

4.6 The detector head unit

In each detector there are four slow photomultipliers. The output of each phototubes are added by a mixer-amplifier, consisting of four emitter followers which their outputs will be amplified in a μA702C differential amplifier integrated circuit after being summed. The out put, then goes to a converter to change the polarity of the pulse from negative to positive. Figure 4.7 shows the circuit of this amplifier. In figure 4.8 the input voltage against output of this amplifier is shown.

4.7 The octal buffer

Since the detectors output pulse had to be recorded both by us and

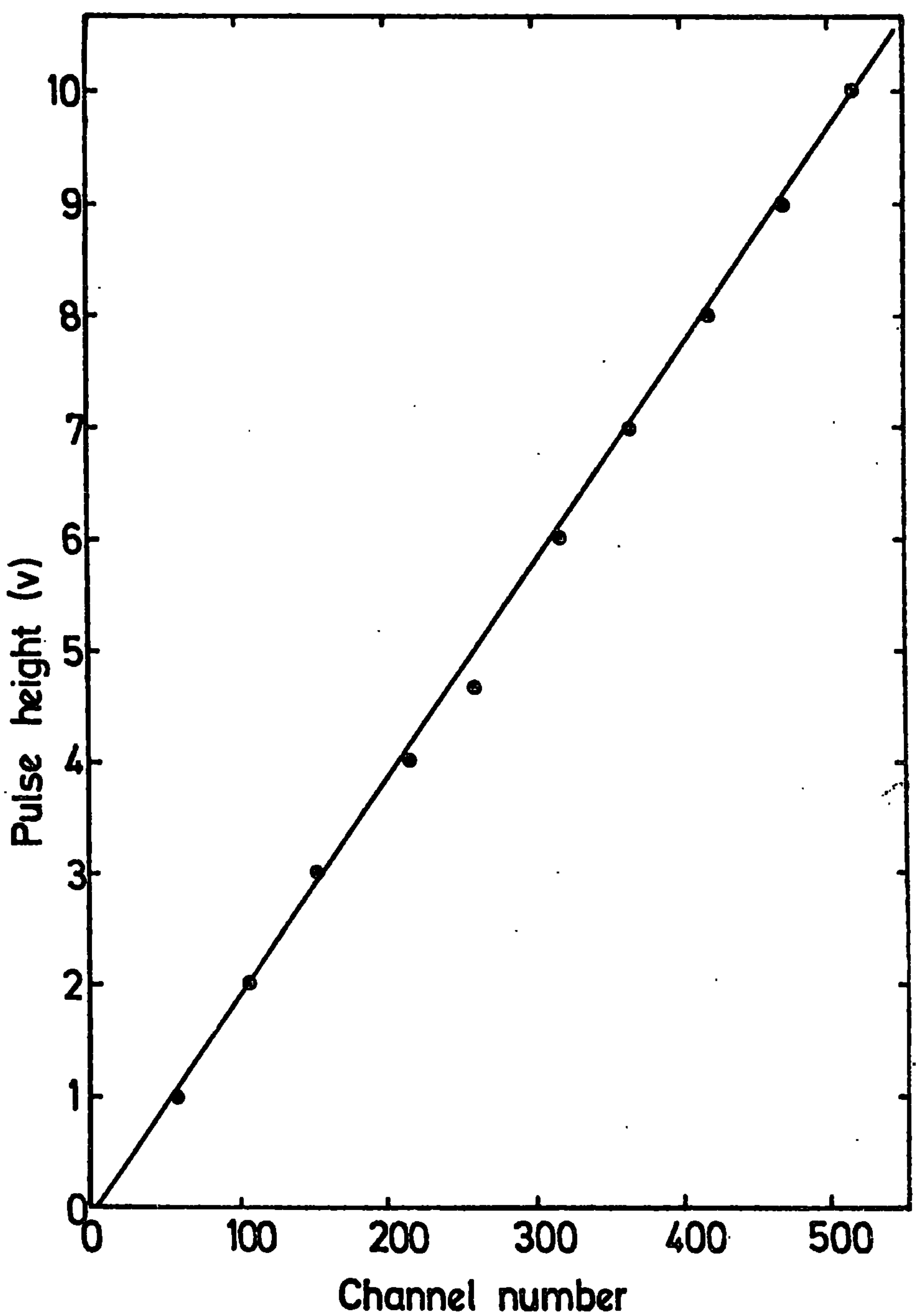

Figure 4.5 Channel number as a function of pulse height

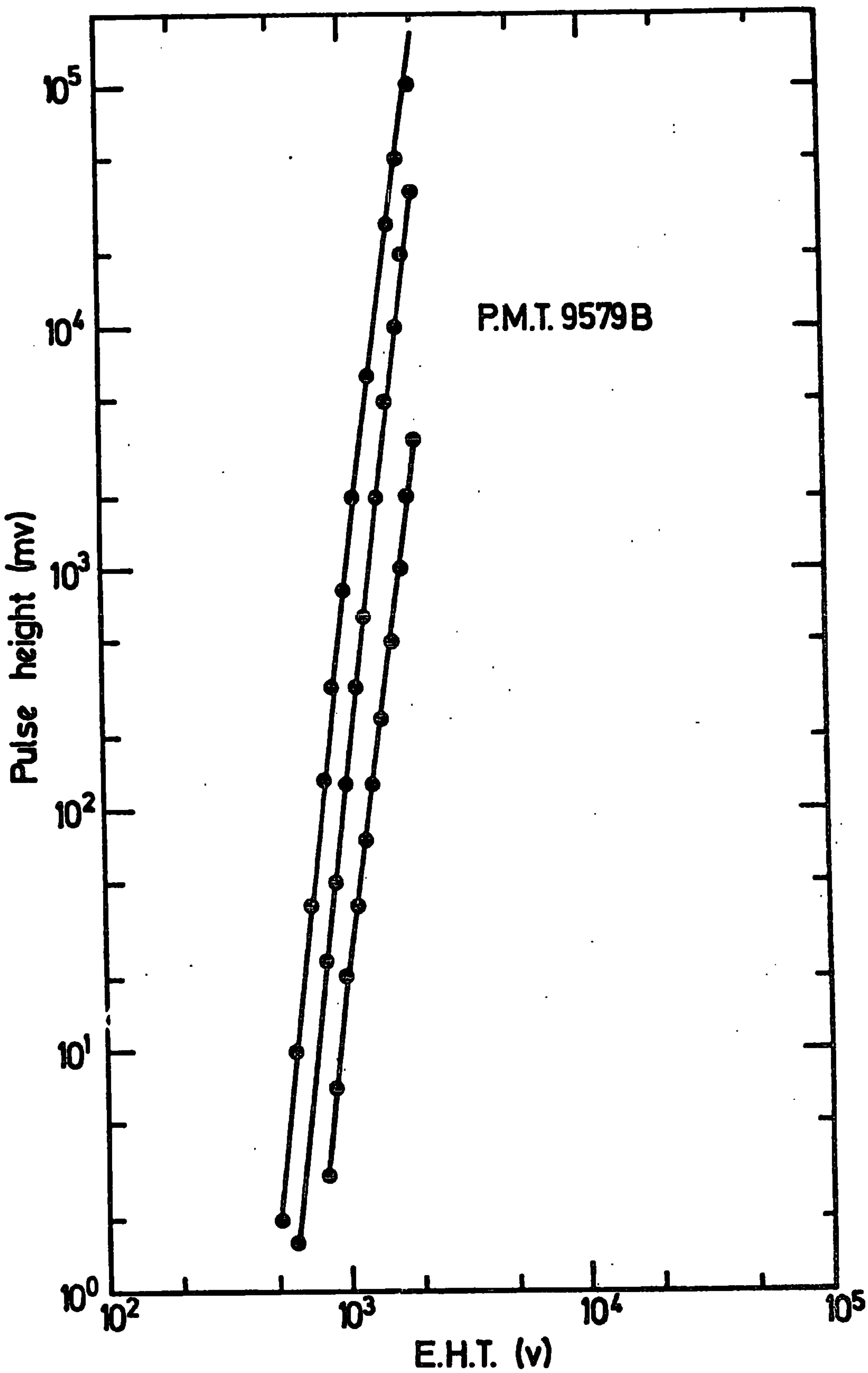

Figure 4.6 The variation of the pulse height with E.H.T., for different light intensity

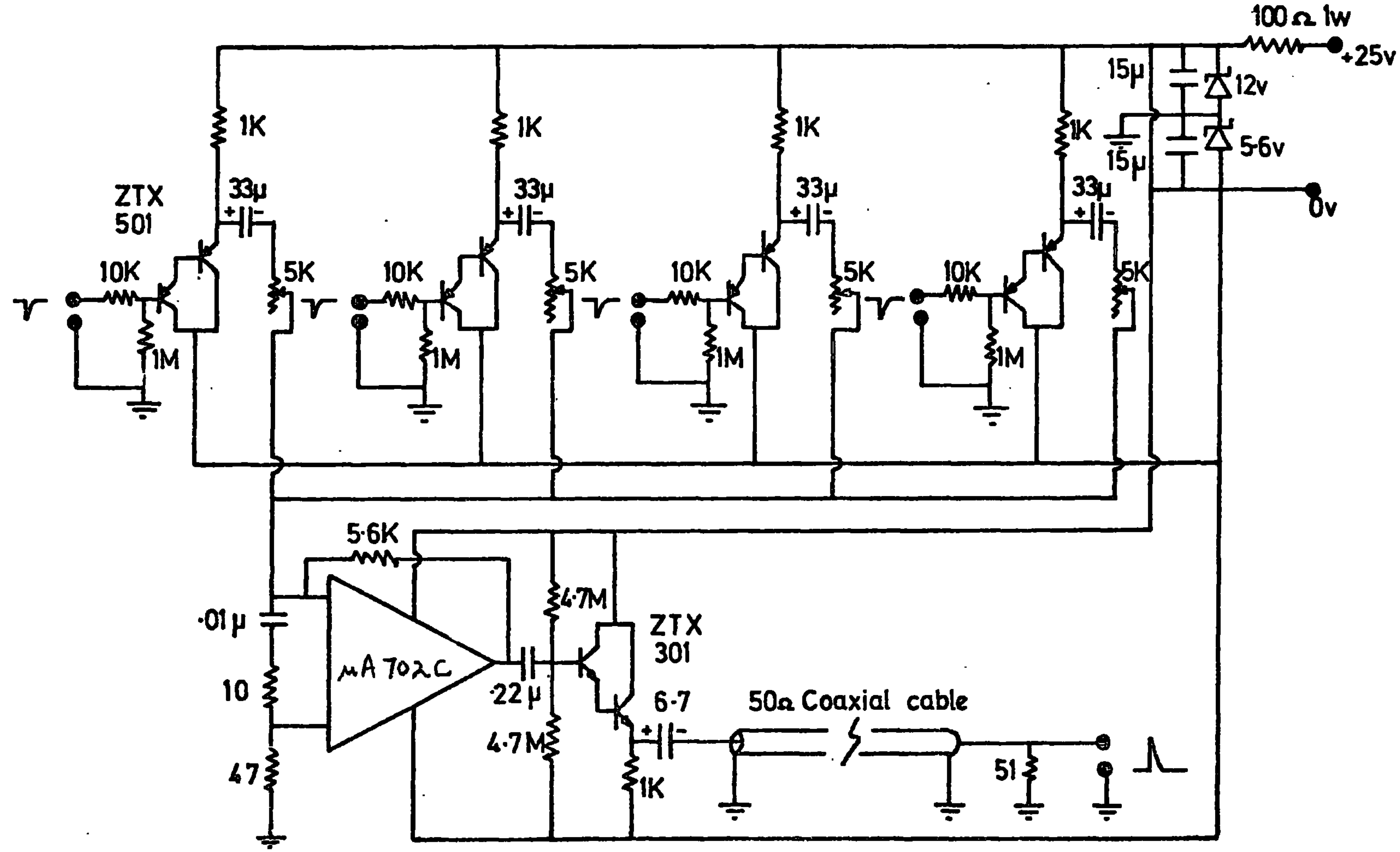

Figure 4.7 Four input ~~mixer~~ adder amplifier. (After Smith, 1976)

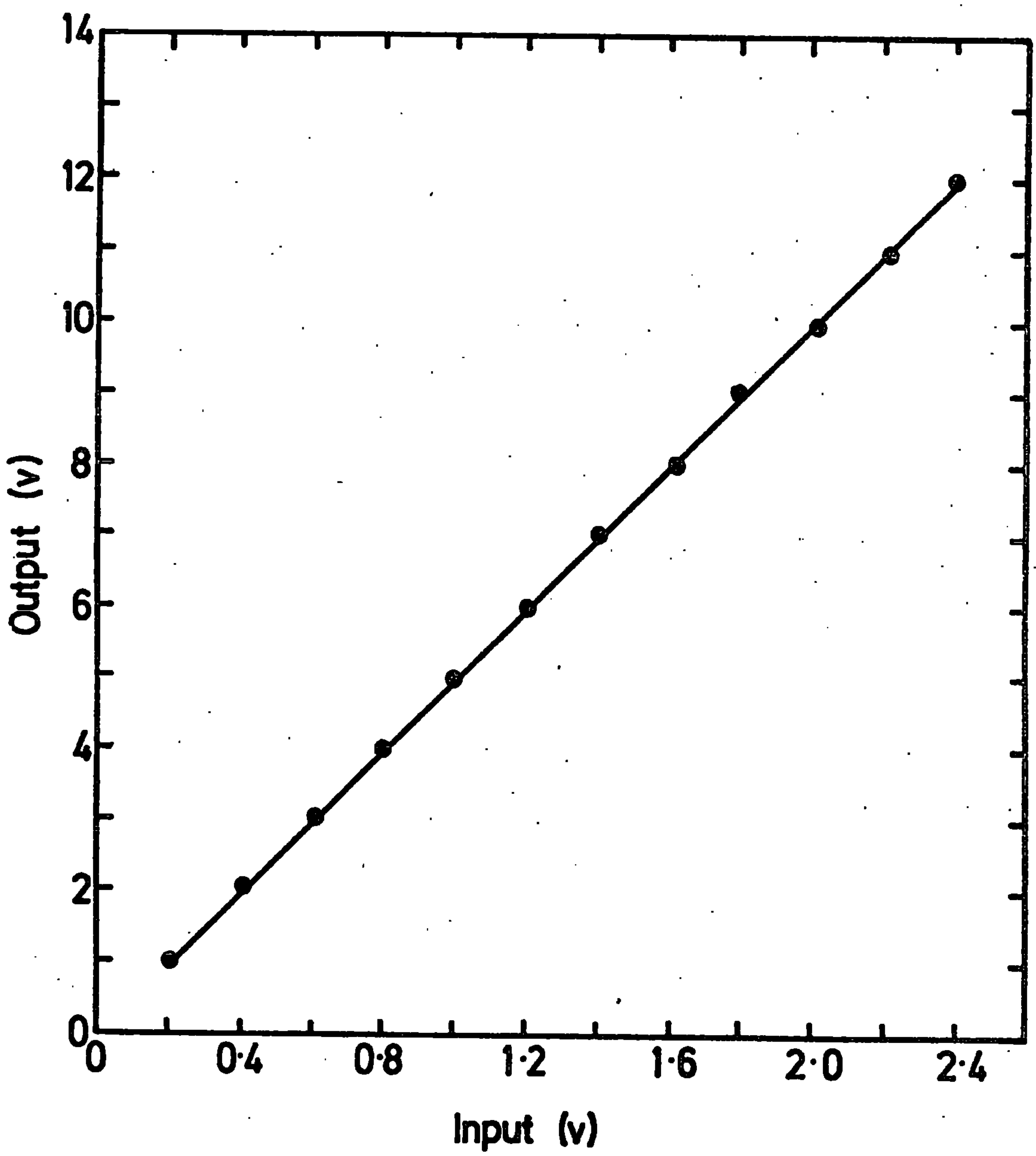

Figure 4.8 The input voltage against output of the amplifier used in the air shower detectors.

MARS group simultaneously, to prevent any affection from our electronics on the original pulse, it was necessary to feed the pulse through an emitter ~~emitting~~ follower. Figure 4.9 and 4.10 shows these emitter followers with its characteristics. This device is composed of 8 emitter followers, positive output pulse from each detector of air shower array (SARA) can be applied to each emitter follower unit. The voltage gain is positive with magnitude 0.95.

Each unit has a high input impedance equal to about 85 KΩ and the output is terminated by a 50-Ω resistor.

4.8 Calibration of the detectors

The procedure for calibration of the detectors as far as the electron density measurement is concerned is decided, to adjust each scintillator photomultiplier tubes such that after dividing the overal pulse height from all 4 photomultiplier tubes by 100 mv, the particle number per square meter at the scintillator will be found. The calibration of the air shower array was carried out by W. Rada.

Figure 4.11 shows the disposition of the Durham Extensive Air shower array. In figure 4.12 the general response of the array is shown (Rada et al 1975 Munich Conference).

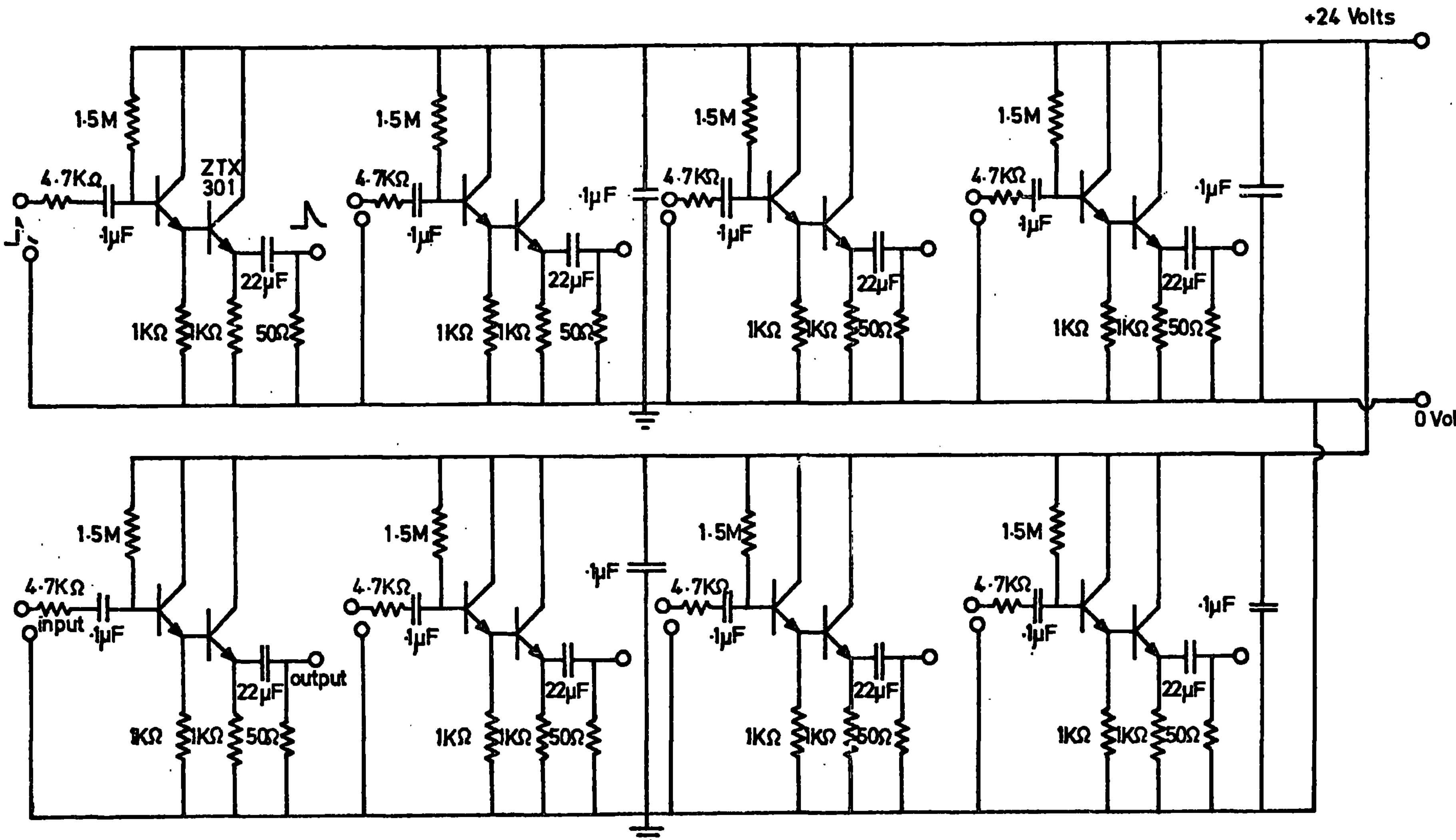

INPUT RESISTANCE ≃ 85 KΩ
OUTPUT " " 50 Ω
GAIN = ·95

Figure 4.9 EMITTER FOLLOWERS

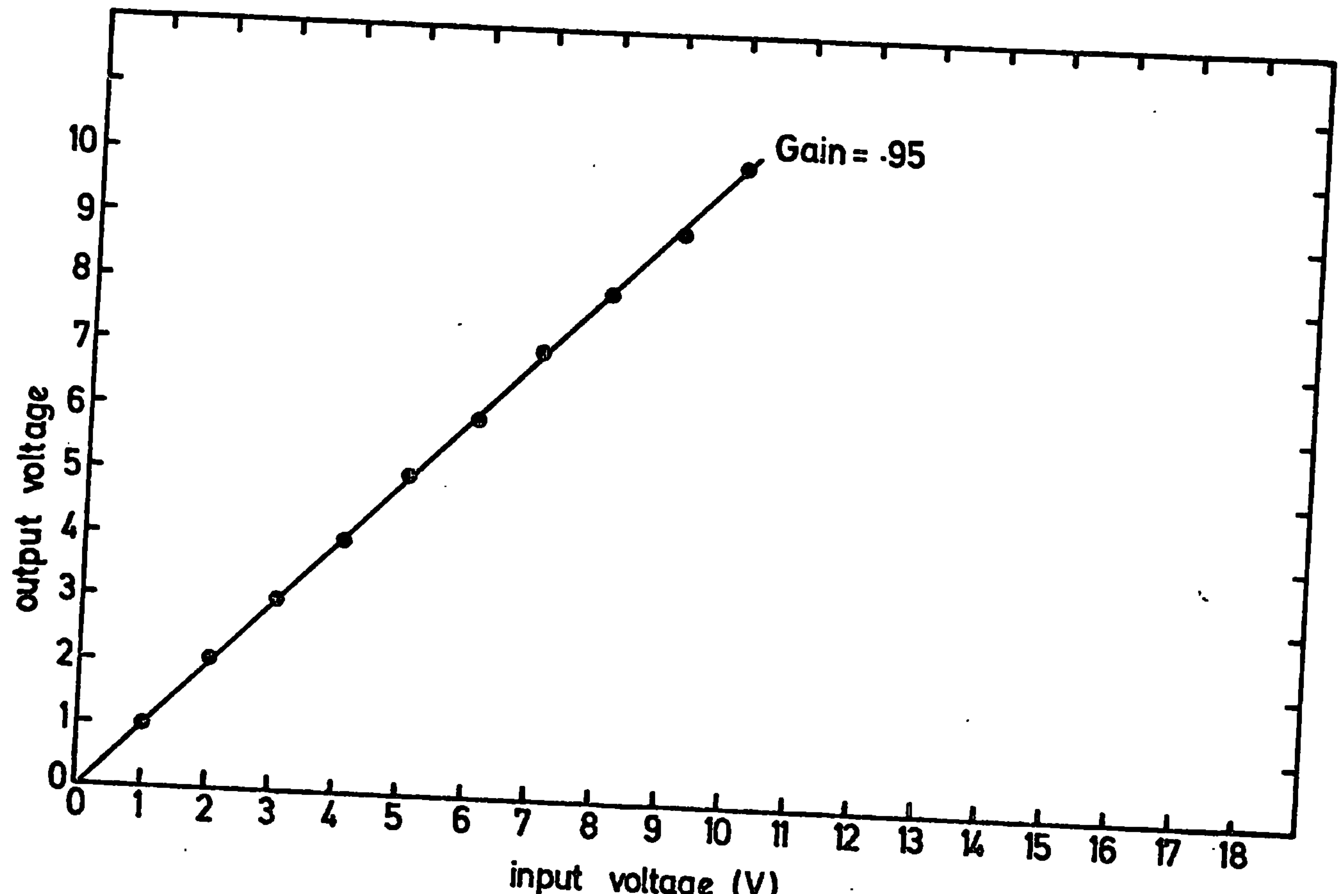

Figure 4.10 The variation of the output voltage against input of the Emitter Follower.

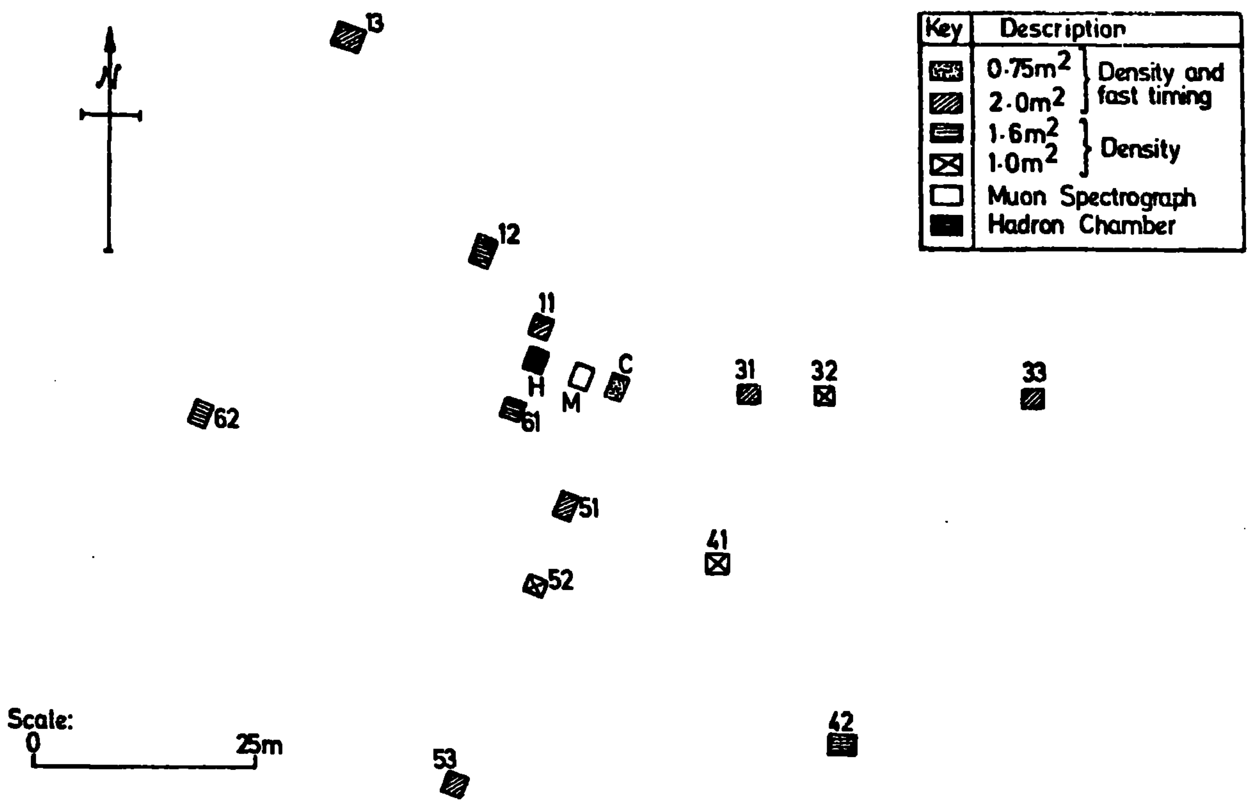

Figure 4.11 . The Durham Extensive Air Shower Automated Research Array.

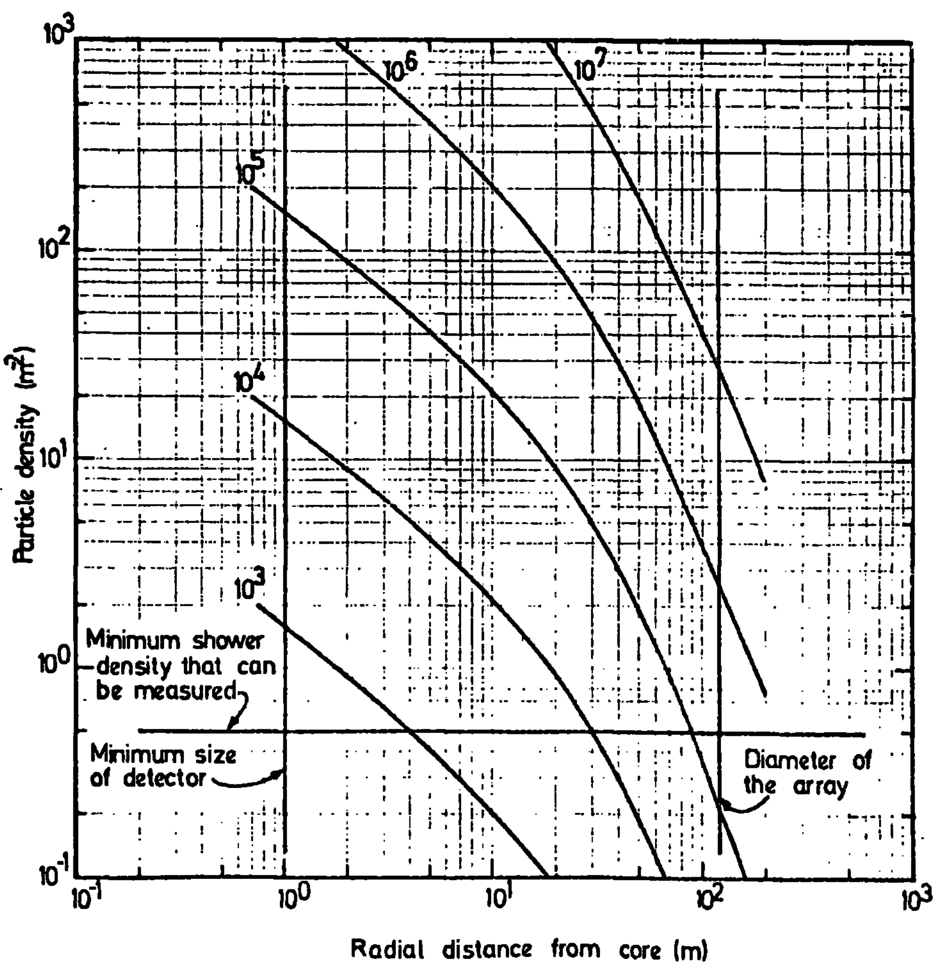

Figure 4.12 The response of Durham E.A.S. Array (Rada et al., 1975)

CHAPTER 5

THEORY OF BURST PRODUCTION IN LEAD AND IRON ABSORBERS

5.1 Experimental methods of hadron energy estimation

5.1.1 Introduction

Different methods can be employed to measure the hadron energy. The techniques vary according to the energy range concerned. These methods are as follows:

5.1.2 The direct method of energy estimation

Charged particles ionize the medium through which they pass. The rate of ionization loss is a function of the velocity or kinetic energy of the particles. The ionization loss for nonrelativistic particles is inversely proportional to the square of the velocity. At low energies it is possible to estimate the proton energy spectrum by observing the rates of particles stopped by absorbers of suitable thickness. Another way of energy determination for low energy charged particles is to put them in a magnetic field and measure the curvature of the particle in the magnetic field, from this measurement the momentum of the particle is determined. By increasing the magnetic field strength the range of energy measurement goes up. By this method the maximum measureable energy extends up to $\sim$200 Gev.

5.1.3 The nuclear interaction method

This method is applicable to particles with energy more than 1 Gev. The nuclear interaction takes place in a thick absorber and in such collisions the produced pions or the evaporation neutrons from the target nuclei can be detected.

5.1.4 The ionization calorimeter method

As a nuclear active particle, interacts with a target material a high proportion of its energy goes into the electron-photon cascades which develop from the neutral pions (π^0). These pions are created in the interaction of primary particle as well as the subsequent interactions of the secondary charged pions. By this method the whole energy of nuclear active particles is absorbed by a target of many nuclear interaction length in thickness. At different development stages of the cascade the electrons are sampled within the target. So the cascade development is known and the nuclear active particle energy is calculated.

5.1.5 <u>The burst producing method</u>

The energy of the nuclear ~~interactive~~ active particles can be estimated by the electron-photon cascades or 'bursts' which develop from neutral pions (π^0) created in single interaction of colliding nuclear active particles. The apparatus for production of bursts can be made as simple as a single layer of a target material about one nuclear interaction length in thickness, above the electron measuring detector. The apparatus should be shielded by a layer of lead to absorb the electron-photon component of any accompanying air showers. Since the interaction can occur in any depth of the target, therefore the development of the cascades vary significantly and the energy estimation for individual hadrons is subject to large errors. Since only one interaction of each incident hadron is observed the fluctuation in $K\pi^0$ is another source of error for energy estimation.

5.2 <u>Production of burst in lead and iron absorbers</u>

As was mentioned earlier a method to estimate the hadron energy is producing a burst (electron-photon cascade) in an absorber and measuring the number of electrons (burst size) under the absorber and converting this burst size to hadron energy.

In the present experiment two different absorbers, lead and iron were used, under each absorber a single detector was employed to measure the number of electrons coming out of the absorbers. If the nuclear interaction processes are fully understood then the hadron energy can be determined.

This is the aim of this chapter to study the nuclear-electromagnetic cascade, produced by the interaction of hadrons, and to discuss the method used in the present experiment to convert burst size to hadron energy. For this purpose first, the pure electron-photon cascade will be discussed, then the discussion will be extended to nuclear-electromagnetic cascades.

5.3 The processes involved in building up a cascade

The nuclear active particles undergo nuclear interaction with matter. The probability of interaction follows an exponential distribution with the amount of matter passed through. After the interaction, a fraction of the energy of the colliding particle goes to the creation of a number of secondaries. This number is dependent on the primary energy among the secondaries the pions ($\pi^{\pm}$, π^{0}) are the most abundant particles. The charged primary pions can be assumed to lose all of their energy in the collision process, while nucleons would lose some fraction of their energy and travel in the absorber, carrying the remaining energy until the next interaction. The fraction of energy lost in an interaction is carried away by the secondary particles. The $\pi^{\pm}$ traverse some distance through the absorber in almost the same direction as the parent particle until they interact or somehow they leave the absorber. In the interaction, $\pi^{\pm}$ will lose almost all their energy. The charged pions can decay before interacting, but, the probability is low for a dense absorber and it can be neglected. The decay time for π^{0} is less than $\pi^{\pm}$, so neutral pions will decay rather instantaneously into two photons (γ). These photons will either materialise, producing election positron pairs, or undergo a Compton collison provided that, the energy of the electron and positron pairs are above the critical energy for the medium. Electrons lose energy predominantly by radiation (photons). This radiation in turn produces electrons. Since the produced secondaries carry energies of the same order of magnitude as that of the primaries, the energy degradation in the cascade is relatively slow and gradually the total number of the cascade increases as the cascade develops in the medium. The above processes continue until the mean energy of the electrons falls below the critical energy, at this stage of cascade development the collision losses become more important than radiation (bremsstrahlung). The total number of particles in the cascade reach a maximum. Since then, the number of particles in the cascade starts to decrease until the energy input to the cascade has gone either into excitation and ionization of atoms in the absorber or the cascade particles emerge from the absorber.

It should be noted that the above consideration was from just one-dimentional point of view, in fact the cascade development has also a lateral spread due to:

a) the transverse momentum distribution of the created neutral pions (π^0)

b) the multiple scattering of the strongly interacting particles

c) the angular separation of photons produced from π^0 decay

d) multiple scattering of electrons in the electron-photon cascade

e) the angular separation of the electrons created impair production.

As was mentioned, to simplify cascade study, first, the pure electron-photons cascade is considered, then, the nuclear cascade that is infact the skeleton of the whole cascade.

5.4 The one-dimentional development of electron-photon cascade

To answer the question: What would be the energy, and the angular distribution for electrons and photons at depth, t of an absorber.

Two possible ways can give the answer:

1) Analytical method

2) Monte Carlo method.

Approaching the problem by analytical method, means establishing a set of diffusion equations to represent the development of the shower at any depth of absorbers.

By Monte Carlo method the problem is tackled by following the primary particle and all subsequent particles produced in the absorber.

To solve the problem mathematically, Rossi (1952) set up the diffusion equations concerning the number of electrons and photons at depth, t, to the number of electrons and photons at depth (t + dt), restricting the problem to the one-dimentional development, the diffusion equations are as follows:

$$\frac{\partial \Pi(E,t)}{\partial t} = \int_E^\infty \gamma(E',t)\varphi_p(E',t)\, dE' + \int_E^\infty \Pi(E',t)\,\varphi_e(E',E'-E)\, dE' - \int_0^E \Pi(E,t)\varphi_e(E,E')\, dE' - \beta\frac{\partial \Pi(E,t)}{\partial E}$$

$$\frac{\partial \gamma(E,t)}{\partial t} = \int_E^\infty \Pi(E',t)\varphi_e(E',E)\, dE' - \int_0^E \gamma(E,t)\,\varphi_p(E,E')\, dE'$$

where $\Pi(E,t)$ represents the number of electrons of energy E at depth t, $\gamma(E,t)$ is the number of photons of energy E at depth t, β is the average ionisation loss per radiation length, $\varphi_e(E,E')$ is the differential probability per radiation length for the production of a photon of energy E' by an electron of energy E, and $\varphi_p(E,E')$ is the differential probability per radiation length for the production of an electron of energy E' by a photon of energy E.

To simplify these equations certain assumptions have to be made. The equation can be solved also numerically by integration, using exact probabilities.

5.5 Solution of the diffusion equations under approximation A and B

To solve the diffusion equations, some approximations have to be considered in the characteristics of interaction processes for the sake of simplicity. To solve the problem under approximation A the energy losses due to ionisation and compton scattering take no part in the solution. Bremsstrahlung and pair production phenomena are considered. This approximation can be made if the particle energy is large compared with the critical energy of the medium. In approximation B the above assumptions are made plus including a constant collision loss.

Both ~~theories~~ assumptions can be applied only to light material through which the cascade develops. In dense materials the total photon absorption coefficient is dependent on energy. It should be noted that in approximation A the number of electrons found is over estimated due to the neglection of ionisation losses. If the depth of absorber is measured in radiation length, the results of approximation A are independent of absorber material. This would be the case of approximation B if energies are expressed in units of critical energy.

5.6 Method of moments

In dense materials the approximation A and B are not applicable. To take into account the energy dependence of the total photon absorption coefficient and the effect of the increased track length due to multiple scattering of the shower electrons an analytical approach to the solution of the cascade diffusion equations has been used by Ivanenko and Samosudov

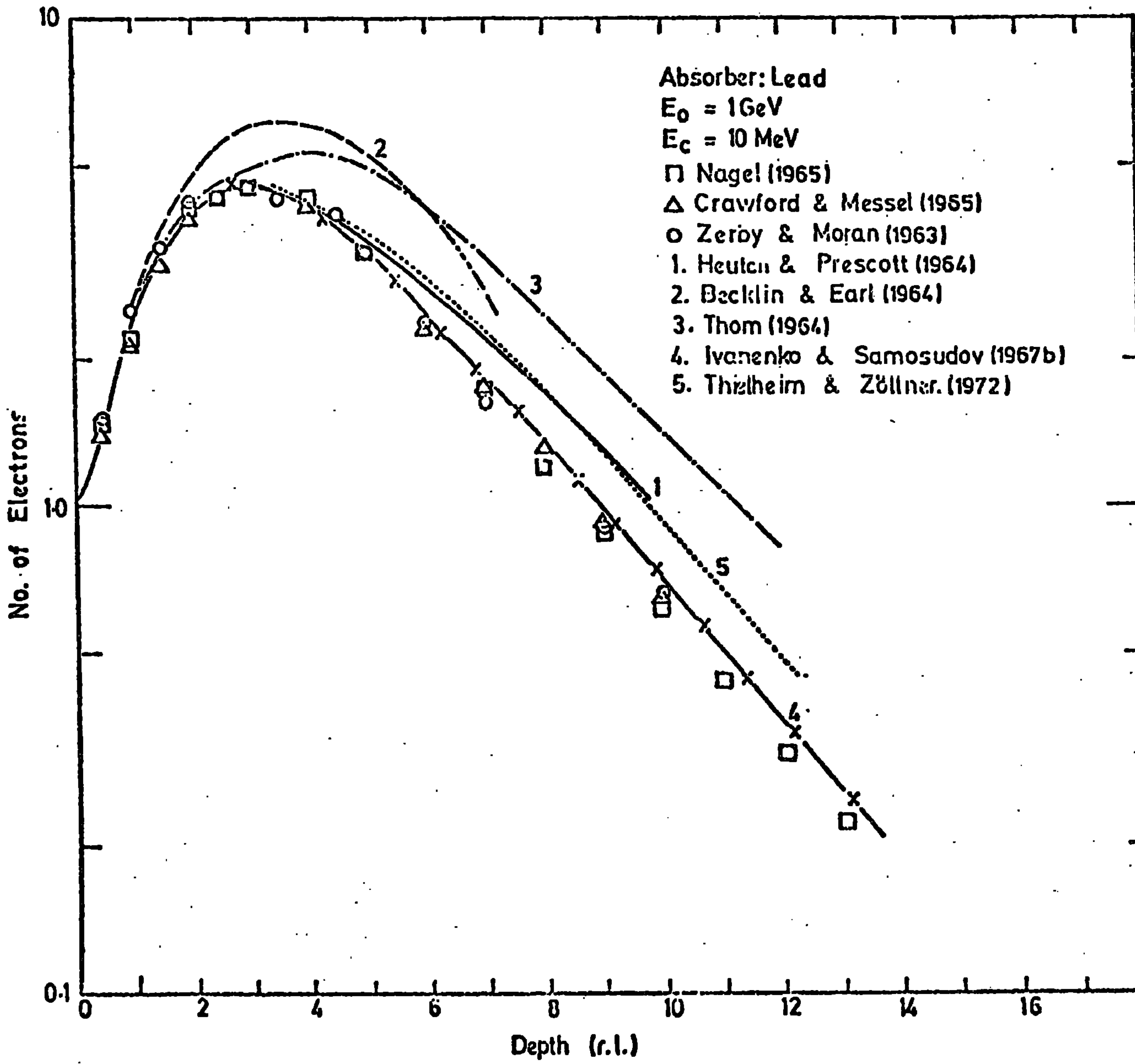

Figure 5.1 Transition curves in lead target for primary electron of energy 1 Gev. The cut-off energy E_c is 10 Mev. The points are the results of Monte Carlo calculator, curves 1, 2 and 3 refer to experiments and curves 4 and 5 are the results of calculation.

(1959, 1967a and 1967b). The method of moments calculates the average behaviour of the cascade by evaluating the cascade moments. As the order to which the moments are calculated increases the degree of accuracy will increase. Ivanenko and Samosudov evaluated the first four moments obtaining an accuracy of 5 - 10%. Calculation has been done for a wide range of energies for materials: Lead, Iron, Copper, Aluminium and Graphite for different electron energy cut-offs.

5.7 Monte Carlo procedure

The computers have made possible to simulate the cascade processes. The results obtained concerning the mean shower characteristics are subject to fluctuations due to the statistical nature of the method. To decrease the error the number of simulations at each energy has to be increased.

It should be noted that the amount of computing time needed to simulate a cascade increases with the primary energy. For this reason only the low energy cascades have been considered and simulated for dense absorbers so far.

5.8 The comparison of simulations with experimental results

A comparison of the results obtained from simulations and experiments are shown in figure 5.1 and 5.2. It can be seen that the Monte Carlo simulation made by Crawford and Messel and the calculation of Ivanenko and Samusodov are in good agreement at low energy (Figure 5.1) although two of the experimental curves are well above the calculations and the experimental curve of Heutch and Prescott. This inconsistancy might be due to the experimental difficulties in defining the cut-off energy. In figure 5.2 the numerical calculations of Thielheim and Zöllner and the predictions of Ivanenko and Samosudov are shown. In this figure the predicted curve of Muller that obtained by fitting data from accelerator results at energies up to 15 Gev is also shown.

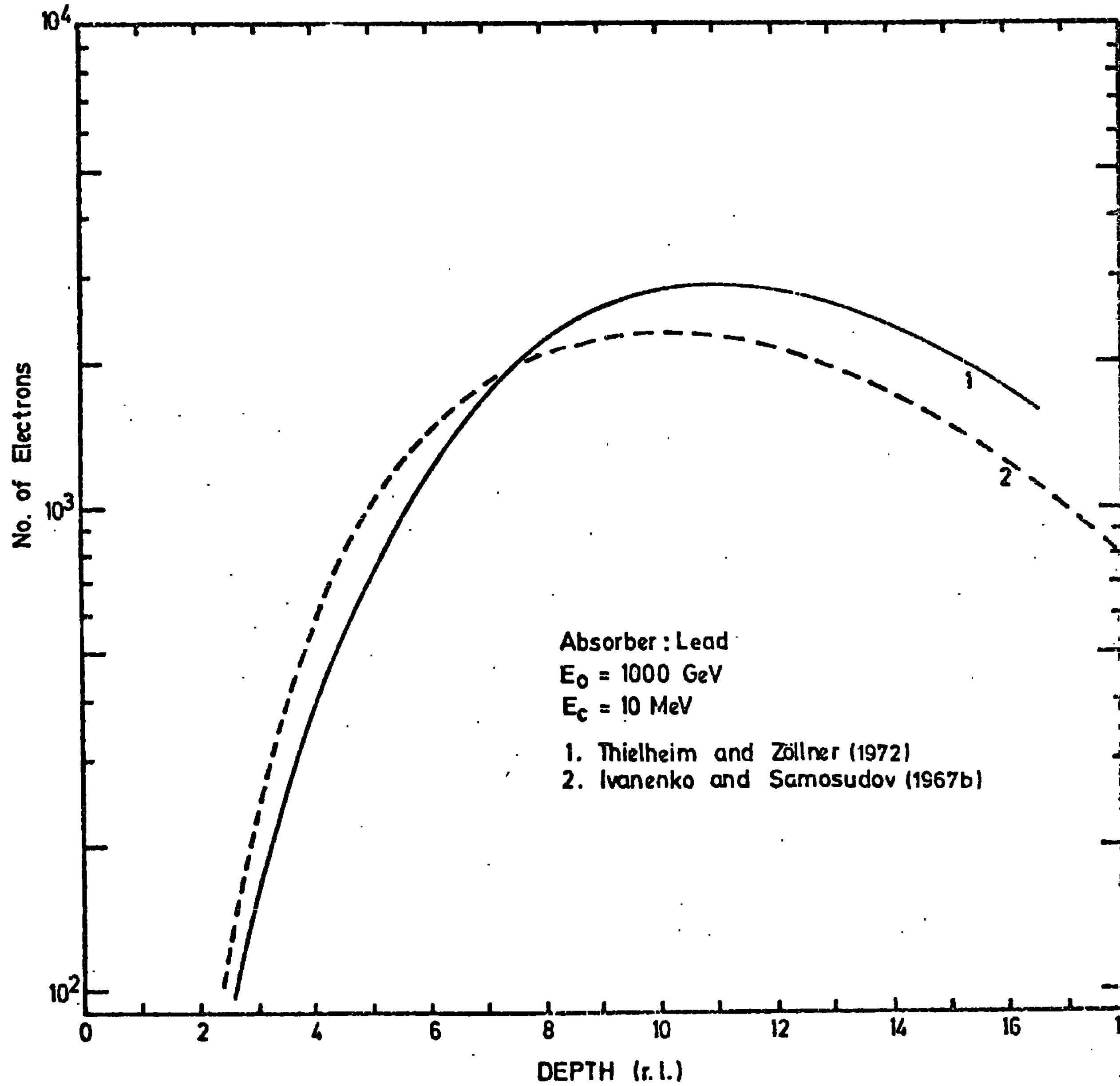

Figure 5.2 Transition curves in a lead absorber for primary electron of energy 1000 GeV. The cut-off energy E_c is 10 MeV. Curves 1 and 2 are results of calculations.

The results of Ivanenko and Samosudov for iron was compared with experimental results in the intermediate region of energies by Coats (1967) which found a reasonable agreement. This comparison shows that these calculations are valid for a wide range of energies in lead and iron absorber. Ivanenko and Samosudov quoted results for an energy cut-off relevant to the present experiment, about 1 Mev. The energy needed by an electron to pass through one flash tube is about this energy. Therefore the transition curves of Ivanenko and Samosudov adopted for the present calculations. In figures 5.3 and 5.4 the transition curves for photon-initiated cascades in lead and iron for an energy cut-off about 1 Mev is shown.

5.9 1 - dimentional nuclear-electromagnetic cascade simulation in a thick absorber.

5.9.1 Introduction

As was mentioned in the beginning of this chapter, one of the methods to estimate the energy of interacting particles is by producing a burst in an absorber, measuring the burst size and converting into the energy. If the burst is purely electromagnetic the energy estimation is rather accurate, since the electromagnetic interactions are thought to be well understood. But in the present experiment the burst are produced by hadrons so they are not purely electromagnetic but have a nuclear cascade superimposed. Unlike electromagnetic interaction the strong nuclear interactions are not fully understood. Therefore the energy estimation is dependent on the type of model adopted to calculate the burst size.

Simulations have been made by several workers. Jones (1969a and 1969b) has predicted cascade curves for protons in iron absorber using a Monte Carlo simulation. The results were compared with the results obtained

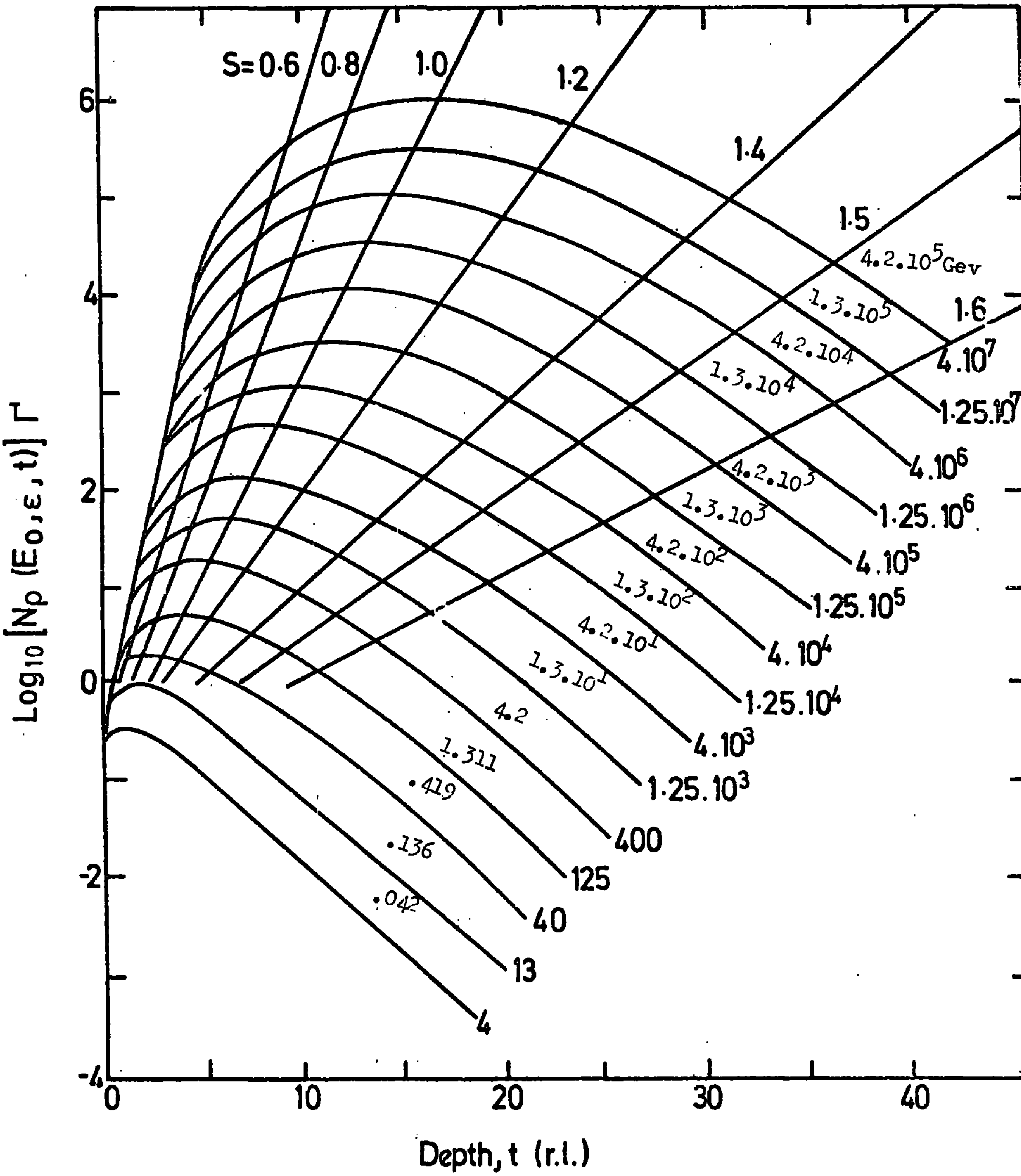

Figure 5.3 The transition curves for photon initiated cascades in iron calculated by Ivanenko and Samosudov. The number by each curve refers to the energy of the primary photon. The energies are in units of 0.437B, where B is the critical energy of the absorber. The cut-off energy E is 0.1 or ~1 Mev. Lines of Constant age parameter (S) have been calculated from approximation A. (.437B = 10.49 Mev)

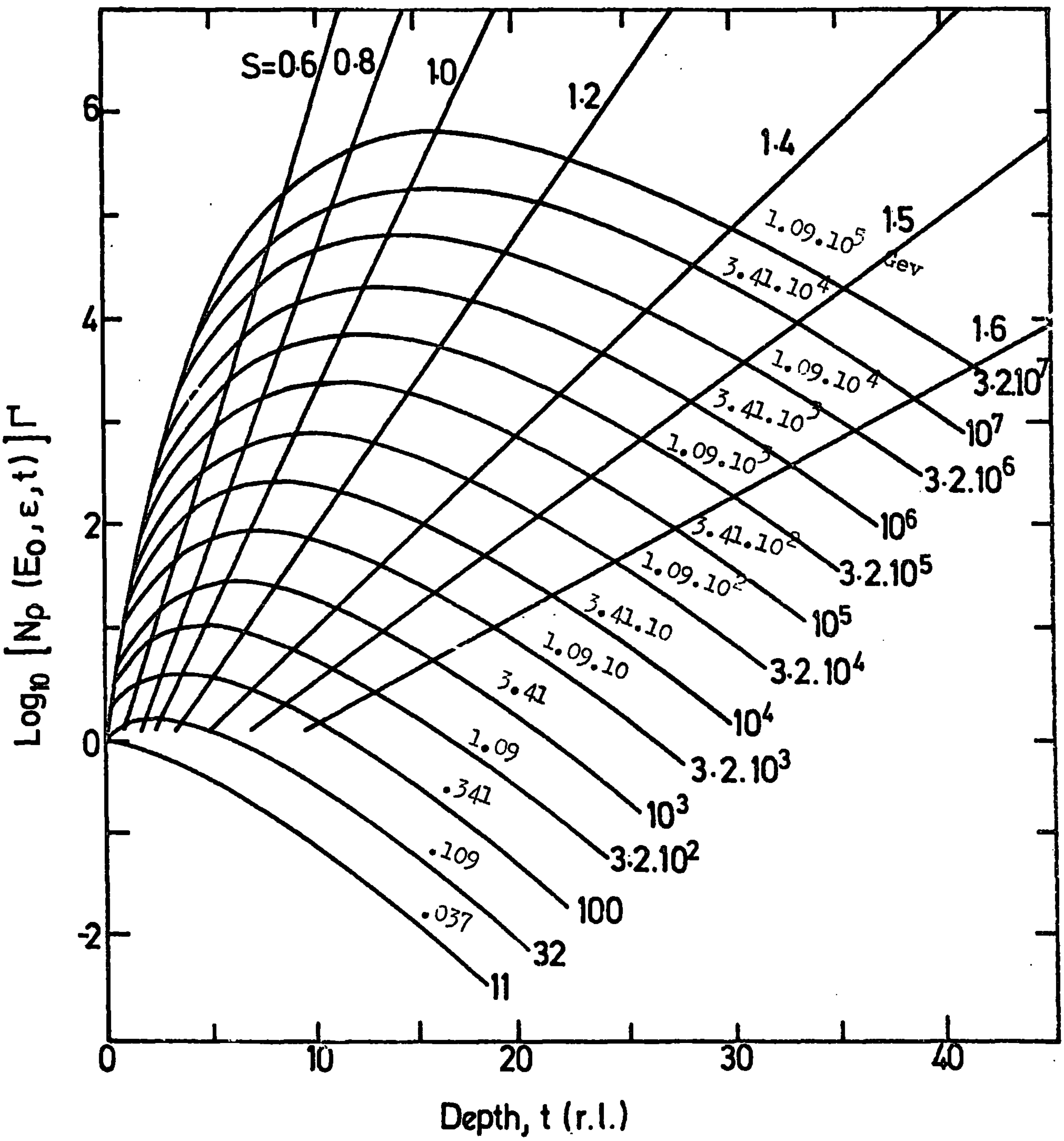

Figure 5.4 The transition curves for photon initiated cascades in lead calculated by Ivanenko and Samosudov. The number by each curve refers to the energy of the primary photon. The energies are in units of 0.437B, where B is the critical energy of the absorber. The cut-off energy E is 0.35 or $\sim$ 1.2 Mev. Lines of Constant age parameter (S) have been calculated from approximation A. (.437B = 3.41 Mev)

when an iron ionisation spectrometer was exposed to protons of momentum 10, 20.5 and 28 Gev/c at an accelerator. Reasonable agreement was found. Vatcha et al (1972) carried out simulation by Monte Carlo method in iron using three different nuclear interaction models for hadron energies up to 10^3 Gev. The simulations were carried out for the same geometry as was used in a multiplate cloud chamber operated at Oatacamund, India. On the basis of the results, Vatcha et al concluded that the absorption of cascades in the Tev region is faster than that predicted by any of the models employed. To interpret his observation he suggested the consideration of the gammanisation process suggested by Nikolski (1967) that the high energy photons are produced directly in nuclear collisions above some energy threshold. They also proposed that a higher inelasticity with a higher multiplicity could explain their results.

Pinkau and Thompson (1966) using Cocconi, Koester an Perkin's (C.K.P.) model estimated the electron numbers as a function of depth in different materials for different inelasticity, K and multiplicity, n_T. The model adopted for the present experiment to calculate the burst size under the lead and iron was basically similar to C.K.P. model to be discussed in the following section.

5.9.2 Nuclear interaction model

Calculation has been carried out on the basis of C.K.P. model (1961) to predict the average number of electrons emerging from 15cm of lead and iron produced by nuclear interaction of protons and pions of different energies. In this calculation several assumptions were made as follows:

a) the energy loss by ionization was neglected for hadrons,

b) the hadrions were assumed to be vertically incident on the absorbers,

c) the hadrons were allowed to interact at successive depth (t), in radiation lengths, according to the probability distribution

$$P(t)\,dt = \frac{1}{\lambda}\ \mathrm{EXP}(^{-t}/\lambda)\ dt$$

where λ is the interaction length of the incident particle in units of radiation lengths.

d) the mean multiplicity of produced pions was calculated from

$$\bar{n}_s = 3.0\ A^{0.19}\ (KE)^{0.25}$$

where A is the atomic mass of the target material, E is the primary energy. The origin of this equation is from a combination of surveys (e.g. Greider, 1971, Wdowczyk, 1973) and the hydrodynamical model of Belenkji and Landau (1956). The created particles are taken to be pions (π^+, π^-, π^o), the neutral pions are one-third of the produced pions and the rest are $\pi^{\pm}$.

e) Inelasticity coeficient for the incident pions was taken to be unity (K=1). The mean inelasticity for protons was assumed to be a function of the target material (Pinkau et al 1969)

f) All produced pions were taken to move in the forward cone and the mean multiplicity was used to estimate the mean energies of the forward pions. The energy is equally distributed among the pions, on average. The probability of energy distribution for produced pions in laboratory system follows the equation:

$$P(E)\ dE = \mathrm{EXP}(^{-E}/E')\ \frac{dE}{E'}$$

where P(E) dE is the differential probability of the createdpions with energy between E and E + dE, E' is the average energy of the forward cone.

g) Neutral pions (π^os) were taken to decay instantaneously into two photons with equal energy initiating the electron-photon cascades. From the curves predicted by Ivanenko and Samosudov (Figures 5.3 and 5.4), the total number of electrons emerging from the absorbers was calculated.

A list of constants applied throughout the calculation is given in table 5.1 and 5.2

5.9.3 Calculation procedure

Taking into account the above assumptions, the 15cm of lead and iron absorbers were divided into four layers (A, B, C and D) of equal thickness. A hadron with energy E allowed to interact in the middle of each layer according to the probabilities calculated from equation mentioned earlier (item C). One-third of the created pions in the first collision was assumed to be π^o and two-third $\pi^{\pm}$. For charged pions the applied cut-off was taken to be ≤ 1 Gev and for π^os ≤ 0.2 Gev. Using the C.K.P. distribution the total number of $\pi^{\pm}$ with energy more than 1 Gev and the π^os of energy more than the cut-off energy (0.2 Gev) was calculated. The mean energy for charged pions is (1 + E') Gev and for π^os (0.2 + E'). This was calculated from:

$$\bar{E} = \frac{\int_E^{\infty} E \exp\left(^{-E}/E'\right) \frac{dE}{E'}}{\int_E^{\infty} \exp\left(^{-E}/E'\right) \frac{dE}{E'}}$$

where E' is the mean energy of the created pions in Gev. The π^os were assumed to decay instantaneously initiating an electron-photon cascade by the following reactions

$$\pi^o \longrightarrow 2\gamma$$

$$\gamma \longrightarrow e^+ \pm e^-$$

The energy between two photons is assumed to be equally distributed. The $\pi^{\pm}$s either interact somewhere deeper in the absorbers or emerging without collisions. The mean depth of successive collisions was computed from the following:

$$\bar{x} = \lambda_{\pi} - \frac{x}{\exp(^{x}/\lambda_{\pi}) - 1}$$

Absorbers	Fe	Pb	Al.	Glass
Density ($g.cm^{-2}$)	7.6	11.34	2.7	2.5
Radiation length X_o ($g.cm^{-2}$)	14.1	6.5	28.4	26.3
λ_{π}	$11.6X_o$	$34.54X_o$	$5.37X_o$	$5.01X_o$
λ_p	$9.94X_o$	$33.08X_o$	4.25	$3.95X_o$
Moliere unit	1.53 cms	1.38 cm		

Table 5.1 A list of constants used in the calculation

Absorber	Fe	Pb
Mean inelasticity of protons ($\bar{K}_p$)	0.63	0.80
Mean inelasticity of pions ($\bar{K}_{\pi}$)	1.0	1.0

Table 5.2 The values of the mean inelasticities adopted for proton-nucleus and pion-nucleus collisions.

Where X is the distance from the bottom of the absorber to the first interactron. The first interaction was assumed to occur in the middle of the layers A, B, C and D, λ_{π} is the mean free path of pions. The proton inelasticity was assumed to be 0.63 for iron and 0.8 for lead. the reason for the energy cut-off of 1 Gev for $\pi^{\pm}$ is that the inelastic cross-section ofpions falls off sharply at this value (Hayakawa 1969). Therefore it can be concluded that the pions do not contribute to the cascade. The neutral pion (π^{o}) cut-off of 0.2 Gev was taken, the photon created by the decay of the π^{o} would not contribute significantly to the electromagnetic components of the cascade.

5.9.4 Burst size-energy calibration, calculation results

Calculation has been carried out for primary energies: 10^1, 10^2 10^3 and 10^4 Gev. The incident particles were assumed to be protons and pions interacting in lead and iron absorbers, 15 cm in thickness each.

The results of the calculation are shown in figures 5.5 and 5.6. These figures show the average number of electrons coming out of 15cm of lead or iron as a function of incident energy. The calculation result shows that for a given material the proton and pion curves are rather parallel, but it can be seen that there is a difference in burst size that can be attributed to different inelasticity. For iron absorber the curve show a flattening at higher energies. It can be interpreted that the cascade at high energies cannot properly develop in iron absorber of 8.19 radiation length thickness. But since there are 26.2 radiation length in lead the cascade can develop. The burst size-energy relation was calculated by (Cooper 1974, private communication) using the Monte Carlo method. The calculation was carried out for protons and pions incident on lead and iron target. In this calculation similar assumptions were made. Figure 5.7 shows the comparison of present calculation with

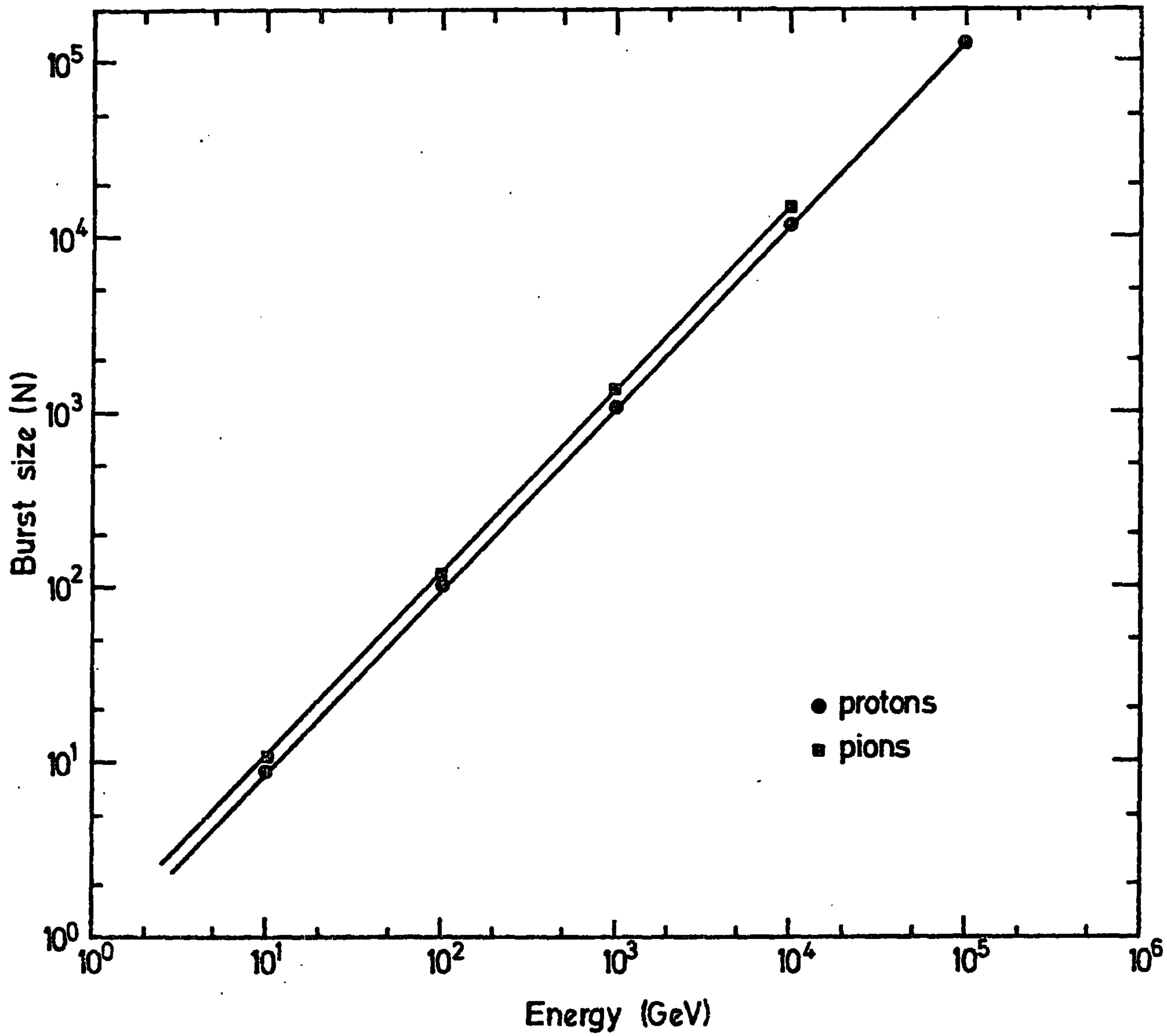

Figure 5.5 The average burst size (N) produced by primary protons and pions, interacting in 15 cms of lead, as a function of energy.

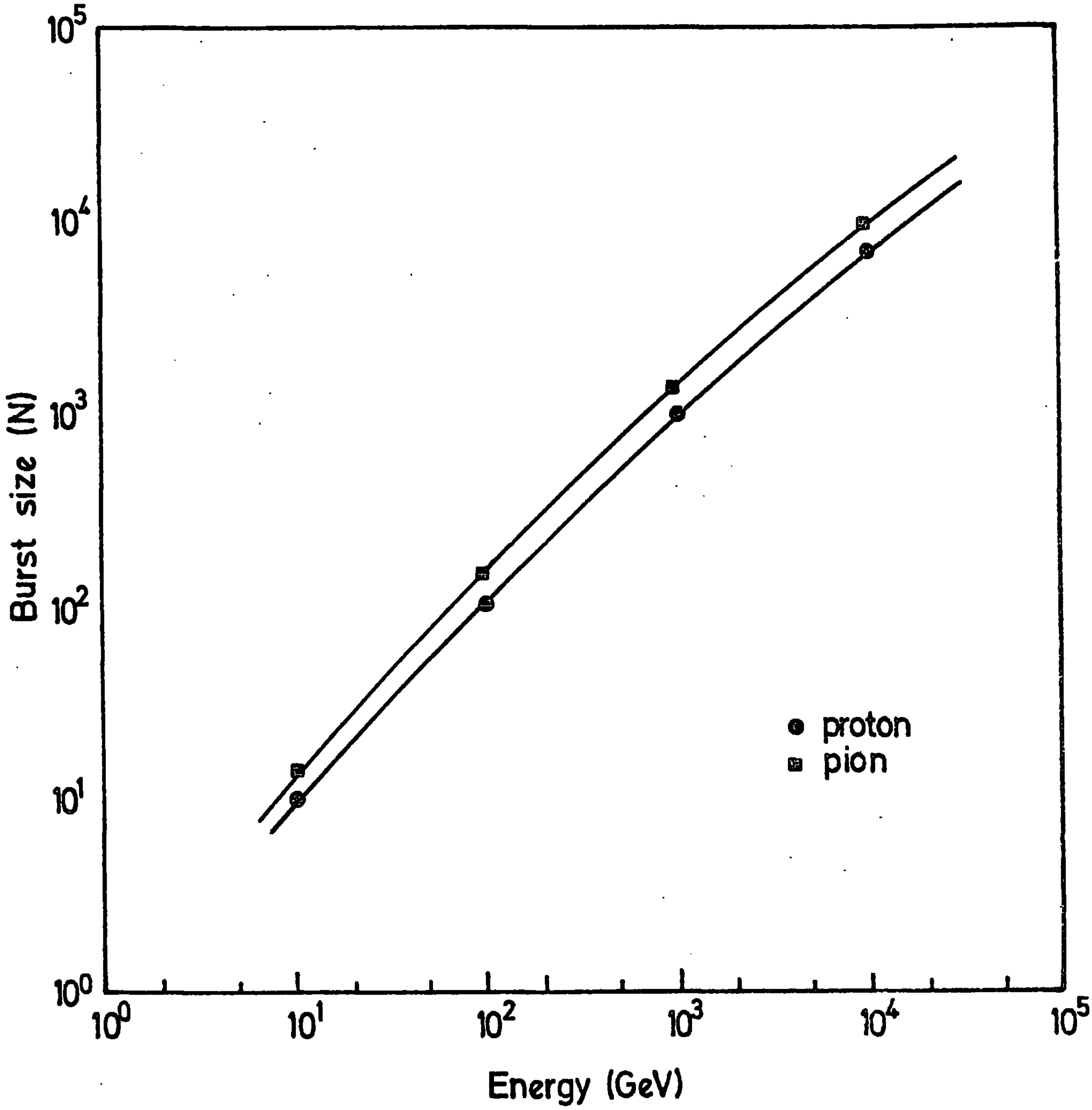

Figure 5.6 The average burst size (N) produced by primary protons and pions, interacting in 15cms of iron, as a function of energy.

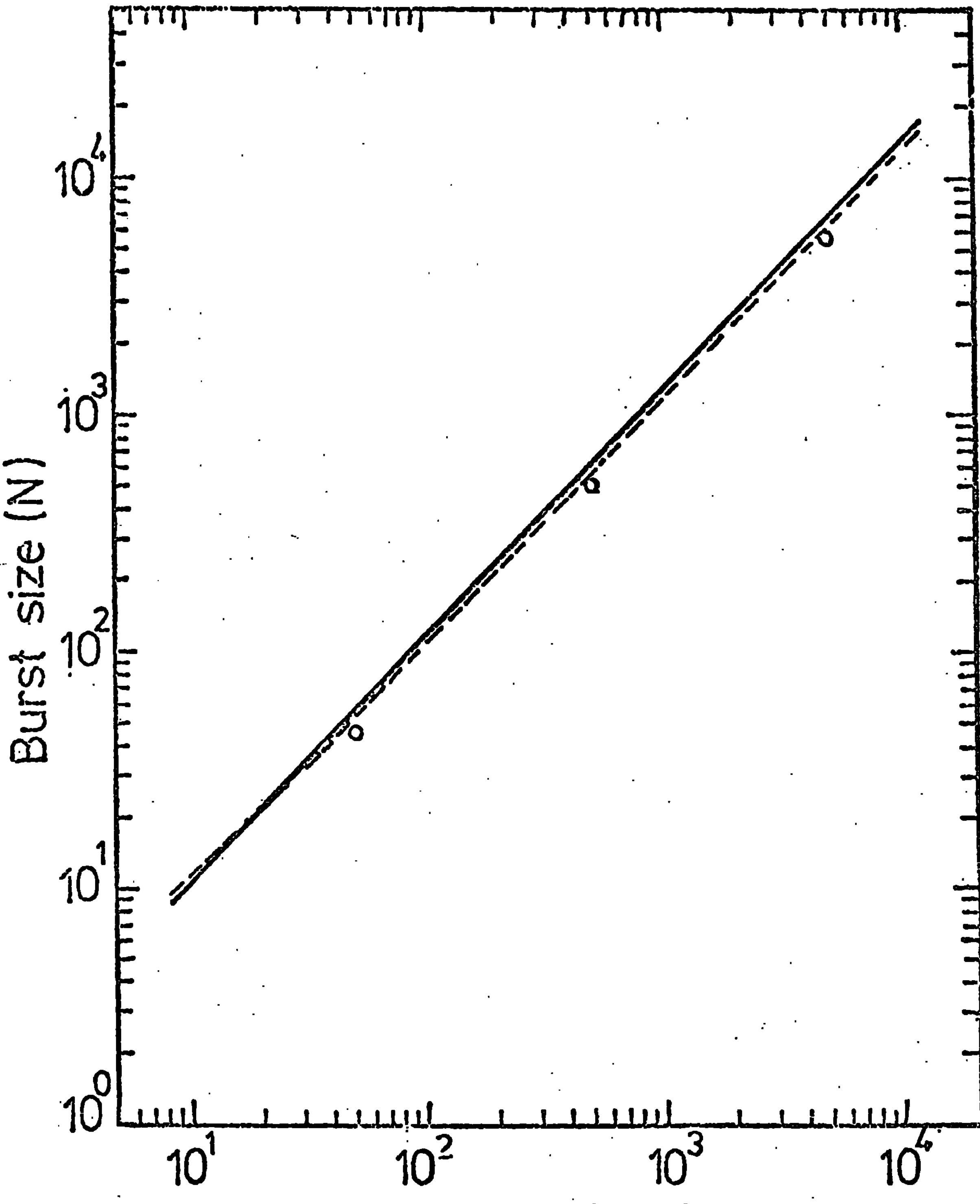

Figure 5.7 A comparison between the average treatment procedure (solid line) and Monte Carlo Method (broken line, Cooper 1974) in calculating the average burst size, N_e, produced by primary pions incident on 15cms of lead target against the energy. The open circles represent Monte Carlo calculations for pions incident at a zenith angle of 30°.

Monte Carlo simulation. It can be seen that the results of both methods are in a good agreement.

5.10 The burst size distribution

The procedure adopted as an average treatment gives information on average characteristics of the cascade produced in the lead and iron absorbers. In figures 5.8, 5.9, 5.10 and 5.11 the distribution of the produced burst size (Ne) below the iron and lead targets against the depth of the first interaction are illustrated for protons and pions of different incident energies. As is seen there is no maximum for the burst size distribution for higher energies, since the cascades are not developed properly in the iron of thickness 8.19 radiation length, the probability of observing a burst of size $\geqslant N_e$ particles for a given energy could be calculated from the previous distributions.

In figures 5.12 and 5.13 the integral probability of pions of energy E producing a burst of size $\geqslant$ N under the iron and lead are shown.

5.11 Conclusion

The burst size energy relation calculated by the procedure explained in this chapter agrees with the method of Monte Carlo calculation. The relationship was used to convert the burst size, measured from the actual events to energy of the incident pions or protons.

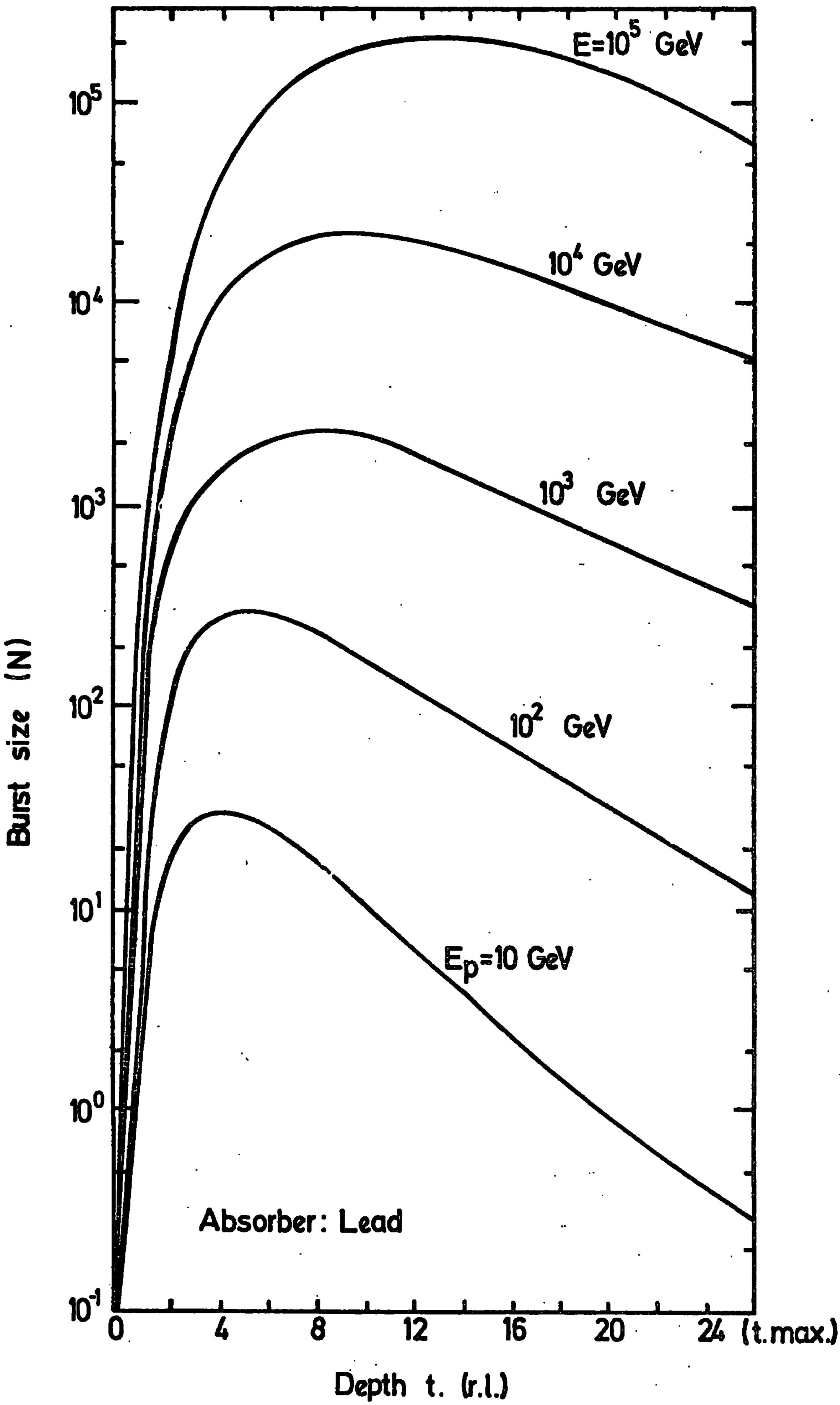

Figure 5.8 The relation between the depth of the first interaction for a proton of different primary energy (E_p) and the burst size (N) below 15 (cm) of lead.

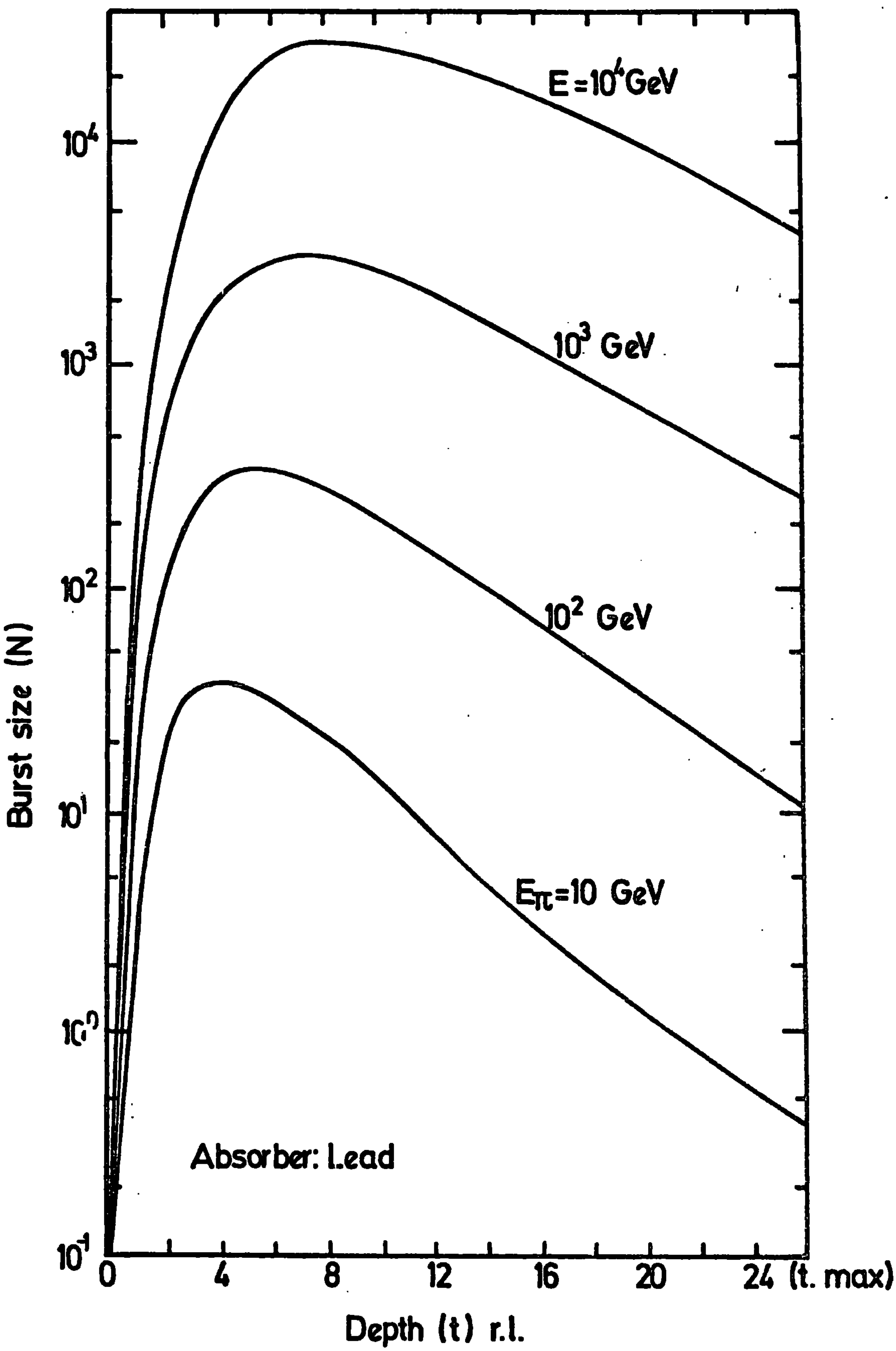

Figure 5.9 The relation between the depth of the first interaction for a pion of different primary energy (E_π) and the burst size (N) below 15 (cm) of lead.

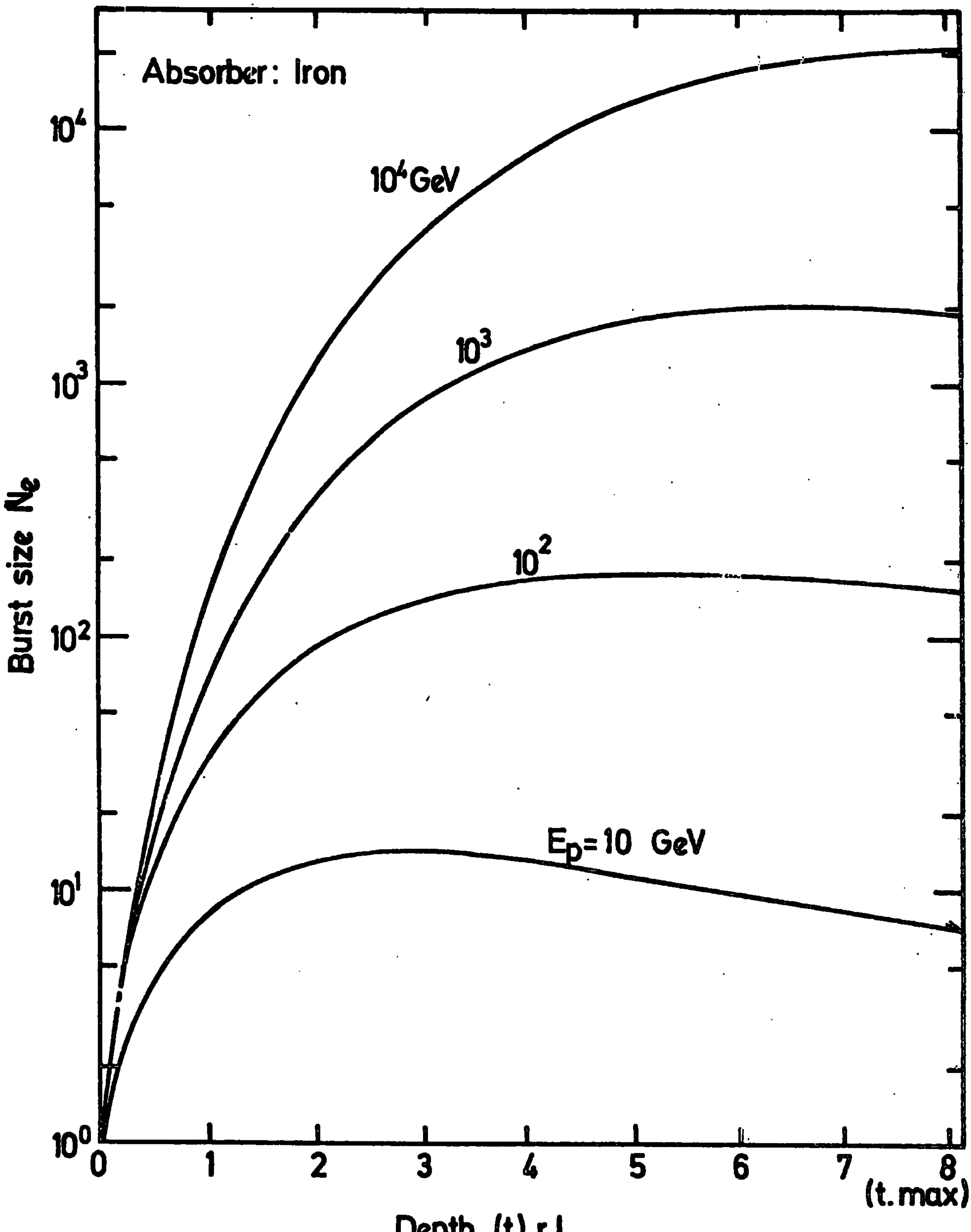

Figure 5.10 The depth of first interaction in iron absorber as a function of the burst size produced by proton of different energies.

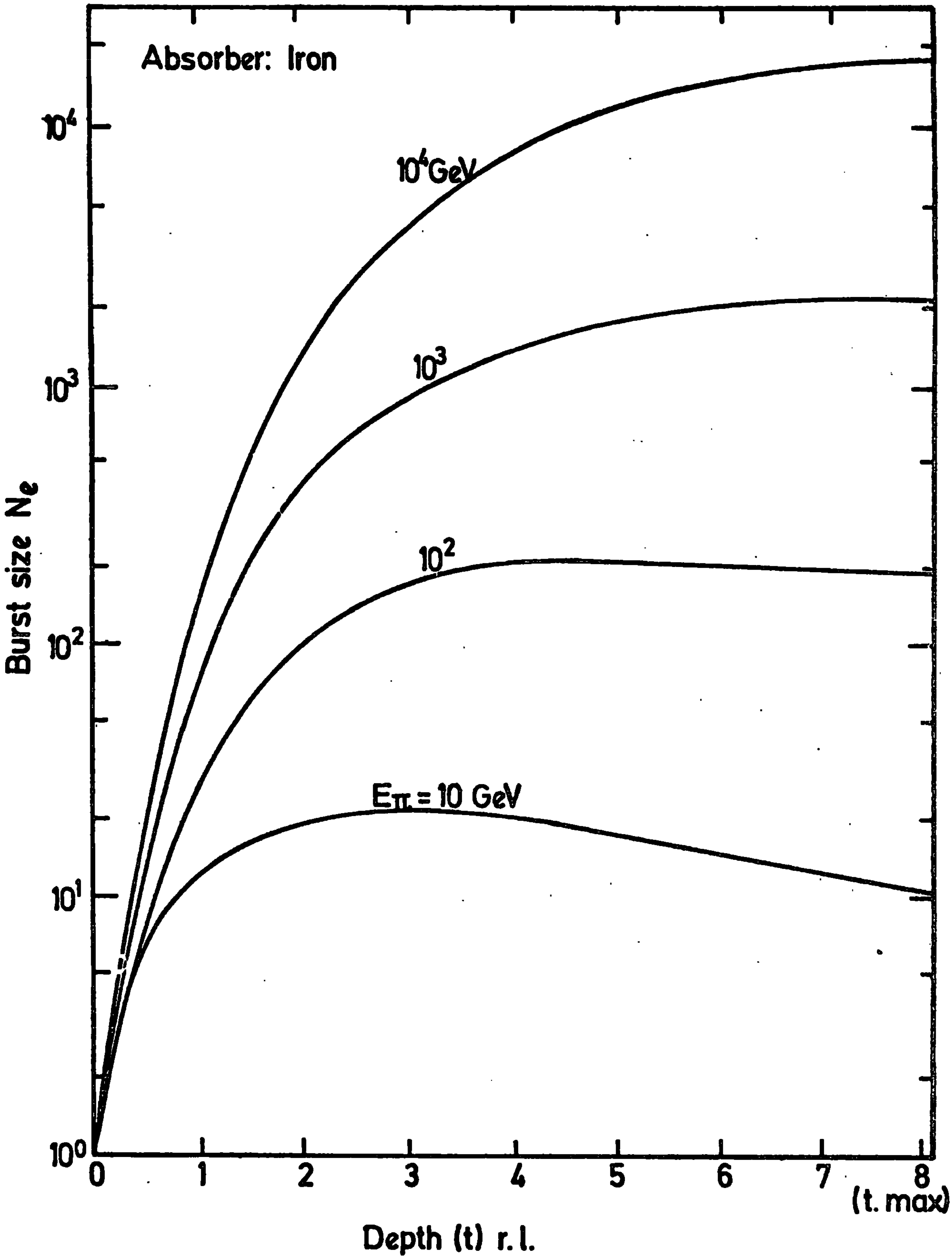

Figure 5.11 The relation between the depth of the first interaction for a pion of different primary energy (E_π) and the burst size (N) below 15 (cm) of iron.

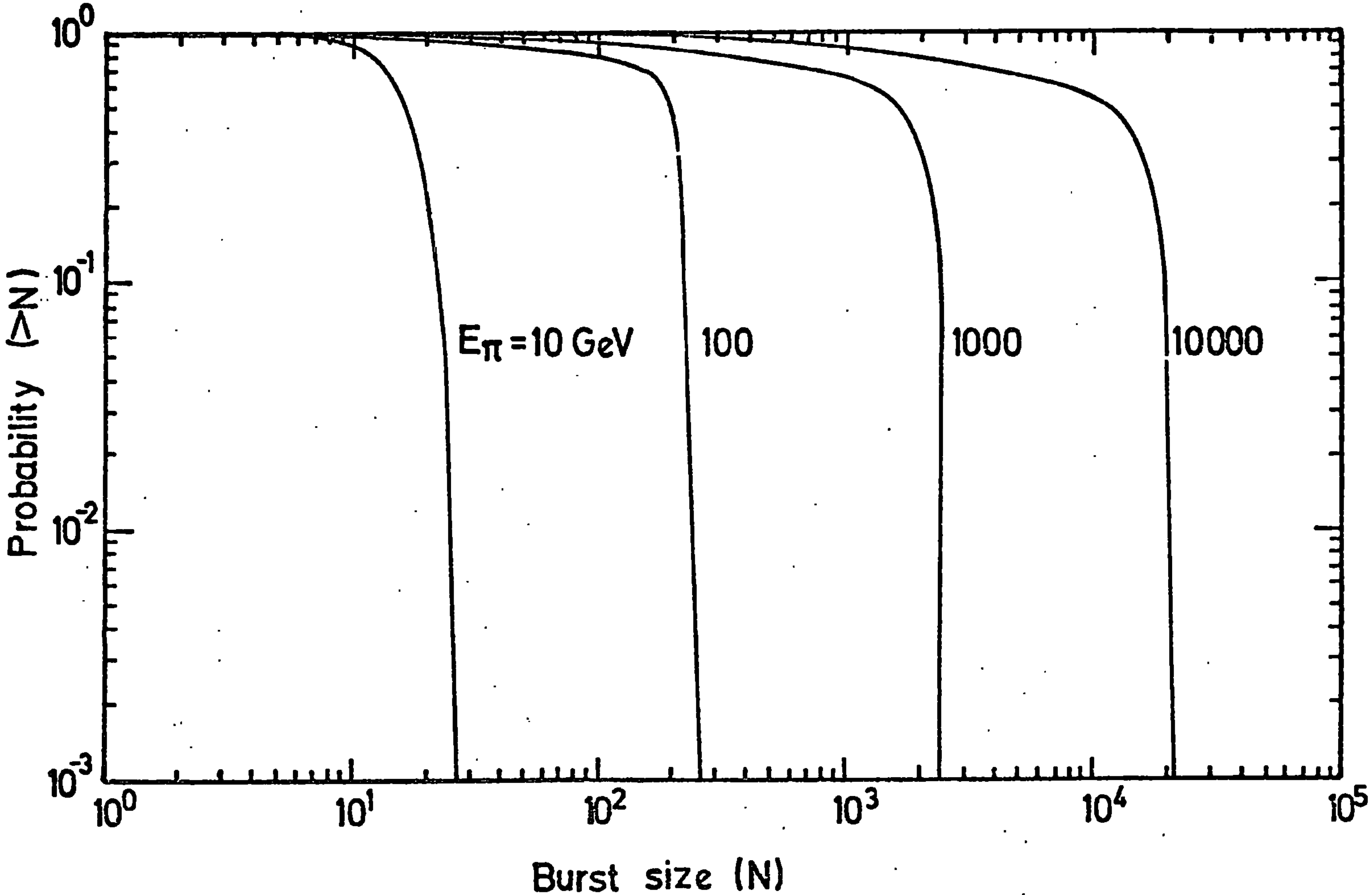

Figure 5.12 The integral probability that a pion of energy E_π will produce a burst of size > N below 15 cmsof iron.

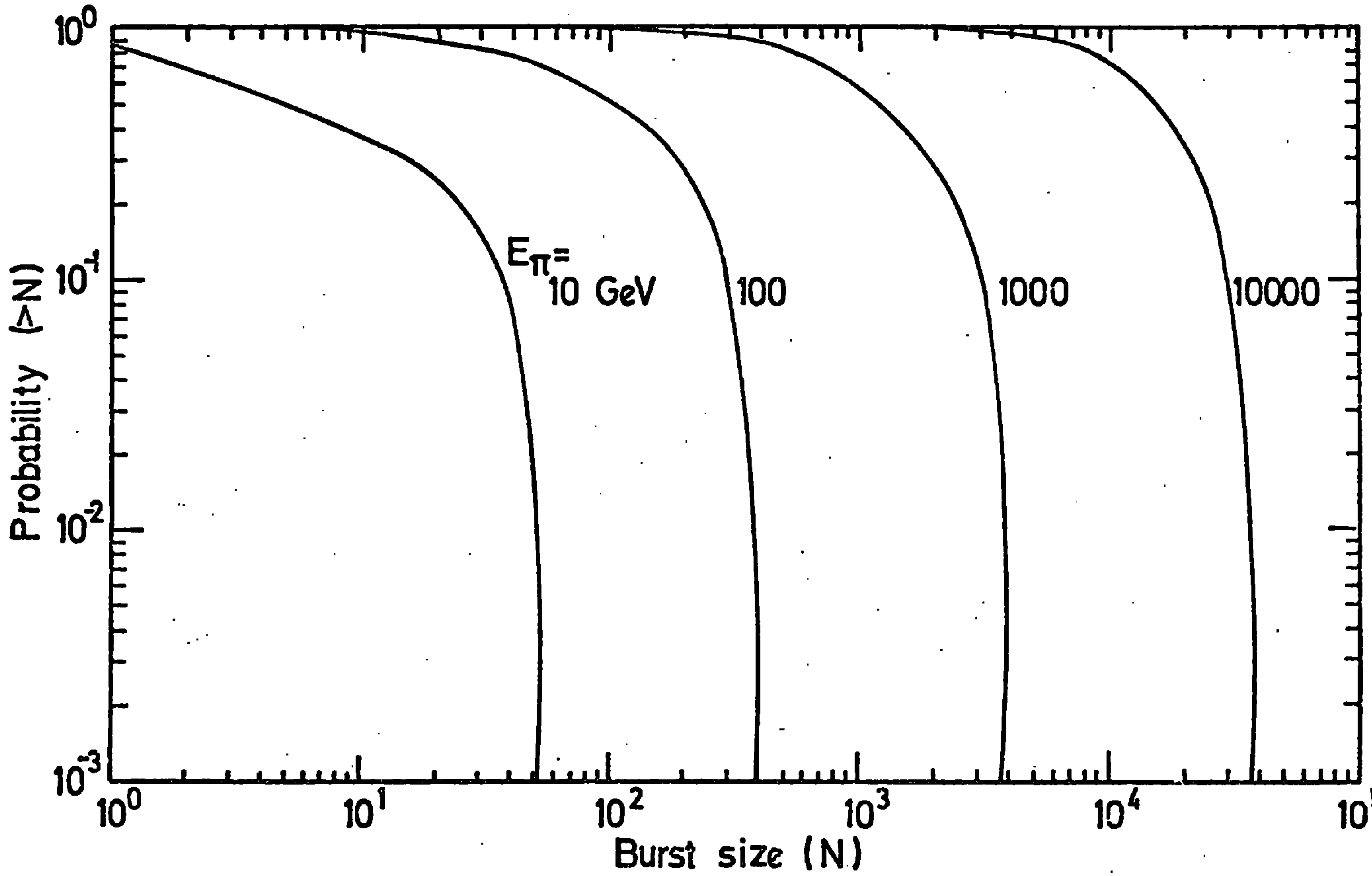

Figure 5.13 The integral probability that a pion of energy E_π will produce a burst of size > N below 15 cmsof lead.

CHAPTER 6

THE NEON FLASH TUBE CHAMBER AND THE EXPERIMENTAL ARRANGEMENT FOR THE STUDY OF HADRONS IN EXTENSIVE AIR SHOWERS

6.1 Introduction

In this chapter the flash tube chamber and the experimental arrangement for the study of high energy nuclear active particles in extensive air showers are described.

The method of air shower core location and shower size determination is also explained.

6.2 Principle of operation of neon flash tubes

When a charged particle, say, a cosmic ray traverses a flash tube a trail of ion pairs is left along the particle trajectory. Placing the flash tube between two electrodes and subsequently applying a high voltage pulse to the electrodes, the tube will flash due to the ion pairs, and the discharge will spread through the tube. The high voltage pulse is usually a few K.V. with a length of a few microsecond. With an array of flash tubes the particle track can be seen.

6.3 The neon flash tube chamber

A flash tube chamber as a visual detector has been used in the present experiment to observe the tracks of cosmic rays and to record the nuclear interactions occuring in the chamber. A scale diagram of the chamber is shown in Figure 6.1.

The chamber has been constructed of about 11000 flash tubes. The tubes are made of soda glass filled with neon gas (98%) and helium gas (2%) with a pressure of 60 cm Hg. Each tube is 2 meters long. The tubes are cylindrical with mean internal diameter 1.58 cms. and mean external diameter 1.78cms. The tubes are covered with polythene sleeving to prevent light transfers to adjacent tubes. The tubes are arranged such that between each two layers of tubes an aluminium electrode (0.122 cms thick) is placed. As can be seen from the scale diagram the chamber consists of, from top to bottom: a layer of 15 cms of lead; a plastic scintillator of area 1 m^2; 8 layers of neon flash tubes (F_{1a}) 15 cms of iron; a further plastic scintillator, area 1 m^2, 116 layers of neon flash tubes. Nuclear active particles interact in the lead or iron target producing bursts, the size of the burst being measured by the scintillators under the lead and iron (C and A respectively).

The 15 cm lead roof and 30cm baryte concrete walls shield the chamber from the soft component of the cosmic radiation.

6.4 The high voltage pulsing system

A high voltage pulse is applied to the electrodes of the flash tube chamber after the triggering requirement is established. This high voltage pulse is supplied by a system, consisting of a H.T. pulsing unit, figure 6.2, and a spark gap, figure 6.3. A 5 volt trigger pulse is used to trigger a thyristor, producing an output of +300 volts. This pulse is applied to a high voltage pulse transformer to produce a trigger pulse for the spark gap. After the application of 16 KV. across the main spark gap, the gap is broken down by the production of photo-electrons (Sletten and Lewis, 1956). This breakdown is caused by the trigger spark.

The shape of the pulse, applied to the electrodes of the chamber is almost rectangular having a height of 8K.V. and a length of 10μs. produced by the circuit shown in figure 6.3. The capacity of the flash tube chamber which this unit supplies is 0.087μF.

6.5 Characteristics of flash tubes

As was mentioned earlier when a charged particle passes through a flash tube a trail of ion pairs and excited atoms of the gas of the flash

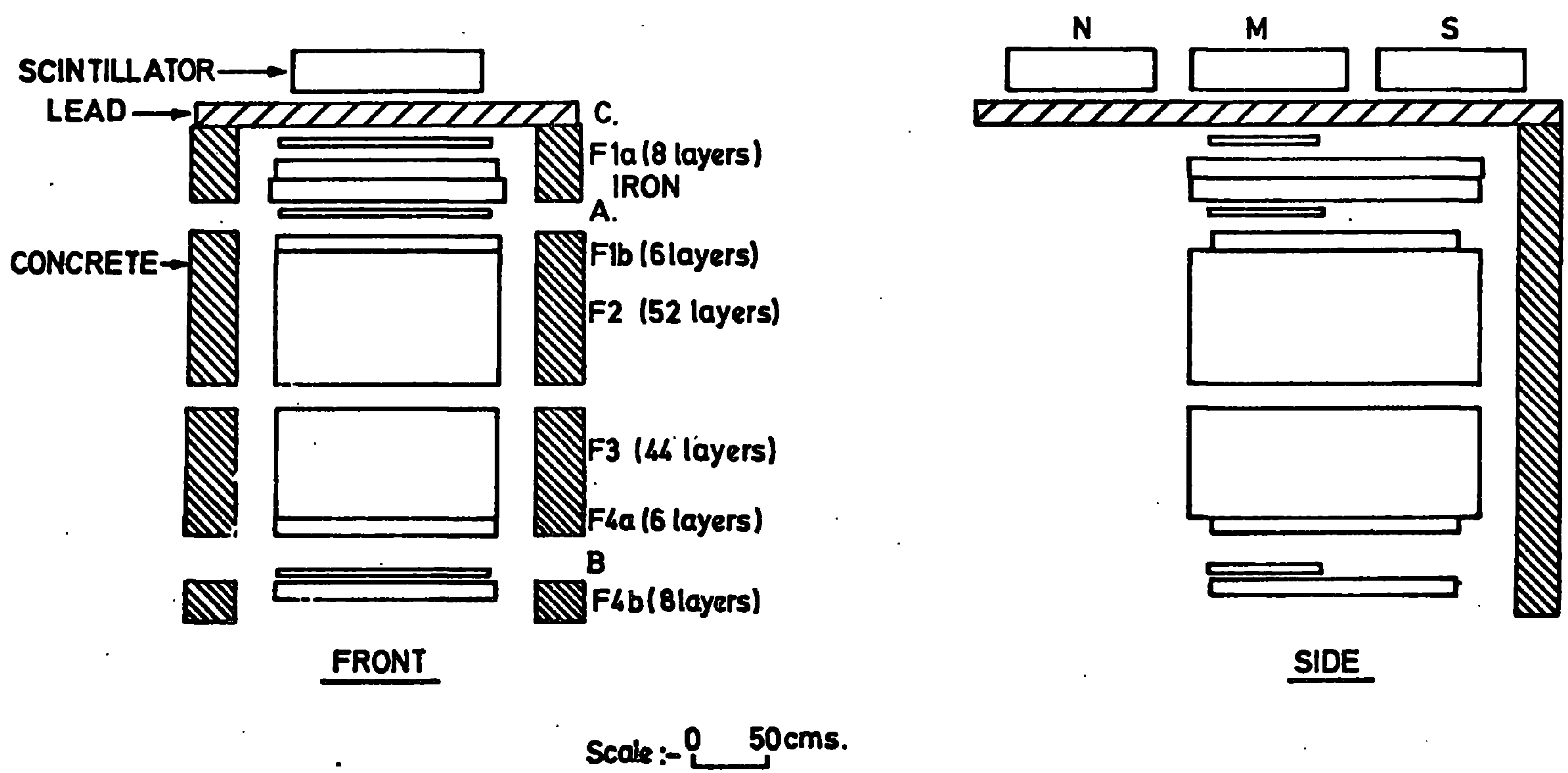

Figure 6.1 Scale diagram of the Flash Tube Chamber.

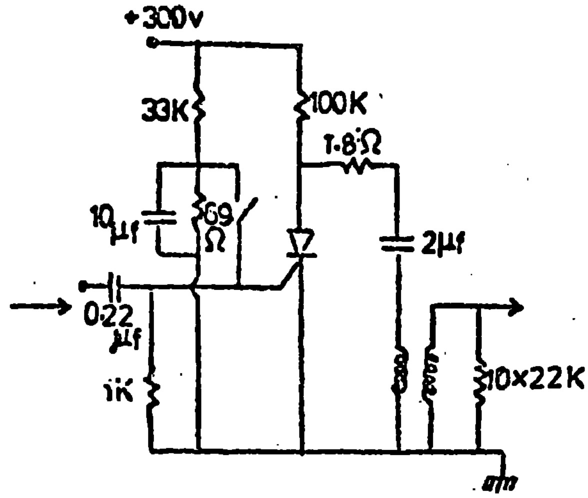

Figure 6.2 High voltage pulsing unit

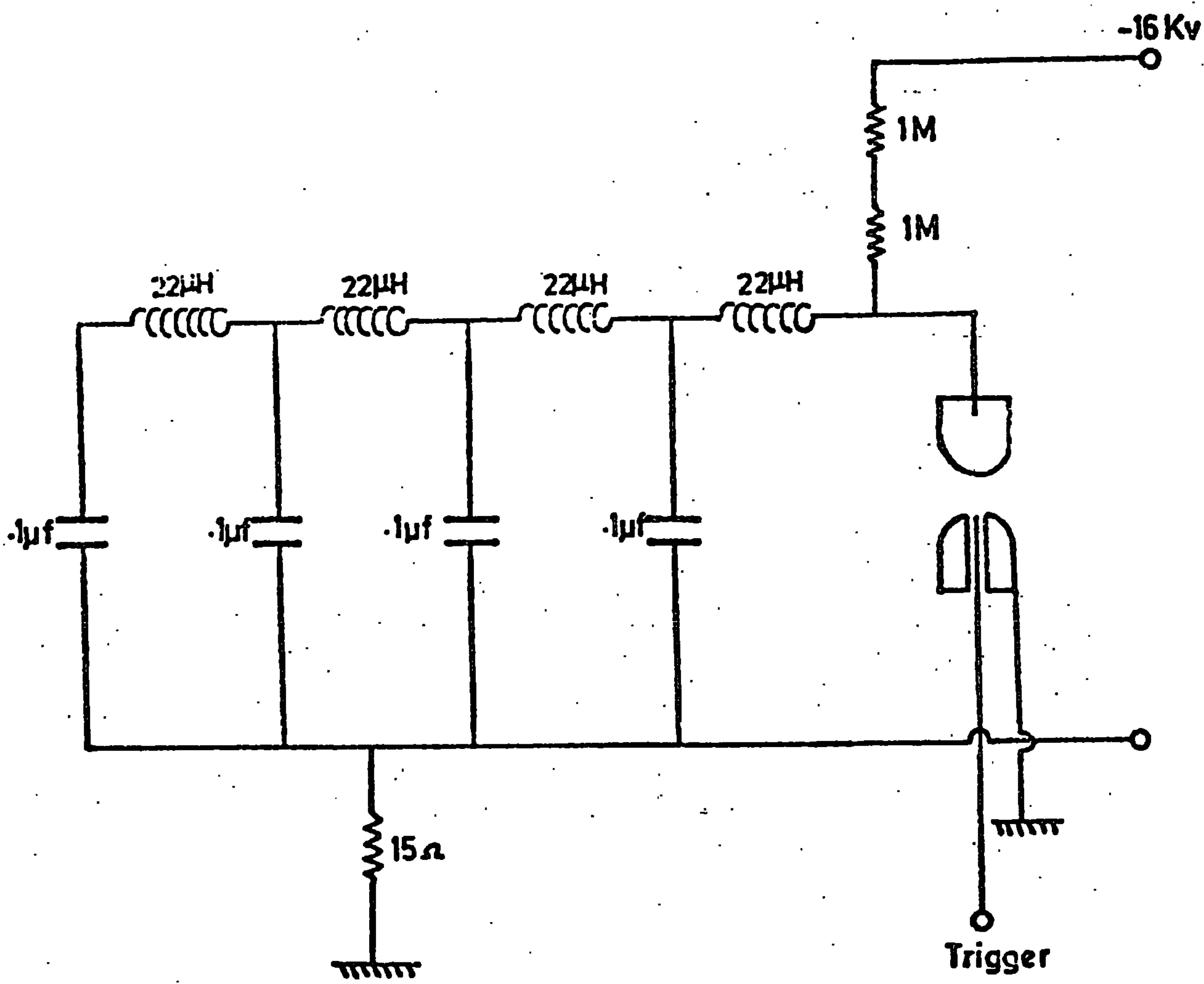

Figure 6.3 Air Spark Gap and Delay Line

tube is left along its track. Lloyd (1960) came to a conclusion that only the electrons of the ion pairs are responsible to discharge the tube. He set up diffusion equations for the electrons produced in the tube and solved them. The solution gave the probability of occuring a discharge if a high voltage pulse is applied after a time from the passage of the ionising particle. This probability is known as the internal efficiency, Lloyd expressed the internal efficiency as a function of $D.Td/a^2$, where D is the diffusion coefficient of Thermal electrons and a is the internal radius of the tube, with $a f_1 Q_1$ as a parameter, f_1 is the probability that a single electron produces an avalanche and Q_1 is the average number of initial ~~probability per unit length~~ electrons produced per unit path length in the neon gas. ~~of the track of the primary particle producing a free electron.~~ The only parameter dependent on the charge of the particle is Q_1 and is related to the ionization loss of the particle in the gas (Q_1 is a function of the square of the electric charge). For an e-charged particle af_1Q_1 is 9 , $Z_e = (a f_1 Q_1/9)^{1/2}$.

The internal efficiency of the chamber as a function of time delay (T_D) for different values of a f_1Q_1 has been calculated using the Lloyd theory. The result of the calculation is shown in figure 6.4. From this figure it is seen that the efficiency of the chamber falls off as the time delay increases. This fact is due to the loss of initial electrons by diffusion to the glass tube walls in the time interval between the passage of the charged particle and the application of the high voltage pulse to the chamber.

In the present experiment a long time delay (330μs) has been used, since only after a long time delay is it possible to locate the axis of the large bursts.

6.6 The comparison of efficiency - time delay measurement with calculation

The probability that one of the tubes of a single layer flashes when a

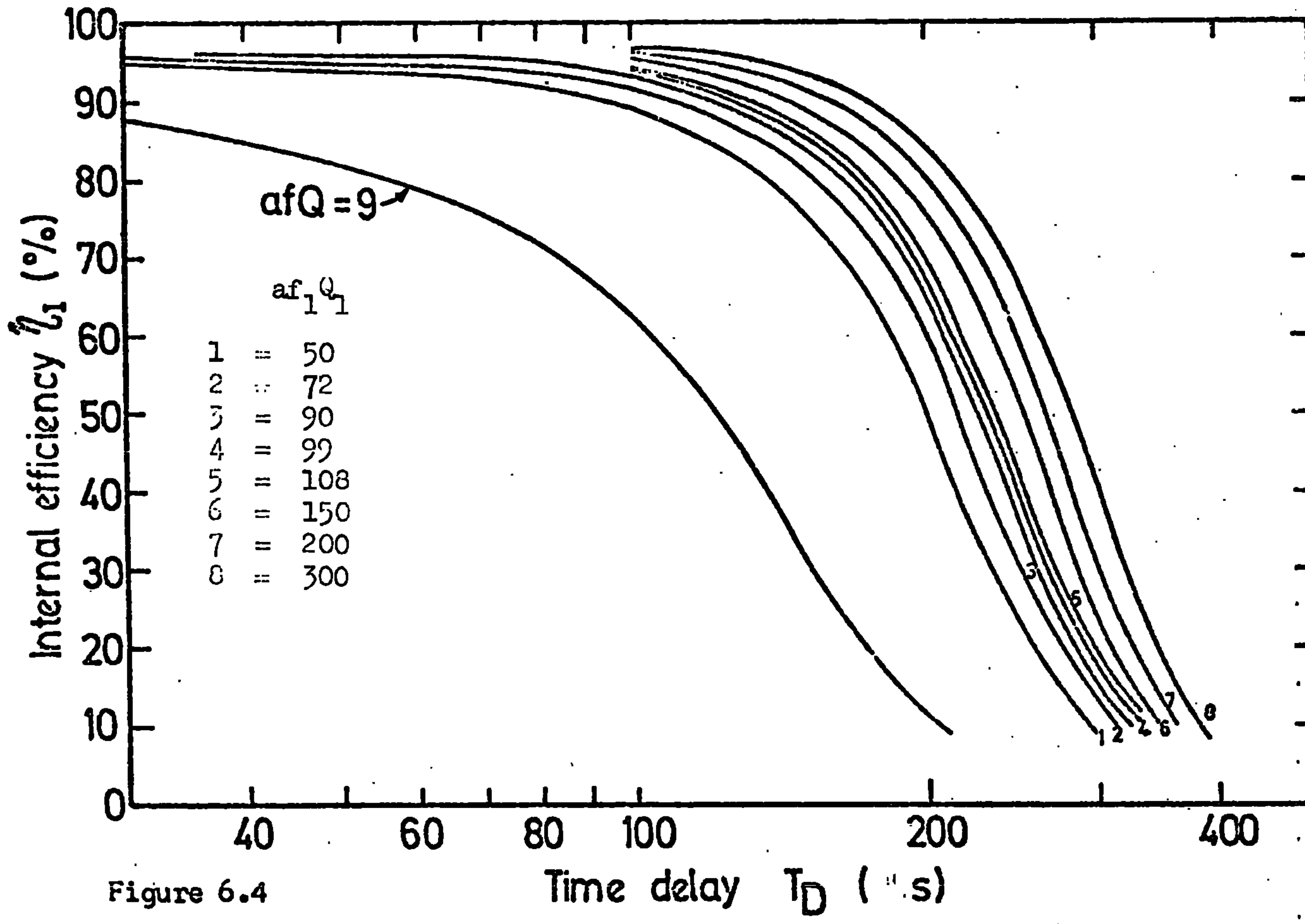

Figure 6.4

Variation of internal efficiency with T_D for the flash tubes a f Q as a parameter.

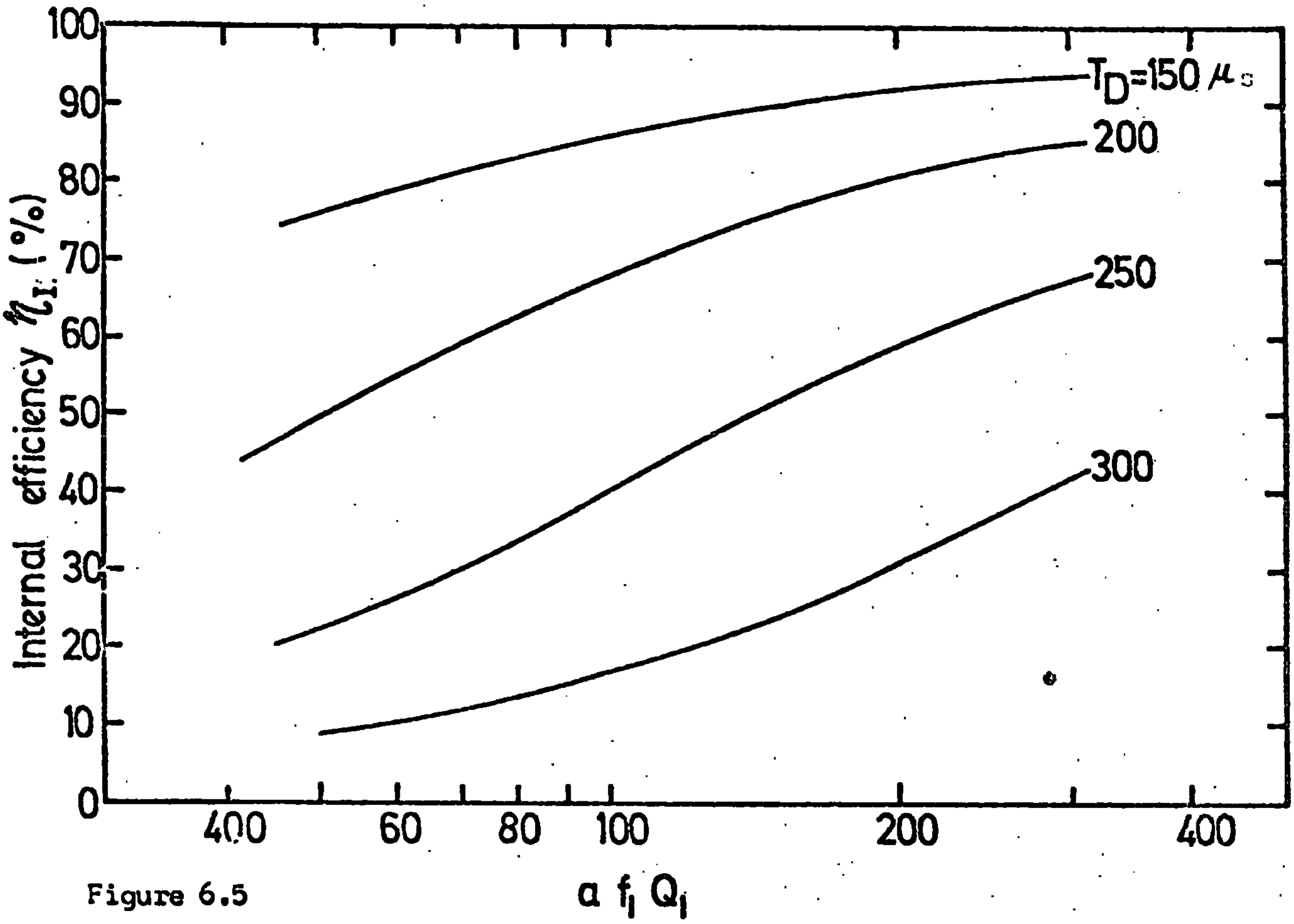

Figure 6.5

Variation of internal efficiency with a f_1Q_1 for the flash tubes for different time delays particle passes through it is called the layer efficiency (η_L). This probability will not be unity since a particle may Traverse through the walls of the tube rather than the gas. The maximum layer efficiency to be expected is found to be:

$$\text{Max. } \eta_L = \frac{\text{inside diameter}}{\text{outside diameter}} \times 100\%$$

this is termed as internal efficiency.

It is sometimes necessary to delay the application of the high voltage pulse. During this time delay (T_D) the ion pairs, produced by the passing particle will commence to diffuse to the walls of the tubes. The efficiency of the tube then will be reduced. One can experimentally measure the layer efficiency as a function of time delay. A measurement was made by (Cooper 1973) in the following way:

Single muons were selected by a two-fold coincidence between two plastic scintillators. For different time delay, a large number of single muon tracks were photographed and analysed.

The layer efficiency, η_L was measured by counting the number of tubes flashed in successive layers along the track in a certain block of flash tubes. To obtain the layer efficiency the number of flash tubes flashed by a single muon has been divided by the total number of layers in the block. To find the internal efficiency (η_I) the layer efficiency has been multiplied by the ratio of the mean ~~internal~~ external diameter of the flash tubes to the mean external diameter of the flash tubes:

$$\eta_I = \frac{1.81}{1.58} \cdot \eta_L$$

The result of the measurement is shown in figure 6.6 and compared with the calculation. It has been found that the best fit for Lloyds parameter, a $f_1 Q_1$ to the experimental points is 9 ± 1 for a singly charged particle.

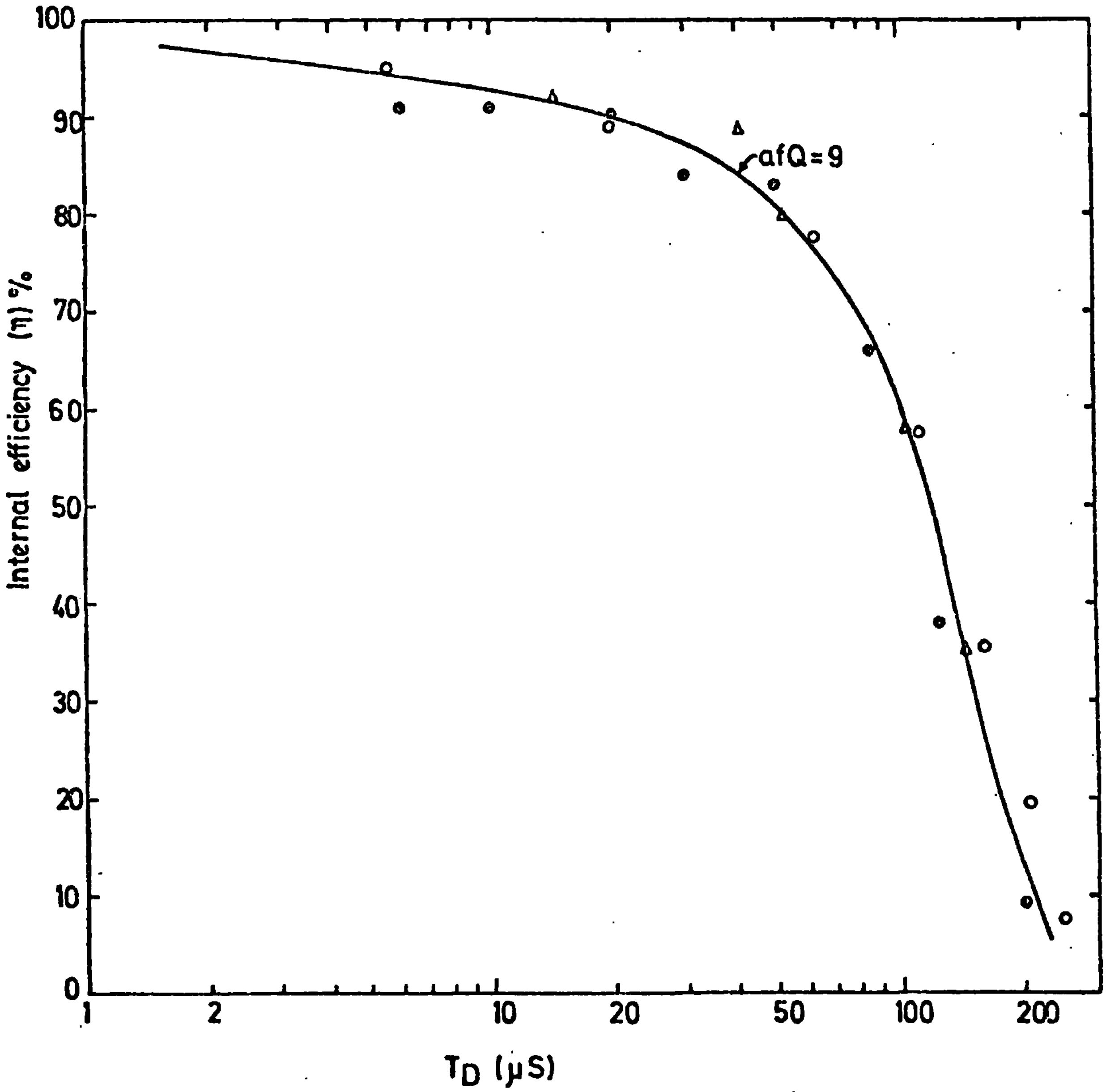

Figure 6.6

The variation of the internal efficiency of the flash tubes as a function of time delay, T_D. The full curve represents the theoretical prediction with $af_1Q_1 = 9$ as a best fit to the experimental points.

6.7 Calibration of the scintillation detectors

The calibration being described here is for detector A, placed under the iron; detector C under the lead and detector M on the top of the chamber, this calibration has been performed by D.A. Cooper (1973). Single muons were selected by a small Geiger telescope and the pulse from the coincidence unit was used to trigger the scope. The loss in pulse height for a pulse transmitted from the phototubes through the electronics has been found. The output/input characteristic for scintillator A, C and M is shown in figures 6.7 and 6.8. The pulse height distribution for single particles passing through the centre of each scintillator in the vertical direction has been measured for different values of H.T. voltage. The potentio meters were adjusted for each tube, separately to give identical output pulse heights for a charged particle passing through the middle of the scintillator. By adding the outputs from photomultiplier tubes the complete scintillator has been calibrated. The calibration curves are shown in figures 6.9 and 6.10.

6.8 The air shower selection detectors.

Figure 6.11 shows the disposition of the selected shower detectors in conjunction with the hadron detector (flash tube chamber). This array is composed of 5 detectors displaced in different distances from the centre of installation.

The detector M (area 1.24 m^2) is located on the top of the chamber.

6.9 The relation between shower size and the collecting area

Since the whole of the collecting area, the area covering a circle of radius 10 meters with the centre at the middle of scintillator M, was not effective for all shower sizes it was necessary to determine the variation of the collecting area with shower size. The minimum measurable density

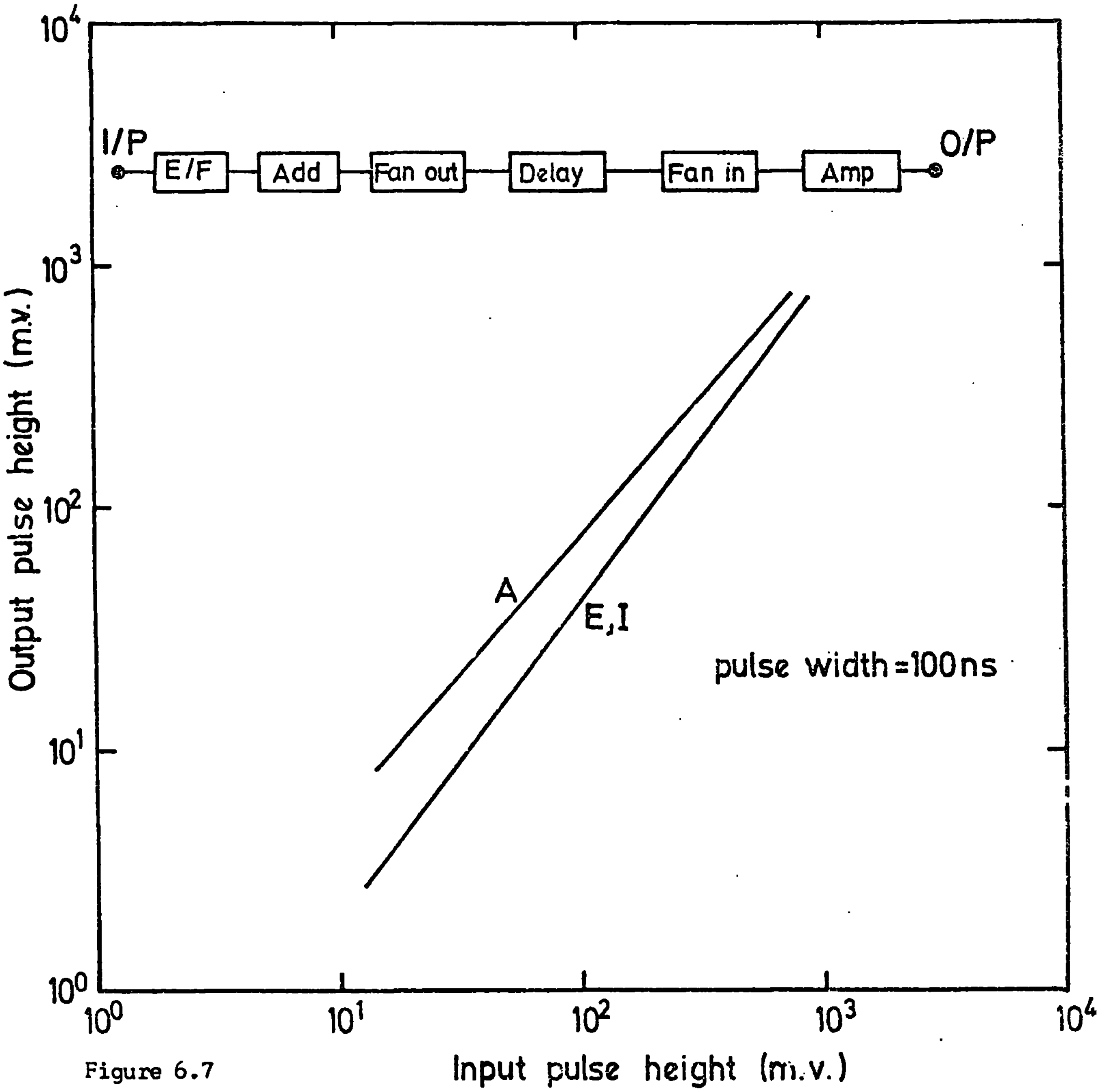

Figure 6.7

The input-output characteristics for the pulses transmitted through the circuit shown above associated with scintillator A and E, measured for square pulses.

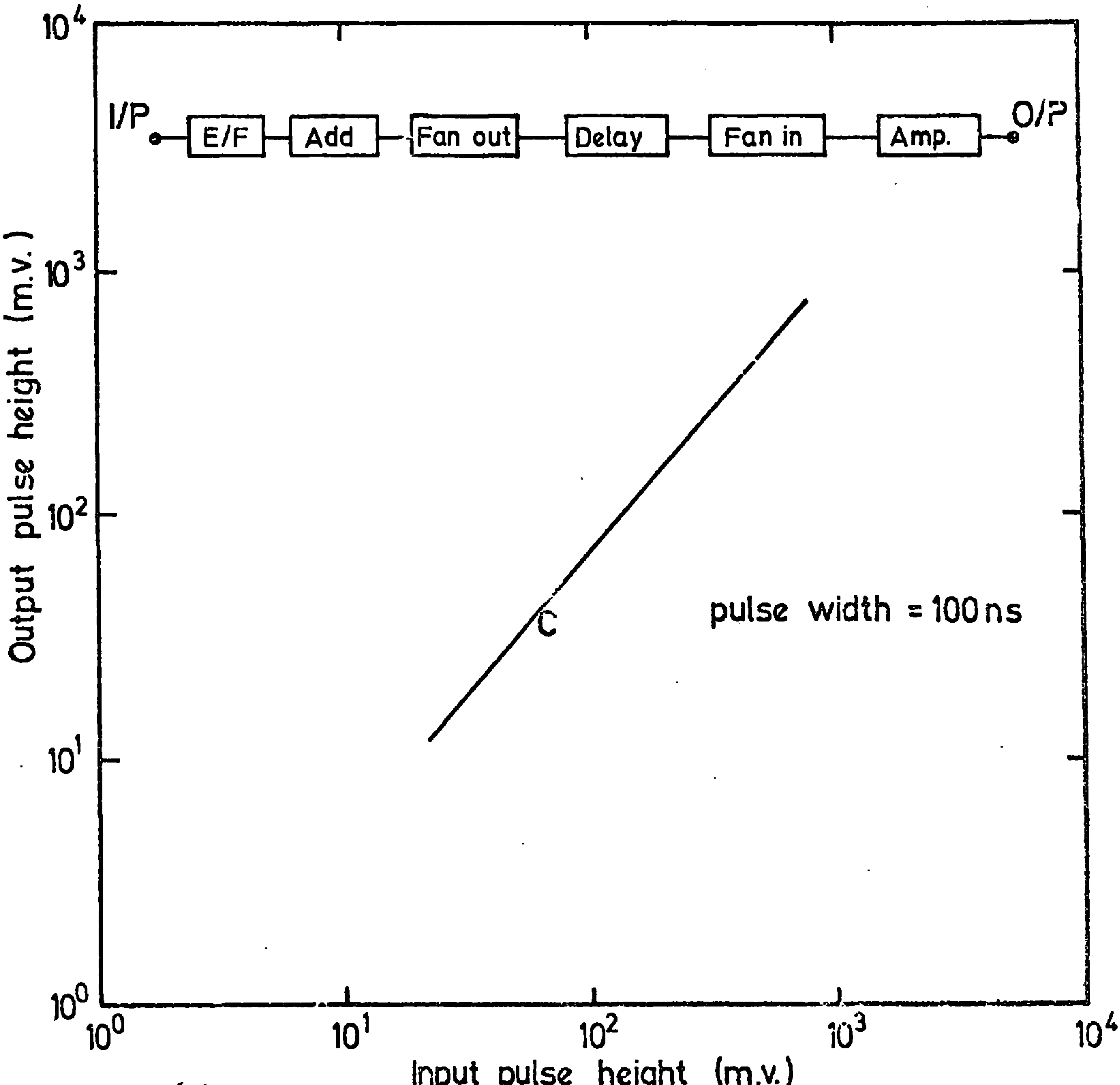

Figure 6.8

The input-output characteristics for the pulses transmitted through the circuit shown above associated with scintillator C, measured for square pulses.

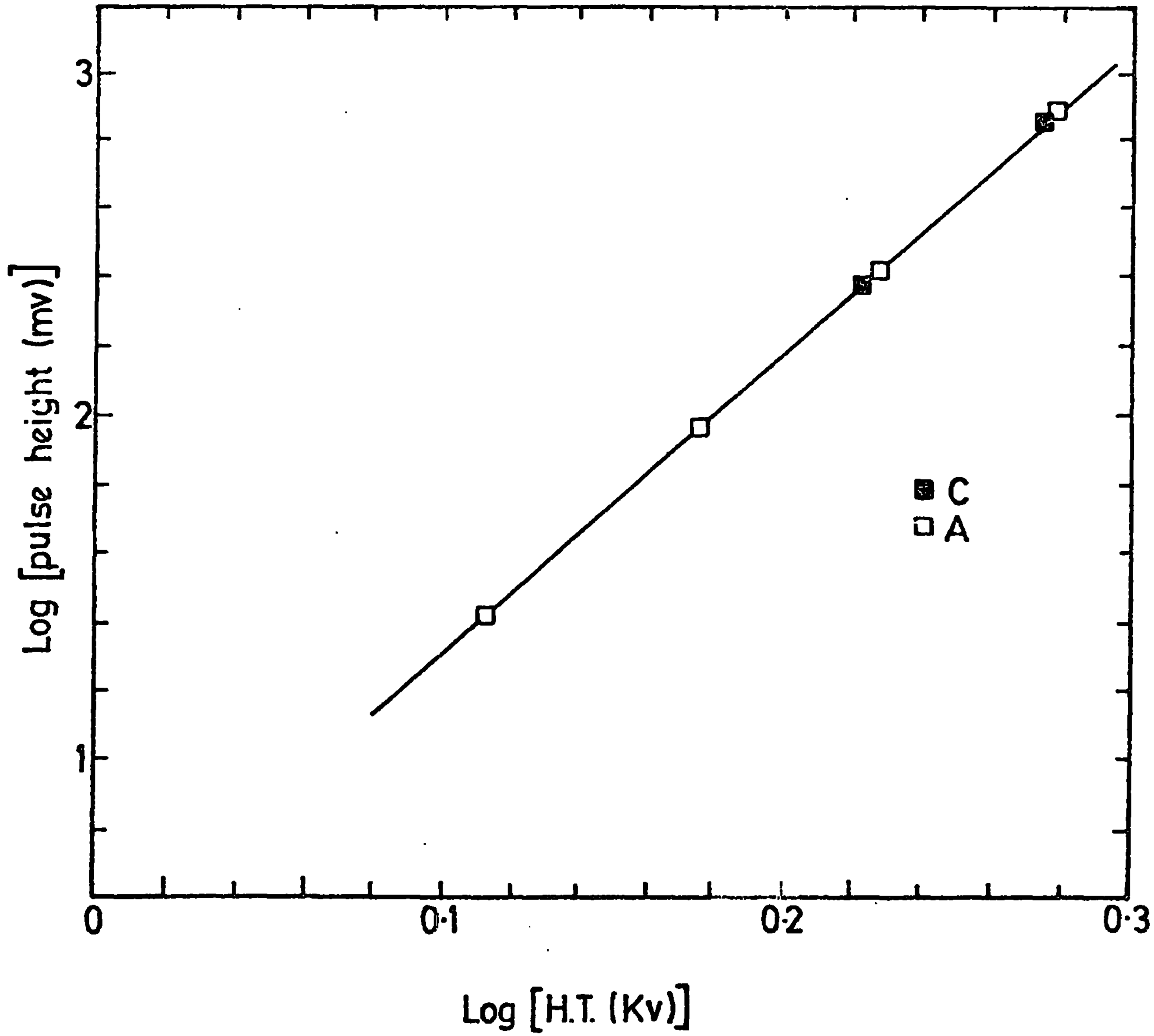

Figure 6.9 The variation of the output pulse height with the H.T. voltage applied to the scintillator A and C. The pulse height is given at the output of the photomultipliers for a single penetrating particle traversing the centre of the counter.

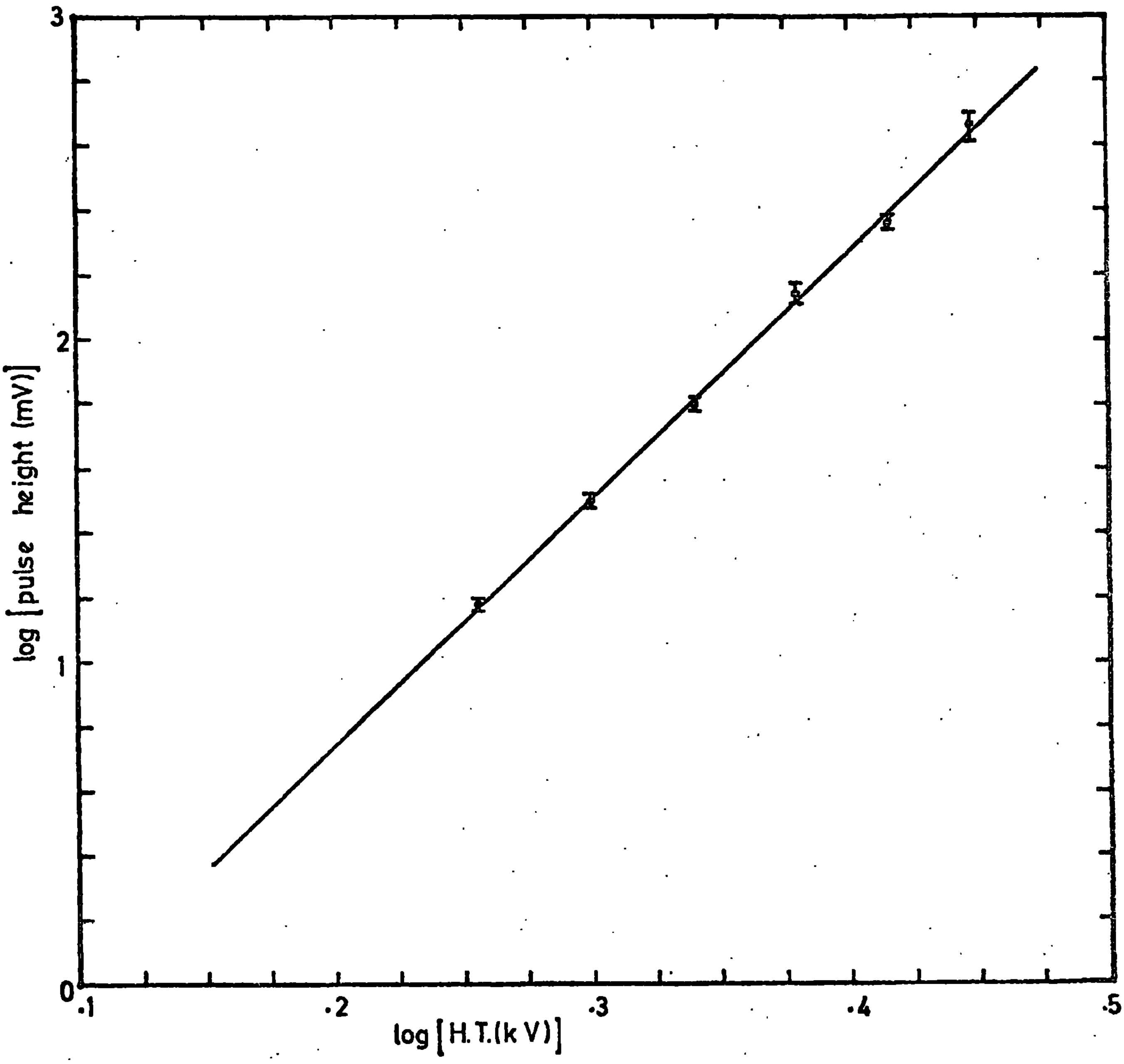

Figure 6.10

Variation of output pulse height with the H.T. voltage applied to the scintillator M. The pulse height is given at the output of the photomultipliers for a single penetrating particle traversing the centre of the counter at vertical incidence.

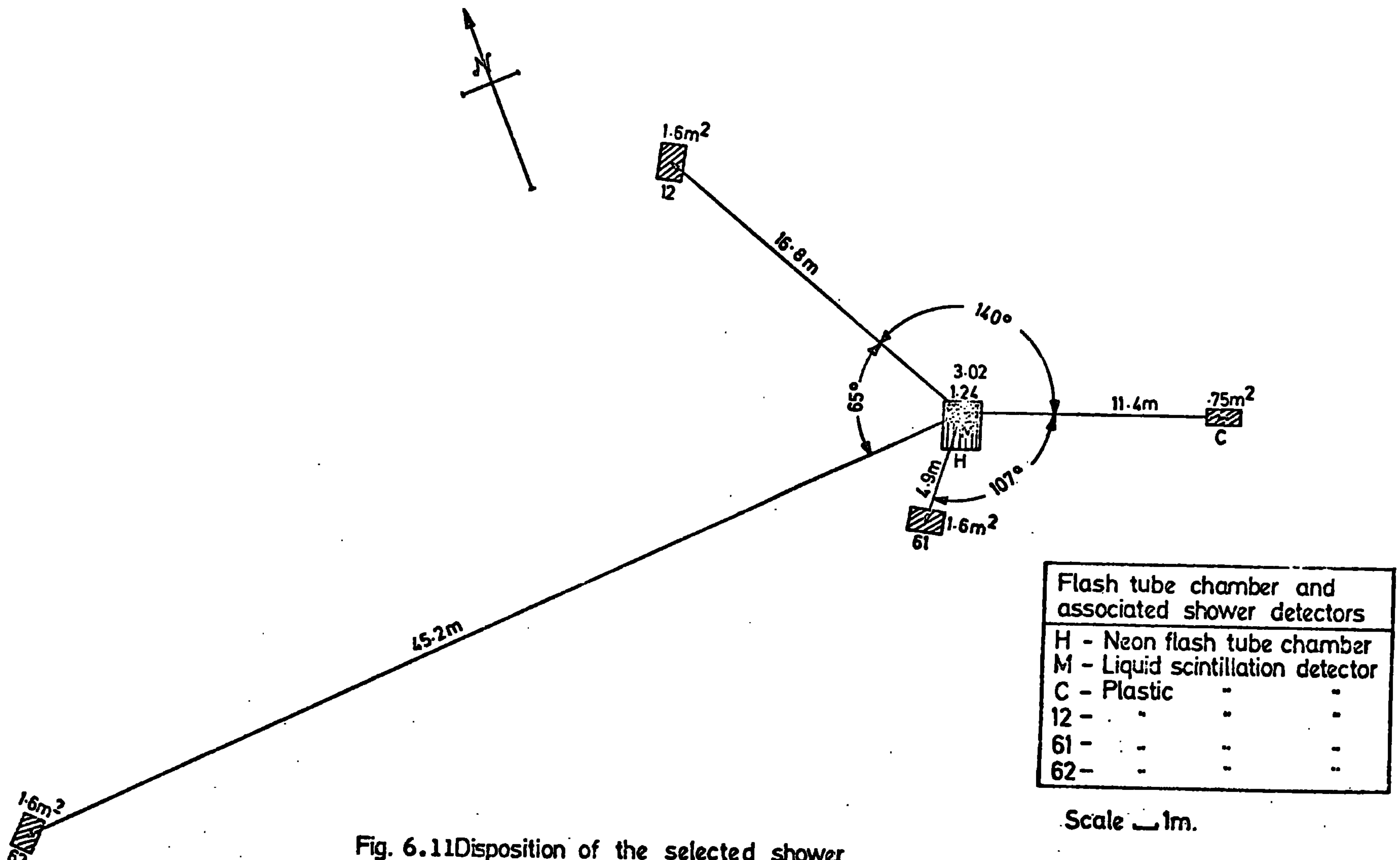

Fig. 6.11 Disposition of the selected shower detectors in conjunction with the Hadron detector.

in all detectors were 3 particles per square meter. Assuming the Greisen lateral structure function, a set of curves giving the election density as a function of core distance for different shower sizes has been produced (figure 6.12). From this figure the variation of collecting area with shower size has been determined (figure 6.13). It can be seen that as the shower size increases the collecting area increases. The minimum shower size for which the whole collecting area is effective is 5.10^4 particles.

6.10 Triggering mode

The apparatus has been set up to fire after a burst of size $\geq$ 400 particles produced either in lead or iron absorbers. The block diagram for the electronic employed in this experiment is shown in figure 6.14. Once the apparatus was triggered the pulses from scintillators A (under the iron)and C (under the lead) as well as the pulse from detector M (on the top of the chamber) were displayed on an oscilloscope trace after being delayed by 0.3 μs and 0.9 μs and 1.6 μs respectively and photographed. At the same time a 4-beam scope to which the outputs of four A.S. detectors were connected, was fired after the production of a burst either in lead or iron to give information on E.A.S. accompaniment. These pulses were also photographed. The 1-beam scope gave the burst size under the lead and iron and the electron density in detector M. The 4-beam scope gave the electron density in 4 air shower detectors. A dead time of 10 seconds has been imposed after every event. This dead time has been applied by means of an RC-controlled delay circuit which switched a relay, earthing the coincidence pulse line. The pulse from either detector A or C was first fed to this 10 second delay generator, then allowed to fire the spark gap to apply a high voltage to the chamber and the cycling system which triggered the micro switches controlling fiducial lights

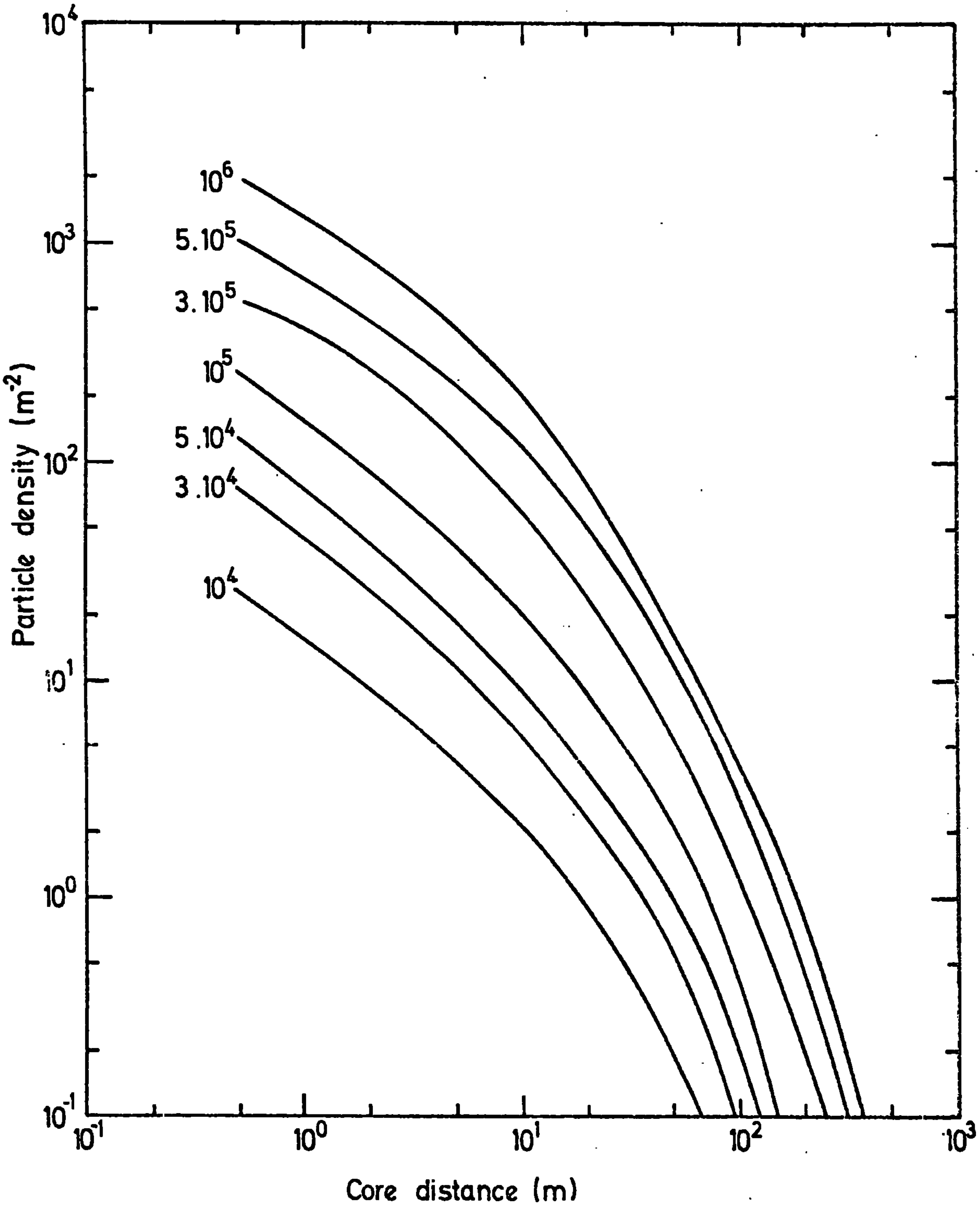

Figure 6.12 The air shower lateral structure for different shower sizes.

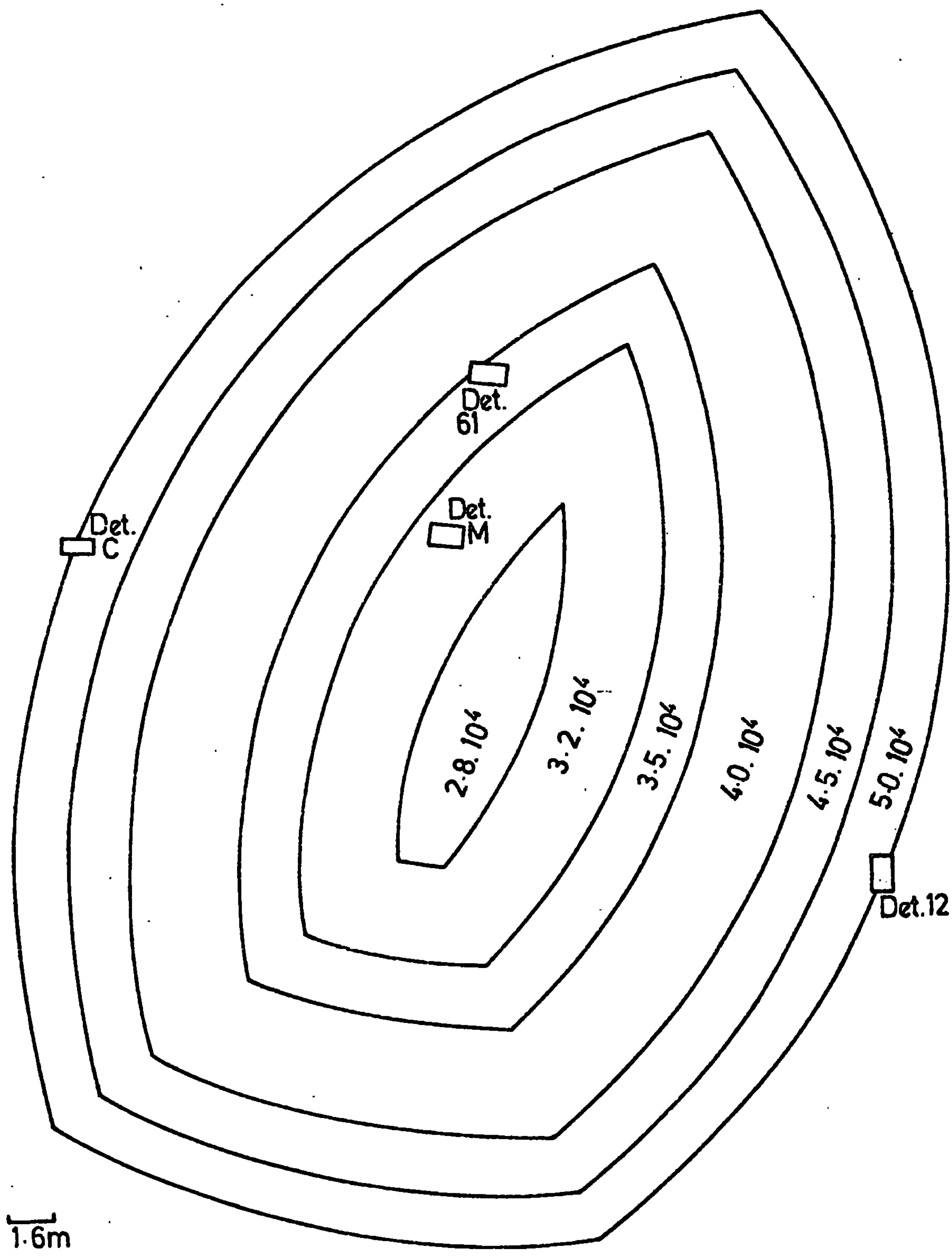

Figure 6.13 Acceptance area for different shower sizes

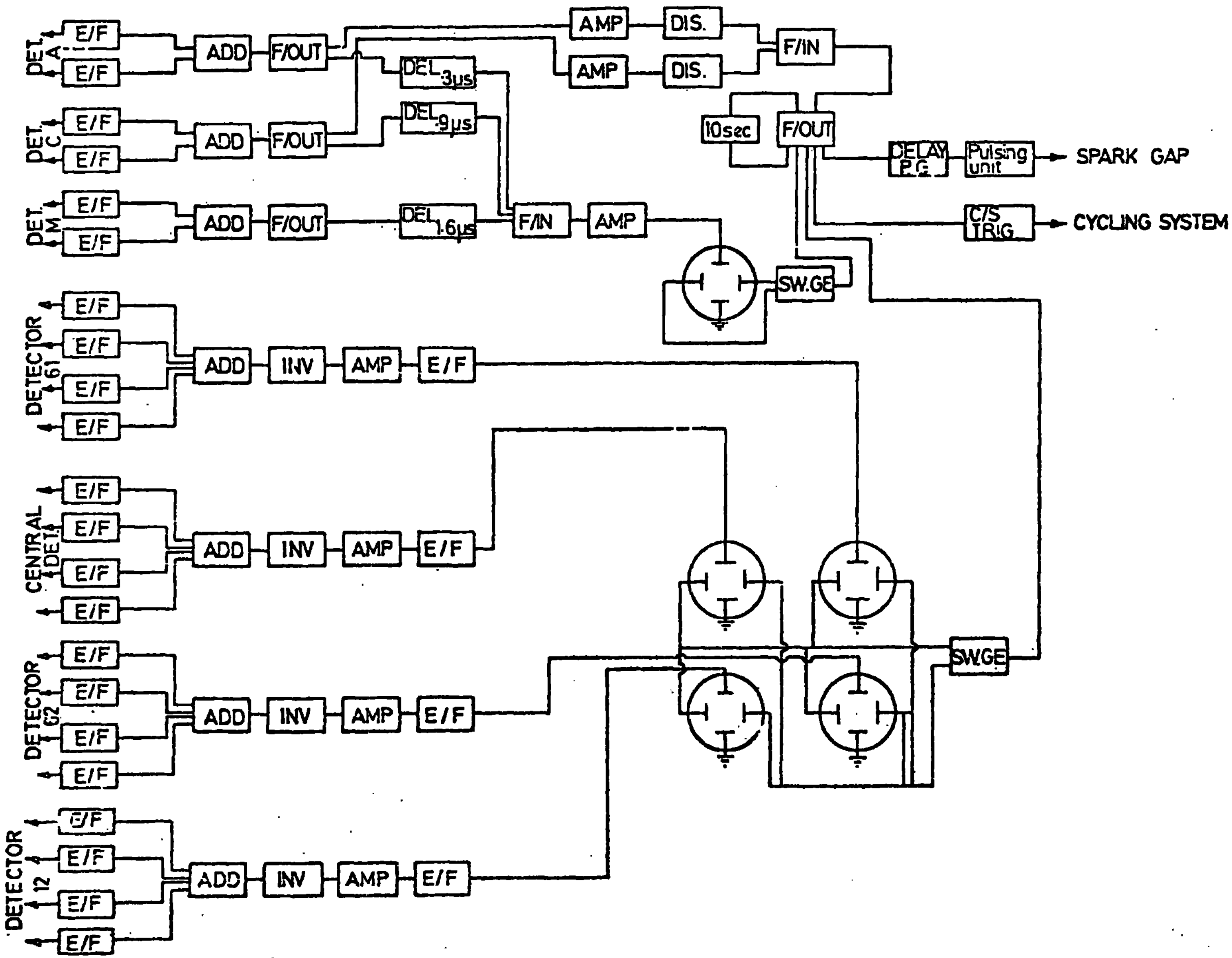

Figure 6.14 BLOCK DIAGRAM OF THE EXPERIMENTAL ARRANGEMENT FOR HADRON EXPERIMENT.

on the chamber, illuminating the clock and winding on the cameras. The cycle takes approximately 7 seconds.

6.11 The method of analysing data

All three films were projected on to a scanning table after being correlated. The geometry of the burst has been determined and the height of the pulses were measured. Figure 6.15 shows the scanning sheet used. The big pulse heights in 4-beam scope were measured by extrapolation.

6.12 A method for estimation of hadron energy from flash tube chamber

A rough calibration to estimate the energy of hadrons interacted in lead or iron absorbers has been made by counting the number of flash tubes flashed in a defined and fixed width over 8 layers in F_{1a} (interaction in lead target) and 6 layers in F_{1b} (burst produced in iron). This was possible when the core of the burst could be located. Figures 6.16 and 6.17 are the scatter plot of the number of flash tubes which had flashed within ± 0.5 cms from the middle of the core on the scanning sheets (scale 1 : 20) as a function of burst size, obtained from scintillators under the two absorbers. Figure 6.18 shows the average relationship of the two scatter plots. Plates 1, 2, 3 and 4 show the typical events recorded.

6.13 The method of acceptance funtion determination

The method adopted to determine the differential apertures of the flash tube chamber was the method used by Lovati et al (1954). They have introduced a procedure to convert the projected angular distribution of particles into the distribution function of particles given by $\cos^n\theta$ in real space.

Lovati et al considered two horizontal rectangular counters, A and B with dimensions 2 Y cm by 2 x cm and [illegible] cm by 2 v cm and placed one above the other at a distance Z cm, figure 6.19. The incoming particle direction

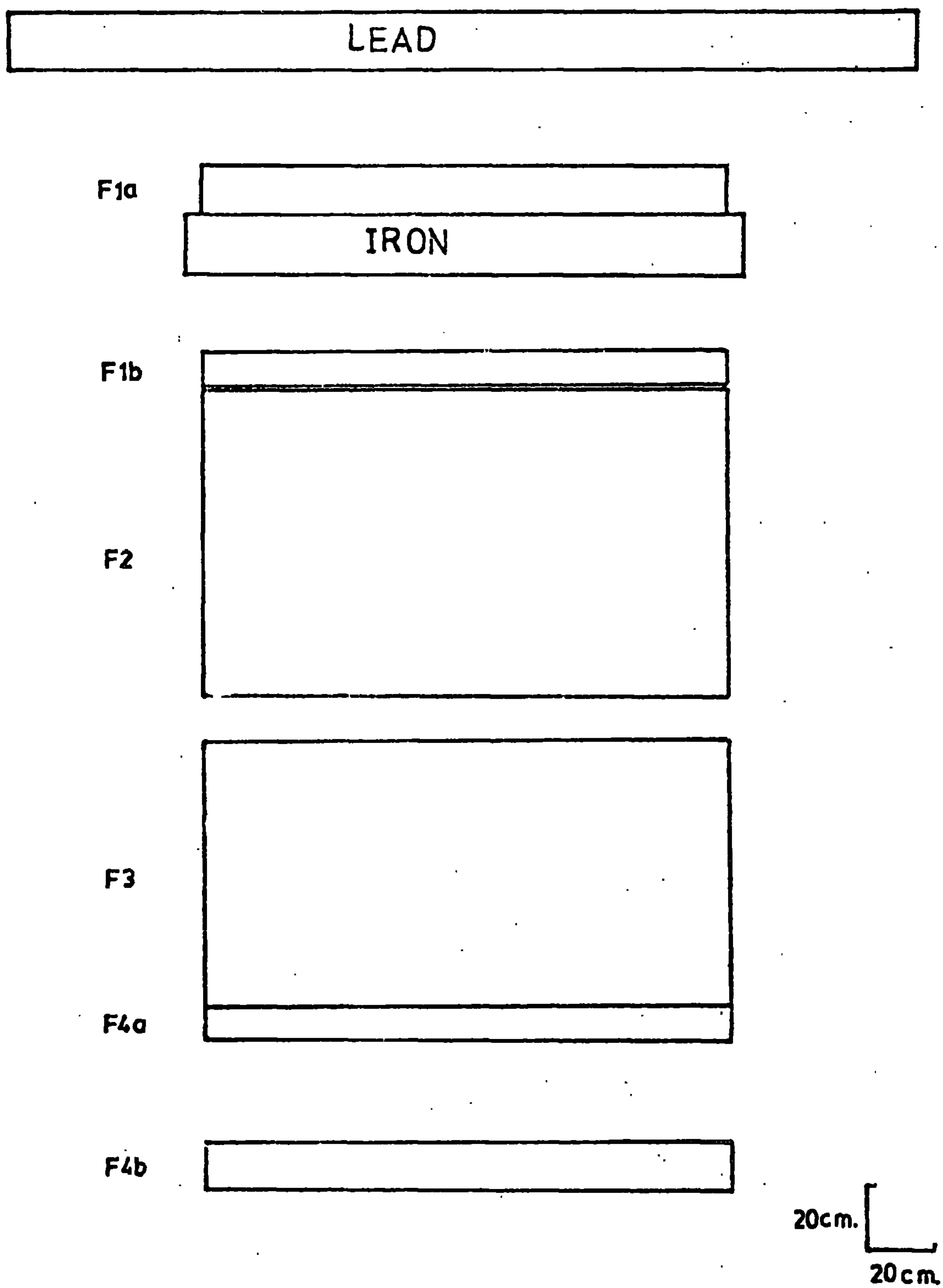

Figure 6.15

The front view of the flash tube chamber as drawn on the scanning sheet.

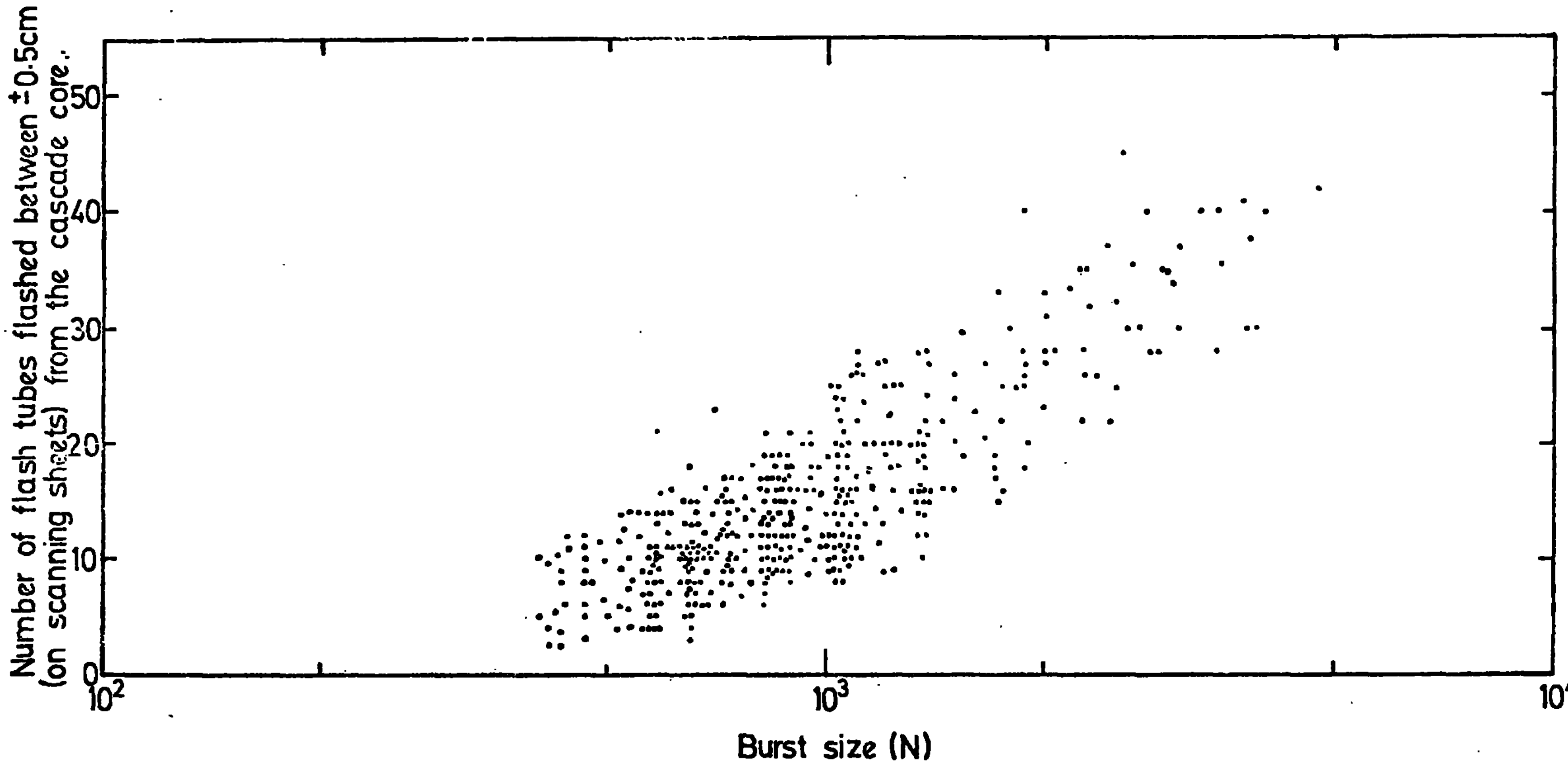

Figure 6.16 The scatter plot giving the relation between burst size N_e measured in scintillator A and the number of flash tubes which had flashed betðen ± 0.5 cm from the centre of the core on scanning sheet (scale 1:20).

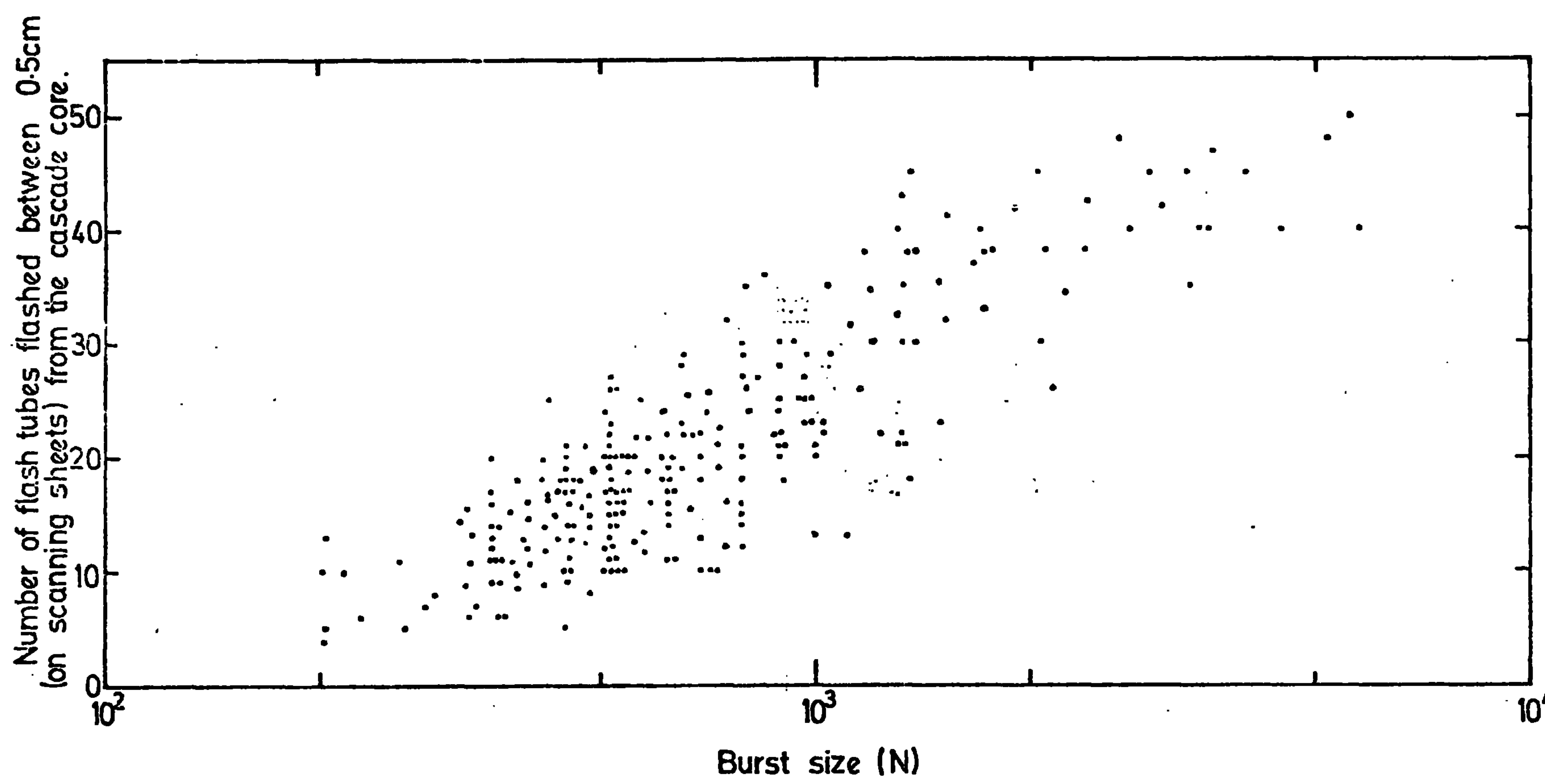

Figure 6.17 The scatter plot giving the relation between burst size, N_e measured in scintillator, C and the number of flash tubes which had flashed between ±0.5 cm from the centre of the core on scanning sheet (scale 1:20).

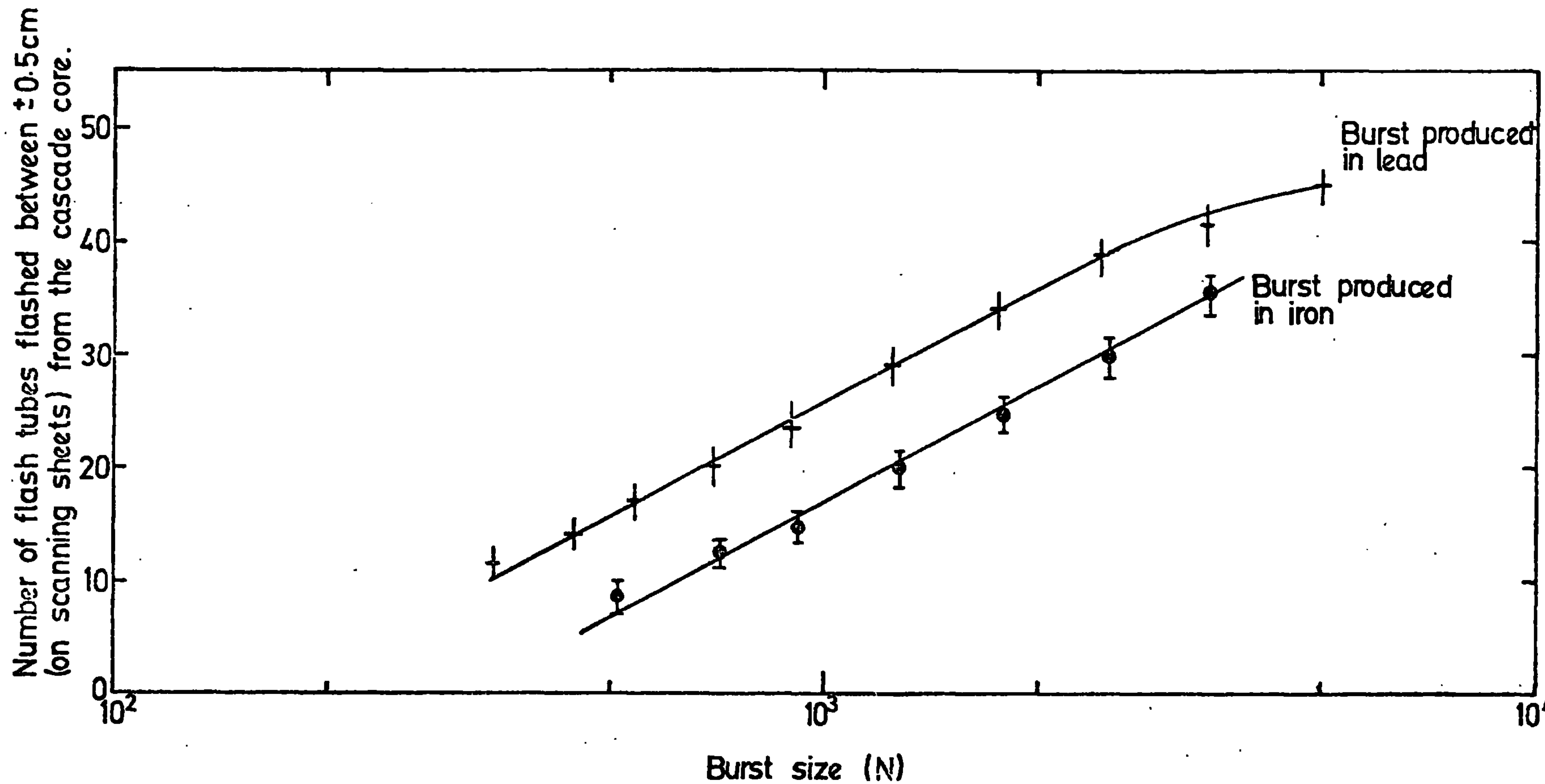

Figure 6.18 The relation between burst size, N_e measured in scintillator C (burst in lead) and A (burst in iron) and the number of flash tubes flashed between ±0.5 cm from the middle of the core on scanning sheet (scale 1:20).

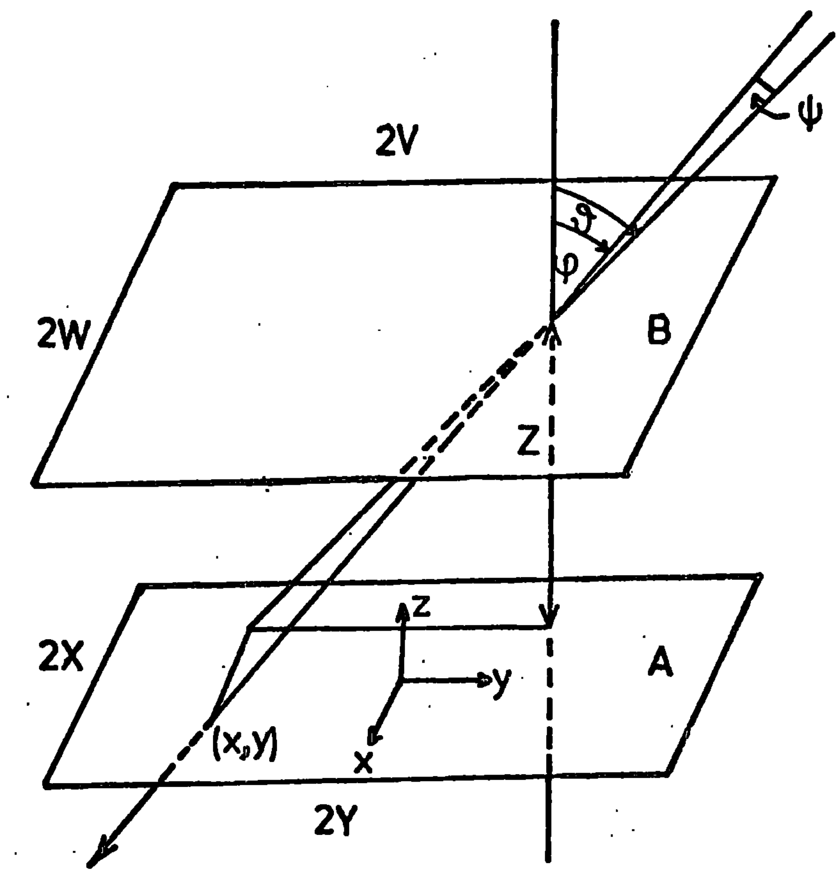

Figure 6.19 The path of a particle through parallel detectors.

is determined by the angles ϑ and ψ which are related to the zenith angle φ as:

$$\cos\varphi = \cos\vartheta \cos\psi$$

If the intensity of incoming particles follows the equation below

$$I(\varphi) = I(V)\cos^n\varphi$$

where I (V) is the intensity of incident particle in vertical direction in units of cm^{-2} st^{-1} sec^{-1} and I (φ) is the intensity at zenith angle φ. The total flux of incoming particles through the two rectangular counters would be as follows:

$$F_t = \iiint dx\, dy \cos\varphi\, I(\varphi)\, dw$$

$$= I(V)\iiint dx\, dy \cos\varphi \cos^n\varphi\, dw$$

where dw is the elementary solid angle and it is represented by:

$$dw = \cos\psi\, d\psi\, d\vartheta$$

Therefore $F_t = I(V)\iiint dx\, dy \cos^{n+1}\vartheta\, d\vartheta \cos^{n+2}\psi\, d\psi$

$$= 2I(o)\int_{\vartheta_1}^{\vartheta_2}\int_{y_1}^{y_2}\int_{x_1}^{x_2}\int_{\psi_1}^{\psi_2} \cos^{n+1}\vartheta\, d\vartheta\, dydx \cos^{n+2}\psi\, d\psi$$

Inverting the order of the integration with the limits :

$\vartheta_1 = 0$, $\vartheta_2 = \tan^{-1}\left(\frac{y+v}{z}\right)$

$x_1 = -x$, $x_2 = x$

$y_1 = -y$, $y_2 = y - z\tan$

and $\psi_1 = \arctan\left(\frac{w+x}{z} . \cos\vartheta\right)$

$\psi_2 = \arctan\left(\frac{w-x}{z} . \cos\vartheta\right)$

Defining $N_n(\vartheta)$ as the orthogonal projection on the vertical plane yz of the angular distribution function then,

$$F_t = \int N_n(\vartheta)\, d\vartheta$$

$$\text{Therefore } N_n(\vartheta) = 2I(V)\, \text{Cos}^{n+1}\vartheta\, (y + v - z \tan\vartheta) \int_{-x}^{x} dx \int_{\psi_1}^{\psi_2} \text{Cos}^{n+2}\psi \, d\psi$$

considering the limitation as:

$$y + x - z \tan\vartheta \geq o$$

$$\text{i.e. } \tan\vartheta \leq (y + v) / Z$$

Integrating the above equation for integer values of the exponent n.

The results of the integration for the different values of n can be shown as:

$$N_o(\vartheta) = \frac{1}{2} K \,\text{Cos}\vartheta \left[(x - w) \text{ arc tan}\left\{\frac{(w-x)\text{Cos}\vartheta}{Z}\right\} + (w+x) \text{ arc tan } \left\{\frac{(w+x)\text{Cos}\,\vartheta}{Z}\right\}\right]$$

$$N_1(\vartheta) = \frac{1}{3} K \,\text{Cos}\vartheta \left[\frac{Z^2 - 2(Z^2 + (w-x)^2 \text{Cos}^2\vartheta}{A_-^{1/2}} - \frac{Z^2 - 2(Z^2 + (w+x)^2 \text{Cos}^2\vartheta}{A_+^{1/2}} \right]$$

$$N_2(\vartheta) = \frac{1}{8} K Z^3 \text{Cos}^2\vartheta \, (A_-^{-1} - A_+^{-1}) + \frac{3}{4} \text{Cos}^2\vartheta \, N_o(\vartheta)$$

$$N_3(\vartheta) = \frac{1}{15} K Z^4 \text{Cos}^3\vartheta \, (A_-^{-3/2} - A_+^{-3/2}) + \frac{4}{5} \text{Cos}^2\vartheta \, N_1(\vartheta)$$

where $K = 4\, I(\vartheta)\, (y + v - z \tan\vartheta)$ and $A^{\pm} = Z^2 + (w \pm x)^2 \text{Cos}^2\vartheta$

pallison (1965) expressed a general equation for $n > 1$ as:

$$N_n(\vartheta) = \frac{KZ^{n+1}\text{Cos}^n\vartheta}{n.(n+2)} (A_-^{-n/2} - A_+^{-n/2}) + \frac{n+1}{n+2} \text{Cos}^2\vartheta \; N_n - 2(\vartheta)$$

Therefore by knowing the acceptance limits of the apparatus the predicted angular distribution can be calculated, comparing the predicted to measured angular distribution the value of n can be determined.

So, to calculate the acceptance aperture of the flash tube chamber in the present experiment it is necessary to define the acceptance limits for which the events are selected (see chapter 9).

6.14 Method of shower core location

6.14.1 Introduction

By sampling the electron density at different points in a shower one can determine the core position of the shower provided that a lateral density distribution function is assumed. Detectors capable for measuring the particle density are G.M. counter, ionization chamber, scintillators and cloud chambers.

There are other methods of air shower core location by measuring other properties of the particles in the shower such as, energy, angle, nature and timing arrival which can be related to the core distance. In the present experiment the method of sampling the electron density was used.

6.14.2 Lateral structure function

The lateral distribution of the electron density is referred to as the structure function. This air shower characteristics have been measured by many people both at mountain altitude and sea level. Greisen (1960) has summarised a great deal of experimental results and obtained an average experimental expression. This expression has been used by many people and is believed to be a good representation of the structure function. This function is expressed as:

$$\rho\,(N,r) = \frac{0.4N}{r_1^{\,2}} \left(\frac{r_1}{r}\right)^{0.75} \left(\frac{r_1}{r+r_1}\right)^{3.25} \left(1 + \frac{r}{11.4 r_1}\right)$$

where ρ is the electron density per square metre for a shower of size N at core distance r (m). r_1 is the characteristic scattering length, called Molier unit, for electrons in air. For core distance $<$ 100 m this function becomes a close approximation to the theoretical function of Nishimura and Kamata (1952, 1958) for pure electron-photon shower with S as an age parameter. Greisen (1956) has given a simplified version as:

$$F\,(r/r_1) = C(S)\left(\frac{r}{r_1}\right)^{S-2}\left(\frac{r}{r_1}+1\right)^{S-4.5}$$

where C(S) is a normalisation factor:

$$\int_0^{\infty} 2\pi\, f(x)\, x dx = 1 \qquad \text{where } x = \frac{r}{r_1}$$

If the lateral distribution is shower size independent the density of electron at a core distance r will have the form:

$$\rho(N,r) = \frac{N^r}{r_1^2} \cdot f(r)$$

The Keil group (Hillas 1970) gives an expression, using a neon hodoscope, as:

$$\rho(N,r) = 1.08 \times 10^{-2} \frac{N}{(r + 1.1)^{1.5}} \exp\left(\frac{-r}{120}\right)$$

Hasegawa et al (1962) expressed an structure function as :

$$\rho(N,r) = \frac{N}{2\pi(120\pi)^{1/2}} \cdot \frac{\exp\left(\frac{-r}{120}\right)}{r^{1.5}}$$

Sydney group measurements, Hillas (1970) gives an expression as:

$$\rho(N,r) = 2.12.10^{-3} \frac{N}{r+1} \exp\left(\frac{-r}{75}\right)$$

A comparison of the different measurements is shown in figure 6.19a there is a discrepancy in experimental results that could be due to the errors in the core location.

6.14.3 <u>Graphical method of core location</u>

Sampling the particle density at four points on an observation level the shower core can be located, assuming an electron lateral distribution function. Any two measurements of electron density ρ's determine a line which the shower axis must intersect as it crosses the observation level. Four electron density determine three lines that will intersect in one point if the lateral distribution is correct. To prepare the core locating charts, for each two detectors the core distance r to one detector was taken to be constant, the distance of the core to the other one was varied and the electron density ratio of two detector was calculated in each

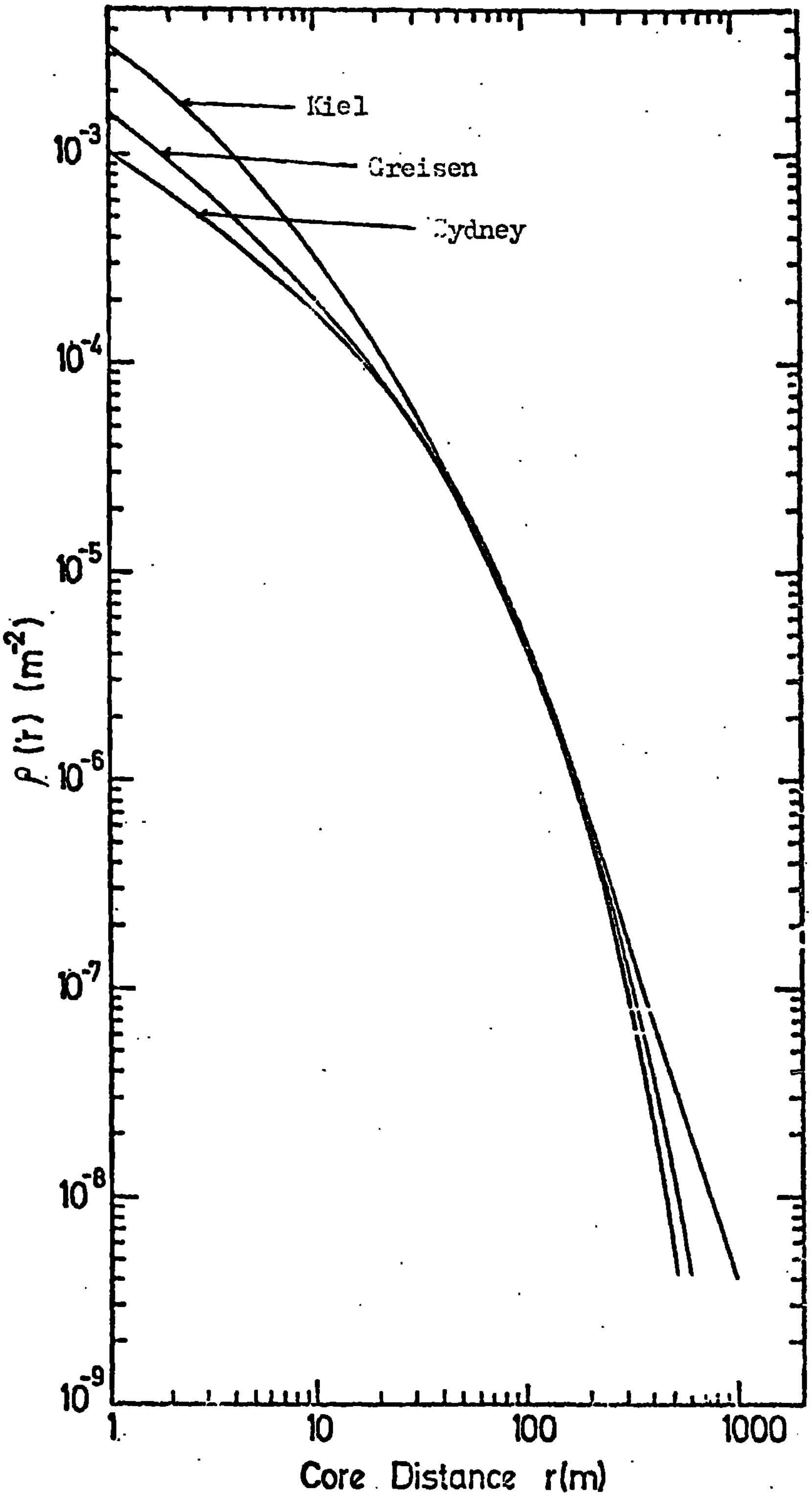

Figure 6.19a Lateral structure function of EAS particles. The curves are due to emperical formula given by Greisen (1960) and observations of Kiel group and Sydney group Hillas (1970a). The ordinate gives electron density for a shower size of N = 1.

case using Greisen structure function (section 6.14.2). Some of the results of the calculation is shown in figures 6.20 and 6.21. From these curves the core locating charts, showing the lines of constant ratio of densities between detectors were determined. To produce the locus of core positions that would produce a constant density ratio between two detectors the curves in figure 6.20 and 6.21 are used. Different r_1 and corresponding r_2 are obtained for a particular density ratio. r_1 determines the radius of a circle on which the core must fall, r_2 determines a similar circle around detector 2. The pairs of the points produced by the intersections of the pairs of the circles give the required locus. Figures 6.22, 6.23 and 6.24 show a chart of these lines of constant electron density ratio for each pair of detectors, each ratio places the shower axis in one line. Knowing the core location and the electron densities in different scintillators the shower size was determined using the lateral structure curve shown in figure 6.25. Figure 6.26 shows an example of the core location.

Taking the errors in the electron density measurement as poissonian the frequency distribution of ΔR was obtained, where ΔR is the maximum error in the core location figure 6.27 shows the frequency distribution in ΔR.

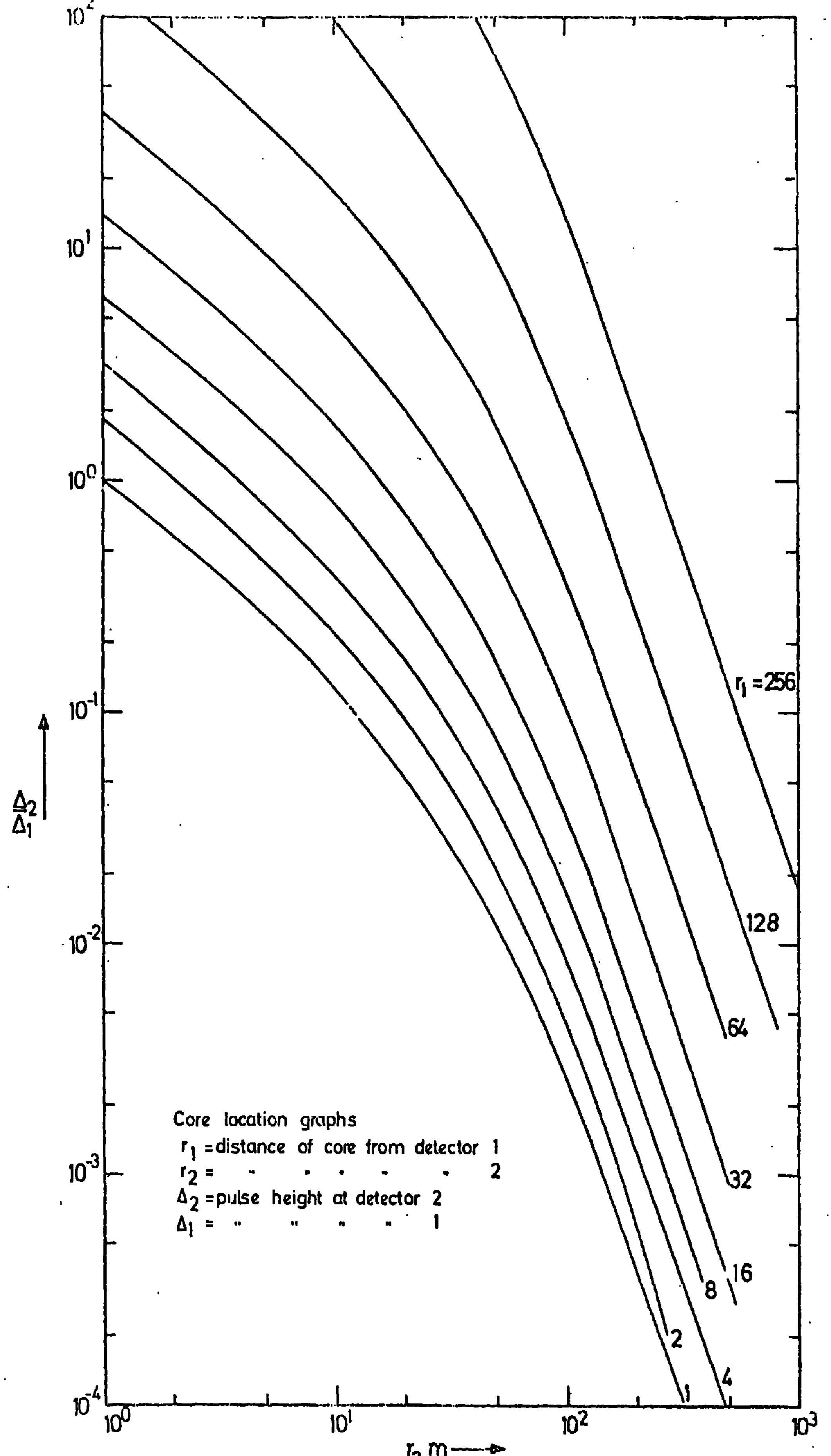

Figure 6.20 The variation of the ratio of the electron density of two detertors against the core distance of one of the two with the core distance of the other as a parameter.

(These curves are valid for any separation D of detectors 1 and 2 provided $r_1 + r_2 > D$).

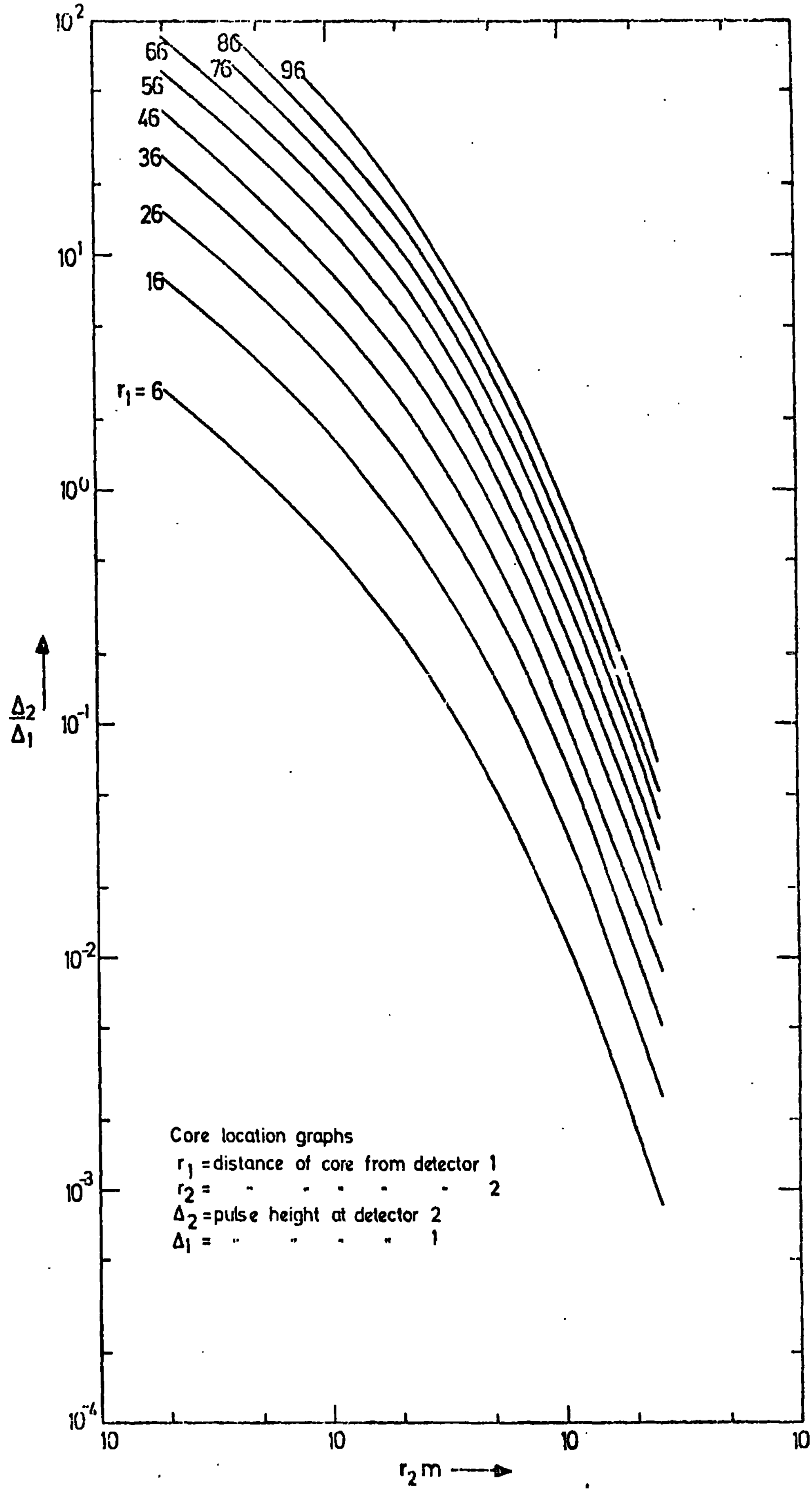

Figure 6.21 The variation of the ratios of the electron density of two detectors against the core distance of one of the two with the core distance of the other one as a parameter. (These curves are valid for any separation D of detectors 1 and 2 provided $r_1 + r_2 > D$).

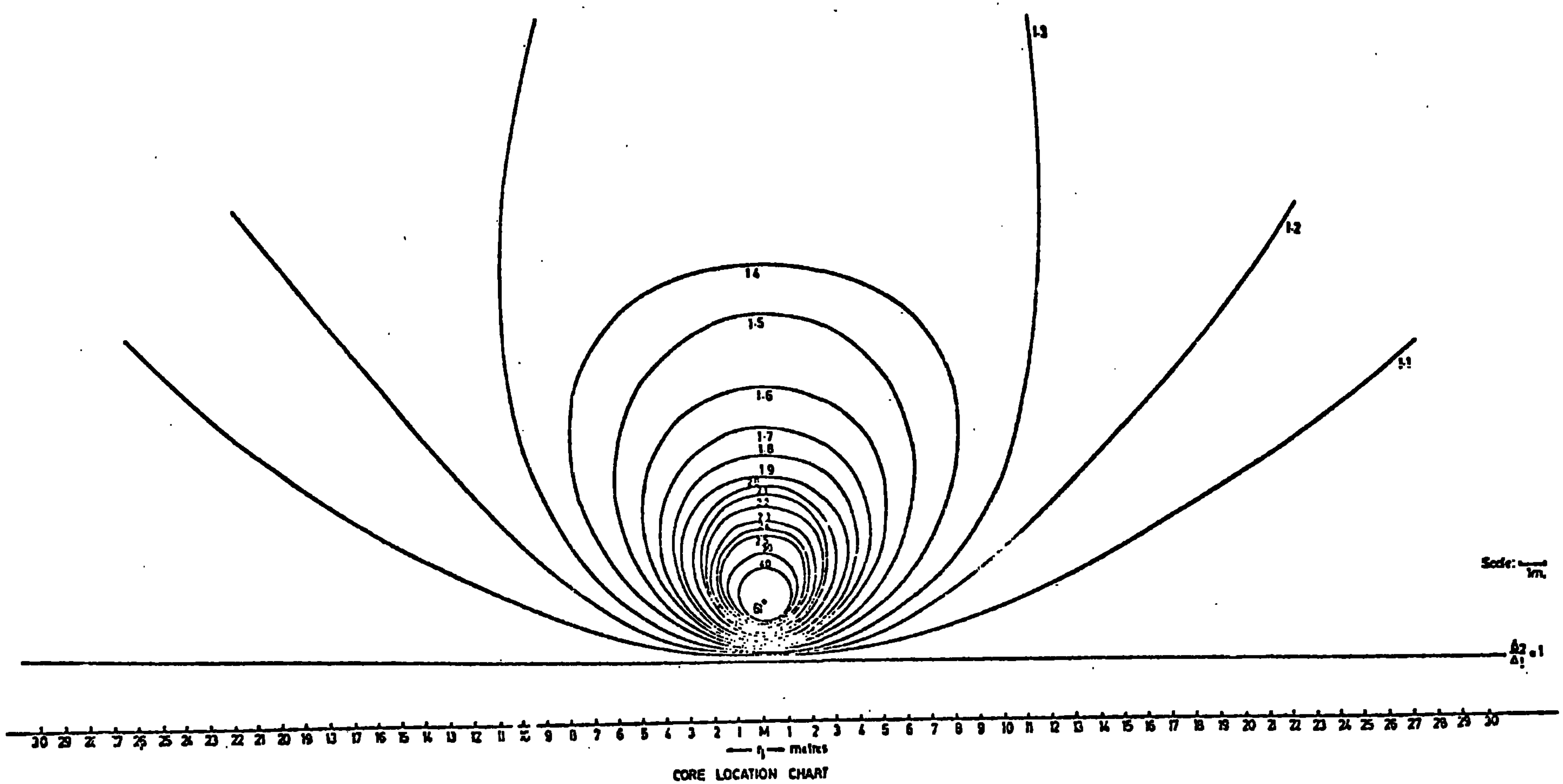

Figure 6.22 The chart of lines of constant ratio of densities between detectors M and 61. The number by the lines are the density ratios.

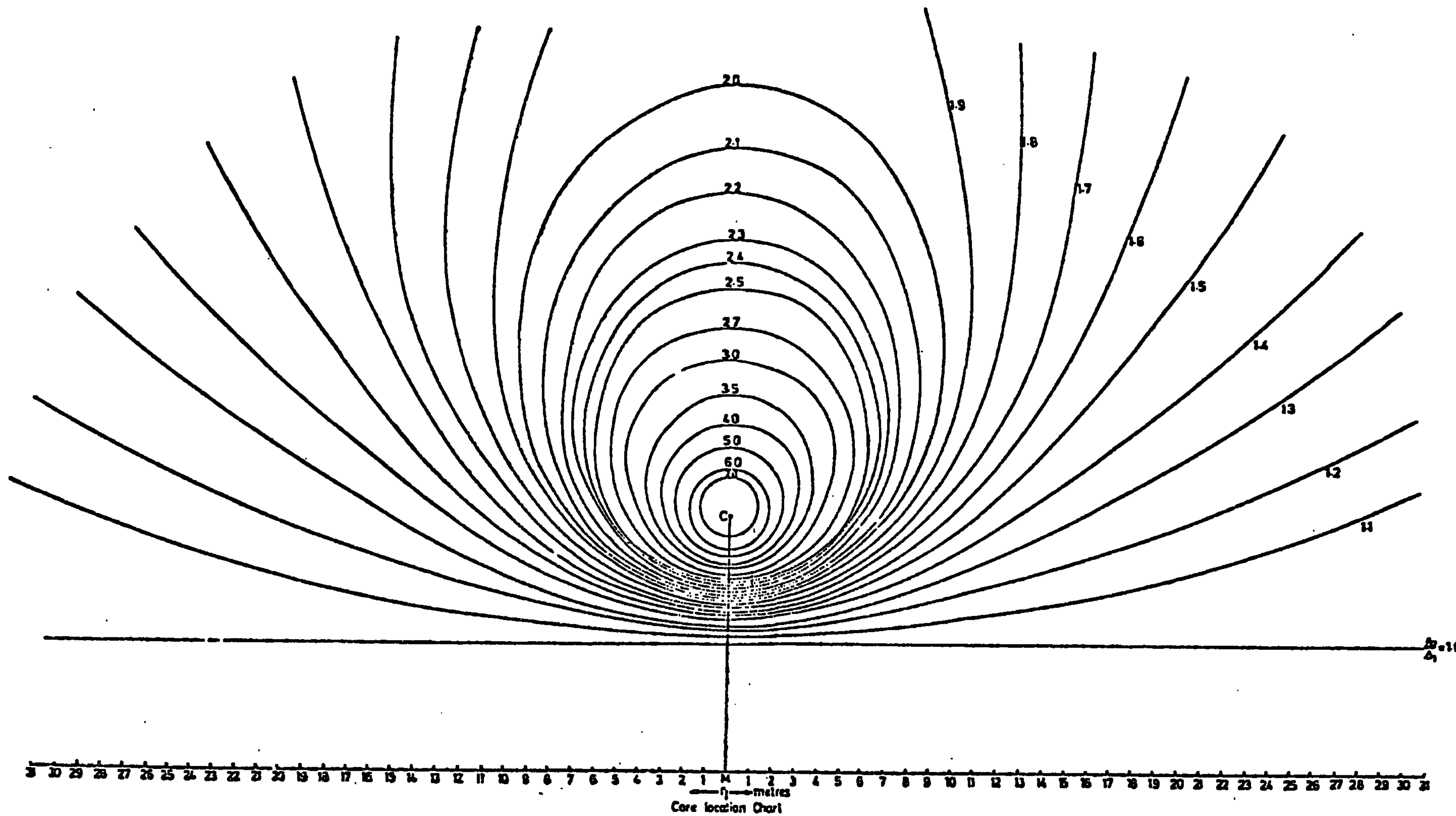

Figure 6.23 The chart of lines of constant ratio of densities

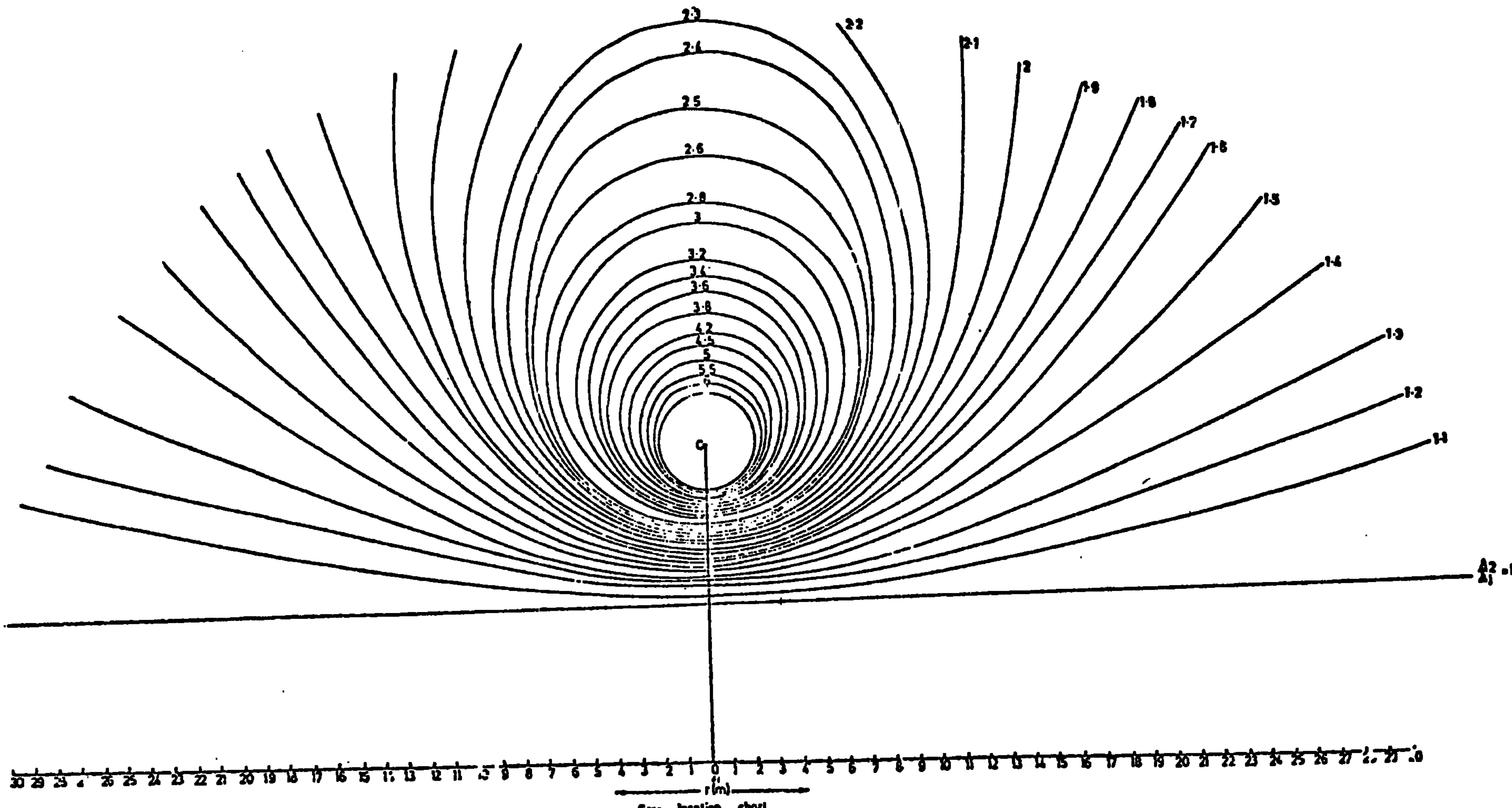

Figure 6.24 The chart of lines of constant ratio of densities between detectors 61 and C.

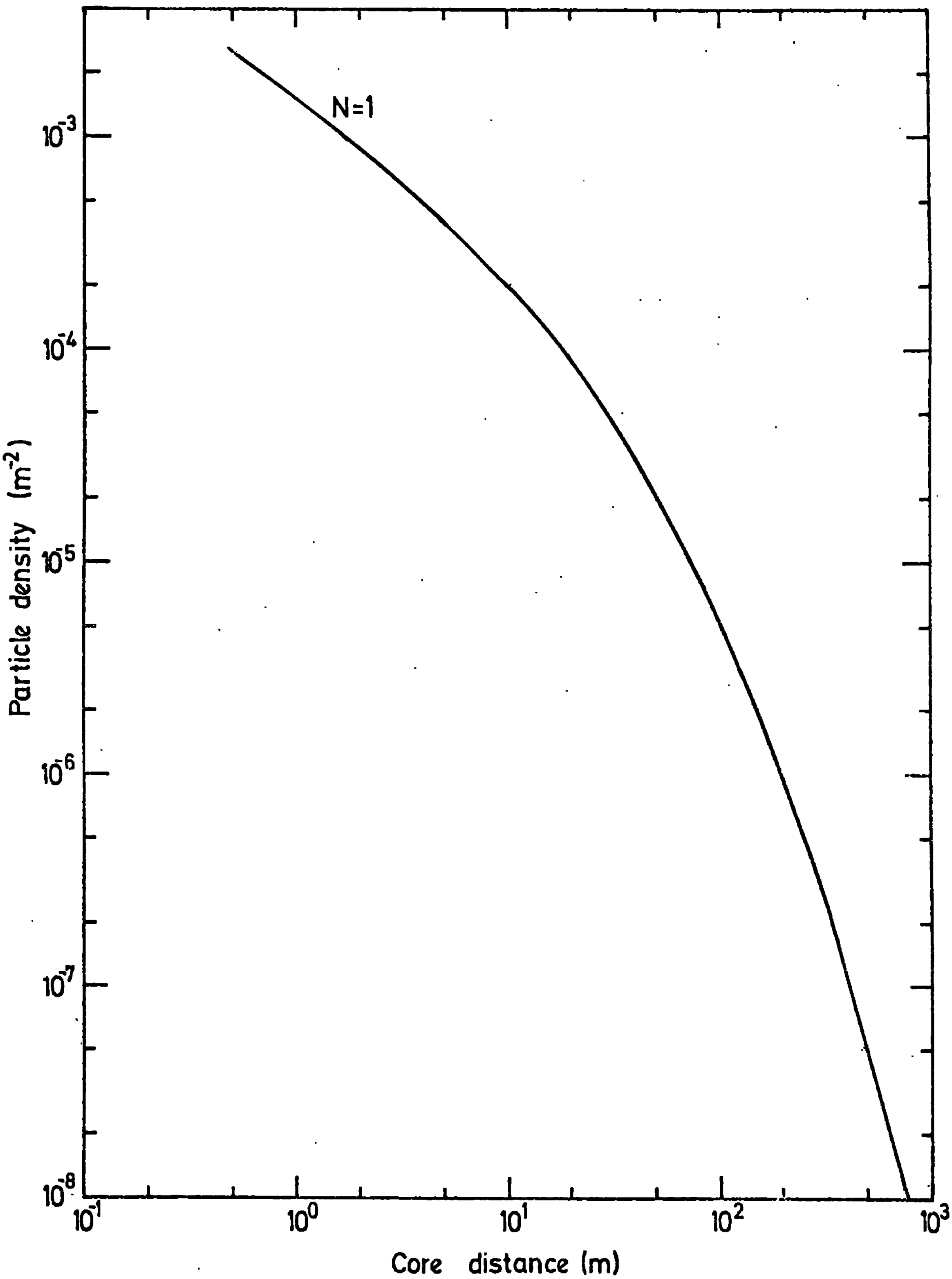

Figure 6.25 The air shower lateral structure, normalised to N = 1

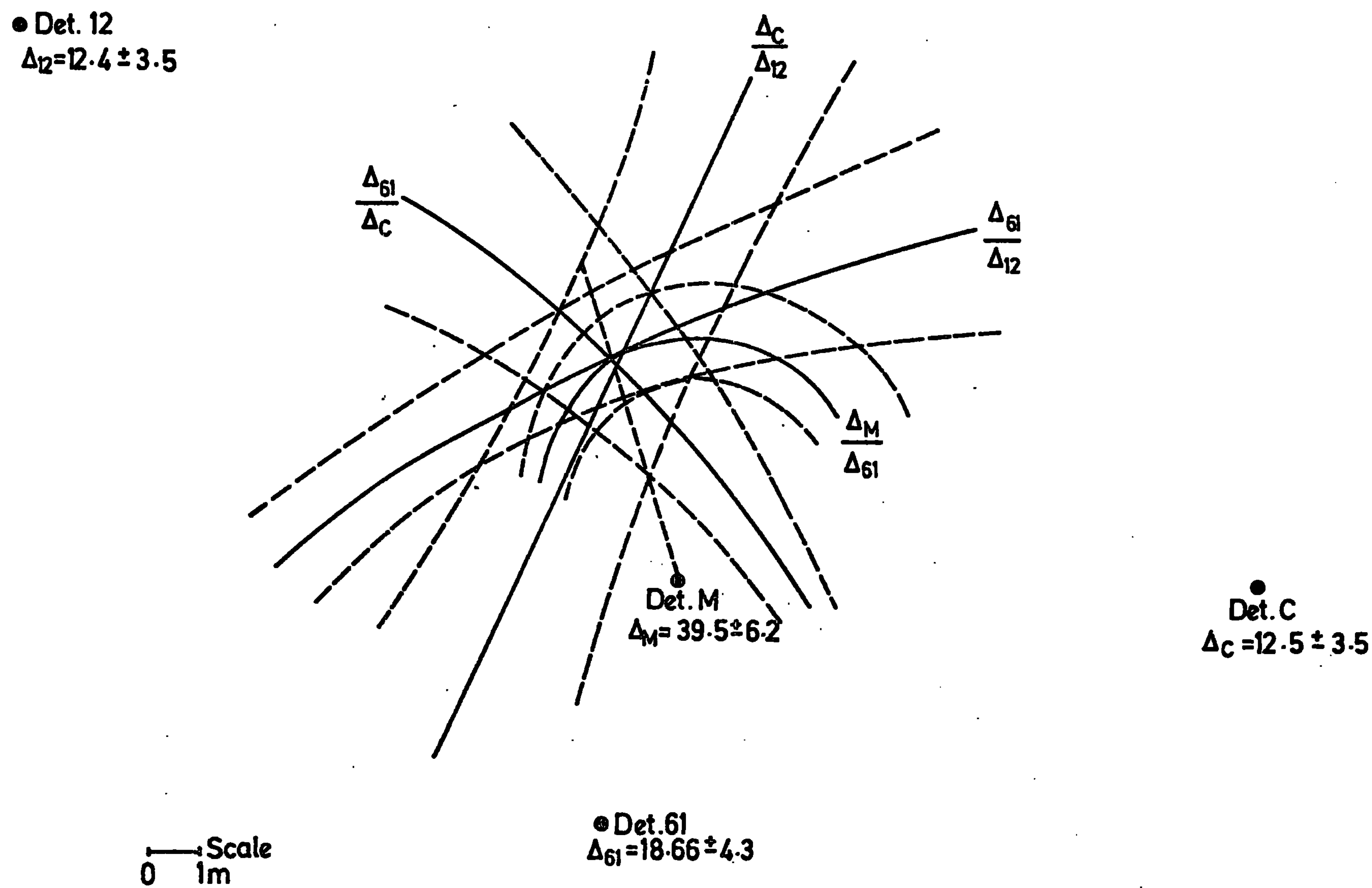

Figure 6.26 An example of core location

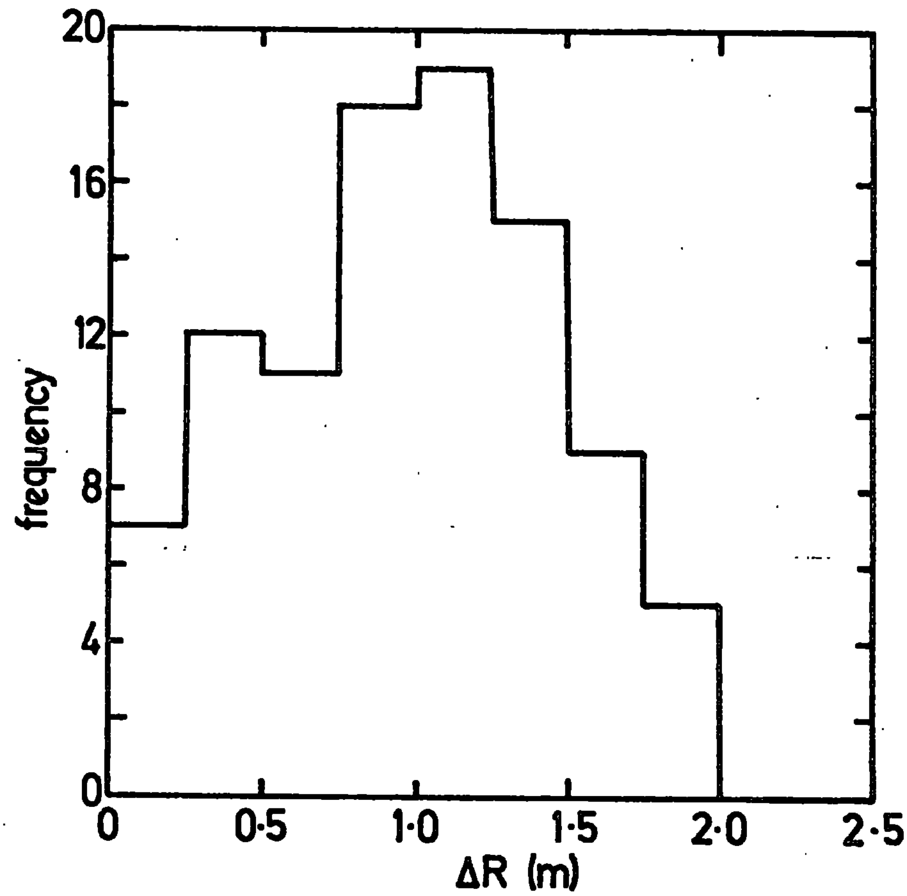

Figure 6.27 Frequency distribution in ΔR, the maximum error in core location.

PLATE 6.1

Event H 11 6-11

A burst produced by an unaccompanied hadron interacted in lead, producing a burst of size 966 particles, measured in scintillator C.

PLATE 6.2

Event H 145 - 4

A burst produced in lead which penetrated the iron, producing outputs from scintillator C and A. With no shower accompaniment, the burst size in detectors C and A is 2700 and 2931 particles respectively.

7.3 Lateral distribution of hadrons

7.3.1 Method of measurement

The lateral distribution of hadrons in the present experiment has been measured on the basis of the following description.

In a running time t, suppose N shower cores per unit area fall in an annulus of width Δr at distance r from the middle of detector M but only n showers spread over the whole annulus give a measureable hadron.

$\Delta(>E,r,N_e) = 1\ m^2$ if 1 hadron of energy >E detected for every shower of median size N_e that falls in the annulus.

Total number of showers that fall in the annulus = $N2\pi r\Delta r$

$$\Delta(>E,r,N_e) = 1. \frac{n}{N2\pi r\Delta r}$$

7.3.2 The size spectrum

Since our chamber was triggered by hadrons we could not measure the shower size spectrum, therefore we have used the sea level number spectrum summarised by Hillas (1970) to calculate the absolute number of showers falling on each ring round the centre.

The analytical representation summarised by the above mentioned author is the following:

$$N < 5.10^5 \qquad R_o(>N) = 2.10^5\ N^{-1.5}\ m^{-2}\ hr^{-1}\ st^{-1}$$

$$5.10^5 \leq N < 3.10^7 \qquad R_o(>N) = 1.42.10^8 N^{-2.0}\ m^{-2}\ hr^{-1}\ st^{-1}$$

$$N \geq 3.10^7 \qquad R_o(>N) = 2.6.10^4\ N^{-1.5}\ m^{-2}\ hr^{-1}\ st^{-1}$$

To get total rate from vertical intensity:

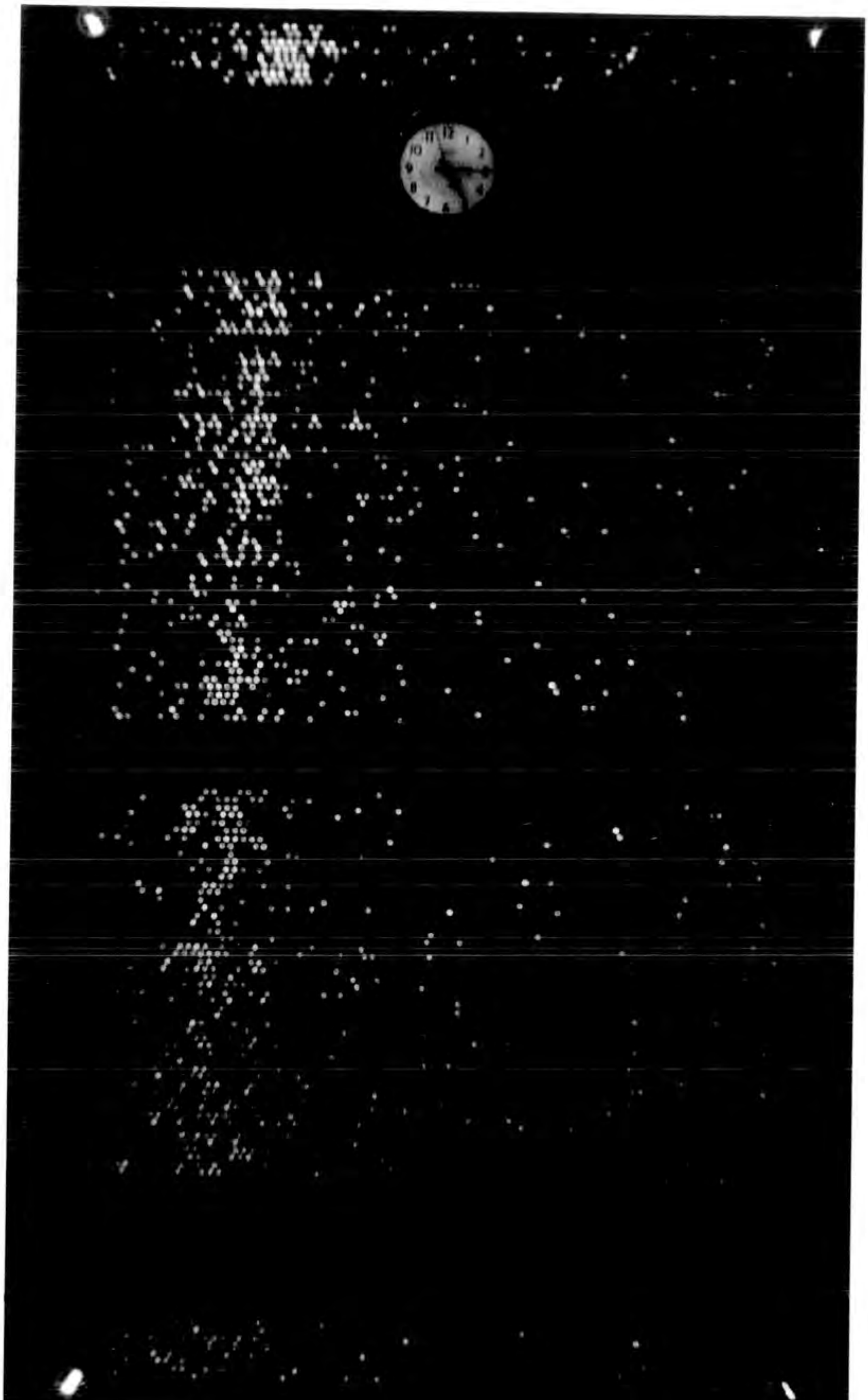

PLATE 6.3

Event H 171 - 3

A hadron interacted in iron producing a burst of size 3540 particles, measured in detector A. With no shower accompaniment.

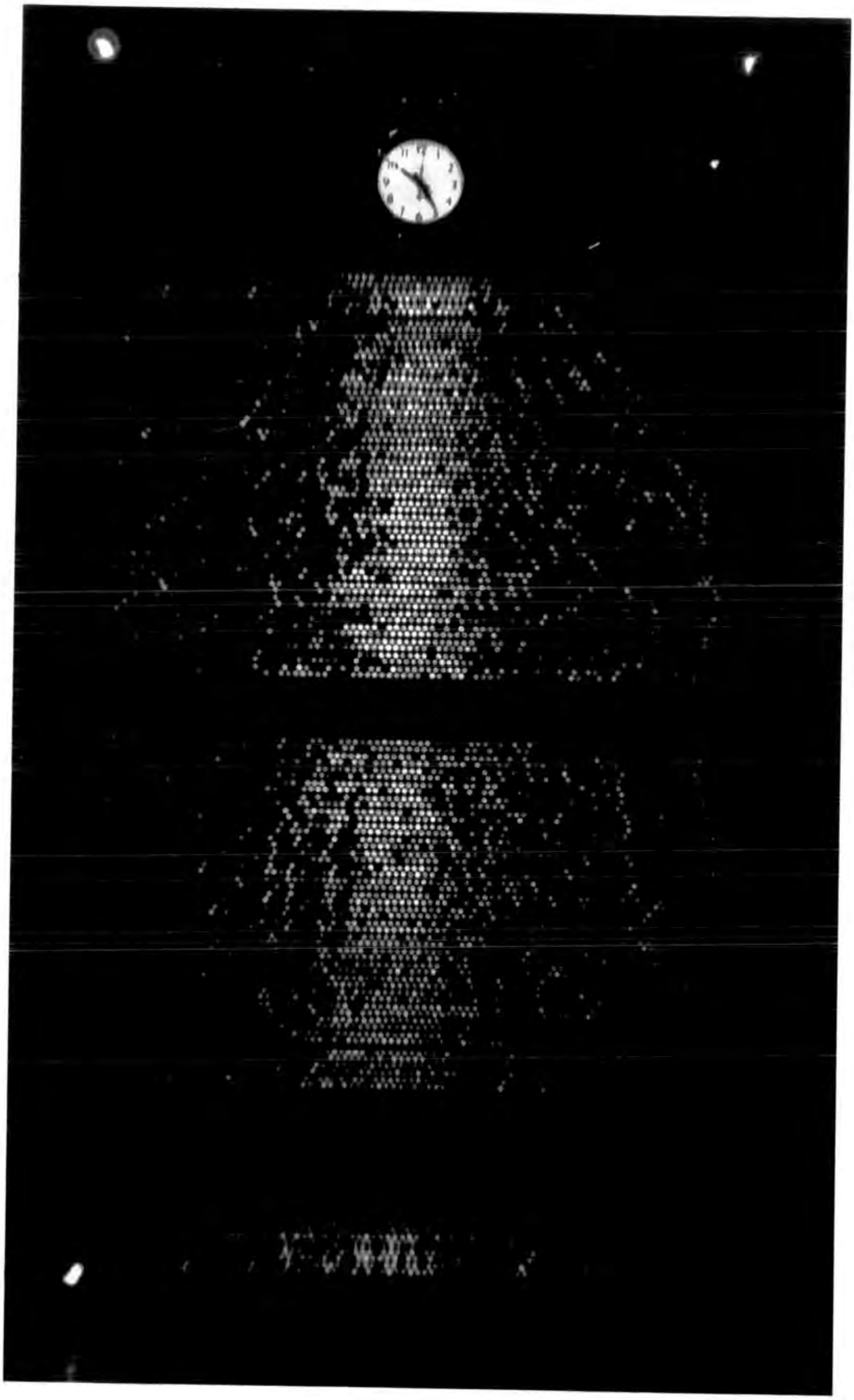

CHAPTER 7

EXPERIMENTAL RESULTS ON CHARACTERISTICS OF HIGH ENERGY HADRONS IN EXTENSIVE AIR SHOWERS

7.1 Introduction

The present accelerators are not capable to give information on parameters, characterising the collision processes at very high energies. The observations obtained in recent years reveal that the nature of strong nuclear collisions may be subject to serious changes as the collision energy increases.

The study of E.A.S. extends the investigation of the behaviour of nuclear collisions to very high energy. The experimental information obtained from the E.A.S. study is far away from the point of first collision. Accurate information can be obtained if all the processes occuring between the primary interaction and the observation level are known in detail.

With the development of fast digital computers it has been possible to feed interaction parameters to a model to calculate the predicted effects on the various experimental quantities, such as density distribution, energy spectra, particle ratios for different components, etc. The construction of a shower model is not easy since not all the processes involved in the interaction are known. The effect due to the primary composition on the collision characteristics increases the difficulty in E.A.S. studies.

The major problems in the relevent experiments are: the energy estimation of the primary particles, core location of the air showers accompaniment and the identification of the different components. Amongst the various created particles in the collision the high energy hadrons, which constitute the skeleton of the air showers, and the high energy muons are more important due to their sensitivity to the primary composition and interaction behaviour in the first few collisions.

A knowledge of the lateral distribution of energetic hadrons near the axis of the air shower is important, since it enables one to get information about some features of the distribution of the transverse momenta of the hadrons received in the collision with air atomic nuclei.

In the present experiment the hadrons of energy ≥ 300 Gev in E.A.S. of size $5.10^4 - 1.6.10^6$ have been studied using a flash-tube chamber, within a collecting area of radius $\leq$ 10m from the centre of installation.

The apparatus was triggered by a hadron interacting in either the lead or iron producing a burst of size ≥ 400 particles. The high voltage pulse to the flash-tube chamber was applied after 330 μs. This long time delay (T_D) was selected to enable the axis of the burst to be located. The triggering requirement was unchanged throughout the experiment. The sensitive time was 2624.5 hours.

The burst size was converted into energy taking the interacting particle as pions. The uncertainty in the energy determination is $\pm 50\%$. The error in core location is about 1m (a simulation has been carried out to estimate the error in core location, assuming a Poissonian distribution of standard deviation $1.2\sqrt{n}$ on sampling n particles by H. Nejabat, private communication).

7.2 The basic experimental results

The basic data is shown in table 9.2. In the study of hadrons in E.A.S. the running time was 2624.5 hours which is less than the running time for measuring the hadron energy spectrum, since the air shower array was off for 80 hours when the chamber was running. Table 7.1 shows the measured parameters of every individual event. To convert the burst size to energy the interacting particles were assumed to be pions. In table 7.2 basic experimental data is presented.

Table 7.1 The measured parameters of every event.

Event no.	Hadron energy (Gev)	Shower size (particles)	Core distan. m	Polar Co-ordinate of core	Δ 61 part/m^2	Δ C part/m^2	Δ 12 part/m^2	Δ M part/m^2	Δ 62 part/m^2
1	450	1.1x10^5	.7	310°	53.2	21.7	12.4	-	6
2	450	3.5x10^5	1.0	310°	143.0	56.0	31.0	-	0
3	450	1.1x10^5	1.8	307°	48.6	20.6	10.2	saturated	-
4	400	4.1x10^5	1.9	180°	143.1	81.2	40.2	-	0
5	850	3.2x10^5	2.0	40°	961	696	348	> 80	-
6	1000	5.6x10^5	2.0	73°	140.2	93.0	59.5	> 80	9
7	710	2.10^5	2.0	90°	56.4	34.2	25.4	> 80	0
8	650	7.3x10^4	1.2	115°	68.4	71.5	24.8	> 80	-
9	330	7.5.10^4	1.7	115°	25.5	12.4	9.3	-	0
10	330	3.1.10^5	1.6	140°	68.4	31.1	24.9	> 80	-
11	400	1.7.10^5	2.0	182°	77.7	25.3	22.3	-	0
12	355	4.3.10^5	1.3	173°	171.4	62.4	50.2	-	15.5
13	350	3.4.10^5	1.0	220°	137.3	47.2	31.0	-	0
14	700	2.2.10^5	1.0	265	90.2	31.0	18.7	> 80	4.6
15	650	5.8.10^4	1.8	240°	35.2	9.3	6.0	11.6	0
16	700	2.2.10^5	1.0	265°	90.2	31.5	18.5	> 80	4
17	800	5.6.10^4	2.2	290°	6.2	3.2	3.7	-	0
18	1400	2.5.10^5	2.6	297°	140.1	46.6	28.1	-	-
19	550	2.8.10^5	3.6	210°	140.6	62.1	25.3	> 80	4.6
20	740	1.03.10^5	3.3	318	46.6	25.0	9.2	32.5	5
21	450	3.7.10^5	2.05	335	130.3	68.3	31.4	-	0
22	450	6.8.10^4	3.0	20	21.8	15.5	6.0	34.2	-
23	400	6.4.10^4	2.4	180°	22.2	16.0	-	48.2	5.6
24	300	6.8.10^5	2.6	45°	176.8	132.6	67.8	> 80	-
25	800	5.4.10^5	3.0	54°	140.4	109.0	56.1	-	0
26	480	3.6.10^5	2.1	55°	146.3	99.5	56.2	53.1	0
27	650	1.1x10^5	2.2	60°	31.0	21.7	12.3	-	0
28	300	2.6.10^5	2.2	73	74.6	49.8	31.1	-	0
29	360	1.0.10^5	3.2	65°	62.0	49.7	28.7	12	0
30	1850	5.7.10^5	2.7	75°	137.7	96.0	62.3	> 80	7
31	350	6.1.10^4	4.0	107°	18.6	12.4	18.6	50	-
32	300	5.5.10^4	3.8	115°	15.5	9.3	9.3	-	0
33	1000	6.7x10^4	4.0	120°	15.8	9.5	9.5	4	0
34	1100	4.7x10^5	3.0	140°	140.1	68.1	71.5	-	-
35	650	1.3x10^6	4.0	142	352.0	169.5	190.0	> 80	-
36	1300	7.2.10^5	4.0	150°	186.6	81.2	102.6	> 80	-

Event no.	Hadron energy (Gev)	Shower size (particles)	Core distan. m	Polar Co-ordinate of core	Δ_{61} part/m^2	Δ_C part/m^2	Δ_{12} part/m^2	Δ_H part/m^2	Δ_{62} part/m^2
37	300	$4.9.10^5$	3.9	172^o	168.0	59.3	71.7	-	7.7
38	580	$4.1.10^5$	3.4	172^o	143.2	50.0	53.5	48	9
39	350	$1.3.10^5$	4.0	176^o	46.6	15.5	18.6	17.7	0
40	800	$1.1.10^5$	2.5	220^o	68.4	3.1	12.4	80.6	0
41	750	$5.8.10^4$	6.0	20^o	15.5	7.7	12.6	-	-
42	300	$4.9.10^5$	4.6	310^o	209.0	107.6	38.6	> 80	-
43	700	$4.6.10^5$	4.3	330^o	143.0	99.5	31.2	> 80	6
44	700	$3.3.10^5$	4.8	197^o	130.0	37.0	40.0	-	0
45	400	$7.0.10^4$	4.3	172^o	15.5	20.0	52.1	-	-
46	1800	$2.8.10^5$	4.3	56^o	16.2	16.0	9.0	-	0
47	400	$3.9.10^5$	4.2	80^o	86.1	68.0	49.7	-	6
48	640	$7.9.10^5$	5.3	86^o	186.6	155.0	130.3	-	-
49	650	$1.03.10^6$	5.0	103^o	217.7	155.5	155.5	> 80	-
50	400	$2.07.10^5$	5.5	110^o	124.4	86.0	99.4	-	-
51	3000	$1.6.10^6$	4.5	128^o	373.1	217.7	249.0	-	-
52	800	$4.2.10^5$	5.8	130^o	93.3	31.1	37.3	25.8	-
53	600	$5.6.10^4$	4.7	140^o	18.7	9.3	12.4	-	0
54	900	$8.4.10^5$	5.7	157^o	218.2	93.2	143.0	-	-
55	750	$4.8.10^5$	4.3	170^o	146.2	56.3	68.2	> 80	5
56	650	$2.9.10^5$	4.3	176^o	103.3	34.1	40.1	-	0
57	1950	$3.9.10^5$	5.0	178^o	140.2	47.0	62.2	-	0
58	480	$4.1.10^5$	5.8	180^o	143.0	46.6	68.4	-	0
59	1400	$4.1.10^5$	5.3	185^o	143.2	31.1	56.3	> 80	11.5
60	640	$3.3.10^5$	4.8	197^o	130.0	37.2	40.0	-	0
61	500	$2.1.10^5$	5.8	215^o	124.4	25.0	25.7	-	12
62	500	$5.6.10^4$	5.0	220^o	86.3	15.5	15.5	-	0
63	430	$1.6.10^5$	5.5	238	177.2	18.6	15.5	-	9
64	340	$7.7.10^4$	4.5	84^o	15.5	12.4	9.3	-	0
65	400	$4.3.10^5$	6.3	320^o	146.2	124.0	28.2	> 80	-
66	600	$5.5.10^4$	6.8	310^o	9.3	15.5	11.6	-	-
67	300	$5.6.10^4$	6.5	315^o	9.6	16.0	11.2	-	-
68	740	$6.3.10^4$	6.1	38^o	6.5	9.5	3.3	-	0
69	700	$4.3.10^5$	6.8	78^o	68.0	68.0	53.3	-	9.3
70	300	$1.3.10^5$	7.0	80^o	37.3	37.5	31.2	-	0
71	500	$4.3.10^5$	6.8	88^o	68.4	62.2	59.1	40.3	3.1
72	1350	$8.6.10^5$	8.0	93^0	137.0	124.0	62.2	-	0
73	810	$8.7.10^5$	8.0	100^o	140.1	115.2	149.0	> 80	14

Event no.	Hadron energy (Gev)	Shower size (particles)	Core distance m	Polar Co-ordinate of core	Δ_{61} part/m^2	Δ_C part/m^2	Δ_{12} part/m^2	Δ_M part/m^2	Δ_{62} part/m^2
74	330	$7.7.10^5$	6.3	120^o	140.2	93.1	151.1	-	0
75	1400	$8.9.10^5$	6.6	148^o	180.6	93.3	164.8	> 80	-
76	300	$1.8.10^5$	7.8	150^o	37.0	18.6	43.5	-	-
77	300	7.10^5	7.3	158^o	140.3	62.3	124.1	-	-
78	1000	$1.7.10^5$	7.8	170^o	37.3	15.5	31.3	48	-
79	1400	$5.4.10^5$	7.4	187^o	140.2	21.8	37.3	> 80	-
80	430	$7.2.10^4$	7.8	195^o	21.7	6.0	9.4	-	0
81	360	$4.1.10^5$	7.0	205^o	143.0	37.3	46.6	-	0
82	565	$1.6.10^5$	7.3	100^o	65.3	15.5	18.6	> 80	0
83	2000	$3.8.10^5$	8.0	210^o	133.2	37.2	46.6	> 80	0
84	1350	$2.7.10^5$	8.0	232^o	132.1	28.3	24.9	-	0
85	600	$5.6.10^4$	8.7	182^o	15.5	9.3	10.1	-	-
86	450	$5.7.10^4$	8.5	202^o	16.0	16.4	10.6	-	-
87	700	$5.9.10^4$	8.0	190^o	15.5	21.7	25.0	-	-
88	410	$9.3.10^5$	8.1	90^o	130.6	124.5	130.2	50.8	-
89	1850	$1.0.10^6$	8.0	108^o	140.1	108.4	171.3	> 80	-
90	1100	$5.8.10^5$	9.0	124^o	93.0	62.3	140.2	-	9.3
91	600	$2.0.10^5$	9.8	166^o	34.2	12.4	43.5	34.3	-
92	800	$5.8.10^5$	9.3	190^o	133.1	43.5	84.1	-	6.2
93	300	$1.8.10^5$	8.0	150^o	37.3	18.6	43.5	-	-
94	680	$7.4.10^4$	9.3	100^o	155.4	49.7	93.2	> 80	0
95	500	$1.0.10^6$	8.0	100^o	168.2	140.2	168.3	-	17.7
96	740	$2.5.10^5$	10	275^o	137.3	46.6	21.7	-	0

Polar Coordinates of the cores are measured with respect to a line joining detectors M and C in anticlockwise direction.

Running time (hours)	2,624.5	
Number of events with a burst of size ≥ 400 particles observed under the lead or iron and in acceptance geometry	lead	40
	iron	56
Number of burst produced by an initial interaction in the lead or iron determined from the flash-tube information	lead	58
	iron	38

Table 7.2 Basic experimental data.

$$R_{\theta}(>N) = R_{o}(>N)\ \cos^{9}\theta \quad m^{-2}\ hr^{-1}\ st^{-1}$$

therefore

$$R_{T}(>N) = \int_{o}^{\pi/2} R_{\theta}(>N)\ \cos\theta\ 2\pi\ \sin\theta\ d\theta$$

$$R_{T}(>N) = \int_{o}^{\pi/2} R_{o}(>N)\ \cos^{9}\theta . \cos\theta . 2\pi\ \sin\theta\ d\theta$$

$$R_{T}(>N) = R_{o}(>N)\ .2\pi \int_{o} \cos^{10}\theta . d(\cos\theta)$$

$$R_{T}(>N) = R_{o}(>N)\ 2\pi \left[\frac{\cos^{11}\theta}{11} \right]_{\cos\theta = 0}^{\cos\theta = 1}$$

$$R_{T}(>N) = R_{o}(>N)\ \frac{2\pi}{11} \quad m^{-2}\ hr^{-1}$$

Figure 7.1 shows the graphical representation of the shower size spectrum used.

7.3.3 <u>The results of the lateral distribution of hadrons</u>

In the course of the experiment 96 events with measurable shower size and hadron energy were collected and analysed. The energy of the hadrons and the core distance of the accompaning showers were determined. The result is shown in figure 7.2. This measurement can be represented as:

$$\Delta_{H}(>E,r) = A \quad \exp(-\frac{r}{r_{o}})$$

where r_o = 1.8 for all hadrons.

7.3.4 <u>Comparison with other experimental results</u>

Many experiments, carried out at different altitudes have measured the lateral distributions of hadrons in showers with different sizes (Kameda et al 1965; Hasegawa et al 1965; Matano et al 1971; Fritze et al 1969; Chatterjee et al 1967; Boehm et al 1972; Miyake et al 1969, and van staa et al 1973). In all those measurements an approximation was used for the relation between the density of hadrons and the core distance as follows:

$$\Delta_{H}(>E,r) \sim \exp(-r/r_{o}).$$

A comparison of present observation with some other data is seen in figure 7.3 from this comparison it can be concluded that the present observation is consistant with many measured lateral distributions.

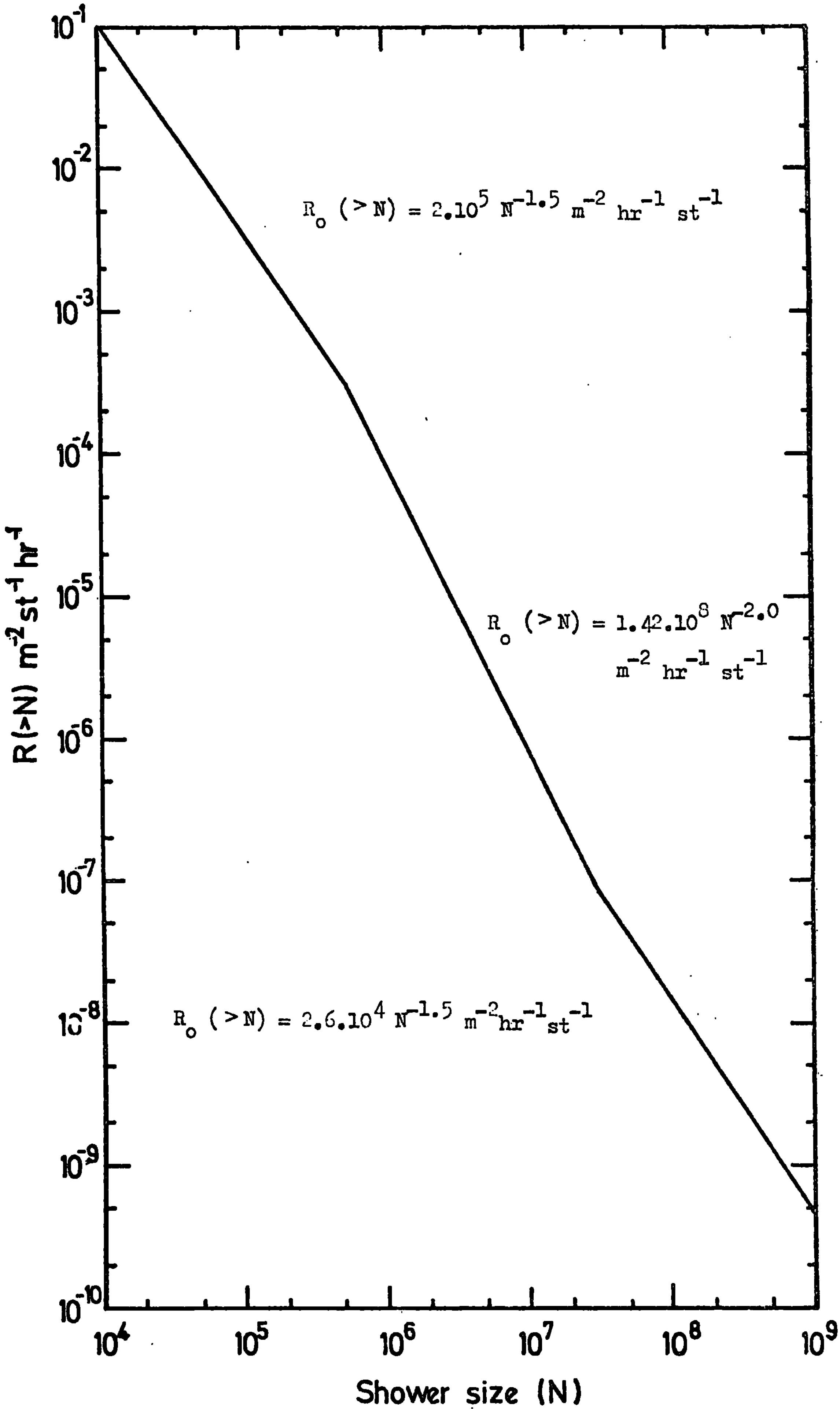

Figure 7.1 The sea level number spectrum calculated from the summary of Hillas (1970)

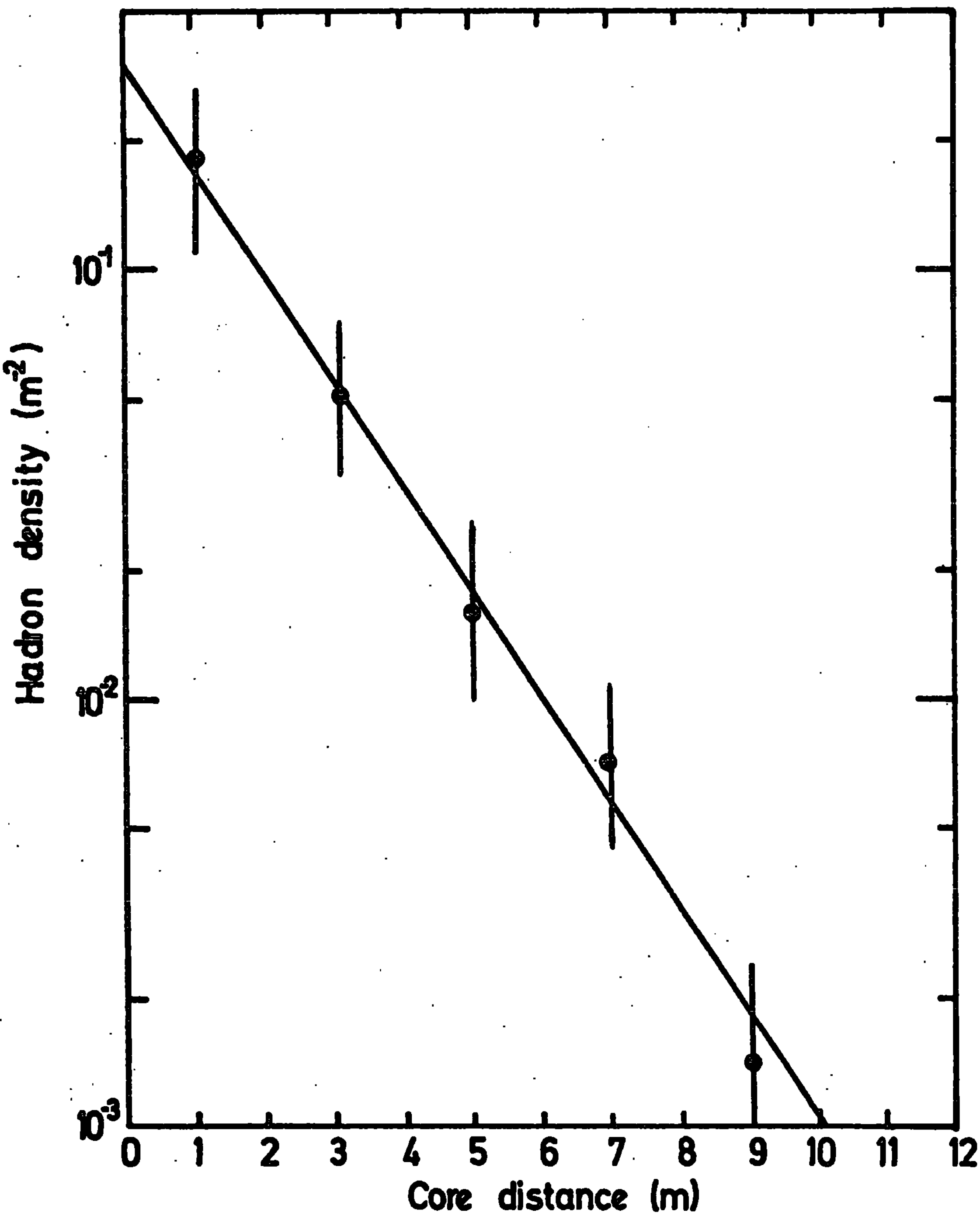

Figure 7.2 The lateral distribution of hadrons of energy $\geq$300 Gev in showers of size $5.10^4 \leq N_e \leq 1.6.10^6$, it can be represented as: $\Delta_H \sim A \exp(\frac{-r}{1.8})$

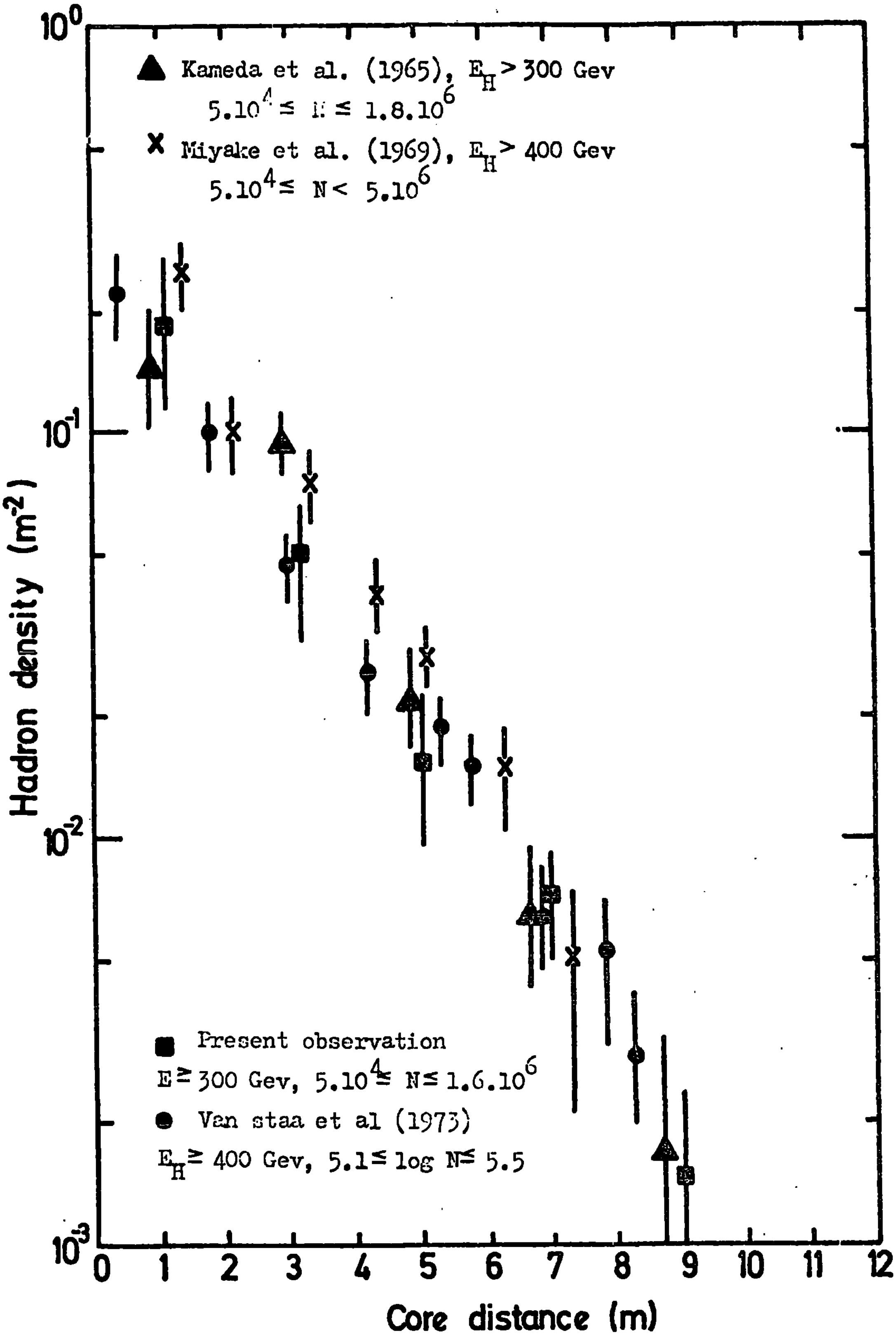

Figure 7.3 The comparison of the hadron lateral distribution of present work with other measurements.

7.3.5 The energy dependence of the lateral distribution

Figure 7.4 shows the lateral distributions of hadrons for two different energy thresholds. It can be seen that for a given size group, the lateral distributions steepens with increase in threshold energies. The characteristic length r_o measured in this experiment is compared with the observation of Kameda et al 1965 within the statistical errors they seem to be compatible (Figure 7.5). The above mentioned authors have given an exp peresion for r_o as follows:

$$r_o = 2.4\, N^{0.32}\, E^{-0.25}$$

where E is in units of 100 Gev, and N in unit of 10^5 particles.

7.3.6 The shower size dependence of the lateral distribution

Figure 7.6 shows the lateral distribution of hadrons of energy (≥300 Gev) for showers of two different sizes a weak effect is seen on lateral distribution such, as the shower size increases the lateral distribution seems to flatten. This effect has been compared with what Kameda et al (1965) observed. From Figure 7.7 it can be seen that the two measured points are compatible with the observations of Kameda et al. The flattening of the lateral distribution of hadrons with increasing size of the shower has been reported in a number of earlier experiments (Chatterjee et al, 1968; Hasegawa et al, 1965; Miyake et al, 1969 and Kameda et al, 1965 at sea level).

7.4 The variation of the number of hadrons with shower size

Since the lateral density distribution of nuclear active particles can be represented in the form of $\exp(-r/_{ro})$, the total number of nuclear active particles of energy threshold E Gev will be obtained as :

$$\text{Assuming,} \qquad \Delta\,(\geq E, N, r) = B\, e^{-r/r_o}$$

The total number of hadrons of energy ≥ E in a shower of size N is calculated by integrating this equation.

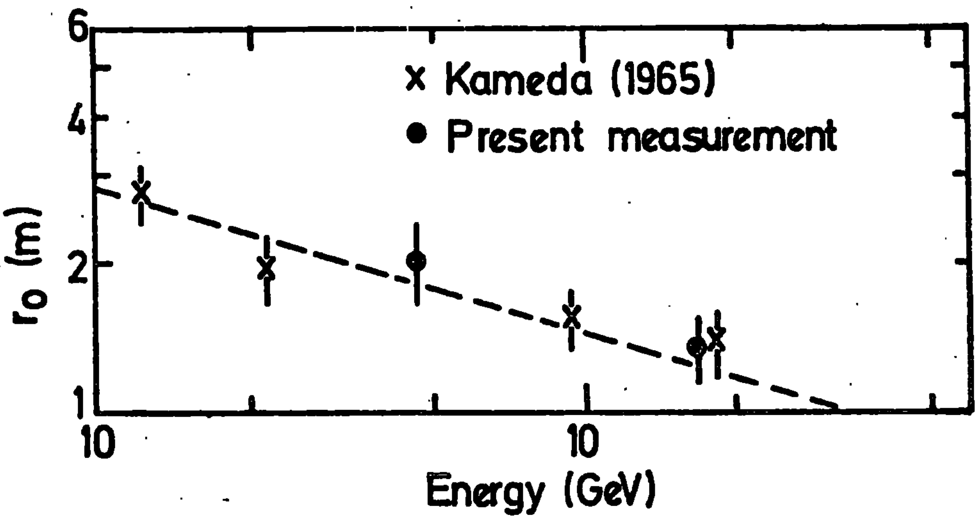

Figure 7.5 Variation of r_o with hadron energy

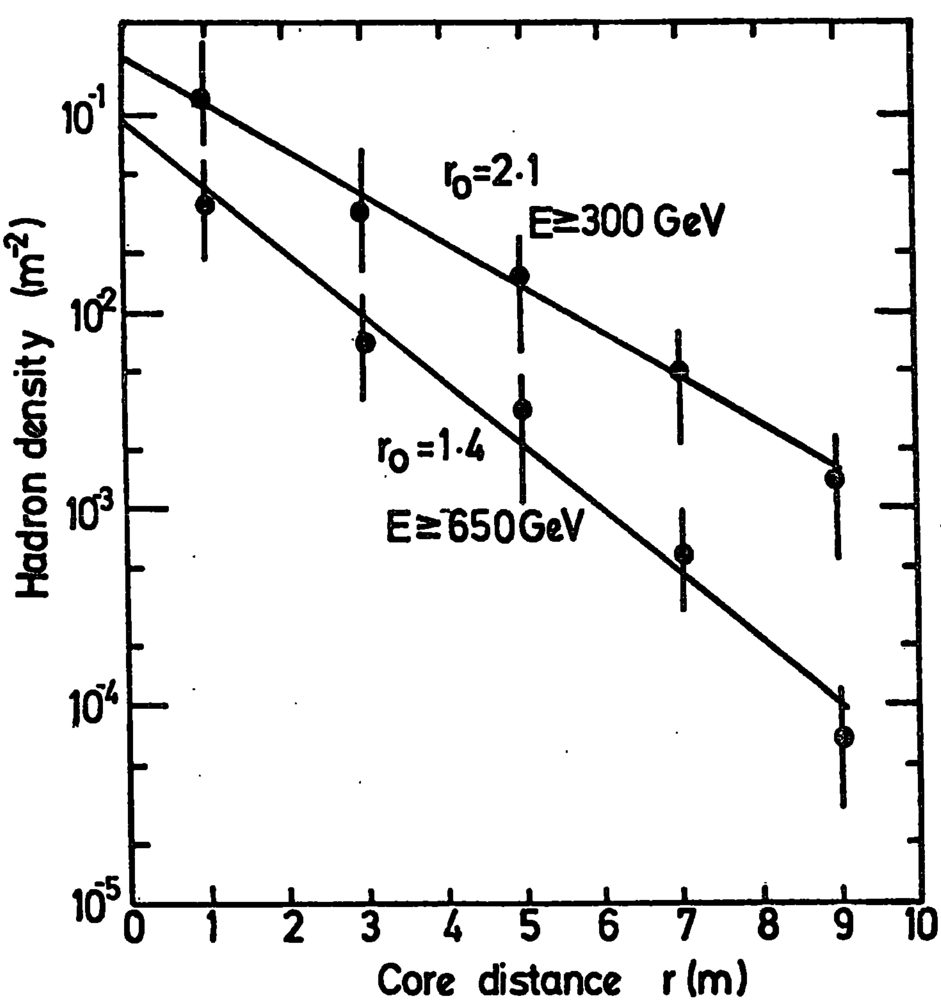

Figure 7.4 The dependence of the lateral distribution on hadron energy

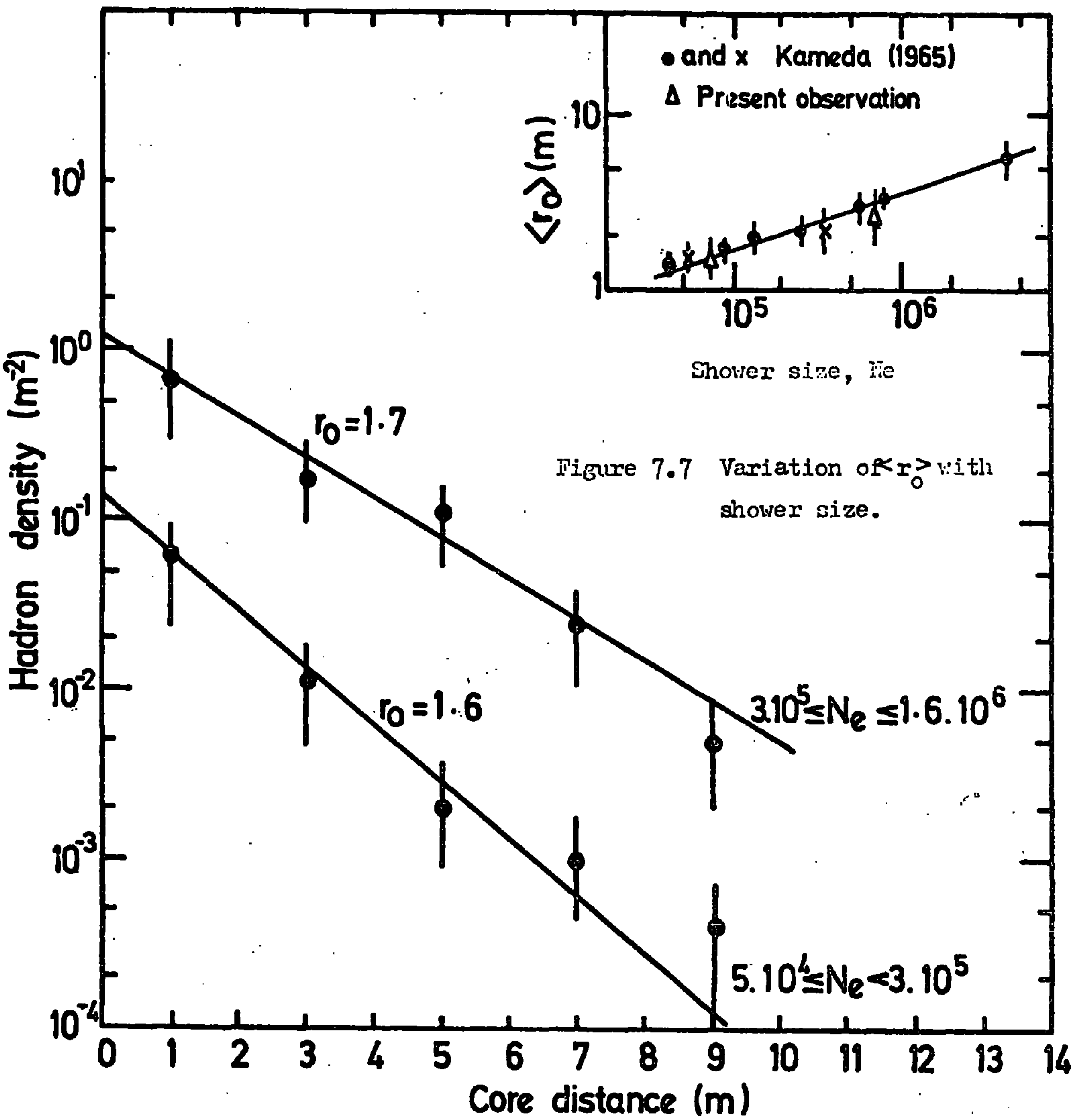

Shower size, Ne

Figure 7.7 Variation of $\langle r_o \rangle$ with shower size.

Figure 7.6 The shower size dependence of lateral density distribution of hadrons

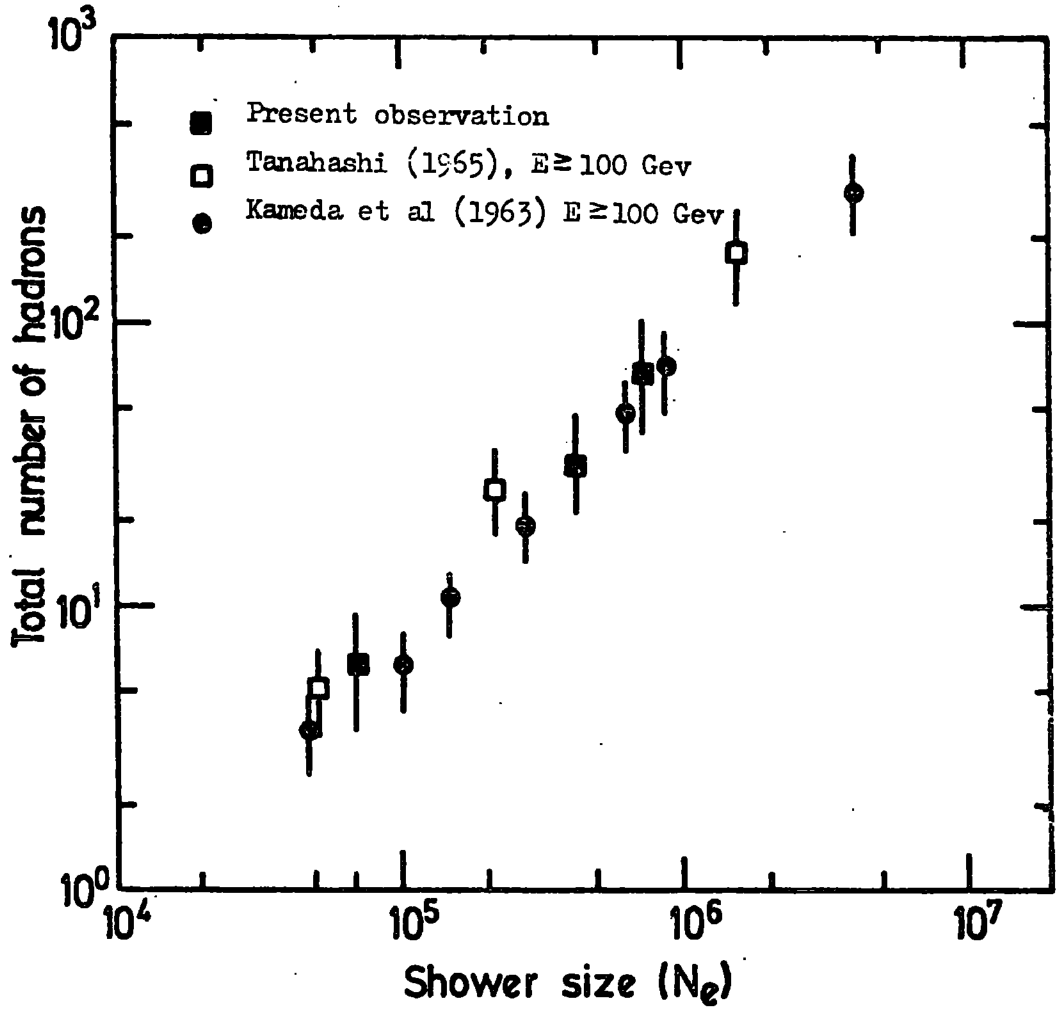

Figure 7.8 The total number of hadrons as a function of shower size Ne, Tanahashi (1965), E ≥ 100 Gev; Kameda et al (1963), E ≥ 100 Gev; present observation. To be comparable directly, the number of hadrons measured with threshold energy ≥ 300 Gev has been multiplied by a factor of 3, it can be seen that the present observation is consistant with the other measurements.

$$n_T(>E,N) = \int_0^{\infty} 2\pi\, r dr\, B_e^{-\frac{r}{r_o}}$$

$$n_T(>E,N) = 2\pi B \int_0^{\infty} r\, e^{-r/r_o}\, dr$$

$$n_T(>E,N) = 2\pi B r_o^2$$

Therefore the total number of hadrons of energy $>$E Gev is simply obtained by the expression $2\pi B r_o^2$, where B is the ordinate of the lateral distribution curve at r = o. In this experiment all data was divided into two groups. The result is shown in figure 7.8.

7.5 Comparison with other experimental results

A comparison of the present result with the other observations is shown in figure 7.8 and also a summary of the results made by different authors is shown in table 7.2. In this table the exponent of size variation and the total number of nuclear active particles for two different shower sizes at various altitudes and different hadron detectors are compared. A big discrepancy is seen in the total number of hadrons as a function of shower size. The present result is in agreement with the results of Kameda et al (1965) Miyake et al 1969 at Mt. Norikura for a shower size of $N_e=10^5$ particles. For this size the total number of hadrons of energy$\geq$100 Gev was found 7. Multiplying the total number of hadrons of energy$\geq$500 Gev by a factor 3 this experiment gives almost the same results as above mentioned results.

The results obtained by cloud chamber is more reliable since the cloud chamber has a better spatial resolution and the energy of individual hadrons can be rather accurately determined by the method described by Vatcha et al (1972), even when more than one hadron is incident, which is generally the case with high energy hadrons close to the shower axis.

Another important advantage of cloud chamber technique is its well

Table 7.2 A survey of variation of total number of hadrons with shower size

no.	Total number of hadrons: shower size 10^5	Total number of hadrons: shower size 10^6	observation level (g/cm^2)	Exponent of size variation	Workers	Energy Threshold (Gev)
1	50	625	1000	1.1 ± 0.1	Fukui et al (1960)	100
2	50	625	1000	1.1 ± 0.1	Tanaka (1961)	100
3	9	110	1000	1.1	Tanahashi (1965)	100
4	10	80	530	0.8 ± 0.1	Hasegawa et al (1966)	100
5	105	630	800	0.78 ± 0.05	Chatterjee et al (1967)	100
6	7.2	72	1000	1.0 ± 0.1	Kameda et al (1966)	100
7	10	100	All altitudes	1.0	Nikolski's survey (1963)	100
8	2	22	S/L	1.1 ± 0.1	Present experiment	300 Gev

defined geometry, only hadron collisions which occur well within the illumination region are considered.

7.6 Theoretical considerations

Calculation has been carried out by Kempa (1976) on some features of hadrons in extensive air showers, in this calculation a combination of the Monte Carlo and analytical methods has been used. The results of the calculation of the mean number of hadrons expected in the vertical direction on the shower size is seen in figure 7.9. For two multiplicity laws and the threshold energy 100 Gev the relation between the total number of hadrons and the shower size is the same. For energy threshold less than 100 Gev model $n_s \sim E^{1/2}$ predicts the total number of hadrons more than the model $n_s \sim E^{1/4}$ but for energy threshold more than 100 Gev the situation would be reverse. For shower sizes $> 10^4$ the variation of the total number of hadrons with shower size can be expressed as:

$$N_H(>E_T) \sim N_e^{\,a}$$

A summary of the experimental measurements of the slope, a, made by Kempa (1976) is given in table 7.3.

Table 7.3 the experimental results of the estimation of the slope, a appearing in relation $N_H(>E_T)$ $N_e^{\,a}$ (Kempa 1976)

a	Δ a	shower size	Hadron energy threshold (Gev)	Author
0.92	0.10	$10^4 - 5.10^6$	low energy hadrons	Boehm et al
1.00	0.15	$4.10^4 - 5.10^6$	100	Kameda et al
0.73	0.20	$5.10^4 - 5.10^6$	500	Miyake et al
1.0	0.1	$10^5 - 5.10^5$	600	Vedeneev et al
1.0		$10^5 - 10^6$	800	Fritze et al
1.3		$2.10^4 - 5.10^6$	1700	Matano et al
0.92)			50)	
0.96)		$5.10^4 - 3.10^6$	100)	Vatcha
0.92)			200)	
1.03)			4400)	

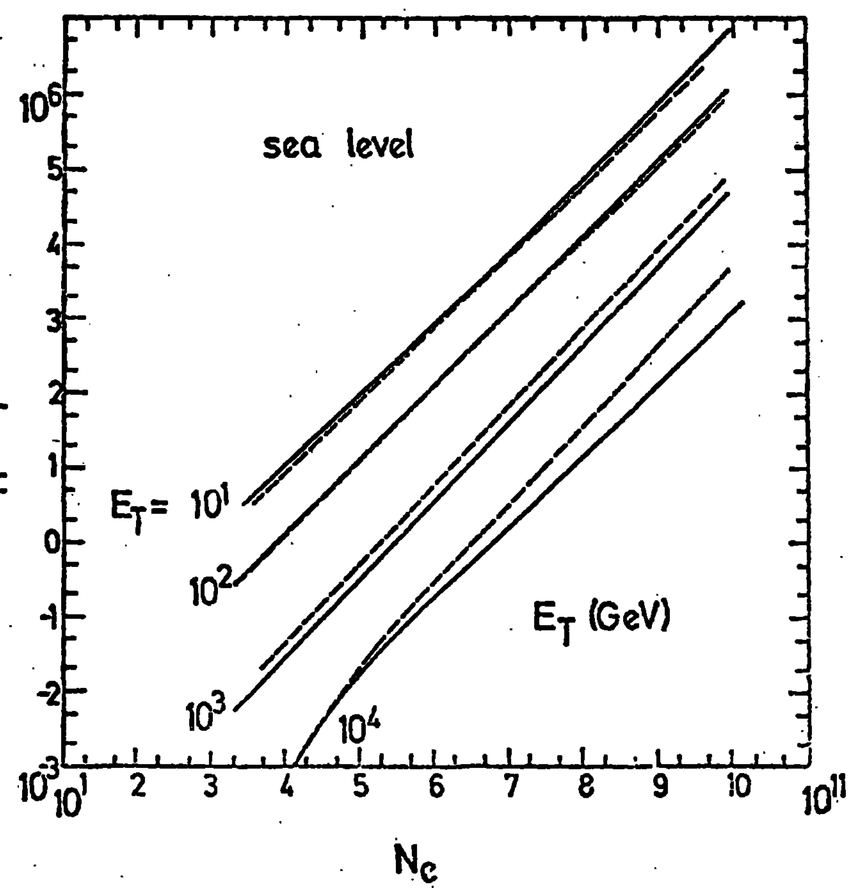

Figure 7.9 The mean number of hadrons as a function of shower size for four hadron energy thresholds. Full line, model, $n_s \sim E^{1/2}$ broken lines: $n_s \sim E^{1/4}$ (Kempa 1976)

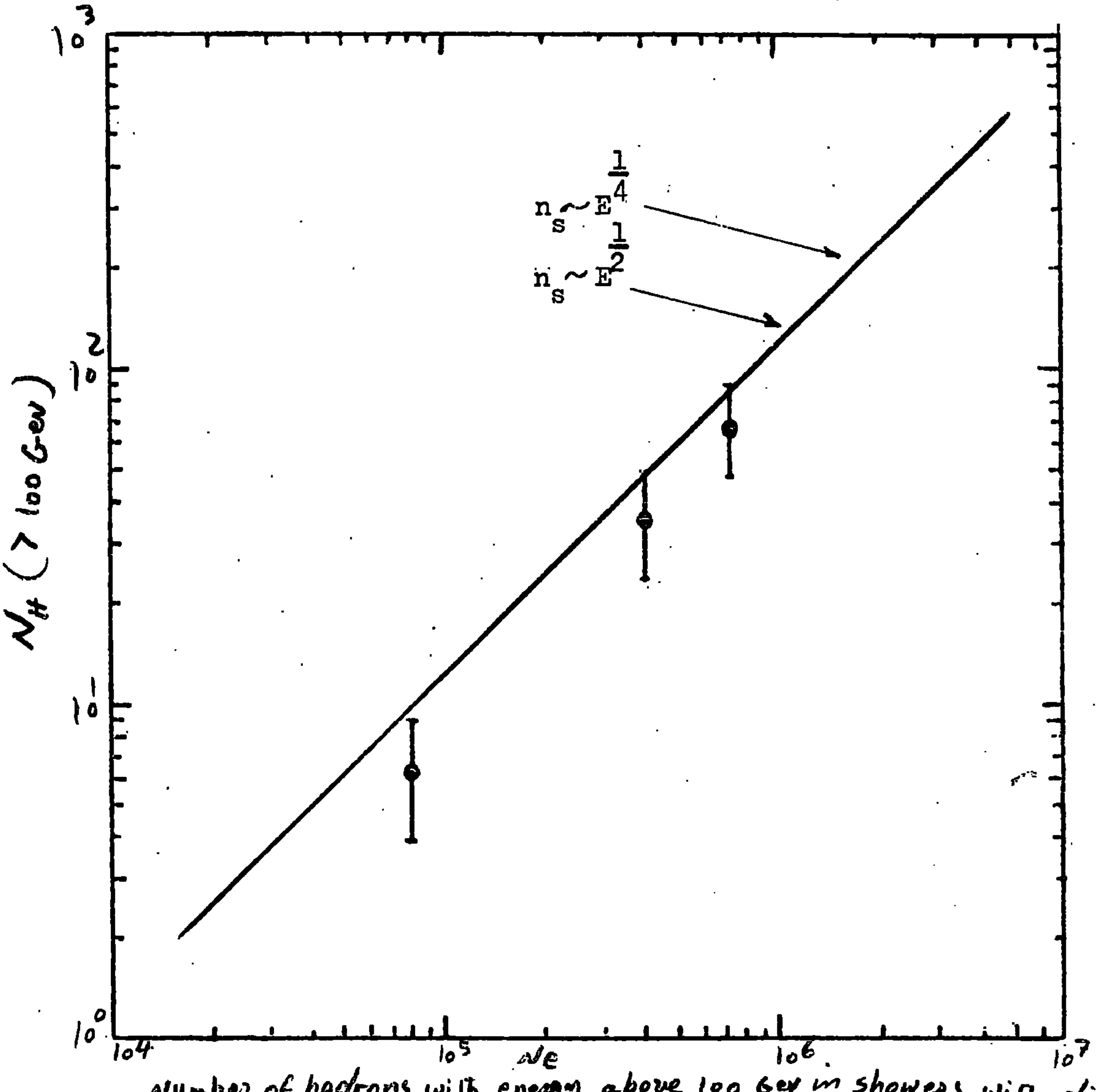

Number of hadrons with energy above 100 GeV in showers with different sizes

Figure 7.10 The comparison of the present measurement (ɸ) and the calculation of Kempa (1976), solid line.
To compare the total number of hadrons measured has been multiplied by a factor of 3 because of the energy threshold 300 Gev. . For a hadron energy Threshold of about 100 GeV both models predict the same number of hadrons

The slope calculated by Kempa is close to unity, that is consistant with the experimental values. A comparison between the theory (Kempa) and the results obtained by this experiment is shown figure 8.10. To compare, the total number of hadrons of energy $\geq$ 300 Gev observed in the present experiment was multiplied by a factor of 3. It can be seen that within the statistical error the results of the present work can be compatible with the results of the calculation of Kempa.

Greider (1970) has calculated the number of hadrons for 10^6 Gev simulations. The result of the calculation is recorded in table 7.4.

E > 10 Gev NAP	E > 100 Gev NAP	Run No. S0910
30	4.5	09
36	7.5	29
80	15	31
100	20	33
70	10	39
75	15	41
90	32	43
90	16	49
60	14	51
102	18	53

Table 7.4 10^6 Gev simulations, absolute number of NAP's per shower.

7.7 Integral energy spectrum of hadrons in E.A.S.

The integral energy spectrum of detected hadrons of energy $\geq$ 300 Gev in showers of size $5.10^4 - 1.6.10^6$ particles is given in figure 7.11. It can be seen that the slope of the spectrum from 300 Gev to about 1000 Gev is almost constant, $\gamma = 1 \pm 0.1$. As the energy increases the slope also gradually increases.

The data was split into two parts for two different shower sizes and the energy spectrum was obtained. Figure 7.12 shows the burst size distri-

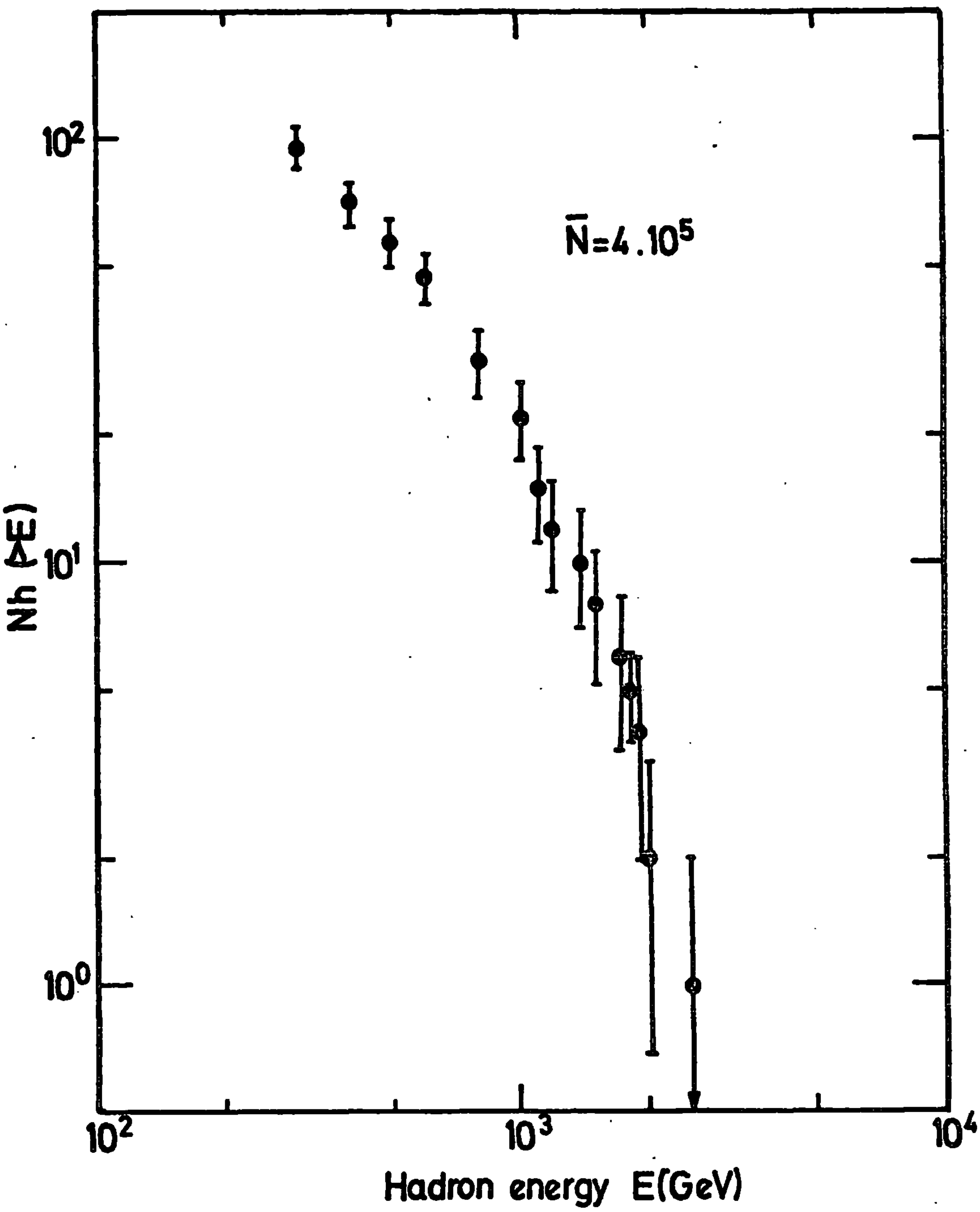

Figure 7.11 The integral energy spectrum of hadrons of energy ≥ 300 Gev in showers of size $5.10^4 \le N_e \le 1.6.10^6$ with a mean of 4.10^5 particles.

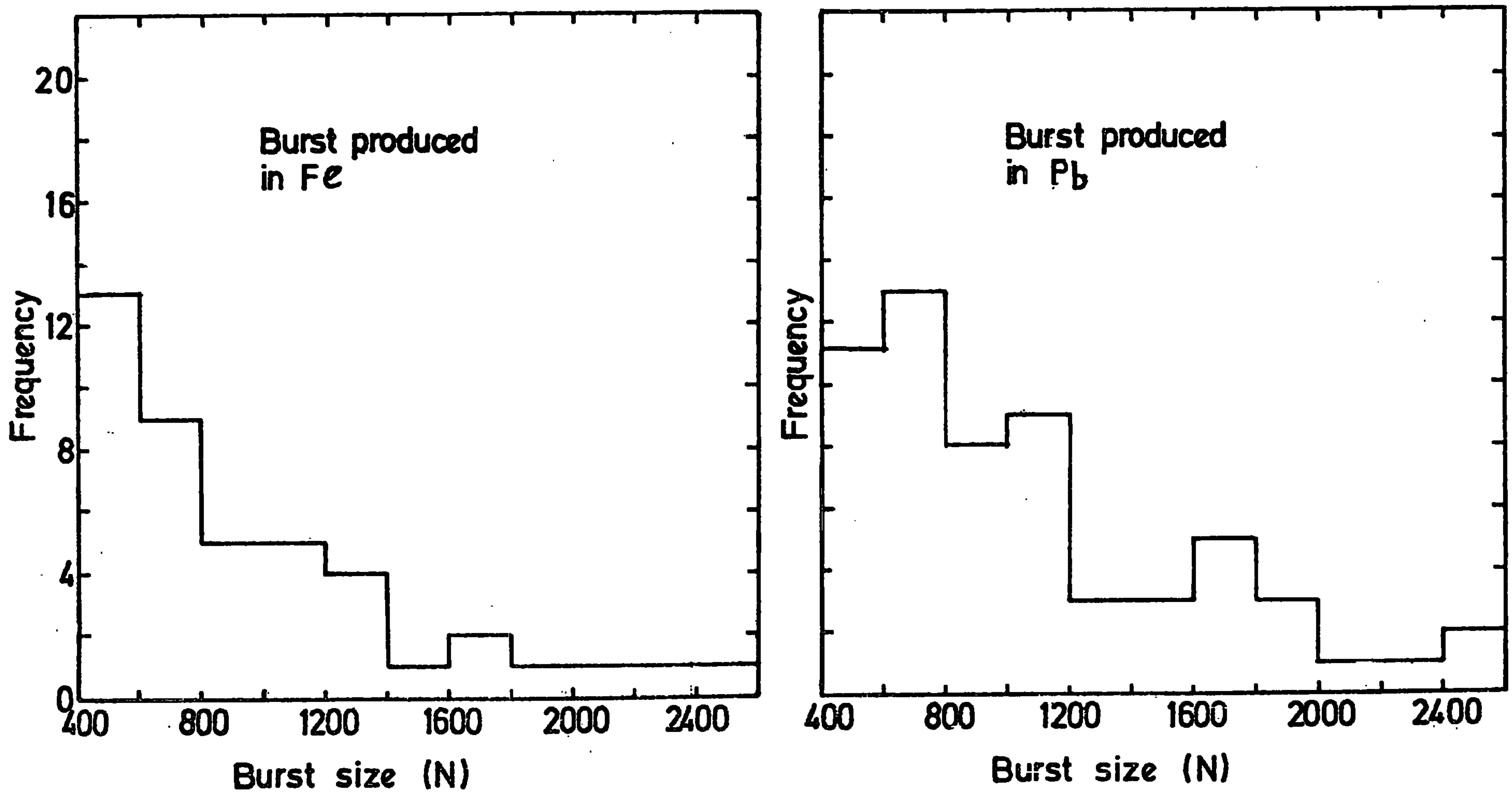

Figure 7.12 Burst size distribution

bution of bursts produced in lead and iron in figure 7.13 the angular distribution of bursts in shown. Figure 7.14 the integral energy spectrum for different shower sizes is shown.

7.8 Comparison with other experimental results

The integral energy spectra of hadrons have been measured in many experiments at different altitudes.

A comparison of the integral energy spectrum is made in table 7.5 In this table the exponents of the energy spectra of different workers are compared for different observation level and various techniques for energy estimation. The present result is compatible with most of the results in the table. From this comparison it will be understood that the exponent of the energy spectrum is almost constant up to energy about 10^3 Gev and then gradually increases with increasing energy. There are some differences in the exponent of the energy spectrum which can be attributed to different energy threshold and various techniques involved. Apart from a few measurements the energy spectrum is almost independent of shower size. It is neccessary to note the characteristic shape of the integral energy spectra of hadrons and the fact that this shape cannot be fitted to a negative power law of the same exponent over a wide range of hadron energies. Table 7.6 shows the results of the simulation carried out by Grieder (1970). It is seen that as the hadron energy increases the integral energy spectrum exponent also increases, consistant with observations.

Table 7.6 10^6 Gev simulation, slope of energy spectra of hadrons at sea level.

Slope of hadron energy spectra at:			Model	Run No. S0910
10 Gev	100 Gev	1000 Gev.		
0.95	0.95	2.18	SFB	09
0.54	1.08	1.78	IDFB	29
0.78	0.95	1.42	IDFB	31
0.72	0.96	1.26	IDFB	33
1.23	0.78	0.96	SFB	39

Table 7.5 A survey of the measurements on hadron energy spectrum in E.A.S.

no.	Slope of the integral energy spectrum	observation level	workers
1	-1.1 ± 0.05	800 g/cm^2	Chatterjee et al (1967)
2	$-1.5\pm.2$	S/L	Baruch et al (1975) E 1000 Gev
3	1.0 ± 0.1	1000 g/cm^2	Tanaka (1961) E = 100-1000 Gev
4	$2.1\pm.2$	S/L	Matano et al (1969) E 1700 Gev
5	1.0 ± 0.1	1000 g/cm^2	Fukui et al (1960) E = 100-1000 Gev
6	0.75 ± 0.1	1000 g/cm^2	Kameda et al (1966) E 100 Gev
7	1	1000 g/cm^2	Tanahashi (1965) E = 100-1000 Gev
8	1.0 ± 0.1	all altitude combined	Nikolski's survey (1963) E = 100-1000 Gev
9	$0.9\pm.1$	530 g/cm^2	Hasegawa et al (1966)
10	$1.0\pm.1$	S/L	Present experiment 300 Gev $\leq E_h <$ 1000 Gev
11	$1.7\pm.2$	S/L	Present work $E_h >$ 1000 Gev
12	1.2	S/L	Goryvnov et al E 500-5000 Gev
13	$.8.3\pm0.10$	S/L	Tanaka & Naranan E = 100-1000 Gev
14	1.1 ± 0.3	S/L	Vernov et al E = 500-1000

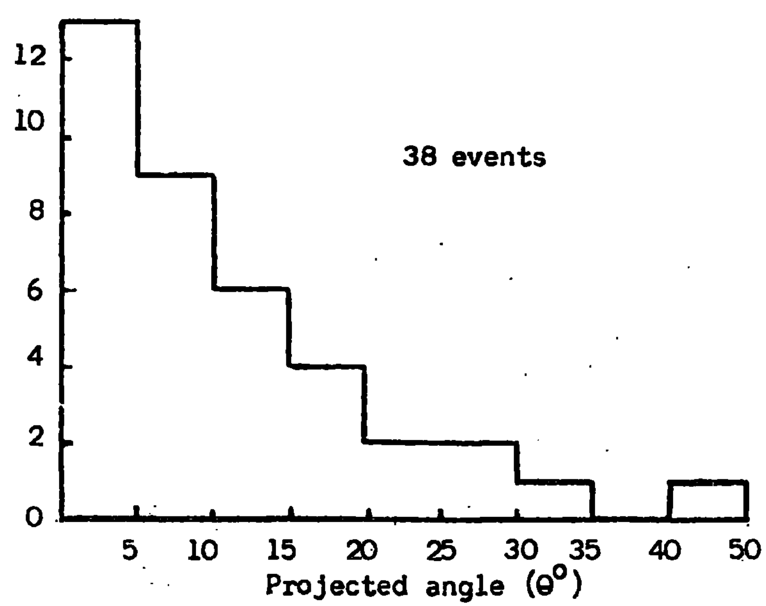

Figure 7.13 Angular distribution of bursts produced in lead

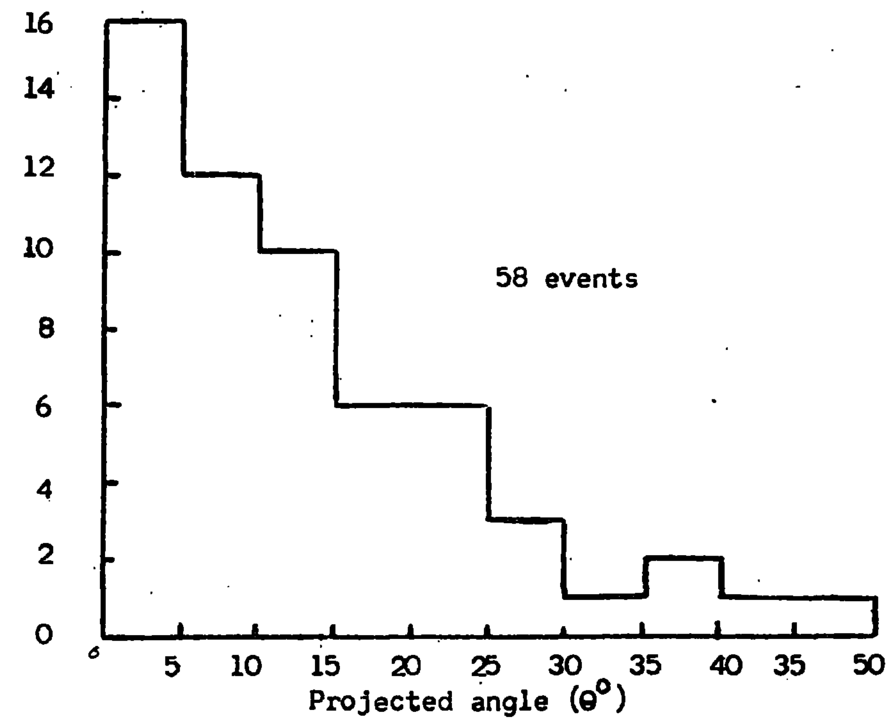

Angular distribution of pursts produced in iron.

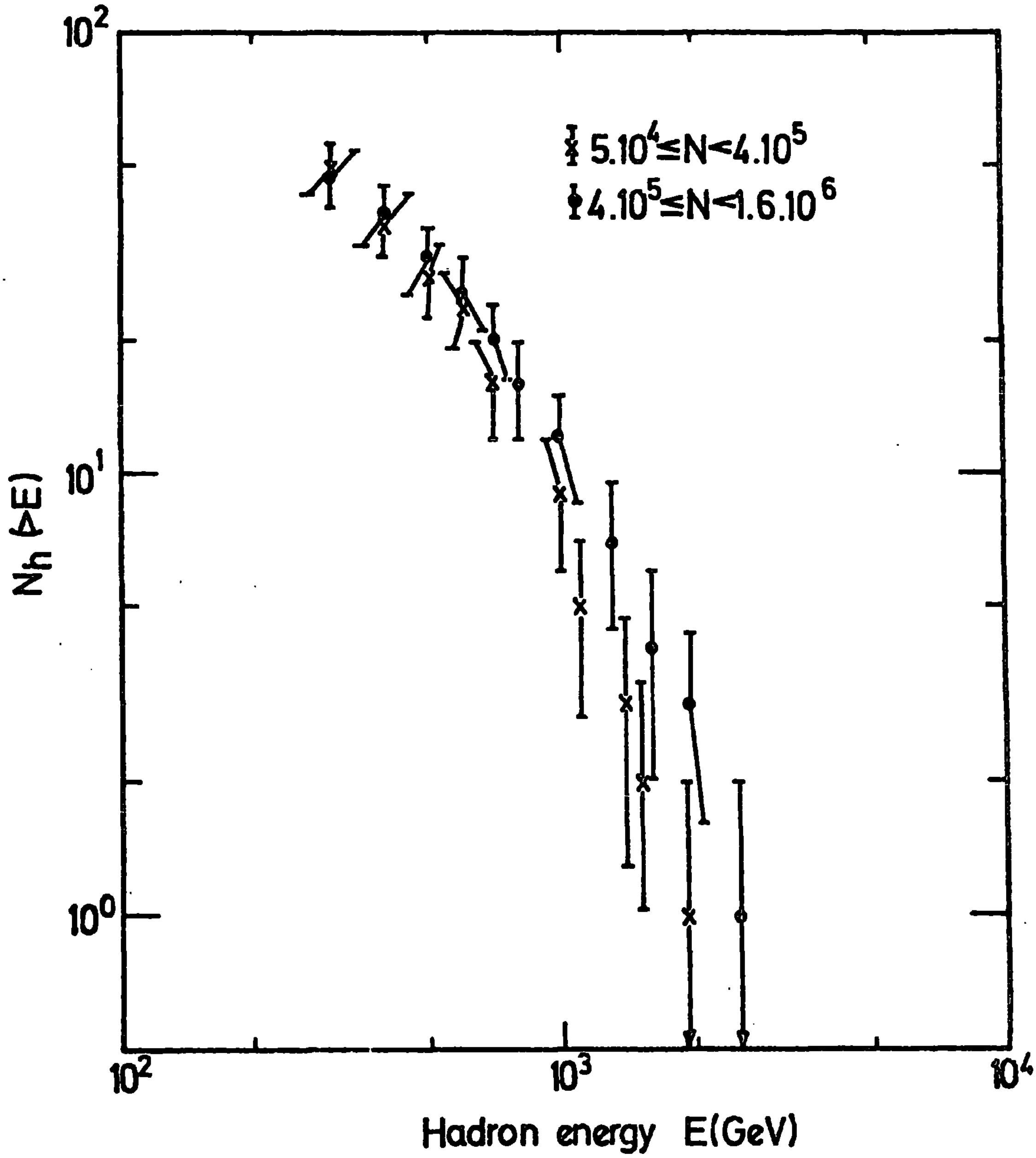

Figure 7.14 The integral energy spectrum of hadrons of energy $\geq$ 300 Gev in two shower size groups:

$5.10^4 \leq N_e \leq 3.10^5$, $3.10^5 < N_e \leq 1.6.10^6$.

Slope of hadron energy spectra at:			Model	Run No. S0910
10 Gev	100 Gev	1000 Gev.		
0.70	1.00	1.85	IDFB	41
0.45	0.70	1.60	NOFB	45
0.60	1.04	1.93	IDFB	49
0.70	0.78	1.98	IDFB	51
0.81	0.90	1.12	IDFB	53

7.9 Discussion and conclusion

The experimental results in this chapter on high energy hadrons can be summarized as follows:

i) the lateral density distribution steepens with increasing hadron energy

ii) there is a tendency for the lateral density distribution to flatten with increasing shower size

iii) the energy spectrum of hadrons in the energy range 300–1000 Gev has an exponent $\gamma = 1 \pm 0.1$, the slope gradually increases with increasing hadron energy

iv) the variation of the total number of hadrons $N_H(>E)$ as a function of shower size N_e may be represented as

$$N_H(>E) = B\, N_e^{\gamma}$$

where γ is about 1.0 ± 0.1

PLATE 7.1

Event H 118 - 30

A hadron interacted in lead, producing a burst that is penetrated in iron, the burst size in lead = 724 particles and in iron 955 particles, it is also accompanied by a shower of size $9.3.10^5$ particles, the shower core has fallen in a distance = 7 metre from the middle of the detector M.

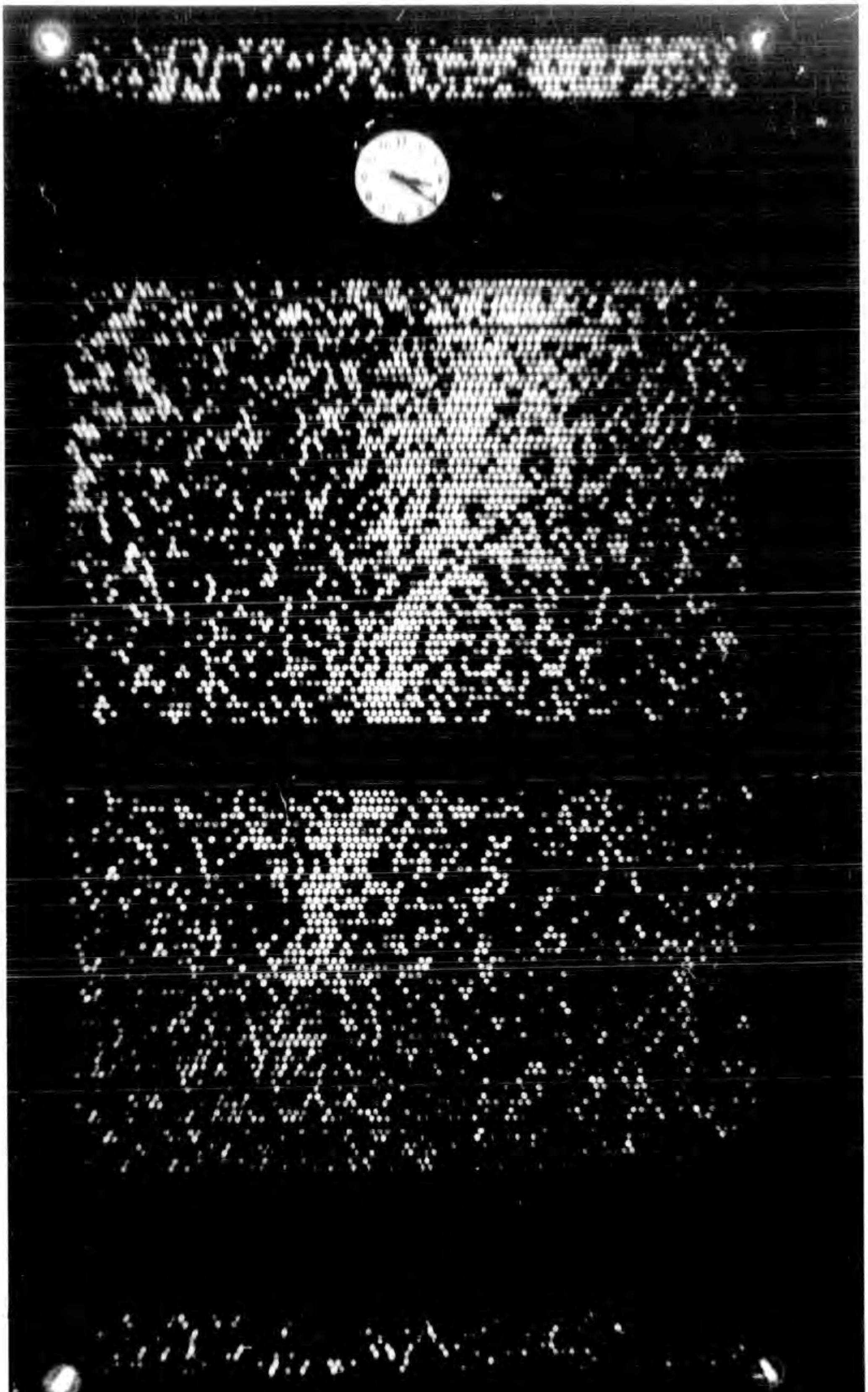

PLATE 7.2

Event H 145 - 12

An interaction in lead, penetrated in iron, the burst size in lead = 3700 particles, associated with an extensive air showers with a size of $1.55 \cdot 10^6$ particles.

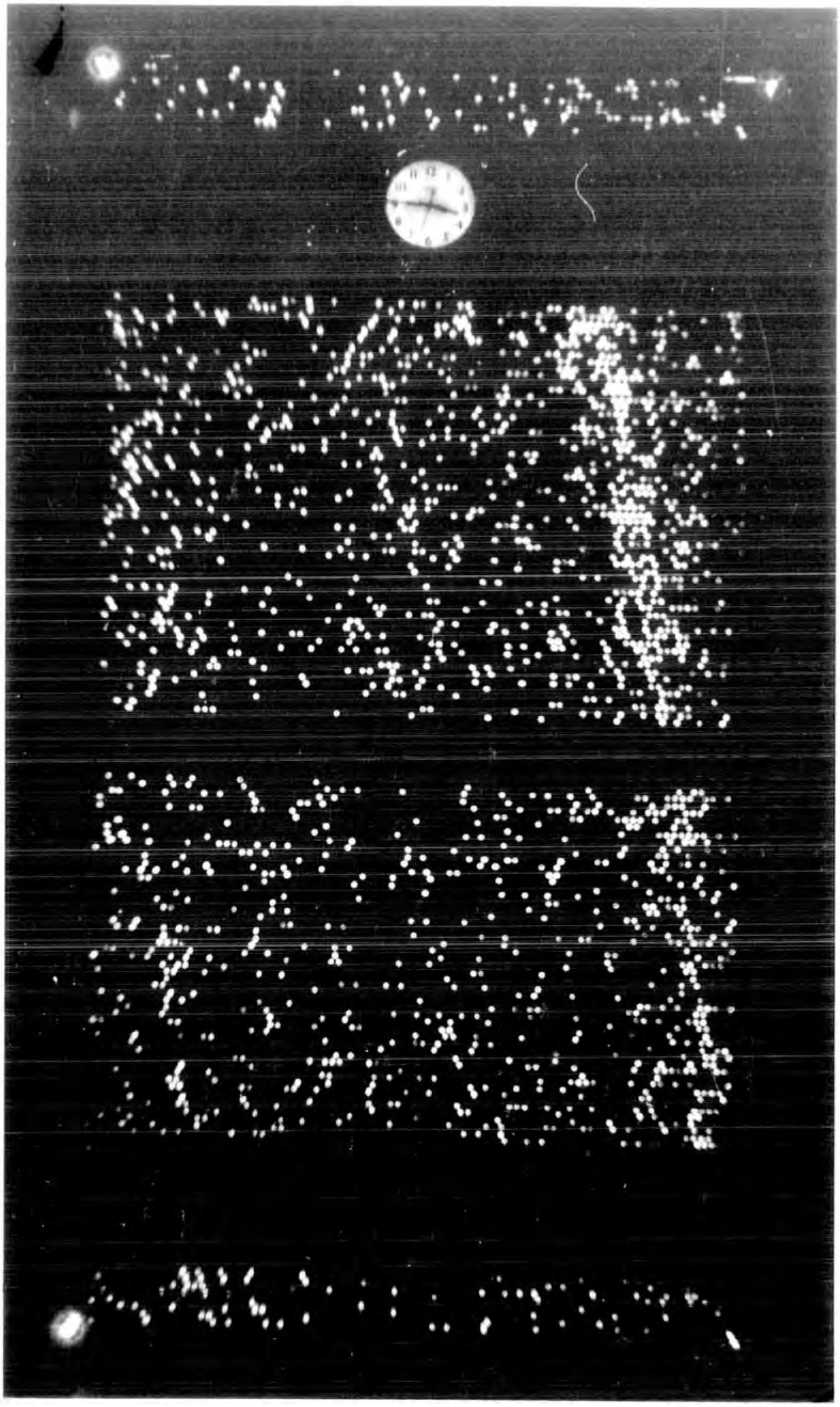

CHAPTER 8

DEPENDENCE OF THE MEAN TRANSVERSE MOMENTUM OF SECONDARY PARTICLES ON COLLISION ENERGY

8.1 Introduction

One of the most important high energy nuclear interaction parameter is the mean transverse momentum of the produced particles in nuclear collision. It has been a question in high energy physics, whether this parameter remains rather constant or rises as the energy of the colliding particle increases. In fact the idea that the mean transverse momentum of secondary particles in nuclear interactions is almost independent of the collision energy with a slight increase with energy was originated by Nishimura in 1956, after a comparison of accelerator data and cosmic ray experiments at energies around 1000 Gev. This invariance has been one of the most fruitful concepts in high energy physics.

The observable quantities that are influenced by the transverse momentum in extensive air showers are as follows:

i) The lateral distribution of high energy hadrons in shower cores

ii) The muon lateral distribution

iii) The core structure of the electromagnetic component.

The problem of transverse momenta can be approached by measuring directly the spatial distribution of very high energy particles in shower cores. Another way is investigating the multi-core showers. If the electron distribution shows a multicore structure one can estimate the energy content of the subcores, the distance of the subcore to the main core and the production height and crudely derive transverse momenta necessary to account for the observed separations. This measurement can be made assuming that the observed subcores are not due to poissonian density fluctuations, or to non-uniformities of the detector array, or to local hadronic interactions in the detectors.

8.2 Determination of transverse momentum, P_T in individual cases

If the energy of the hadrons and the distance between the hadrons and shower cores is estimated providing the hadrons are produced at a fixed height, the transverse momentum is determined as:

$$P_T = \frac{E_h . r}{h . c}$$

Where E_h is the hadron energy, r the distance of the hadron to the shower core and h the production height, assuming that their parents are close to the axis of the shower. If the production height is independent of the hadron energy, the value $E_h . r$ reflects the transverse momentum. In this experiment variation of $E_h . r$ with mean hadron energy and shower size (or primary energy) have been investigated. The energy of the hadrons were estimated using the calculated burst size-energy relation, discussed in chapter 5 and the shower cores were determined by the method explained in chapter 6

8.3 Shower size-energy conversion

The variations of the total number of electrons (N_e) with primary energy E_p for showers in the near vertical direction has been calculated by Kempa (1976) for primary protons and different models the result of the calculation for the model $n_s \sim E^{1/4}$ and sea level is shown in figure 8.1. This plot was used to convert the shower size into primary energy.
The minimum of the ratio E_o/N_e for showers at maximum was estimated as follows:

$$E_o/N_e = 2 \text{ Gev/particles}$$

8.4 A summary of measurements of high transverse momenta

8.4.1 Oda and Tanaka (1962)

Oda and Tanaka studied the high energy hadronic component in extensive air showers using a neon hodoscope of area 7 m^2 and an array of glass fronted spark chambers of area 20 m^2 at sea level. This experiment primarily was arranged to study the detailed distribution of the electronic component in extensive air shower cores. They found the total number of electrons and muons in the showers by the use of a considerable array of their detectors.

They were also able to study the high energy hadrons. They found 14 events in the showers of size$>10^5$ particles with transverse momentum between 5 to 50 Gev/c. Their integral distribution could be represented by a power law of exponent -1.7 ± 0.2.

8.4.2 Miyake et al (1963)

This group used a two closely packed layers of scintillators separated by 2m of water plus a more widely spread array of 100 0.25 m^2 scintillators. They reported high transverse momenta of the sub-cores ranging up to several tens of Gev/c.

8.4.3 Bakich et al (1969)

The Sydney group has investigated the occurrence of high transverse momenta in air showers of primary energy greater than 10^{15}ev, using 64 scintillator array. For any multiple cored shower an estimate of the transverse momentum has been obtained by determining the subcore separation and estimating the energy and the height of production of the cascade from their age and number of particles within a certain distance from the axis. The cascades were assumed to be near maximum of their development. The energy and production height of cascades were determined using electron-photon cascade theory. The transverse momentum estimated from, $P_t = rP_L/h$. the results is shown in figure 8.2a and 8.2b. They have also proved that the multiple core structure observed cannot be attributed to fluctuations in the scintillator response or to instrumental errors. From their results it can be understood that the mean transverse momentum increases with shower size and therefore with mean collision energy.

8.4.4 Sreekantan (1971)

The Brazil-Japan Emulsion Chamber collaboration obtained the results that the mean transverse momentum received by the particles produced in nuclear collisions of the primary energy above 10^{14}ev is significantly greater than for interactions at 10^{12}ev. They also concluded that the cross section for the production of transverse momenta of >2 Gev/c at 10^6 Gev is significant and throughout the range 10^{14} to 10^{17}ev both the mean transverse momentum and the cross section for the production of high P_T is increasing. Figure 8.3 shows the increase in transverse momentum for the higher energy (SH) events.

8.4.5 Dake et al (1973)

This group used an emulsion chamber of 6.4 m^2, 6 cms Pb, having 5 sensitive layers. They also had fifty-five spark chamber, 0.5 x 0.5 x 0.07 m^3 and underneath of the emulsion chamber 26 scintillators each 0.5 x 0.5 x 0.03 m^3. The shower direction was determined by two spark chambers placed vertically with their axes at right angle. At a distance of 65$\pm$10 cms from the main core of a shower they found a γ-ray family of ΣE_γ= 16.4 Tev in the emulsion chamber. The production height and the energy of the $\pi^o{}_s$ were calculated. On the assumption of π^o was produced in the axes of the shower the minimum value of the transverse momentum was 17$\pm$4 Gev/c.

8.4.6 Miyake et al (1969)

This group has studied hadrons of energy $\geq$200 Gev in E.A.S. of size 3.10^5 - 10^6 particles using 26 scintillation counters and a multiplate cloud chamber of 1.3 x 2.0 x 0.7 m^3. They have seen a dependence of the lateral density distribution of hadrons with shower size in the form of

$$r_o \sim N_e^{0.16}$$

Where r_o is the reciprocal of the lateral distribution and N_e is the shower size.

They have concluded that if the production height is independent of

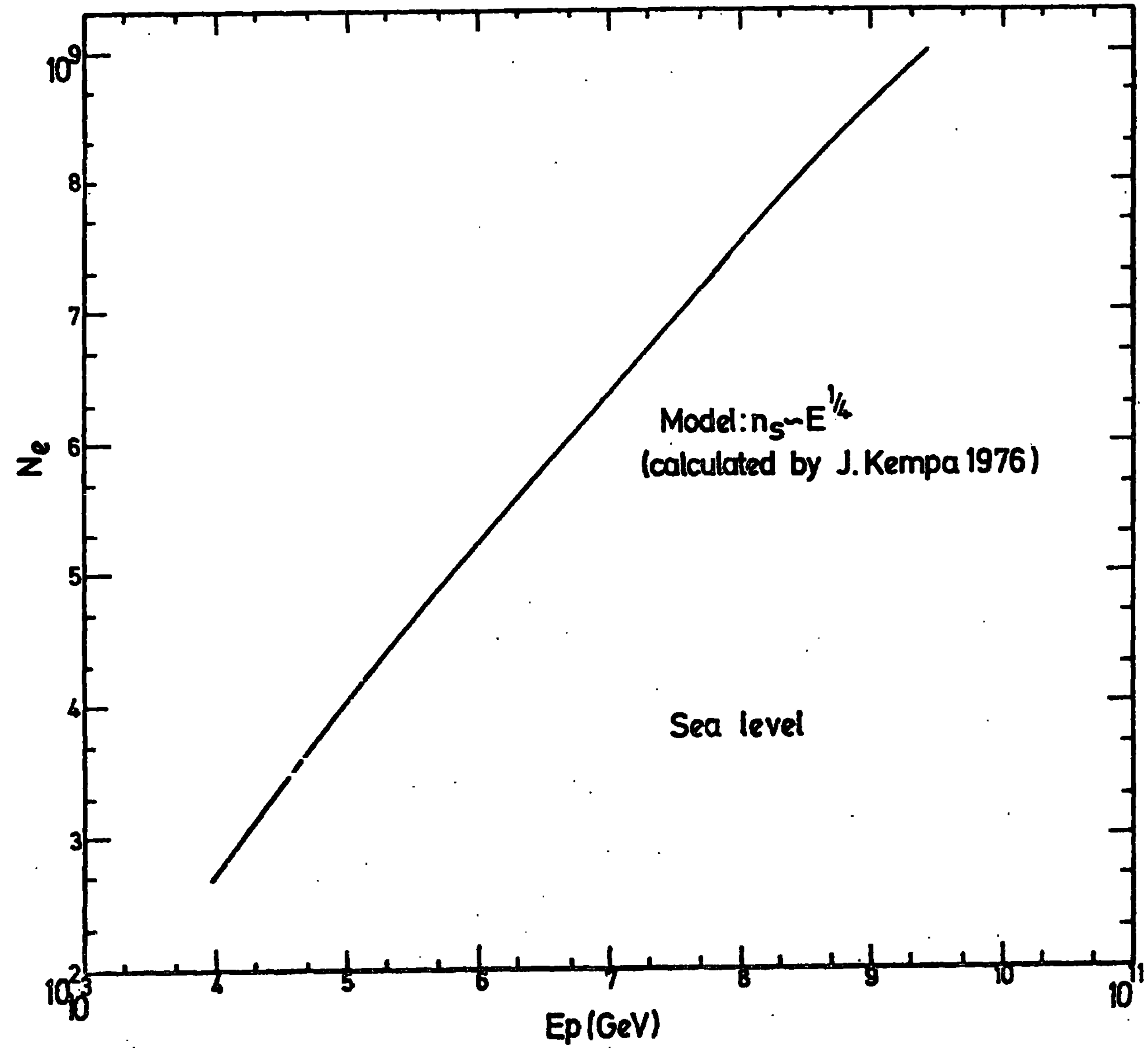

Figure 8.1 The variation of the number of electrons N_e with primary proton of energy E_p, calculation has been made for vertical showers, (Kempa 1976)

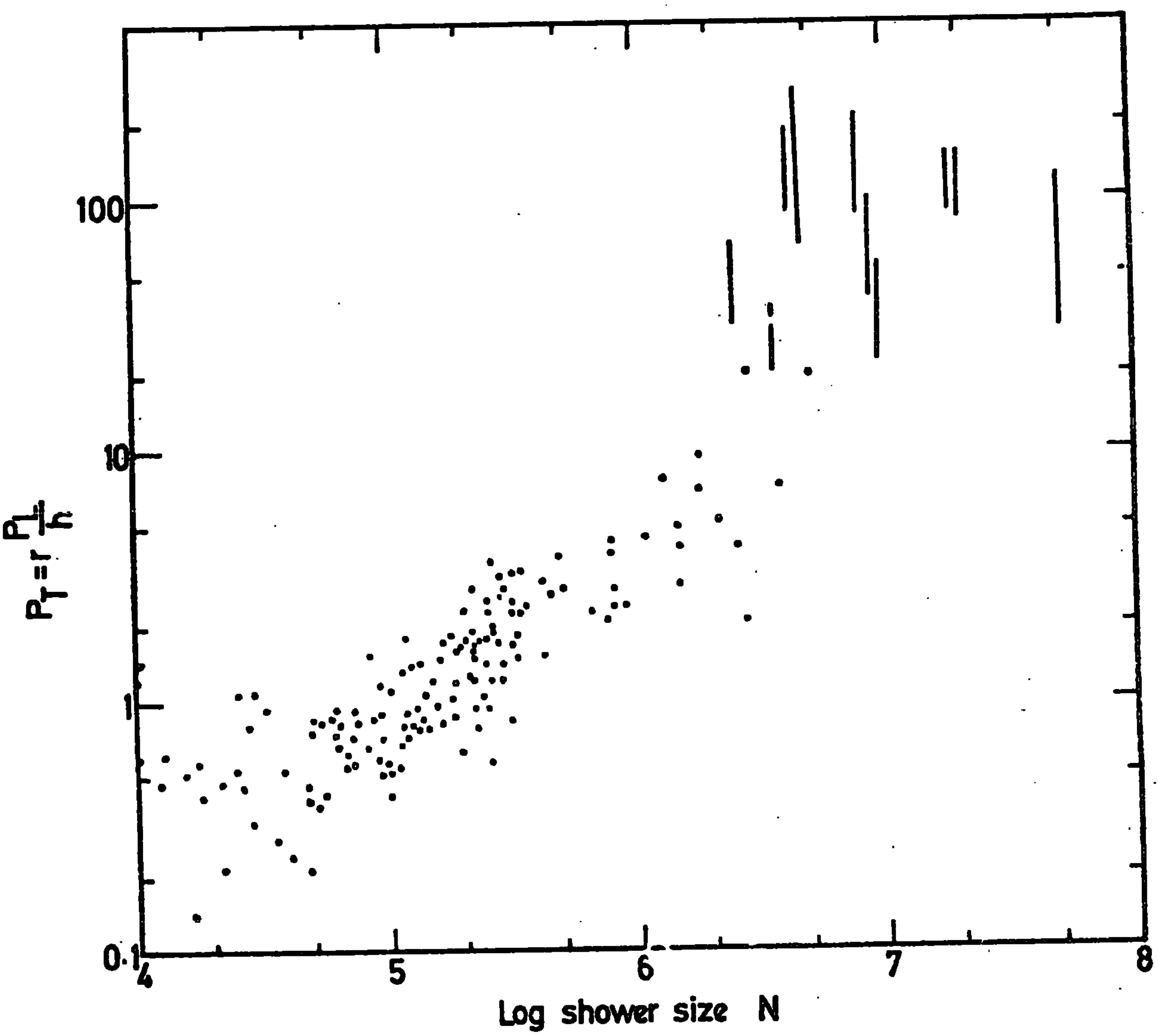

Figure 8.2a Transverse momentum as a function of shower size.
(Bakich et al 1969)

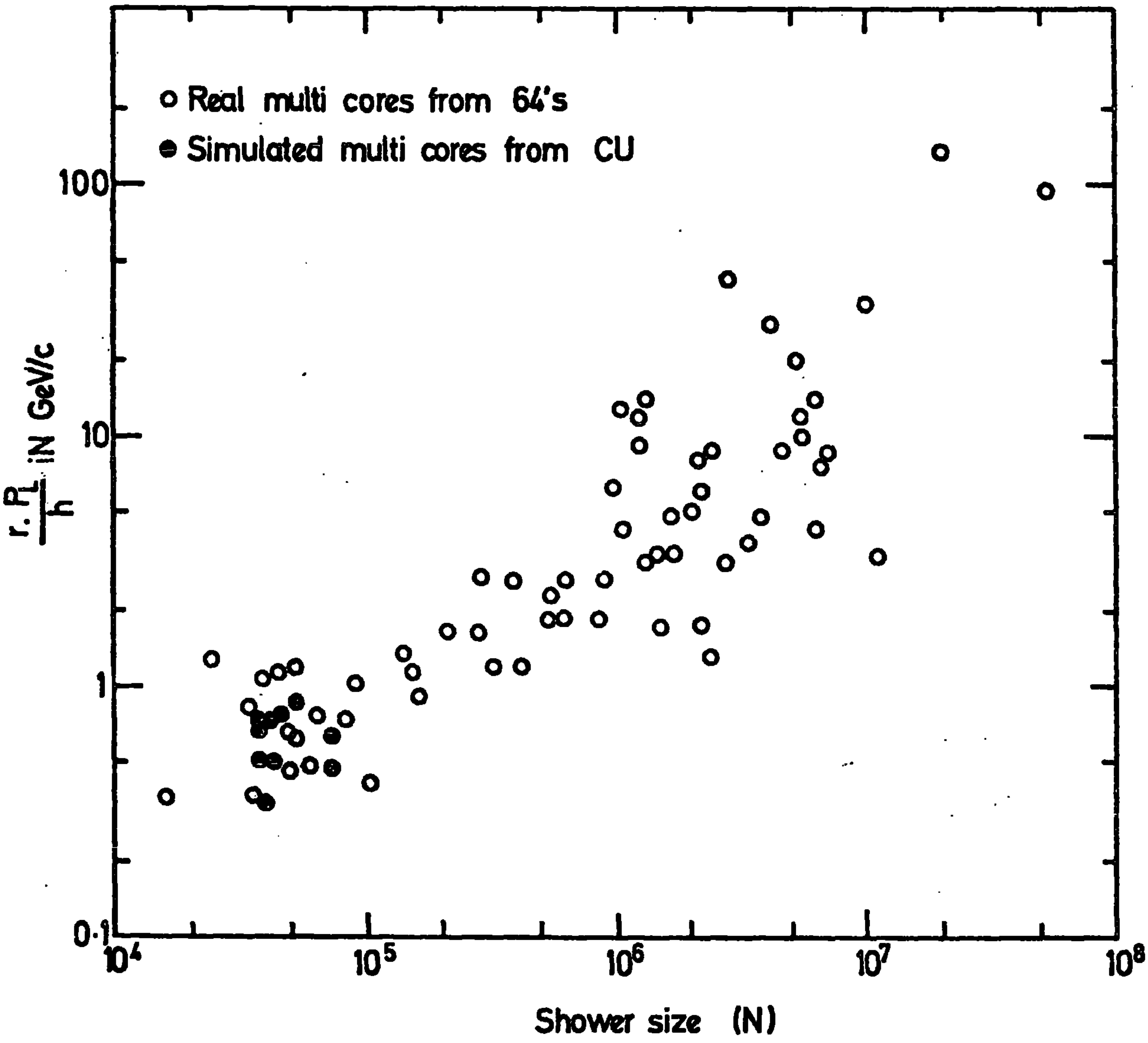

Figure 8.2b A plot of the quantity $r\,\frac{P_L}{h}$ in Gev/c for all multicored showers with $N > 10^6$ observed in the sydney 64-scintillator experiment together with a random selection of multicored showers from the same experiment with $N < 10^6$ particles. The solid circles are for simulated showers using 10^{15}-ev copper primaries and a mean transverse momentum of 0.5 Gev/c (McCusker et al 1969)

the energy of the hadrons, the transverse momentum, P_t, calculated from the equation:

$$P_t = \frac{E_N \cdot r}{h}$$

increases with the energy, since r_o is a slowly decreasing function of hadron energy E_N :

$$r_o \sim E_N^{-0.33}$$

similarly the value of P_t increases with the size of E.A.S. for fixed E_N and for assumed production height due to the ~~rel-ating~~ relation of r_o and N_e.
On the basis of the above estimations, P_t seems to be much higher when compared with the low energy region, 0.4 Gev/c, and still increases with energy of the hadron and with the accompanying shower size.

8.4.7 ~~Nestrerova~~ Nesterova et al (1973)

The Tian-shan group used an ionisation calorimeter of area 36 m^2 and depth 1440 g/cm^2. The shower core was found by a layer of 64 scintillators located above the calorimeter. The arrival direction was also determined. The position of the high energy hadrons with respect to the shower core was determined. The energy of the hadrons was estimated by the calorimeter. The value $E_h.r$ could be measured, knowing the production height, P_T could be found by equation $E_h.r = P_T.h.c$. They also considered events with more than one hadrons and measured the distance r of two hadrons and obtained the quantity

$$\frac{E_1 E_2}{E_1+E_2} \cdot \frac{r}{2} = P_T h$$

By the first method they found that 5% of the events with shower size $>10^5$ particles at the observation level of 3.3 Km above sea level had values of $P_T.h > 2.10^4$ Gev/c .m. For 190 multi hadron events the second method gave 15 events with $P_T h \geq 2.10^3$ Gev/C$\cdot$m. It was also found that as the showers get

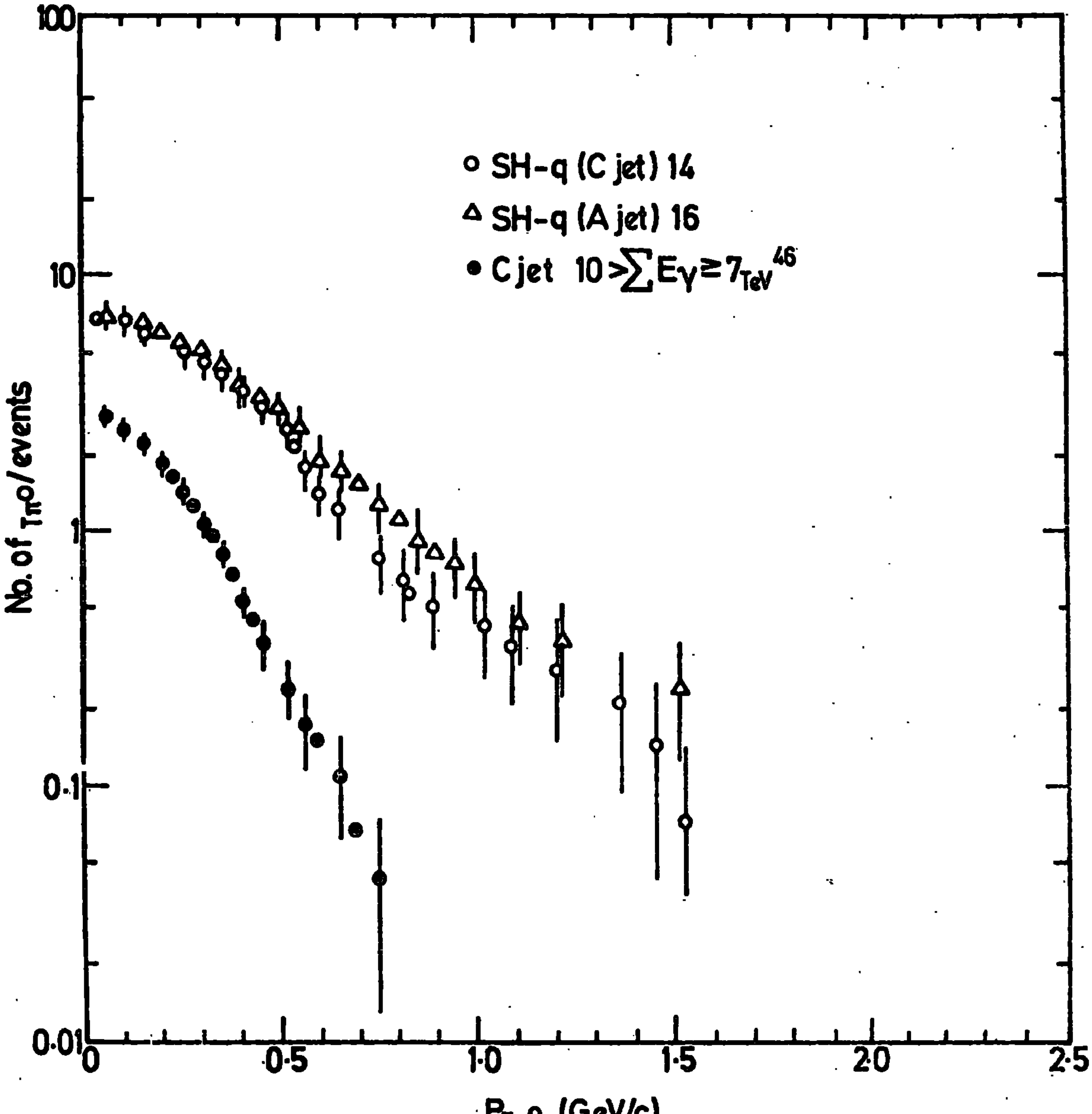

Figure 8.3 The integral P_T distribution of the number of π^o_s, per event for the low and high invariant mass events of the cosmic ray experiment. (Sreekantan, 1971)

bigger and bigger in size the values of $P_T h$ also follow this increase. A study of the cascade resulting from the neutral pions produced gives an estimate of the mean height of production $< h >$, equal to 0.6 ± 0.1 kms, therefore the mean transverse momentum was obtained to be

$$< P_T > = 15 \pm 3 \text{ Gev/C}$$

8.4.8 Hazen et al (1973)

This group found six showers which had two cores in their cloud chamber and a number of more complicated events. Their highest transverse momentum was about 70 Gev/c.

8.4.9 Matano et al (1975)

This group have observed high energy hadrons and multiple cores of E.A.S. with emulsion chambers installed in the air shower array and with the 20 m^2 spark chamber in the array. They have determined transverse momentum for each event with respect to the air shower axis. The average energies of hadrons and subcores are 9 Tev and 5 Tev respectively. The subcores have been analysed to determine the initiating height and the energy in the same way as the INS group using the particle distribution near the centre of the subcore and the calculation of Nishimura and Kidd. They have found 13 single hadrons associated with E.A.S. with energy above 3.3 Tev. having an average energy 9 Tev. The transverse momentum for each hadron has been determined with respect to the axis of E.A.S. The transverse momentum of the subcores, observed with the spark chamber is also determined. They have compared their results of integral spectra of P_T obtained by investigation of hadronic component and subcores and compared with accelerator results. They concluded that the average P_T increases and the spectrum of P_T becomes flatter with the energy of interacting particles.

8.4.10 Aseikin et al (1975)

The hadronic component of extensive air showers has been investigated

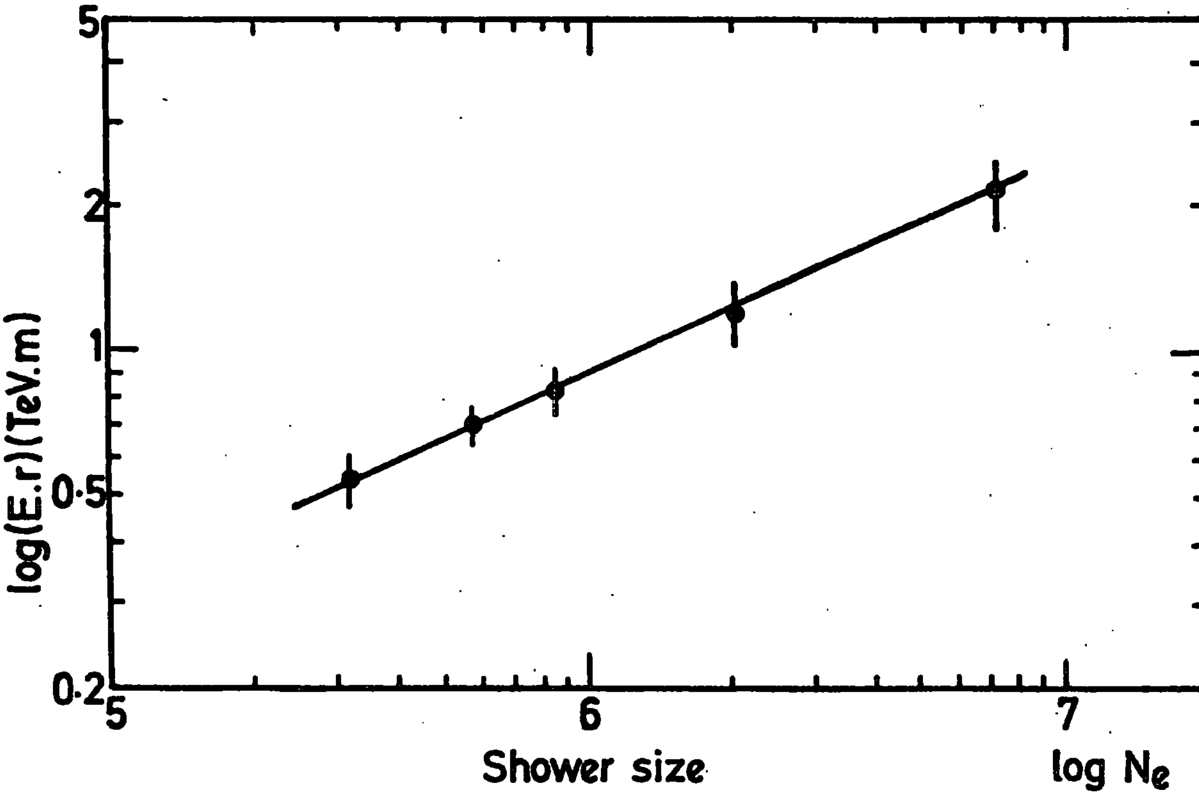

Figure 8.4 The dependence of the E.r on shower size. (Aseikin et al 1975)

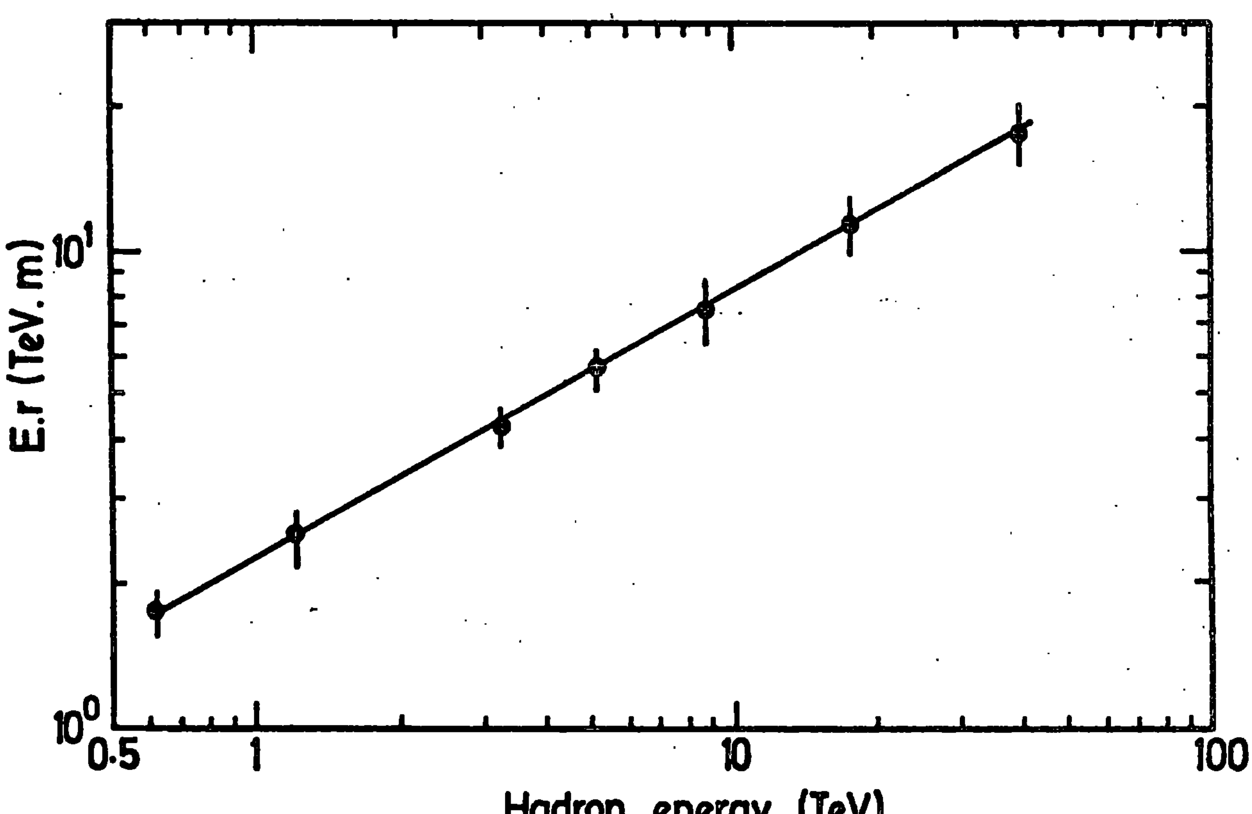

Figure 8.5 The dependence of the E.r on hadron energy (Aseikin et al 1975)

using the Tian-shan complex installation of P.N. Lebedev physics institute using the ionisation calorimeter. The shower parameters were obtained by an array of scintillation and G.M. Counters. Nearly 1600 showers of size $N_e \geq 1.6.10^5$ were analysed. The distance from the centre of installation to the axis of E.A.S. r is $\leq$ 3.0m.

The value $y = E_h.r$ was determined. Here E_h is the hadron energy and r is the distance between the hadron and the shower axis. The dependence of $y = E_h.r$ on the mean energy of hadrons was obtained. This dependence is shown in figure 8.5. It also obtained the dependence of $y = E_h.r$ on shower size, figure 8.4. It can be seen that as the shower size or mean hadron energy increases the value $y = E_h.r$ also increases on the ground of their results and the comparison to other results, they concluded the following hypothesis. The mean transverse momentum of nuclear interactions is constant to some energy of collision and its value is $< P_t > = 0.3 - 0.4$ Gev/c. Then the medium value $< P_T >$ increases significantly with increasing energy of interaction. The threshold energy may be about 100 Tev.

8.4.11 <u>Nesterova et al (1975)</u>

The energy of hadrons, E_h and the distance between the hadrons and the shower core Δr, also between several hadrons in the same shower were measured by the ionization calorimeter and scintillation counters in showers with $N_e \geq 10^5$ particles at 3340 m above sea level. The distribution of $E_h . \Delta r$ was obtained. The comparison of experimental results with calculation shows the existence of anomalous transverse momenta in the interaction of hadrons at the energy $E_p \geq 10^{15}$ev.

8.4.12 <u>Vatcha et al (1973)</u>

Vatcha and Sreekantan using a $2m^2$ multiplate cloud chamber at the centre of TIFR air shower at Ooty (800 gms/cm^2), studied the properties of high energy hadrons of energy $2.5.10^{10} - 10^{13}$ev. They have interpreted their observations in terms of collison characteristics at ultra high energies a need for drastic changes in the collision characteristics at energies $> 10^{12}$ ev. They concluded their experimentally obtained distribution of the quantity $y = E.r$ is not consistent with the mean transverse momentum of ~ 0.5 Gev/c, but requires $< P_T > 2$ Gev/c. They claim if their energy estimate of high energy hadrons is lower by a factor of 5, which may seem to explain the discrepancy in absolute numbers with the observation of others, then the mean transverse momentum $< P_T >$ required would be 10 Gev/c.

8.5 Result s of the present experiment

The experiment was in operation from May, 1975 to February 1976. The sensitive time was 2624 hours, during this period 96 hadrons of energy ≥ 300 Gev associated with shower in the size range $5.10^4 - 1.6.10^6$ have been analysed. The arrangement of the experiment is explained in chapter 6. The triggering requirement was the interaction of hadrons either in lead or in iron producing a burst with the size more than or equal to 400 particles, simultaneously we were able to sample the electron density of the associated shower.

Figure 8.6 shows the frequency distribution of the value E.r. In this figure is also shown the analytical distribution of E.r, deduced from C.K.P. model.

In Figure 8.7a and 8.7b the data has been split into two different shower size groups, hadron energies and the distribution for each group has been obtained, it can be seen that for larger showers and higher hadron energy the mean of the distributions are shifted to the right. In figure 8.8 and 8.9 the integral distribution of E.r is shown. Figure 8.10 shows the location of the showers within 10 meters from the centre of the installation.

In figure 8.11 the dependence of the mean hadron energy on shower size can be seen.

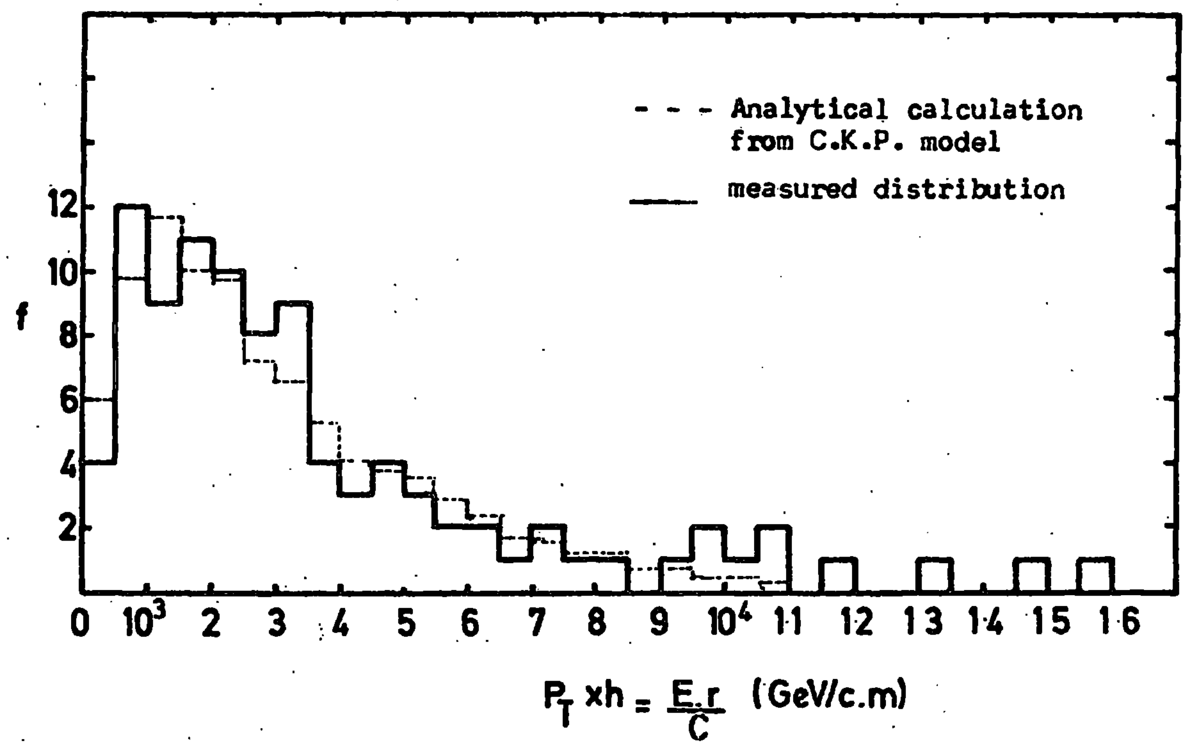

Figure 8.6 The differential $\frac{E.r}{C}$ distribution for $5.10^4 \leq N_e \geq 1.6.10^6$ particles and $E \gtrsim 300$ Gev the total number of events = 96. The mean of the distribution has $\frac{E.r}{C} = 3.3.10^3 \frac{Gev}{C}.m$ In this figure is also shown the analytical distribution of E.r, deduced from C.K.P. model, assuming h, is constant: $N(E.r)\,d\,(E.r) = A(E.r)\,e^{-E.r/(E.r)_o}\,d(E.r)$, $< E.r > = 2(E.r)o$ or $< E.r > = 3.3$ Tev m

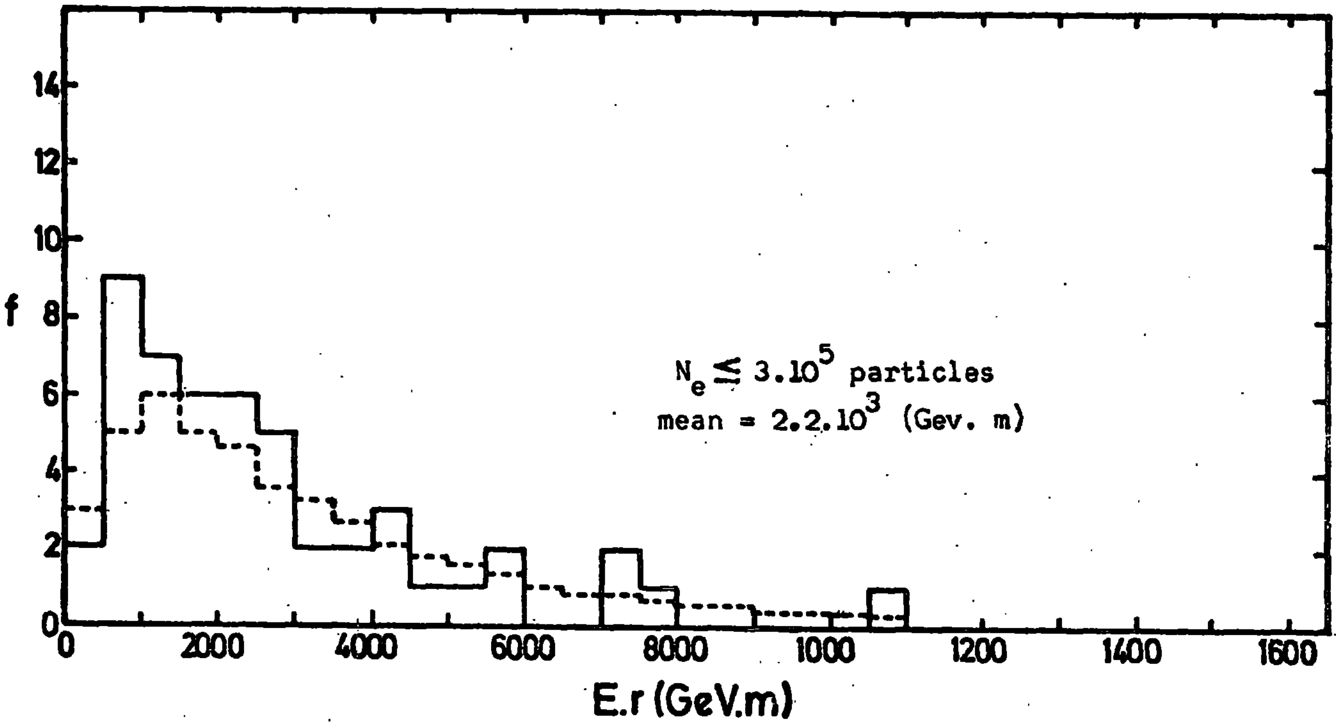

Frequency distribution of E.r for the shower size $N_e \leq 3.10^5$ particles, based on 48 events.

------- analytical representation

——— experimental distribution

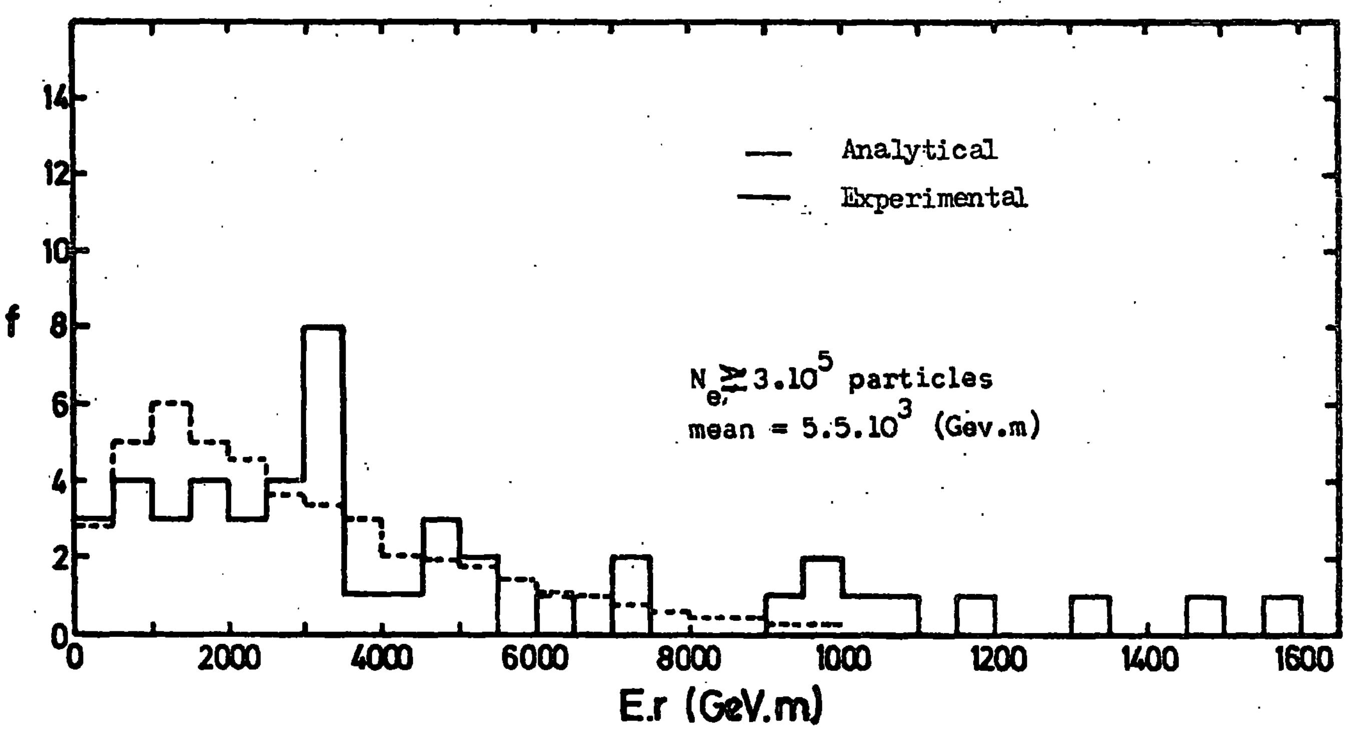

Figure 8.7a The differential $E.r = P_T.^h/c$ distribution for $N_e \geq 3.10^5$ and hadron energy ≥ 300 Gev.

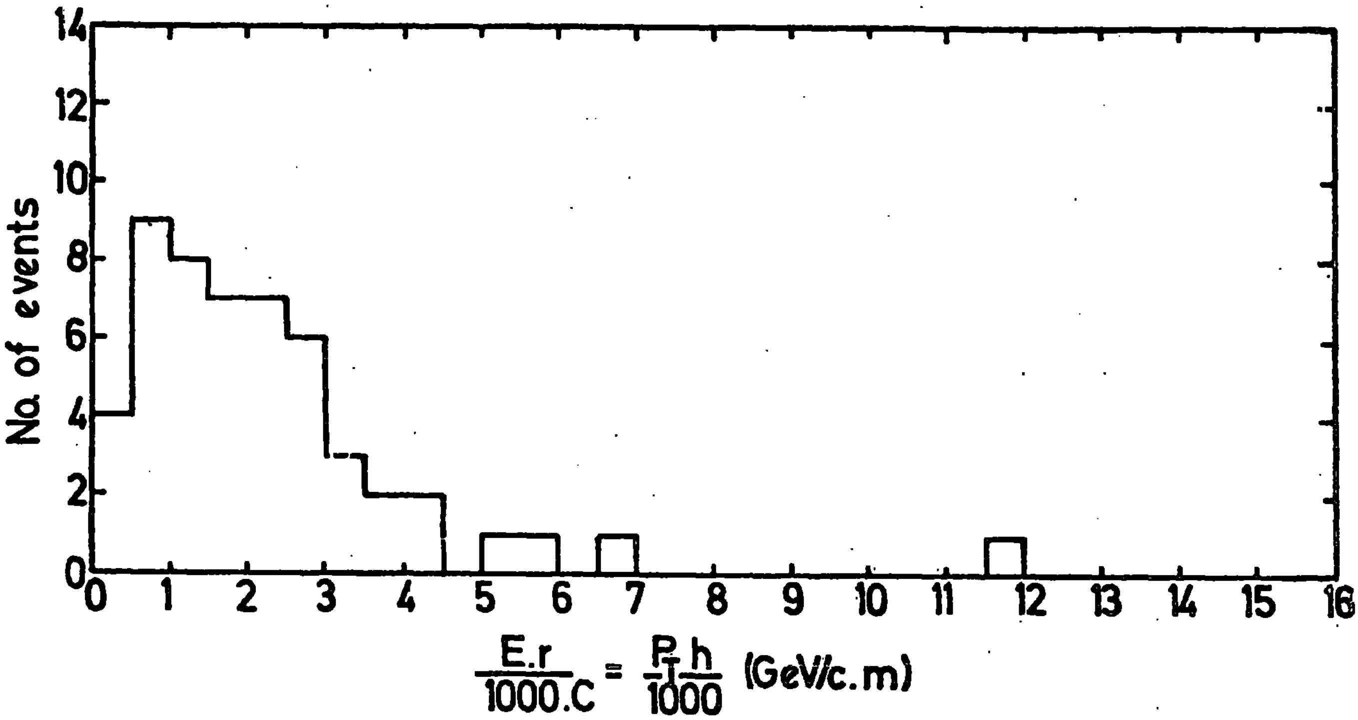

Differential $^E/C \cdot r = P_T.h$ distribution for $5 \times 10^4 \leq N \leq 1.6.10^6$
and hadron energy 300 Gev $\leq E \leq$ 650 Gev
Total no. of events = 52. The mean of the distribution
has $^E/C \cdot r = 2.2.10^3$ ($^{Gev}/c$ m.)

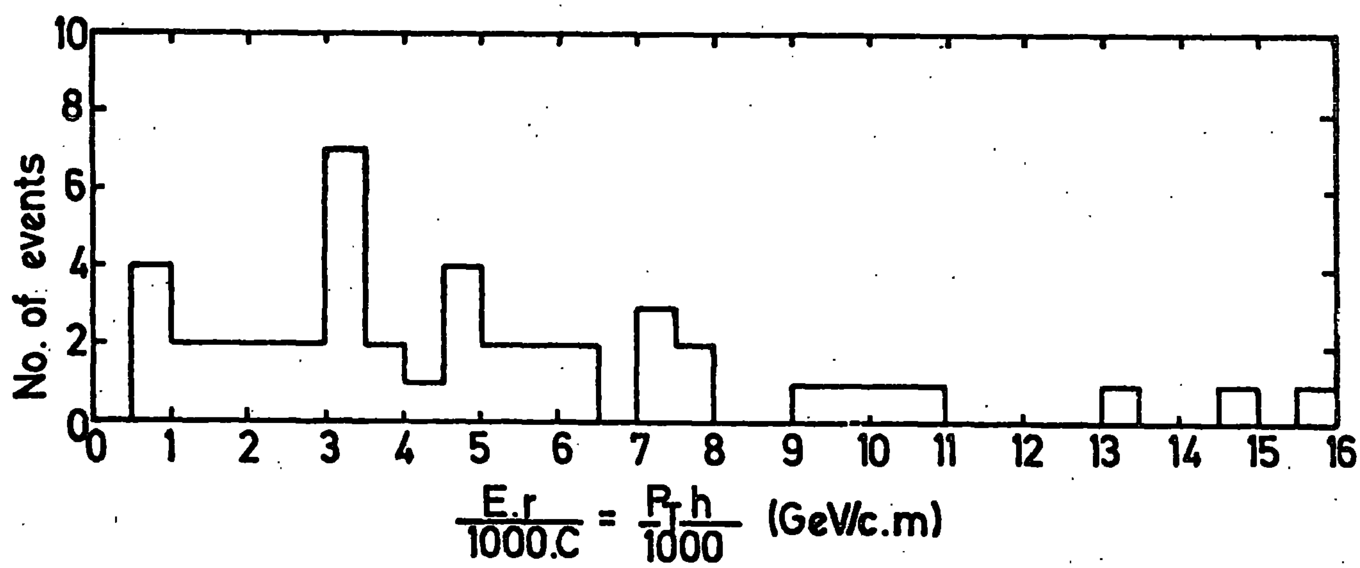

Figure 8.7b Differential $^E/C \cdot r = P_T.h$ distribution for $5 \times 10^4 \leq N \leq 1.6.10^6$
and hadron energy 650 Gev $\leq E \leq$ 3000 Gev.
The mean of the distribution has $^E/C \times r = 5.5.10^3$ Gev/$_c$ m.
Total no. of events = 44

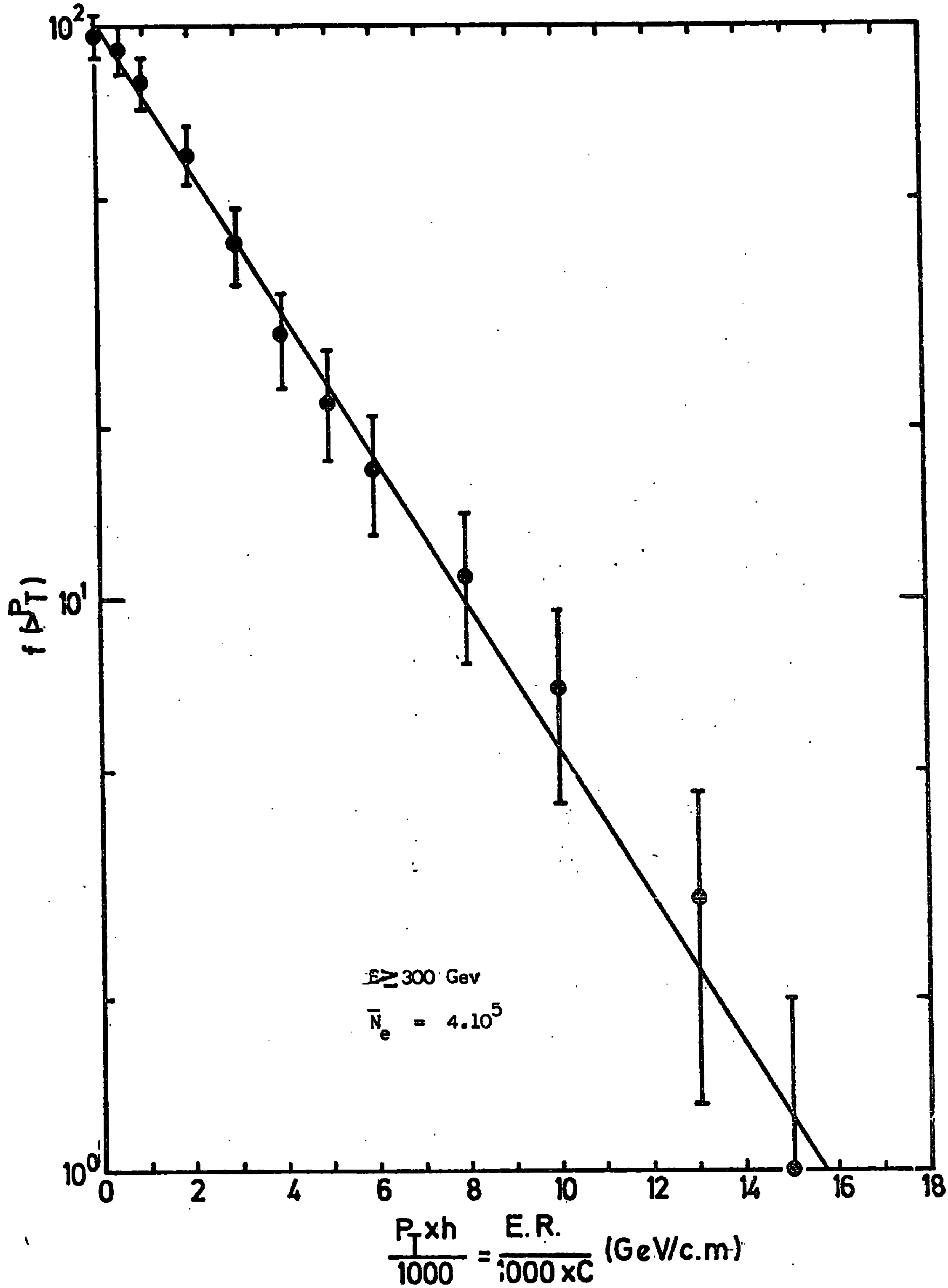

Figure 8.8 The integral E.r distribution for hadron energy ≥ 300 Gev and a mean shower size 4.10^5

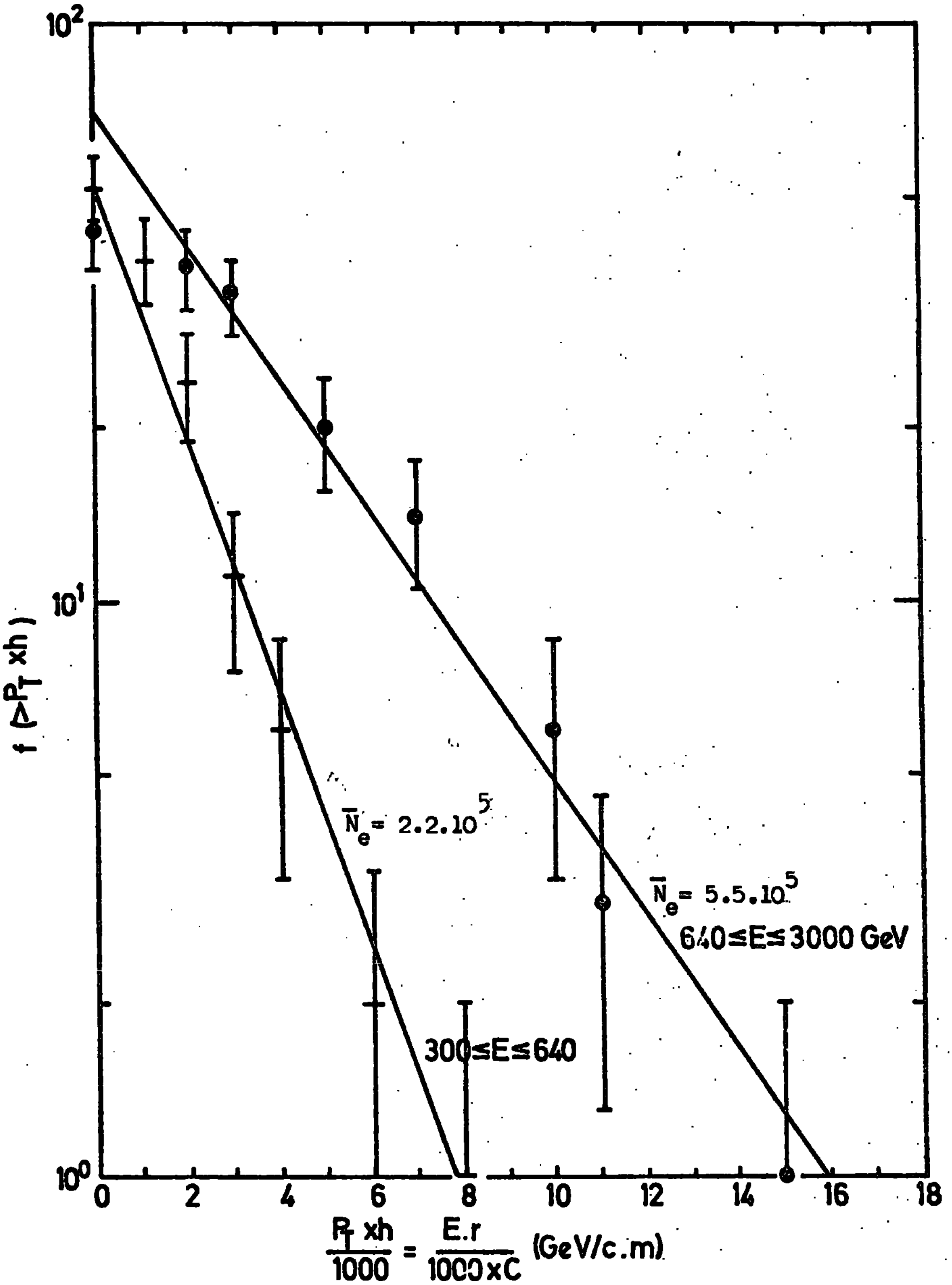

Figure 8.9 The integral E.r distribution for two different hadron energy range and two different mean shower size associated.

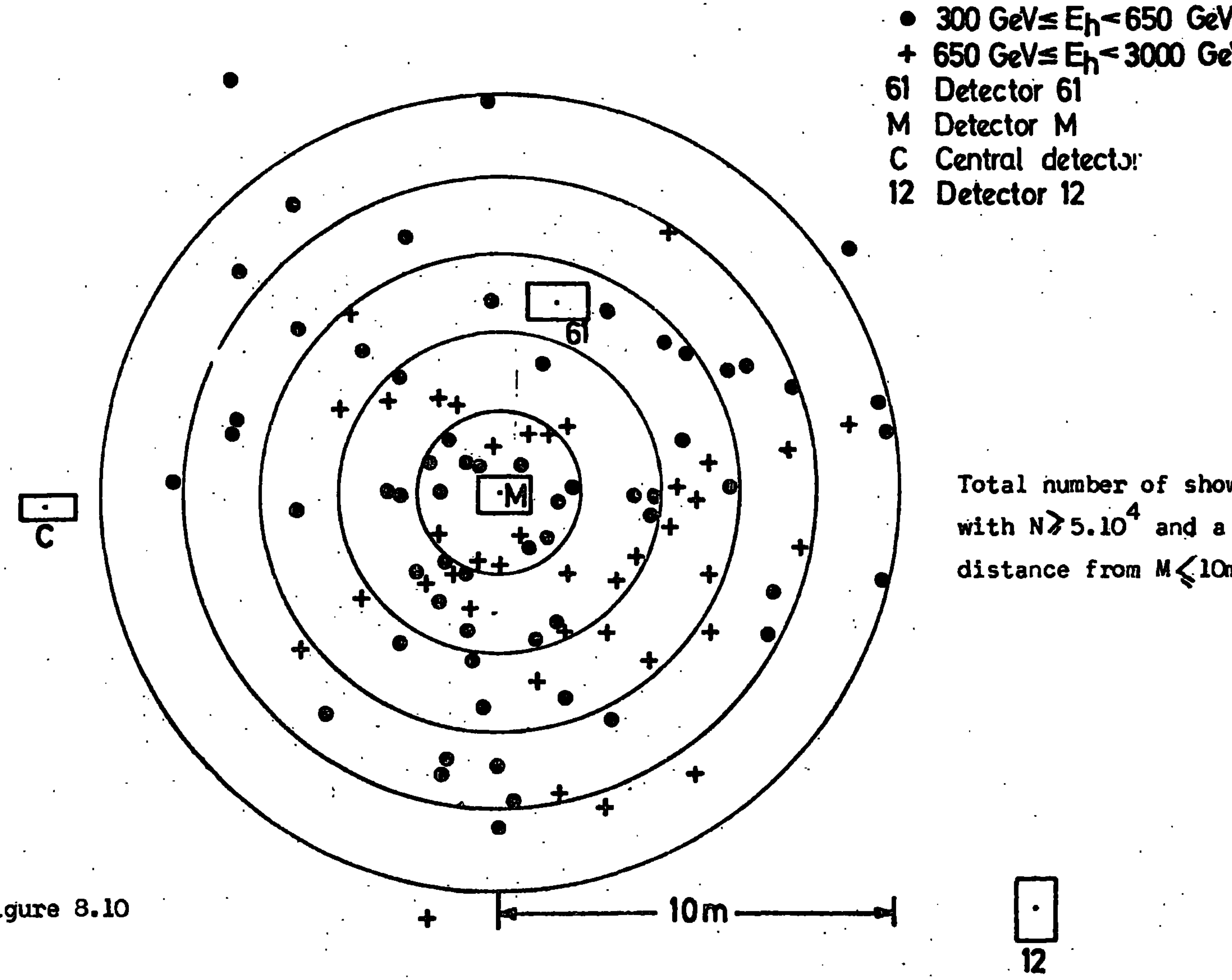

Total number of showers with $N \geqslant 5.10^4$ and a core distance from $M \leqslant 10m = 96$

Figure 8.10

The distribution of shower core location.

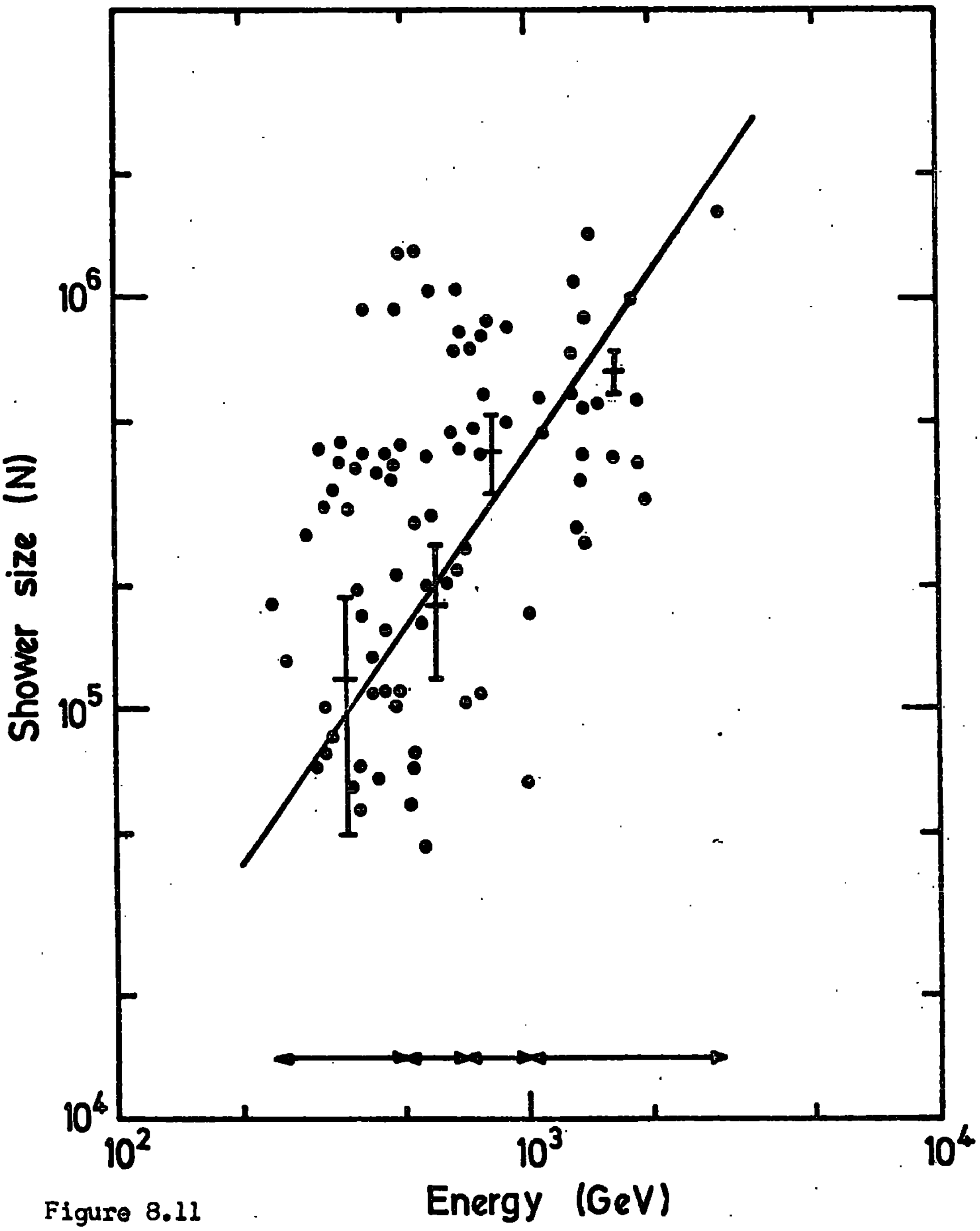

Figure 8.11

The dependence of shower size on average hadron energy, The dots represent individual measurements and the crosses are average values. The average behaviour can be represented by $N = AE^{\alpha}$ Where $\alpha = 1.4$, with E in Gev.

Figure 8.12 shows the dependence of E.r on hadron energy.

The dependence of E.r on shower size can be seen in figure 8.13.

Figure 8.14 shows the shower size frequency distribution of showers associated with 96 energetic hadrons.

8.6 Comparison with other results

The results of this experiment is compared with McCusker et al (1969) observations (obtained from the investigation of the core structure of electromagnetic component);Bakich et al (1969), Vatcha et al, 1973 (their information came from the observation of high energy hadrons) and Aseikin et al(1975) who measured energetic hadrons in air showers. Our results are compatible with these workers, see figure 8.15. The variation of the mean transverse momentum with primary energy is shown in Figure 8.16, (ɸ ✶) to convert shower size to primary energy the calculation made by Kempa 1976 has been used, (figure 8.1), ɸ obtained by normalysing to the measurement made by McCusker ▲, 1969. Taking the production height 1 Km. (120 g/cm^2, the mean free path for pions) above the detector, point, ✶ has been obtained.

The present measurement has been compared with the measurements made for lower primary energies. It can be seen that from the primary energy 10^4 Gev the mean transverse momentum drastically increases as the energy increases. The sources of the points 1, 2, 3, 4, 5, 6 is shown in the following pages.

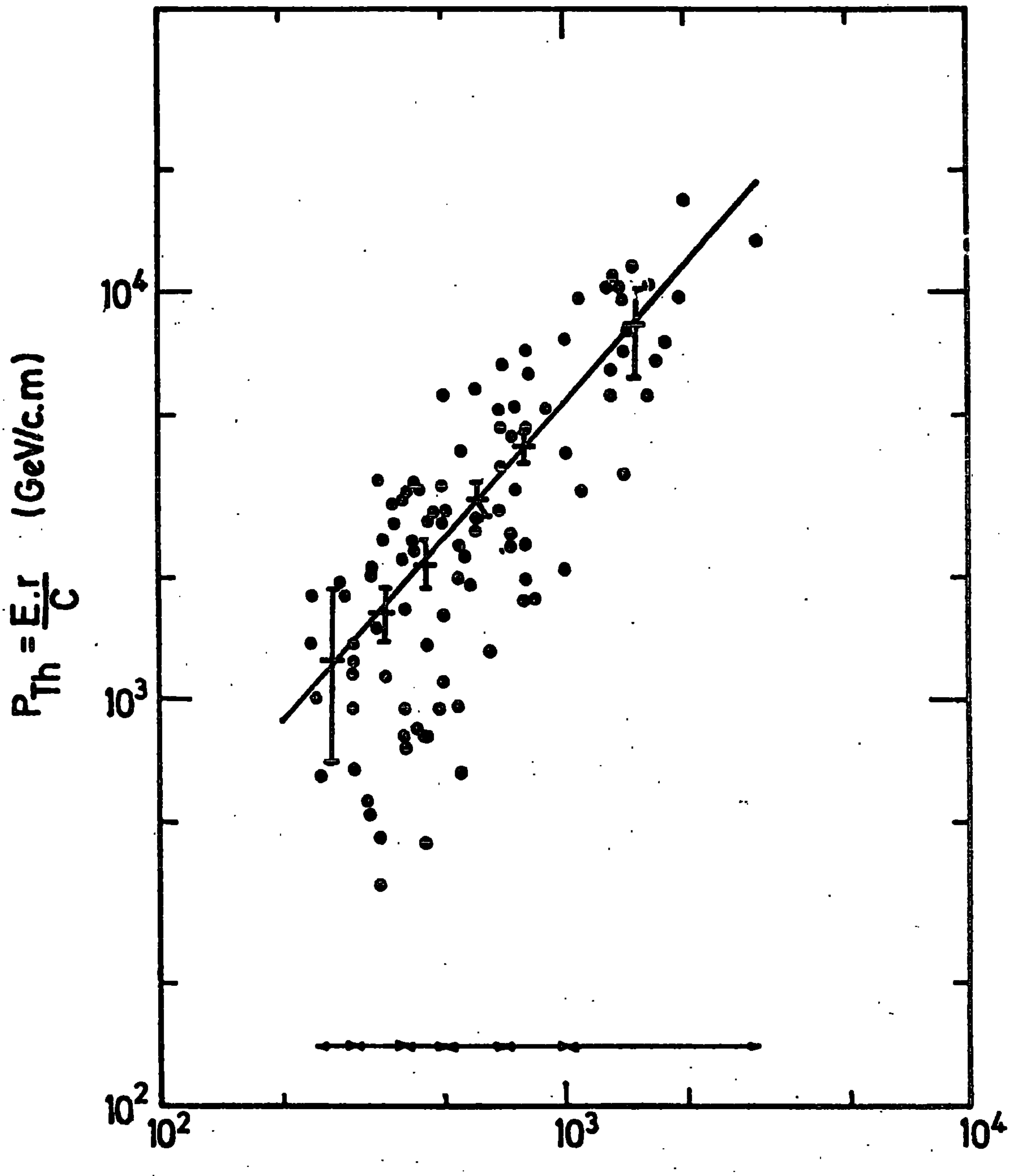

Figure 8.12

The dependence of E.r on average hadron energy.

The dots represent individual measurements and the crosses are average values of E.r over the range of energy indicated by arrows. The average behaviour can be represented by $E.r = AE^{\alpha}$ where $\alpha = 1.1$ with E.r in Gev. m.

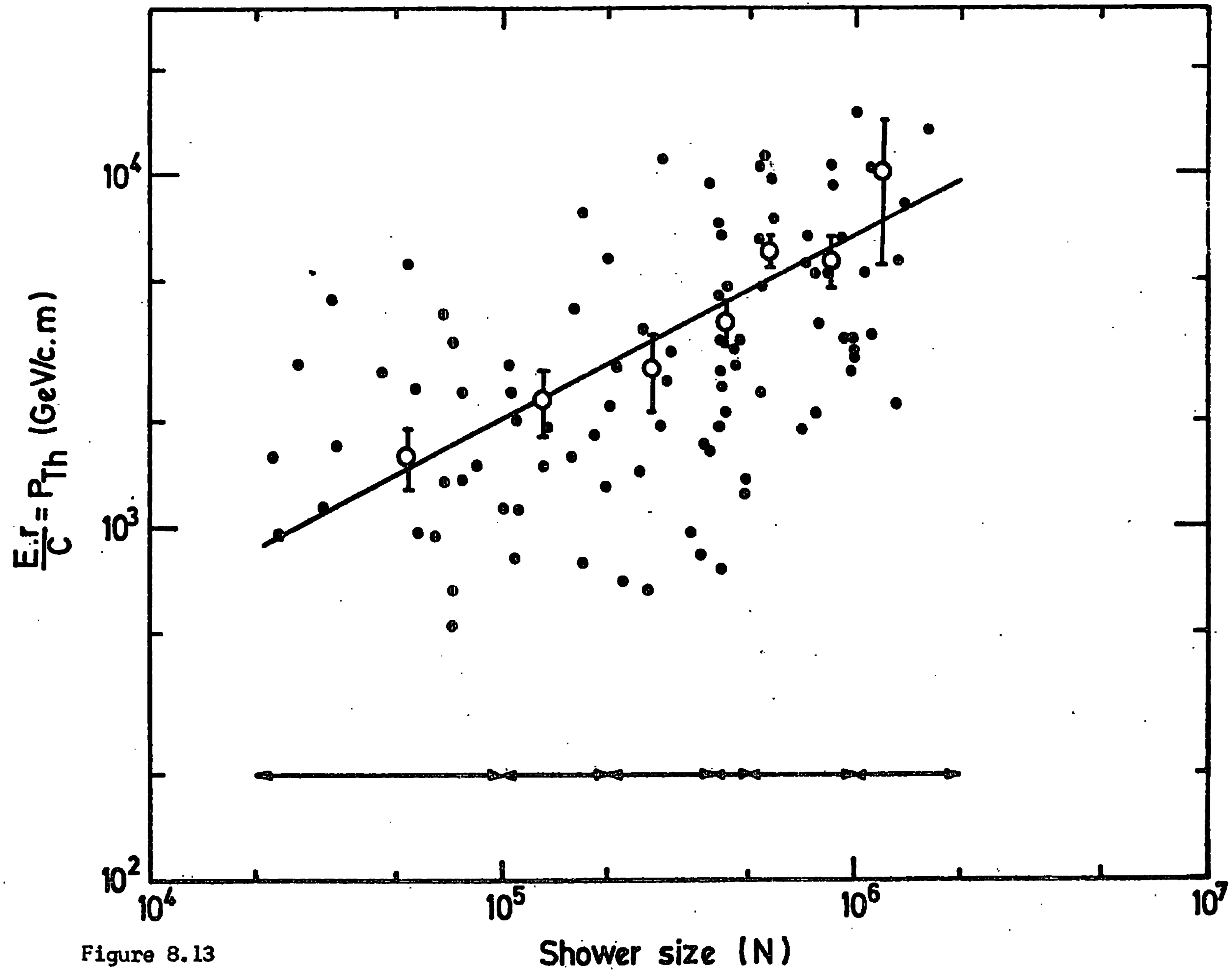

Figure 8.13

The dependence of E.r on shower size. The dots represent individual measurement and the circles are average values of E.r over the range of shower size indicated by the arrows.
The average behaviour can be represented by $E \times r = AN^{\alpha}$ where $\alpha = .51$ and $E \times r$ is in Gev. m.
Total number of showers = 96   With $N \gtrsim 5.10^4$ and $r \lesssim 10$m.

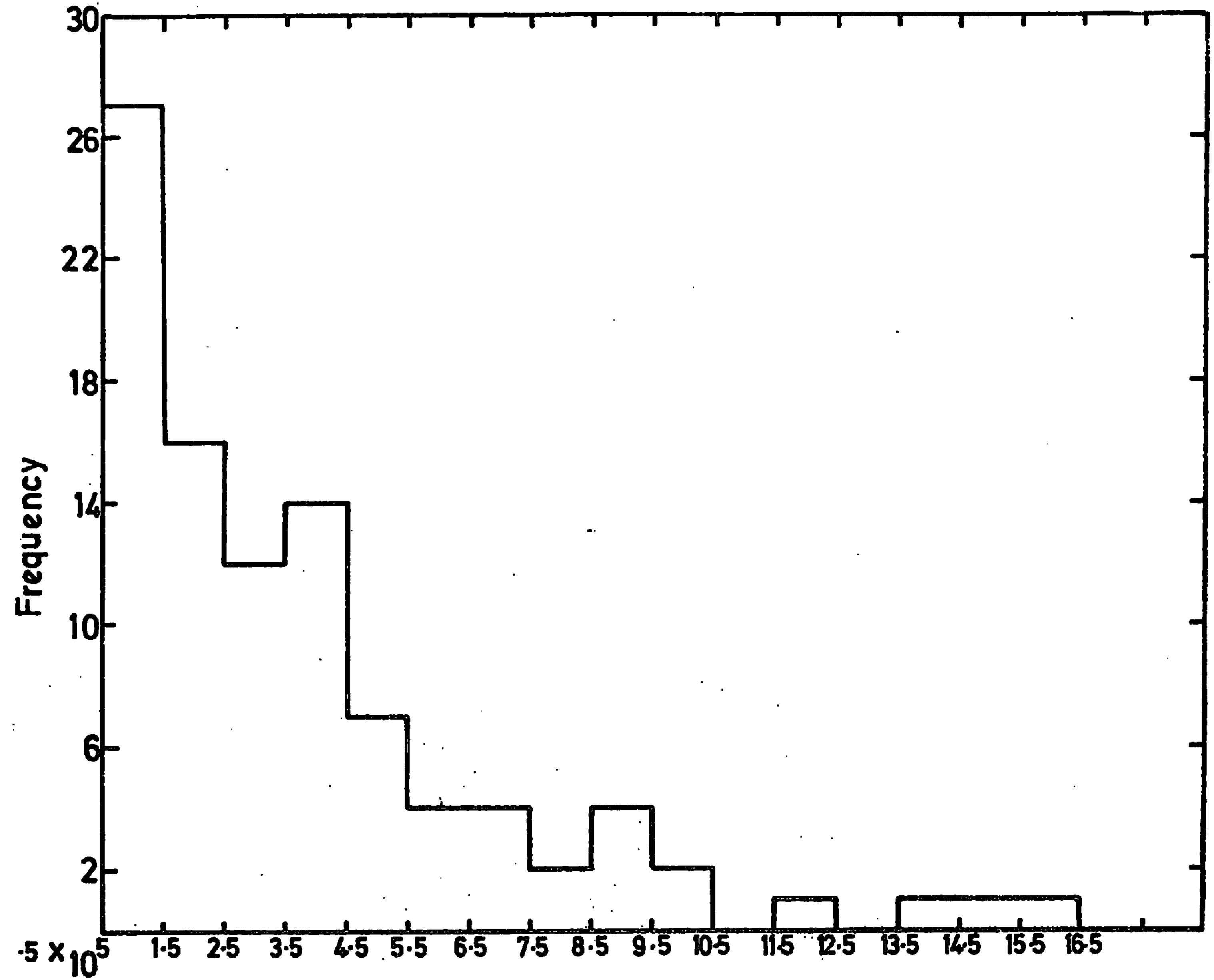

Figure 8.14

The frequency distribution of showers sizes of 96 events analysed in Figures 8.9, 8.10 and 8.11.

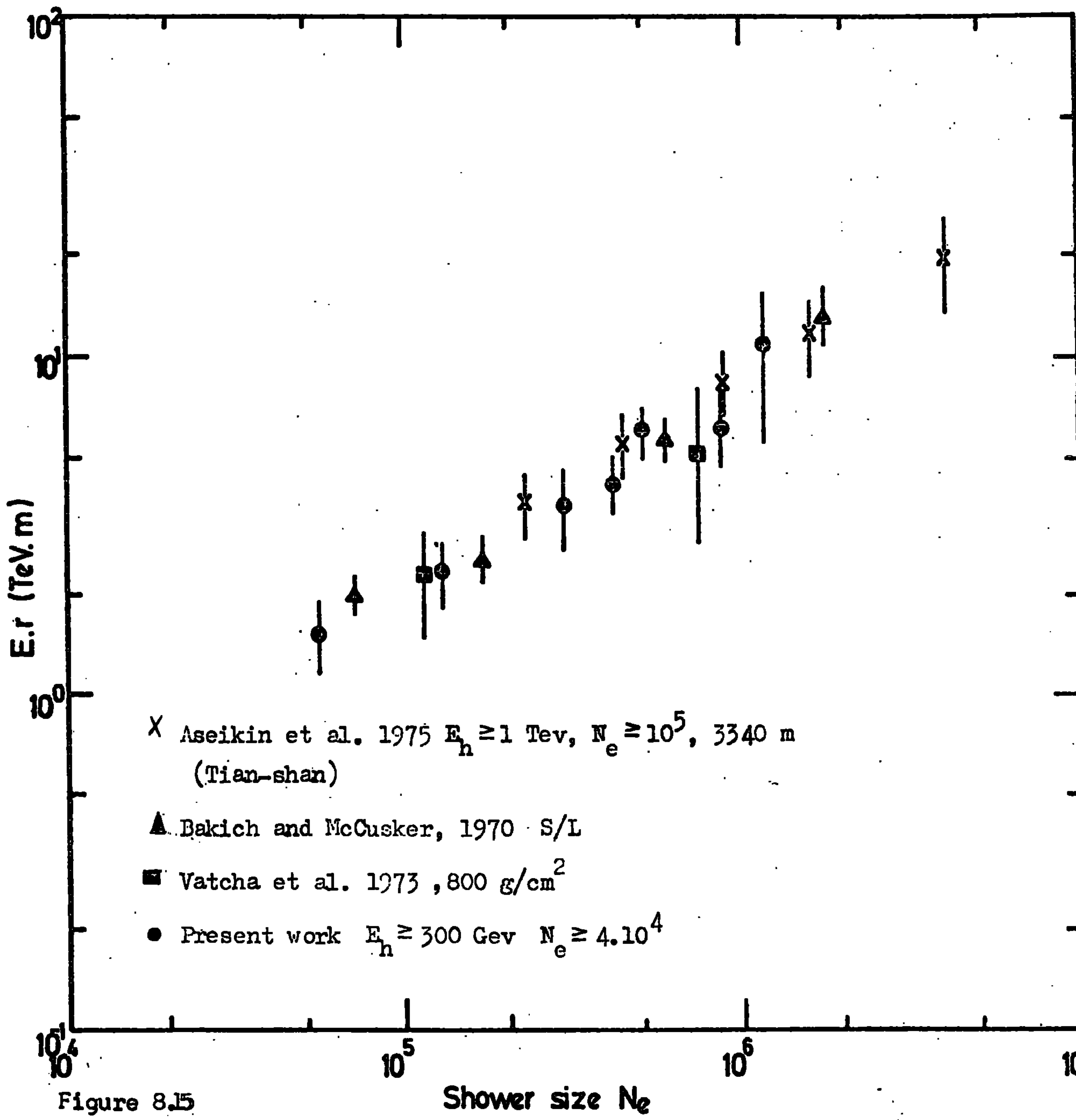

Figure 8.15

The comparison of E.r versus shower size of the results of three different groups with present results.

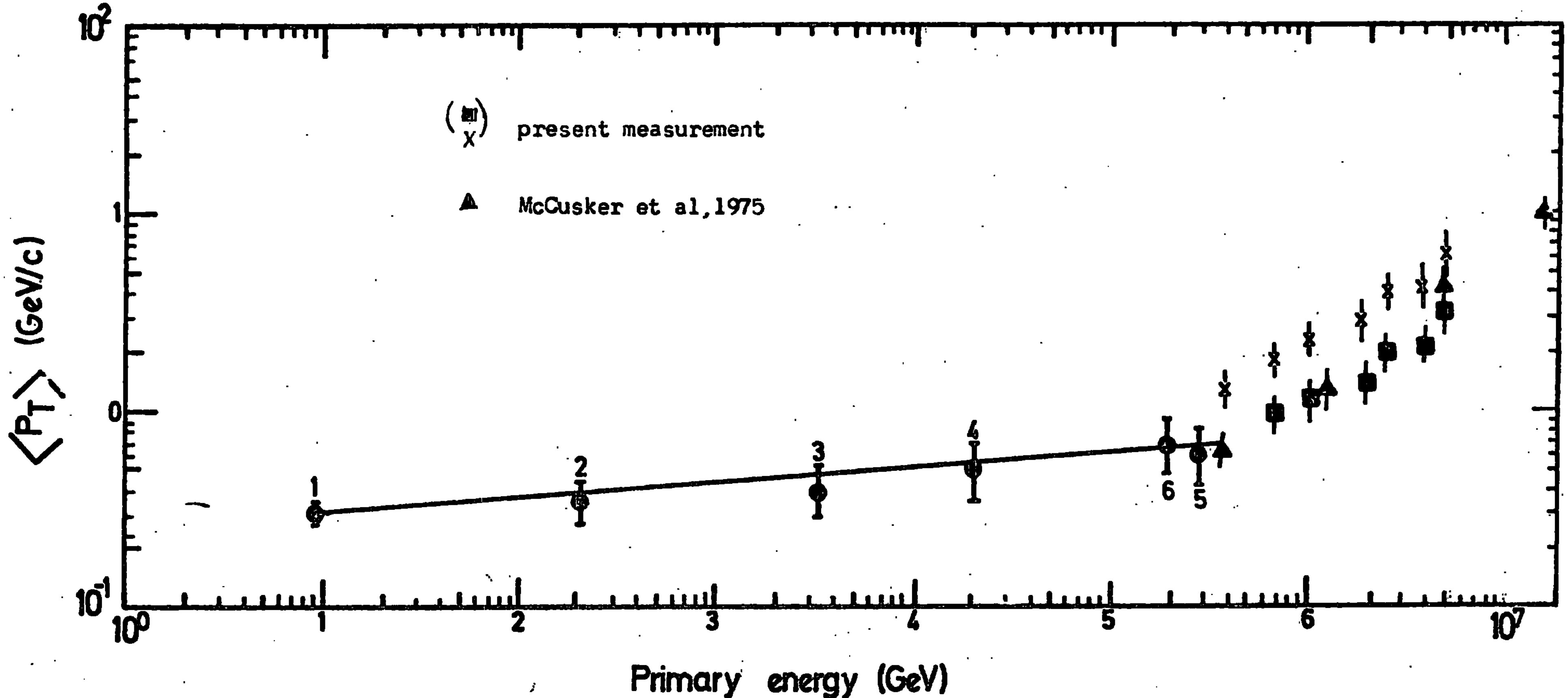

Figure 8.16 Variation of mean transverse momentum with Primary energy. ■ obtained by normalising to the measurement made by McCusker et al, 1969; × obtained by taking the production height of the hadrons 1 K.m. above the detector. The points 1,2,3,4,5,6 obtained by averaging different measurements made by different authors (see the relevant caption)

SOURCES OF POINTS IN FIGURE 8.16

The points 1, 2, 3, 4, 5, 6 are the average of the following sources:

Point 1

Godksack, G., Riddiford, L., Tallini, B., French, B., Neal, W., Norbury, J., Skillicorn, I., Davies, W., Derrick, M., Mulvery, J. and Radojicic, D., Nuovo Cim., 23, 941 (1962)

Bigi, A., Brandt, S., de Marco-Trabucco, A., Peyrou, Ch., Soenowski, R. and Wroblewski, A., Nuovo Cim., 33, 1265 (1964)

Femino, S., Jannelli, S. and Mexxanares, F., Nuovo Cim., 31, 273 (1964)

Point 2

Fujioka, G., J. Phys. Soc., Japan, 16, 1107 (1961)

Brisbout, F., Cauld, C., Lehane, J., McCusker, C., Malos, J., Nishikawa, K. and Van Loon, L., Nucl. Phys., 26, 634 (1961)

Adwards, B., Losty, J., Perkins, D., Pinkau, K. and Reynolds, J., Phil. Mag. 3, 237 (1958)

Point 3

Edwards, B., Losty, J., Perkins, D., Pinkau, K. and Reynolds, J. Phil. Mag. 3, 237 (1958)

Minakawa, O. et al. Supp. Nuovo Cim., 11, 125 (1959)

Debenedetti, A., Garelli, C., Tallone, L. and Nigone, M., Nuovo Cim., 4, 1142 (1956)

Schein, M., Haskin, D., Lohrmann, E. and Teucher, M., Phys. Rev., 116, 1238 (1959)

Point 4

Edwards, B. et al., Phil. Mag., 3, 237 (1958)

Malhotra, P. et al., Nuovo Cim., 40, A404 (1965).

Awunor-Renner, E. et al., Nuovo Cim., 17, 134 (1960)

Minakawa, O. et al., suppl. Nuovo Cim., 11, 125 (1959)

Nishikawa, K., J. Phys. Soc., Japan, 14, 879 (1959)

Point 5

Ciok, P. et al., Nuovo Cim., 6, 1409 (1957)

Hasegawa, S., Nuovo Cim., 14, 909 (1959)

Kazuno, M., Nuovo Cim., 24, 1013 (1962)

Kazuno, M., Ph.D. Thesis, 1967 Dublin Institute for Advanced Studies.

Point 6

Adcock, C., Coats, R.B. Wolfendale, A.W., and Wdowczyk, J.
J. Phys. A., 3, 697 1970.

8.7 Summary and Conclusion

The behaviour of 96 high energy hadrons $E \geq 300$ Gev associated with E.A.S. in the size range $4.10^4 - 1.6.10^6$ particles have been investigated. The result is compared with others, figures 8.15 and 8.16. On the ground of the present observation and the results of other workers, it can be concluded that the mean transverse momentum of secondaries produced in nuclear interactions increases slowly to some collision energy. Then the mean value of transverse momentum increases drastically with increasing the primary energy. The threshold energy for this phenomenon may be about 5.10^4 Gev.

PLATE 8.1

Event H 117 - 61

An event with two secondaries receiving large transverse momentum after the collision, the interaction is in lead, the bursts have penetrated through the iron absorber.

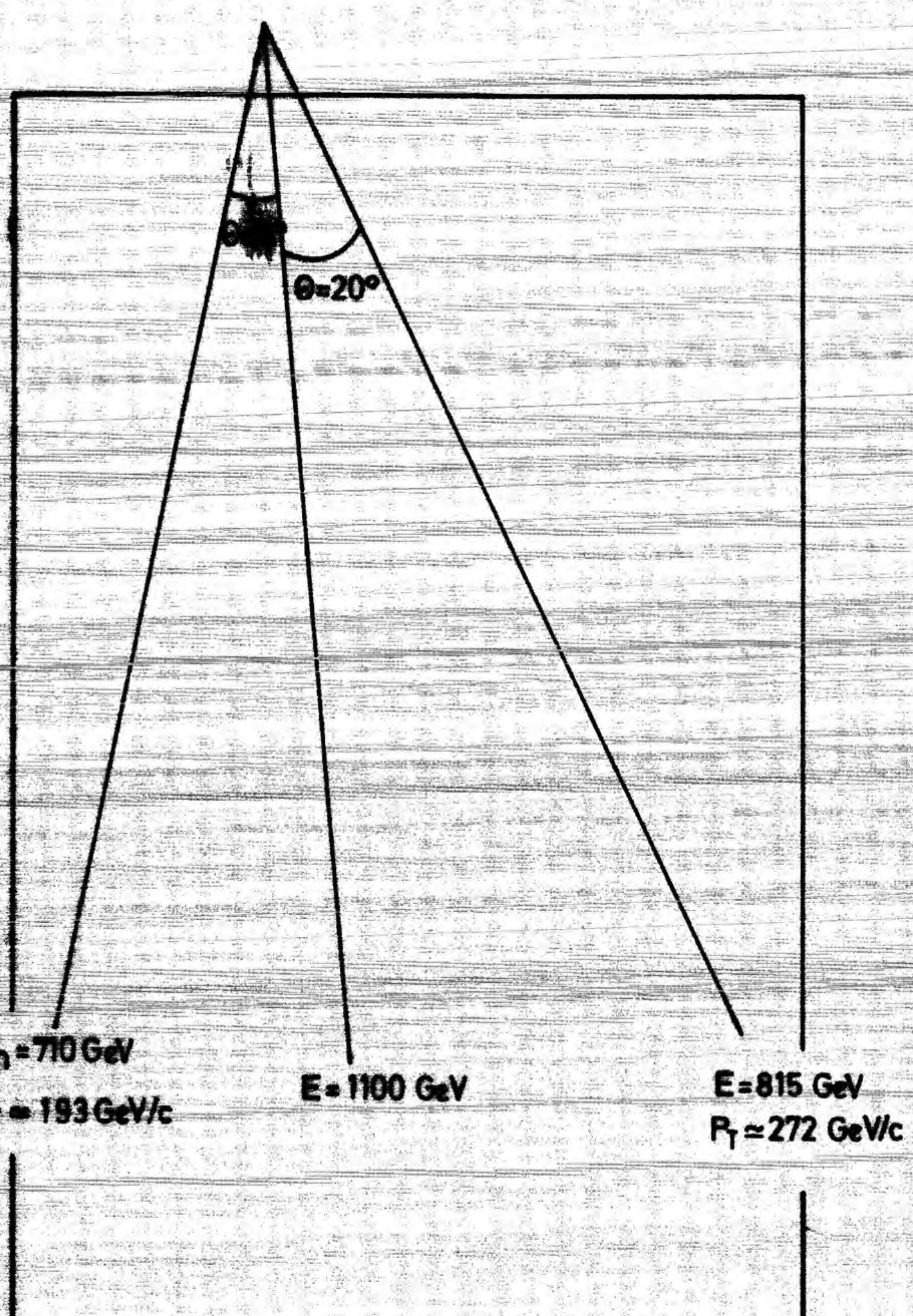

θ=20°
E_n = 710 GeV
P_T ≃ 193 GeV/c
E = 1100 GeV
E = 815 GeV
P_T ≃ 272 GeV/c

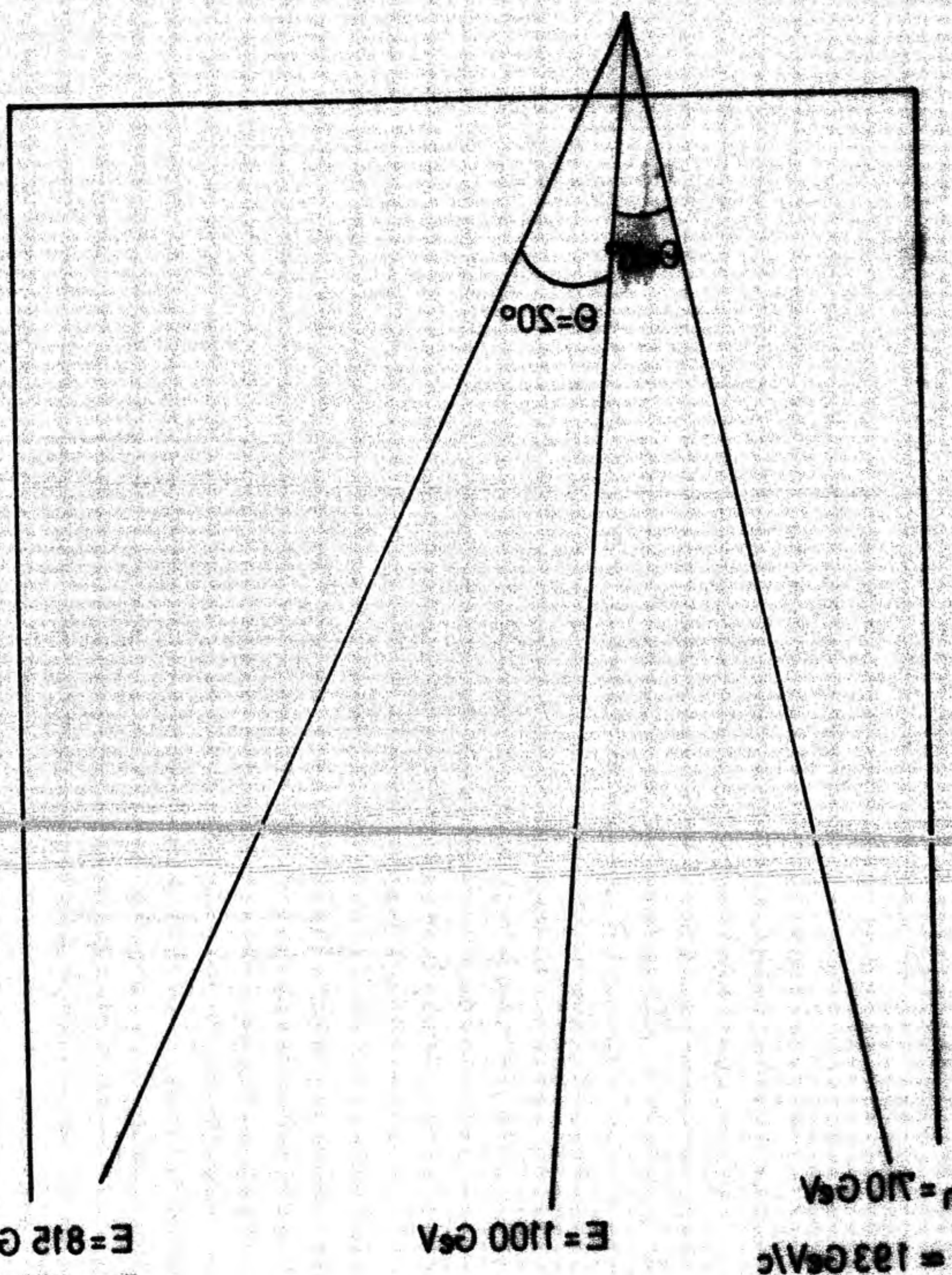

Θ=20°
Θ=15°
E = 815 GeV
P_T = 272 GeV/c
E = 1100 GeV
E_n = 710 GeV
P_T = 193 GeV/c

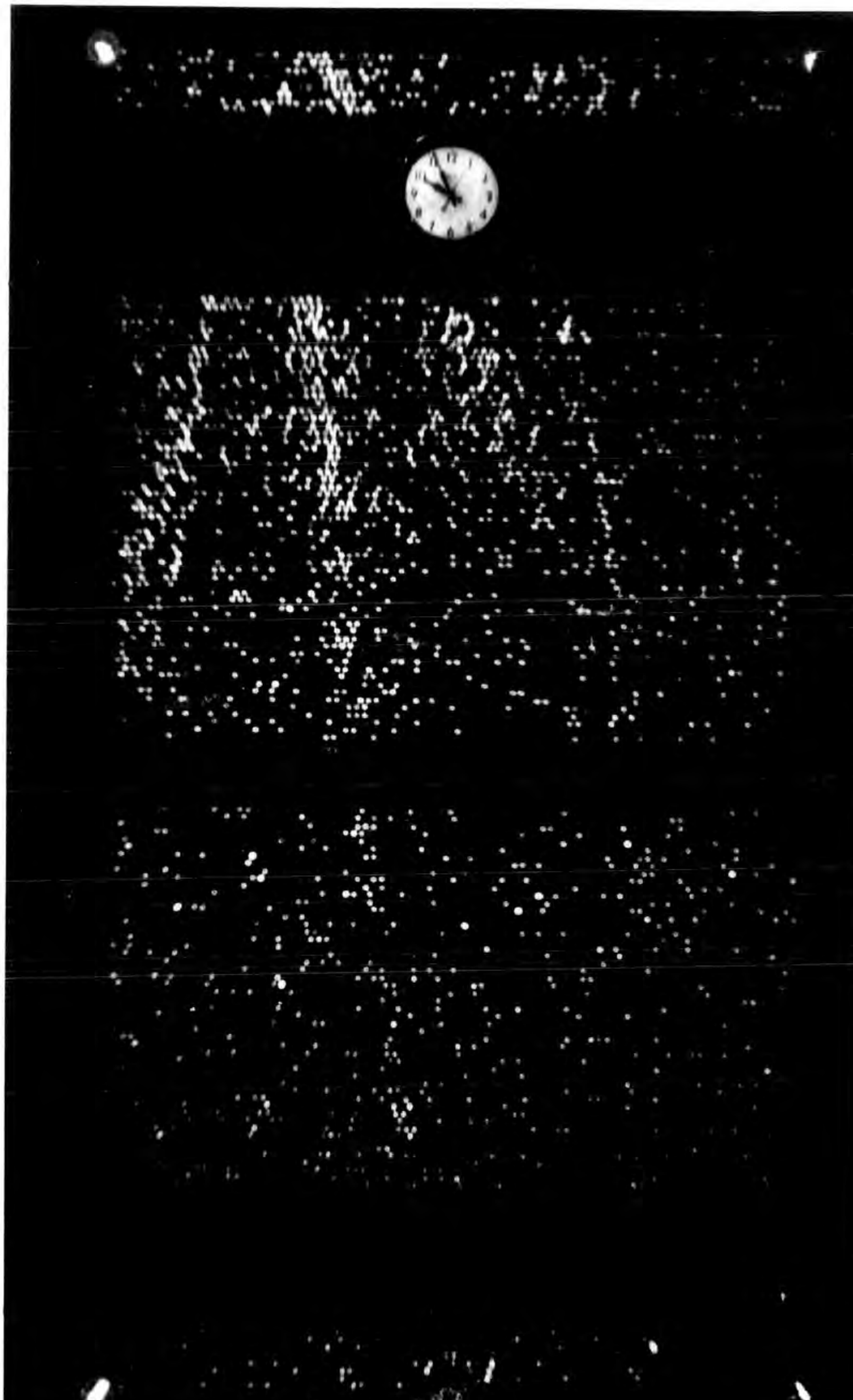

R = 10

$N = 1.14.10^6$

Burst size = 5063

PLATE 8.2

Event H 116 - 38

A hadron with large transverse momentum interacted in lead producing a burst of size = 5063 particles associated with an extensive air shower of size $1.14.10^6$ particles.

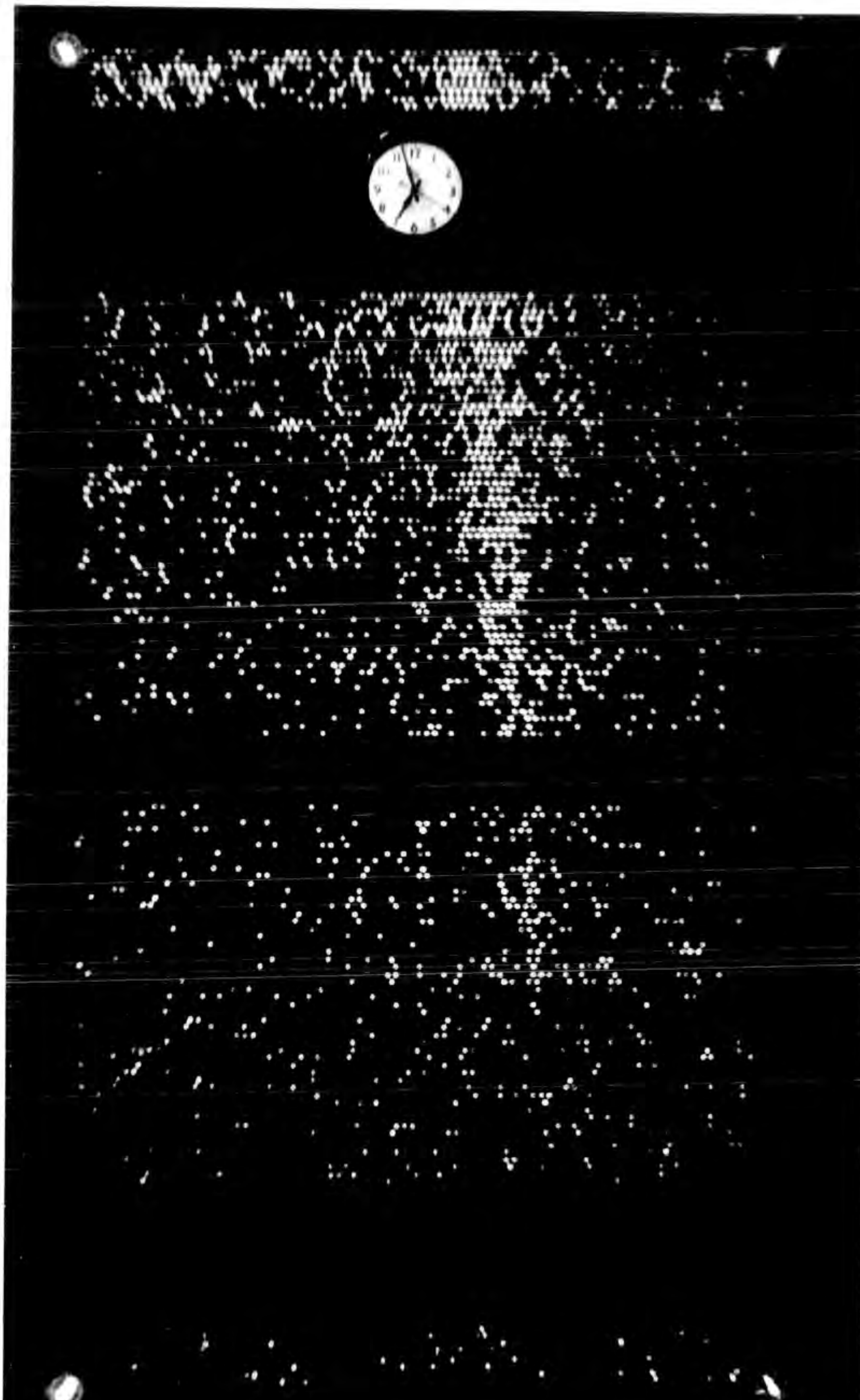

$R = 8.2$

$N = 1.10^6$

Burst size = 2450

PLATE 8.3

Event H 110 - 3

An event receiving large transverse momentum. The hadron has interacted in lead, producing a burst = 2450 particles, penetrated in rion. The size of the air shower accompanied is 1.10^6 particles.

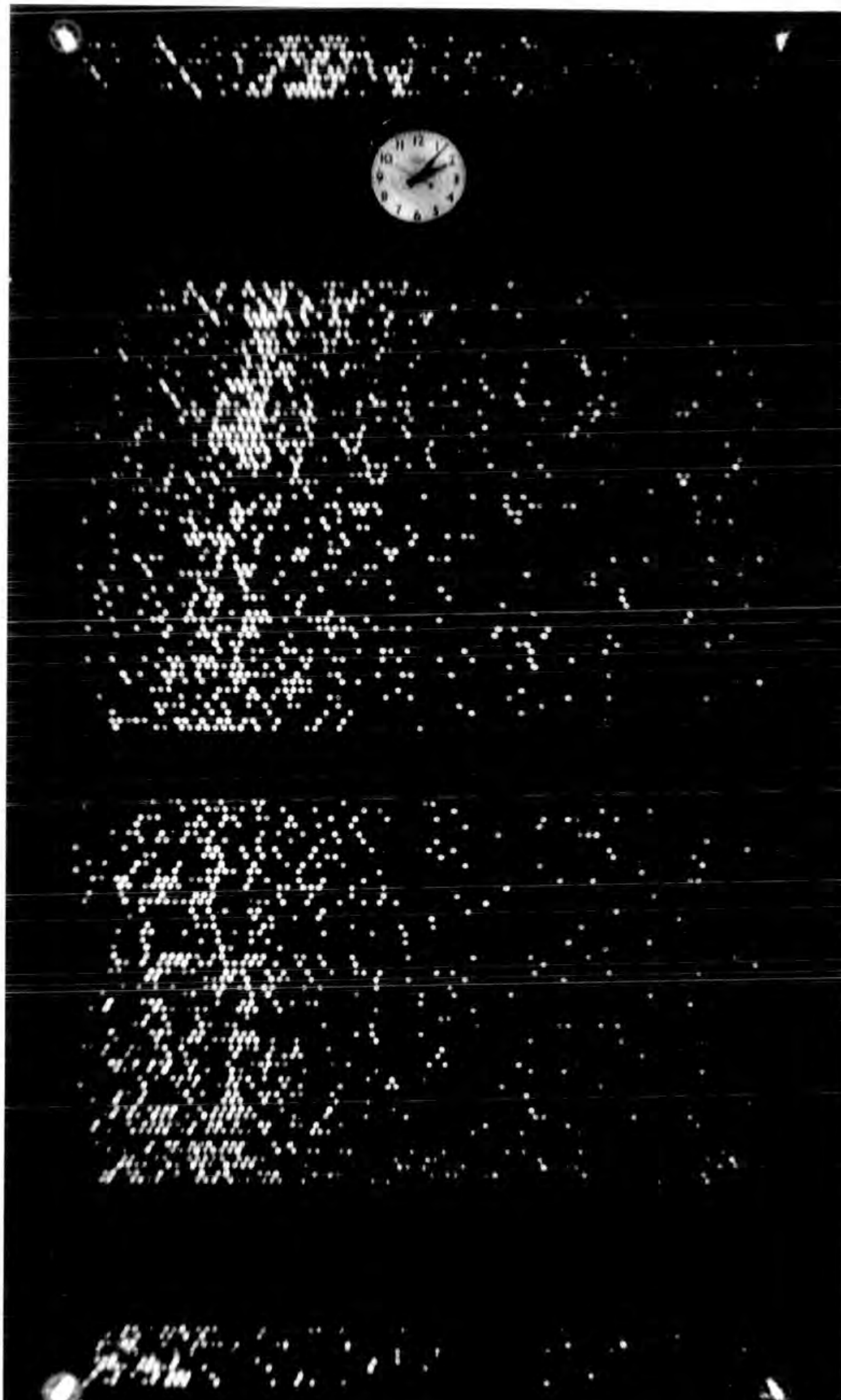

CHAPTER 9

THE INCOHERENT HADRON ENERGY SPECTRUM AT SEA LEVEL

9.1 Introduction

Since our apparatus has been triggered after the interaction of a hadron in lead or iron targets, whether accompanied with E.A.S. or not, we were able to measure the energy spectrum of incoherent hadrons at sea level. This measurement increased the statistics of the previous work carried out by Ashton and Saleh, 1975 initiated for the investigation of the step seen by Baruch et al. in the energy range 2-8 Tev, reported in Munich Conference, 1975.

The energy spectra of hadrons at different observation levels in the atmosphere can give information about the behaviour of the nuclear interactions of hadrons in the way to the earth through the atmosphere.

The triggering level of this experiment was the production of a burst $\geqq 400$ particles either in the lead or iron. The conversion of burst size to hadron energy has been made by the calculated burst size-energy relationship curves discussed in chapter 5. The result of the present observation shows a constant slope. The spectrum can be represented by $E^{-2.74 \pm .16}$ in the energy range 400 Gev to 8 Tev.

9.2 A survey of measurements of incoherent hadron energy spectra at different altitudes

9.2.1 Grigorov et al (1965)

This measurement has been carried out at Mt. Aragats (700gcm^{-2}). In this experiment the intensity of hadrons has been measured up to 3.10^3 Gev. The apparatus used has been an ionization calorimeter of 10m^2 sensitive area, consisted of 12 trays of ionization chambers located under filters of lead, graphite and iron. After an effective time of 1,015 hours of running the experiment 633 events were recorded. The integral energy spectrum of unaccompanied hadrons is plotted in figure 9.1.

9.2.2 Jones et al (1970)

To study the interactions of Cosmic ray nuclear active particles with protons, this group made an experiment at Echo Lake, 700gcm^{-2} Colorado. They used 2000 litre liquid hydrogen target, spark chambers and an ionization calorimeter. The calorimeter was constructed of iron and plastic scintillator with a total thickness of 1,130gcm^{-2}. During the running time they recorded 1,000 interactions above 70 Gev. The energy of the incident hadrons were estimated from pulse heights of the detectors in the calorimeter. The energy resolution of the calorimeter was estimated to be about $\pm$15%. The integral energy spectrum measured, was represented by $N(>E) = 3.10^{-7}E^{-2}$ ($m^{-2}st^{-1}sec^{-1}$), where E in the unit Gev. The results of this experiment is plotted in figure 9.1.

9.2.3 Kaneko et al. 1971

The measurement was carried out at Mt.Chacaltaya 550gcm^{-2}. They recorded high energy nuclear burst produced by unaccompanied hadrons with energy greater than 3.10^{12}ev. The apparatus used, consisted of 10 vertical telescopes each consisted of 2 and 3 unshielded counters placed above a shielded counter under 386 gcm^{-2} of absorber. Their result is shown in figure 9.1.

9.2.4 Siohan et al. 1973

To measure the charged hadron intensity they used an ionisation calorimeter at the altitude of 730 gcm^{-2} (2,900 meters) at SRCRL in New Mexico. A layer plastic scintillator of total area 3.3 m^2 was placed in anticoincidence to record the shower accompanied hadrons. Their result is plotted in figure 9.1. The differential energy spectrum is represented by:

$$dN/dE = (7.95 \pm 0.9) \times 10^{-5} (E/100)^{-3.2 \pm 1} \text{ particles } /m^2 \text{ sec st Gev}$$

in the energy range 100 - 1,200 Gev.

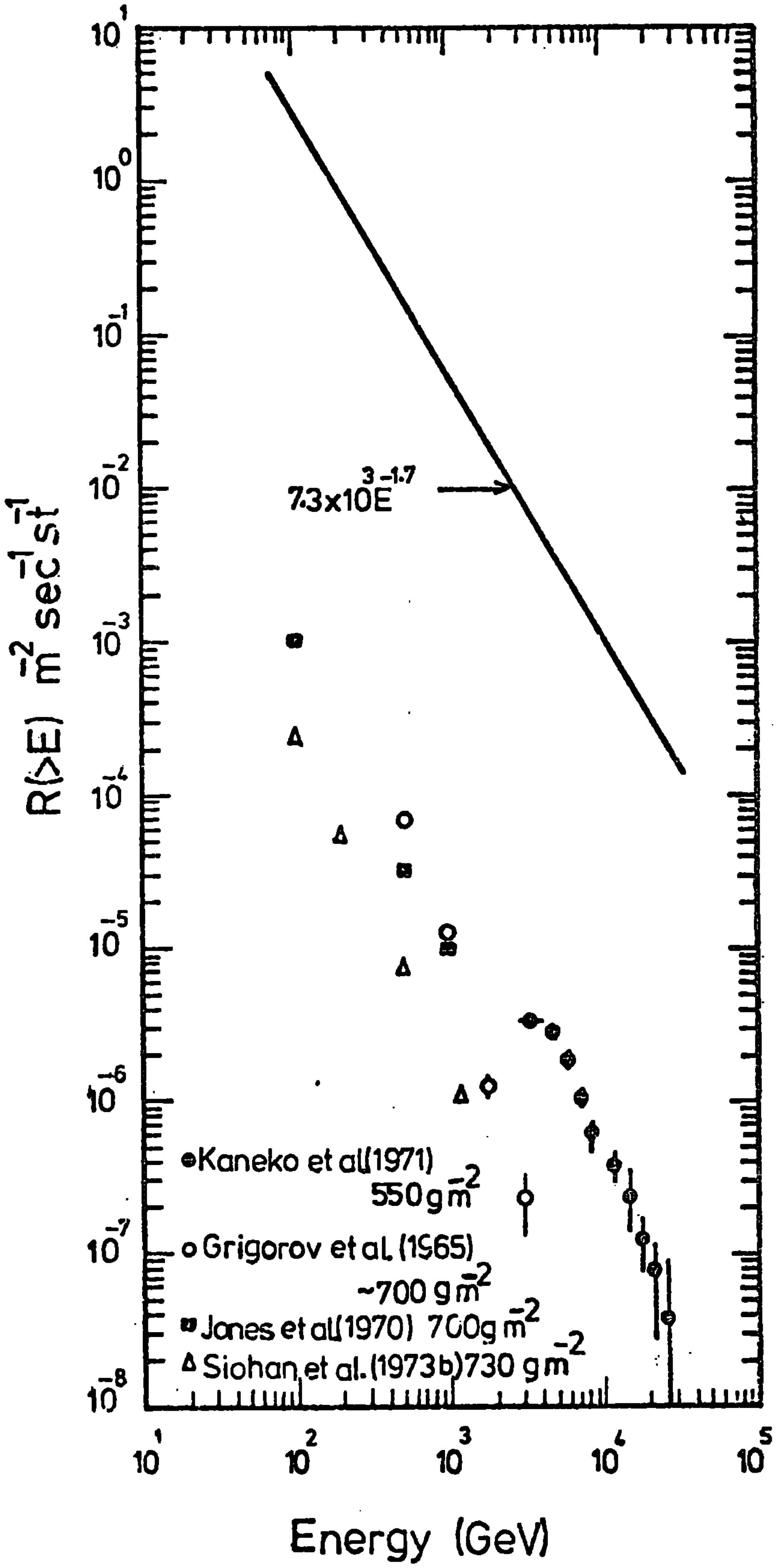

Figure 9.1 Integral hadron spectrum R(> E,X). The upper line for X = 0 corresponds to the primary spectrum of protons given by Ryan et al. (1972). The lower points corresponds to unaccompanied hadron spectra as measured at different depths in the atmosphere. The difference between the upper and lower curves is a measure of the interaction length of protons in air,(after G.Yodh,1972).

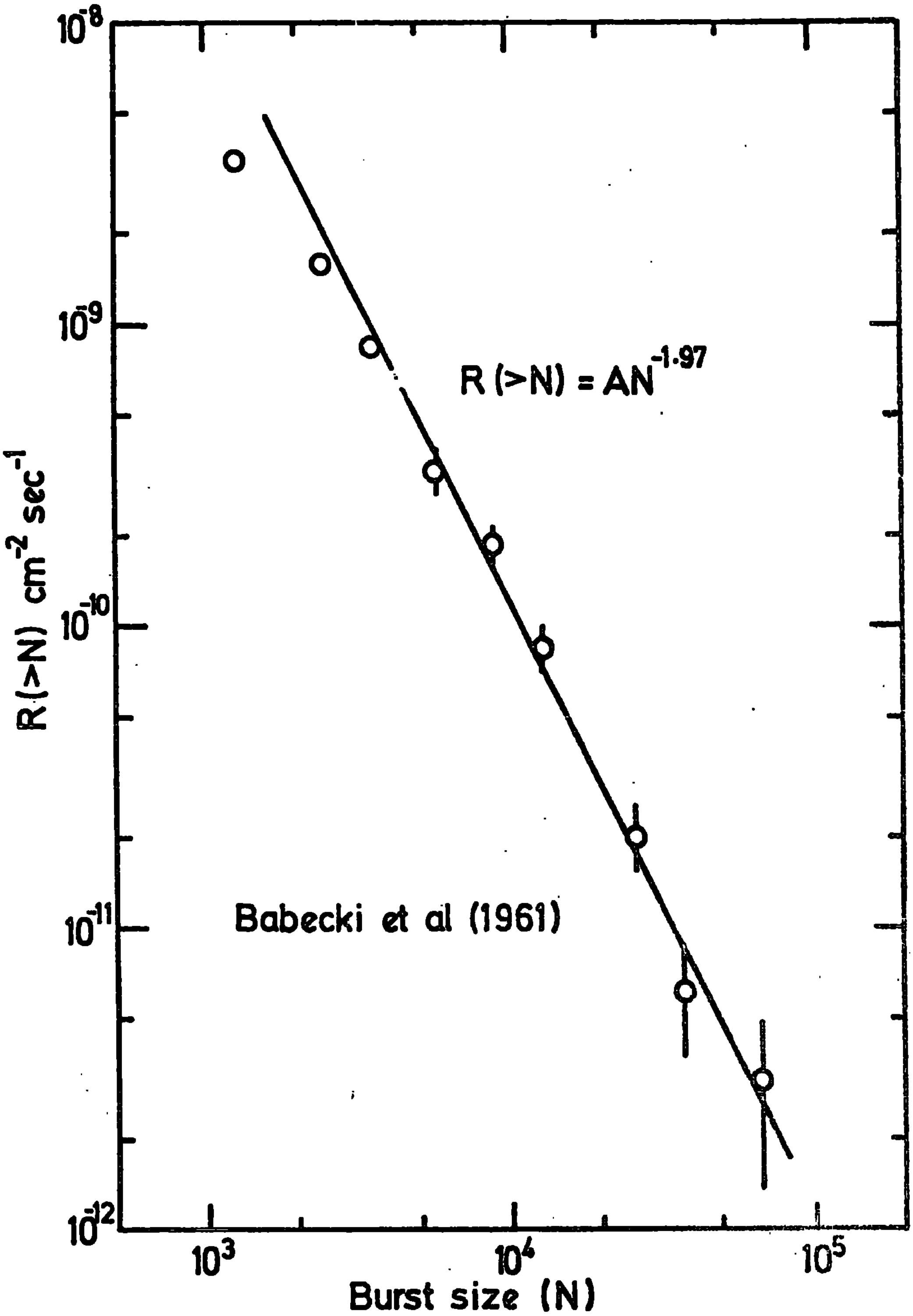

Figure 9.? The integral burst spectrum from single hadrons at ?/?

9.2.5 Babecki et al. 1961

The energy spectrum of hadrons in the energy range $10^{12} - 10^{13}$ ev was measured, using an array constructed of four rows of ionization chambers between which were lead and graphite filters of different thickness. The events were recorded if the total ionization was greater than the threshold simultaneously, in each of any two of the layers of ionization chambers. They found the integral burst spectrum with exponent -1.9 ± 0.03. The result is shown in figure 9.2.

9.2.6 Brooke and Wolfendale, (1964)

The momentum spectrum of Cosmic ray protons in the range 0.6 to 150 Gev/c was measured by a magnetic spectrograph. The spectrograph consisted of four measuring levels, two above and two below the magnet and the deflections. The momenta of the triggering particles were determined by the interaction of their trajectories with the four levels. In figure 9.3 the measured differential vertical momentum spectrum of protons is shown.

9.2.7 Brooke et al (1964)

The same apparatus used by Brooke and Wolfendale for the measurement of momentum spectrum of protons, was used to measure the momentum spectrum of π^- in the vertical direction in conjunction with a neutron monitor. Pions were detected by means of their interaction and subsequent neutron production in the monitor. The ratio between positive and negative pions is assumed to be unity. In figure 9.4 the result of the experiment is shown.

9.2.8 Diggory et al (1974)

The vertical energy spectrum of pions was measured by this group at sea level using a spectrograph with the same construction as the one used by Brook and Wolfendale. The result is compatible with the results of Brook and Wolfendale. The result can be seen in figure 9.4 that is

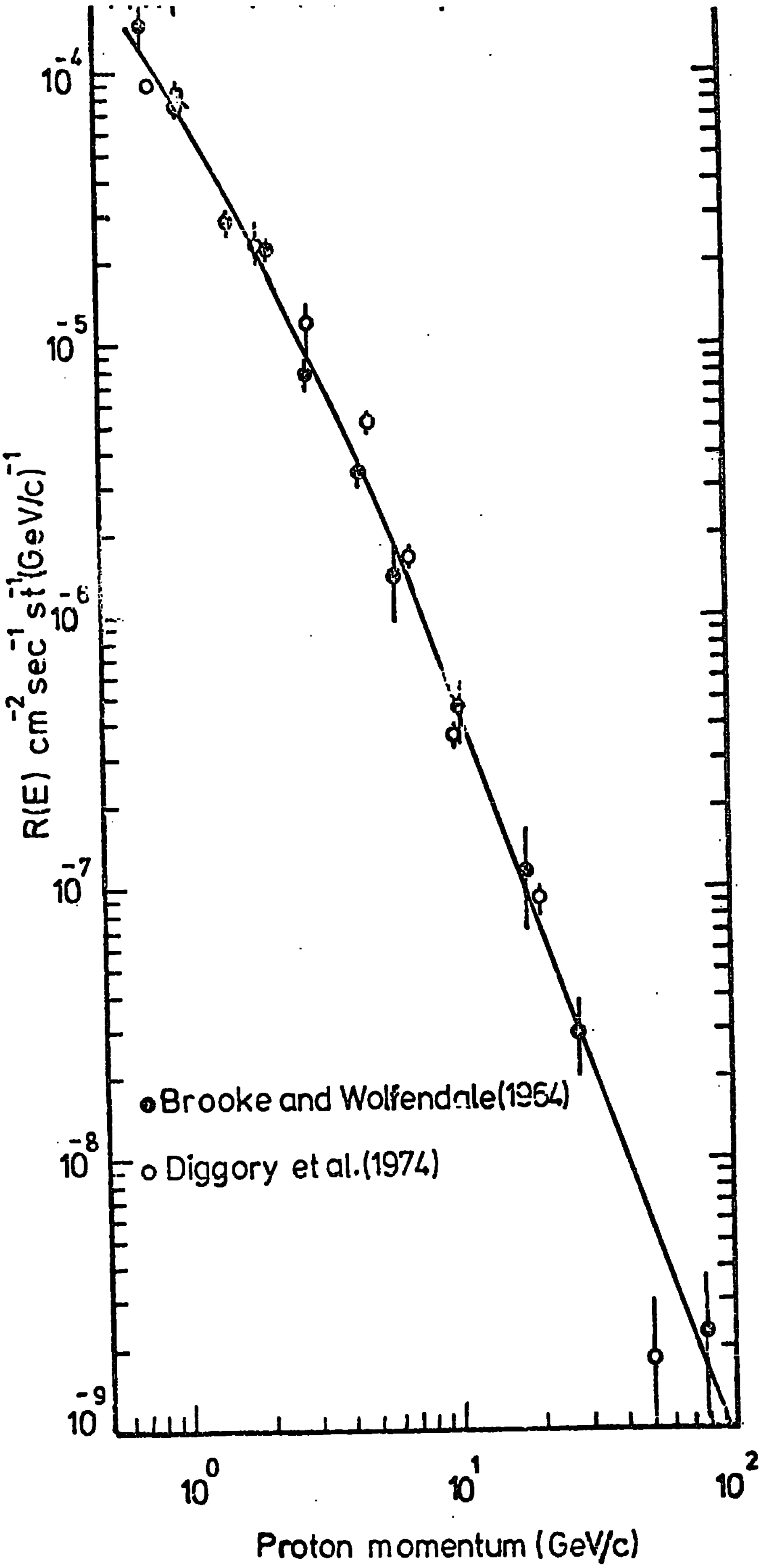

Figure 2.5 The vertical momentum spectrum of single protons at sea level.

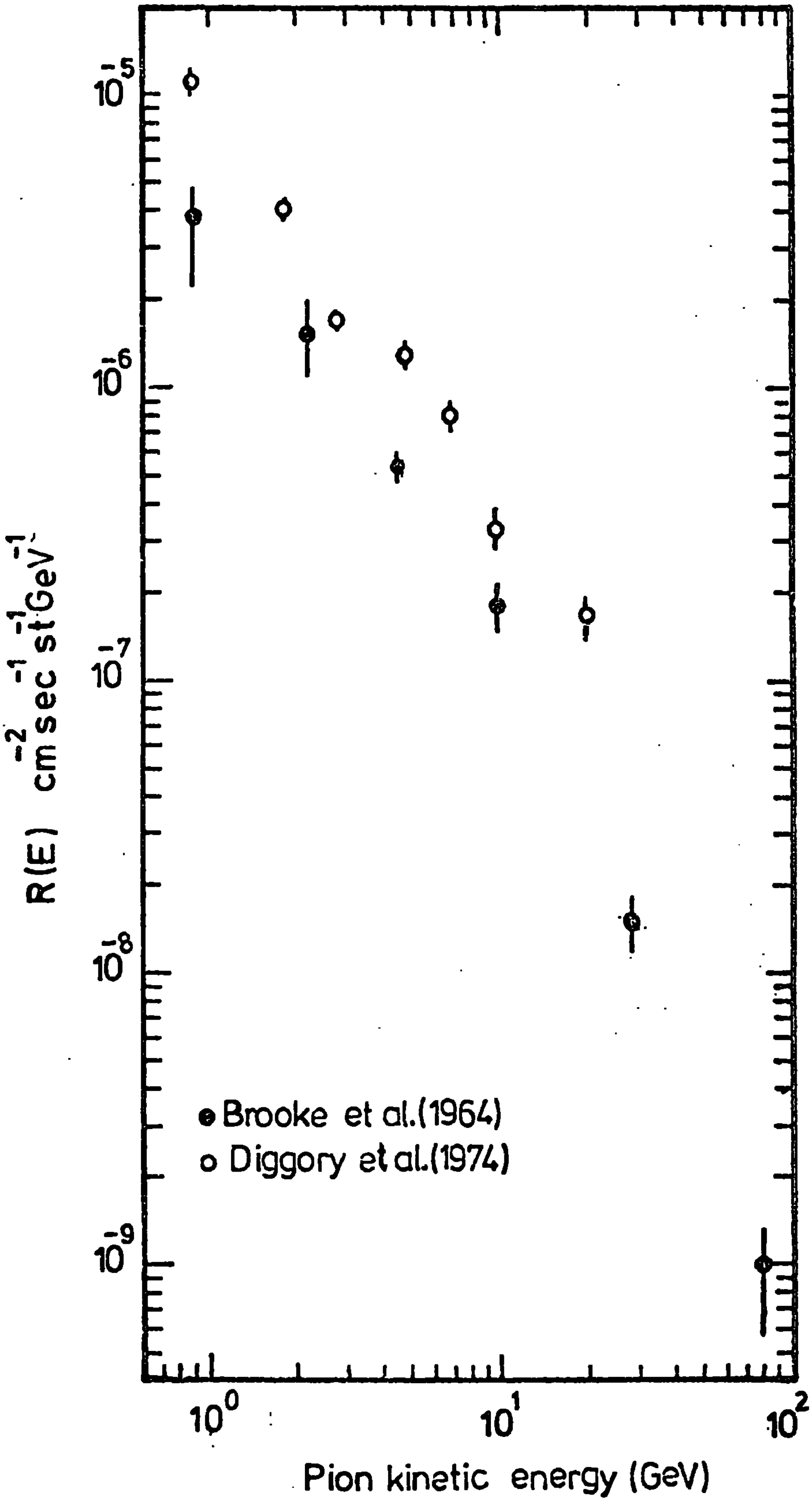

Figure 9.4

The vertical differential energy spectrum of pions ($\pi^{\pm}$) at sea level.

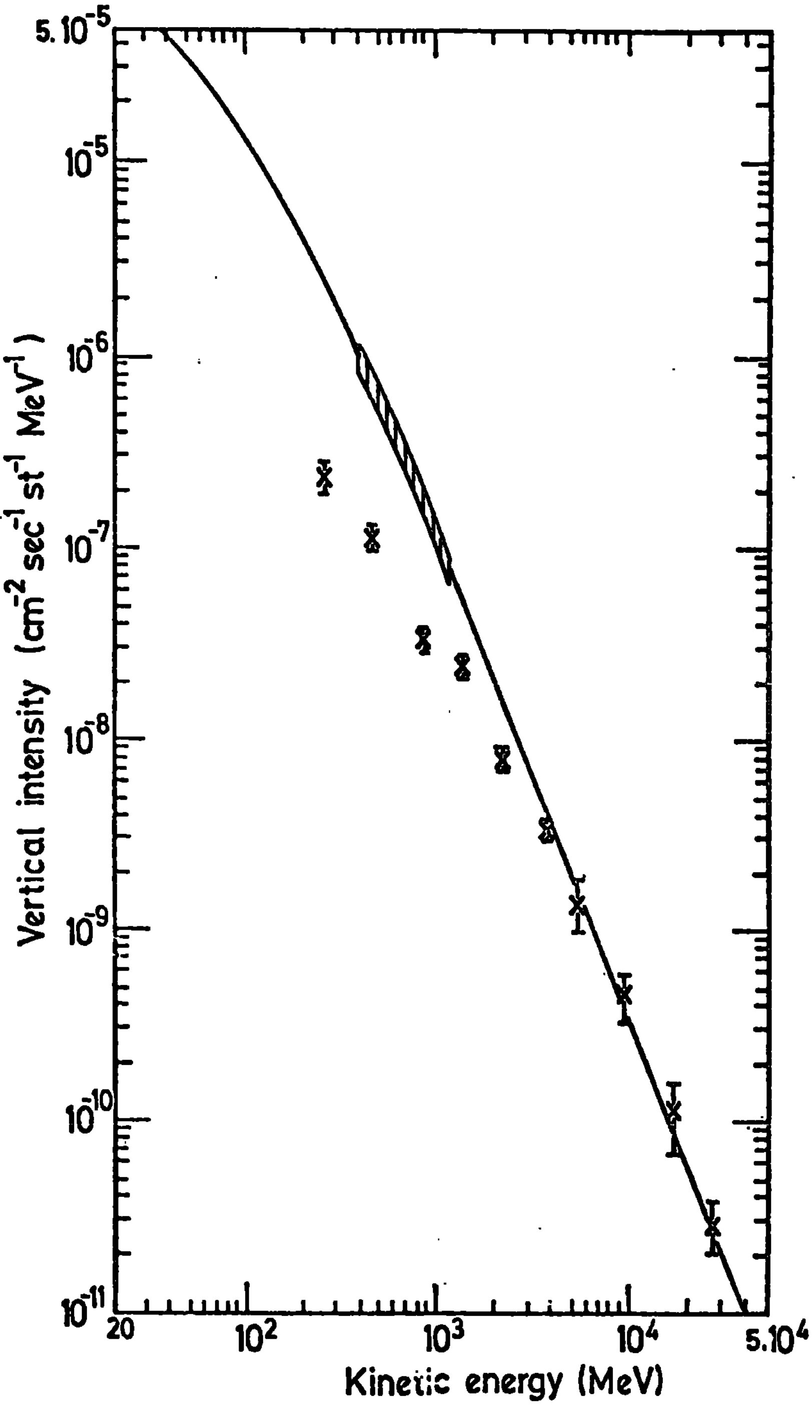

Figure 9.5 Summary of the sea level vertical neutron and proton spectra. The full ine is the vertical neutron ~~neutron~~ spectrum calculated from global spectrum given by Hughes and Marsden (1966). The crosses are proton measurements of Brooke and Wolfendale (1964) and the hatched area is the vertical neutron spectrum given by Ashton et al. (1971b). After Ashton (1973).

compared with the results of Brooke et al.

9.2.9 Ashton (1973)

The energy spectrum of neutrons in the region 0.4 - 1.2 Gev (1971a) has been measured using the charge exchange reaction n+p → P+n.

In figure 9.5 the result of the low energy neutron spectrum is plotted and compared with the other results. At higher energies (>20 Gev) the neutron energy spectrum has been measured from the burst spectrum produced by neutral primary particles in a thick steel target (1970). The vertical differential energy spectrum is plotted in figure 9.5. It can be seen that in the region 50 - 1000 Gev the spectrum can be represented by $N(E) = AE^{-\gamma}$ with the exponent $\gamma = 2.95 \pm 0.1$.

9.2.10 Cowan and Matthews (1971)

The energy spectrum of unaccompanied hadrons and a study of hadron interaction was carried out using an ionization calorimeter together with nine cloud chambers operated at 250 m above sea level. The energy spectra of pions and protons have been calculated from the measured charged spectrum using the neutral to charge ration 0.9. Figure 9.6 shows the energy spectrum of charged hadrons.

9.2.11 Dmitriev et al (1960)

A study of hadronic component was carried out by this group using ionisation chamber. During the operation time, 1,3000 hours 948 burst were registered each corresponding to the passage of 1000 relativistic particles. The energy spectrum of the hadrons is shown in figure 9.6.

9.2.12 Siohan et al(1973)

The energy spectrum of charged hadrons was measured using an ionization calorimeter. A Monte Carlo simulation for the calorimeter was used to obtain the energy of primary incident hadrons from the equivalent muons. The measured vertical spectrum of hadrons in the energy range 350 - 1,000 Gev is shown in figure 9.6.

9.2.13 G.B. Yodh 1974

The differential energy spectrum of high energy hadrons at sea level, using an ionization calorimeter has been measured (Private Communication) in the energy range 1 Tev to 6 Tev (figure 9.6).

9.3 The present basic experimental results

The recording of the events has been by photography such as a particle interacted in the lead or iron targets, producing a burst ≥ 400 particles, the apparatus was triggered. The pulse from the scintillators under the lead and iron was photographed. The front view of the chamber was also photographed. The scintillator pulses give the burst size and the chamber photograph shows the geometry of the burst. The experiment has been in operation for 2704 hours. The triggering level and the time delay remained unchanged. The acceptable events were those having pulse height information. The axis of the burst also had to be locatable within the defined criteria (see figure 9.12) with a projected zenith angle $\leq 30^{\circ}$.

The limit on the projected zenith angle was imposed in order to exclude side events produced in the walls of the chamber by high energy muons. Table 9.1 shows the general information about the experiment. In table 9.2 the basic experimental result is shown. In table 9.3 the present basic result is compared with the previous work (Ashton and Saleh 1975b).

Scintillator	Scope sensitivity mv/cm	Trigger level ($\geq$ N) particles	Single particle pulse height (m.v.)	Voltage of photo-Multiplier Power supply (K.V.)
C	500	≥ 400 particles	.28	.8
A	500	≥ 400	.28	.8

Table 9.1 General information about the experiment.

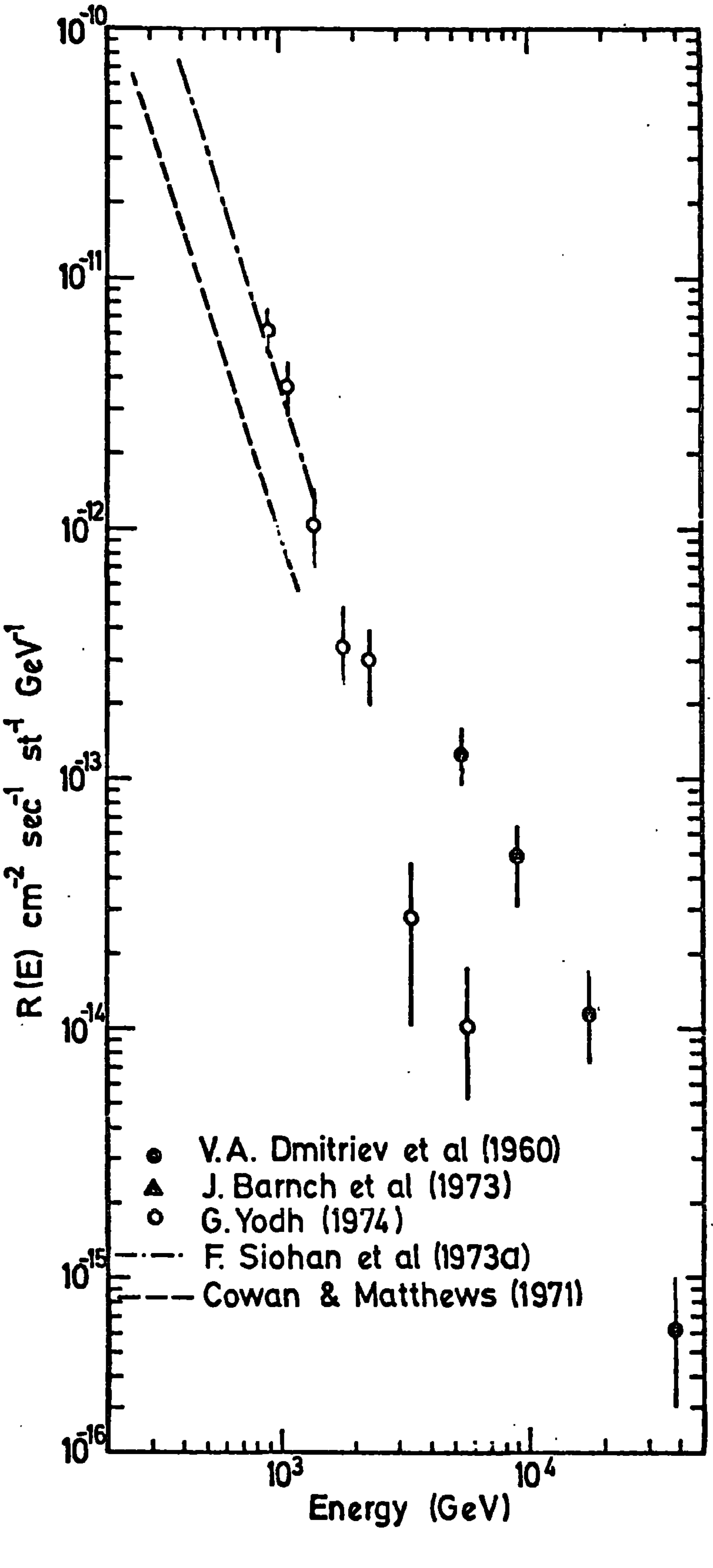

Figure 9.6 Summary of the sea level vertical high energy hadron spectrum.

Trigger level (equivalent muons)		400 particles
Time delay of high voltage pulse		330 μs
Running time		2,704 hours
Total number of triggers		1,500
Number of bursts within $\pm 30^{\circ}$ to the vertical and in acceptance geometry with a burst of size $\geq$ 400 particles observed under the lead or iron	lead	246
	iron	493
Number of bursts within $\pm 30^{\circ}$ to the vertical and in acceptance geometry produced by an initial interaction in the lead or iron determined from the flash tube information	lead	478
	iron	261
n in $I(\theta) = I(0) \cos^{n}\theta$	lead	7.0 ± 2.0
	iron	8.5 ± 1.5
Total aperture for bursts from lead		$.53 m^2 st$
Total aperture for bursts from iron		$.52 m^2 st$
Ratio of number of bursts starting in lead to number starting in iron, $\frac{n(Pb)}{n(Fe)}$ determined from flash tubes		$1.83 \pm .14$
Expected $\frac{n(Pb)}{n(Fe)}$ assuming bursts produced by hadrons	nucleons	2.17
	pions	2.24

Table 9.2 Basic experimental data

		Previous work (Ashton and Saleh)					present work
Trigger level (equi. pts)		≥ 20	≥ 100	≥ 200	≥ 400	≥ 500	≥400
Running time (hour)		0.63	26.35	223.76	176.47	3411.25	2704
Time delay (μs)		20	20	20	330	330	330
Total numbers of triggers		149	173	560	122	1420	1500
Number of bursts within $\pm 30^{\circ}$ to the vertical and in acceptance geometry with a burst of size ≥ 400 particles in the lead or iron	Pb	21	26	101	23	256	246
	Fe	charge 29 neutral 3 total 32	25 7 32	93 8 101	39	356	493
No. of bursts within $\pm 30^{\circ}$ to the vertical and in acceptance geometry produced by an interaction in the lead or iron determined by F/T data	Pb						478
	Fe						261
Assumed n in $I(\theta) = I(o) \cos^{n} \theta$	Pb	6.0 ± 2.5	6.0 ± 2.5	6.0 ± 2.5	8.5 ± 1.5	8.5 ± 1.5	7.0 ± 2.0
	Fe	4.0 ± 2.0	4.0 ± 2.0	4.0 ± 2.0	7.5 ± 1.3	7.5 ± 1.3	8.5 ± 1.5
Total aperture for bursts from iron or lead ($m^2 st$)	Pb	0.64	0.64	0.64	0.54	0.54	0.53
	Fe	0.70	0.70	0.70	0.53	0.53	0.52
$\frac{\text{Pb aperture}}{\text{Fe aperture}}$		0.91	0.91	0.91	1.0	1.0	1.0
Ratio of number of bursts starting in lead to number starting in iron $\frac{n(Pb)}{n(Fe)}$ determined from flash tubes	Scin.	$.66 \pm .18$	$.81 \pm .25$	$1.00 \pm .14$	$.92 \pm .13$	$.59 \pm .15$	$.50 \pm .04$
	F/T						$1.83 \pm .14$
Expected $\frac{n(Pb)}{n(Fe)}$ assuming bursts produced by hadrons	Nucleons	2.00	2.00	2.00	2.17	2.17	2.17
	Pions	2.09	2.09	2.09	2.24	2.24	2.24

Table 9.3 the Comparison of the basic data of the present experiment with the previous work.

It is expected theoretically that over the energy range covered in the present experiment the majority of bursts produced by particles incident with zenith angles $< 50^{o}$ to the vertical are due to hadrons and that only for zenith angles $> 50^{o}$ does the effect of muon electromagnetic interactions become important. This can be tested by measuring the ratio of the number of bursts produced by primary particles that interact in the lead and iron for hadrons at normal incidence this ratio is

$$\frac{n(Pb)}{n(Fe)} = \frac{1 - e^{\frac{-Y_{Pb}}{\lambda_{Pb}}}}{e^{-Y_{Pb}/\lambda_{Pb}} \left(1 - \frac{Y_{Fe}}{\lambda_{Fe}}\right)}$$

where Y_{Pb} and Y_{Fe} are the thickness of the lead and iron and λ_{Pb} and λ_{Fe} are the interaction length of hadrons in lead and iron the ratio is found to be 2.17 and 2.24 for nucleons and pions respectively. The measured ratio of 1.83 ± 0.14 is thus consistent with expectation for hadron initiated bursts.

A further test is to determine the spatial angular distribution of particles producing bursts from the measured projected angular distribution in the front plane using an extension of the method described by Lovati et al (1954). Assuming a spatial zenith angle distribution of the form $I(\theta) = I(o) \cos^{n}\theta$ the best fit values of n found from the data are 7.0 ± 2.0 for bursts originating in the lead and 8.5 ± 1.5 for bursts originating in the iron. Again these values are consistent with expectation for hadron initiated burst.

The basic experimental data in the previous work (Ashton and Saleh 1975b) bursts were classified as occuring in the lead or iron according to whether the burst size under the lead or iron is the larger of the two and not as to whether the initiating interaction occurred in the lead or iron. Accordingly the figures in the table cannot be used to calculate $\frac{n(Pb)}{n(Fe)}$ as indicated in the present experiment and compared with expectation for hadron initiated bursts. However using the flash tube information to determine whether a burst was initiated by a first interaction in the lead or iron, the resulting value of $\frac{n(Pb)}{n(Fe)}$ is found to be consistent with hadron initiated bursts.

Figures 9.7 and 9.8 show the burst size distribution of bursts initiated in lead and iron respectively.

9.4 The angular distribution of hadrons

The projected zenith angle of hadrons has been assumed to be the same as the direction of the axis of the bursts to the vertical. Figures 9.9a and 9.9b shows the projected zenith angle distribution of the hadrons recorded from the front view of the chamber. We had no flash tube information of the bursts in the side plane of the chamber, just a crude estimate of the maximum projected zenith angle of incidence by measuring the axis of the burst from top of F_2 (see figure 6.1) to the point where the bursts left the chamber in the fron view. Figures 9.10 and 9.11 show a crude information of the events in the side plane. Although crude these measurements indicate that the majority of accepted bursts had zenith angle $< 50^{\circ}$ in this plane.

9.5 The chamber acceptance functions

To calculate the differential aperture for bursts produced in the chamber the method of Lovati et al (1954) was used; this has been discussed in chapter 6. The differential aperture of the chamber has been calculated, with n as a parameter, on the basis of the criteria shown in figures 9.12 and 9.13. The result of the calculation is shown in figure 9.14. The acceptance geometry for bursts in the lead and iron is the same. The value of the

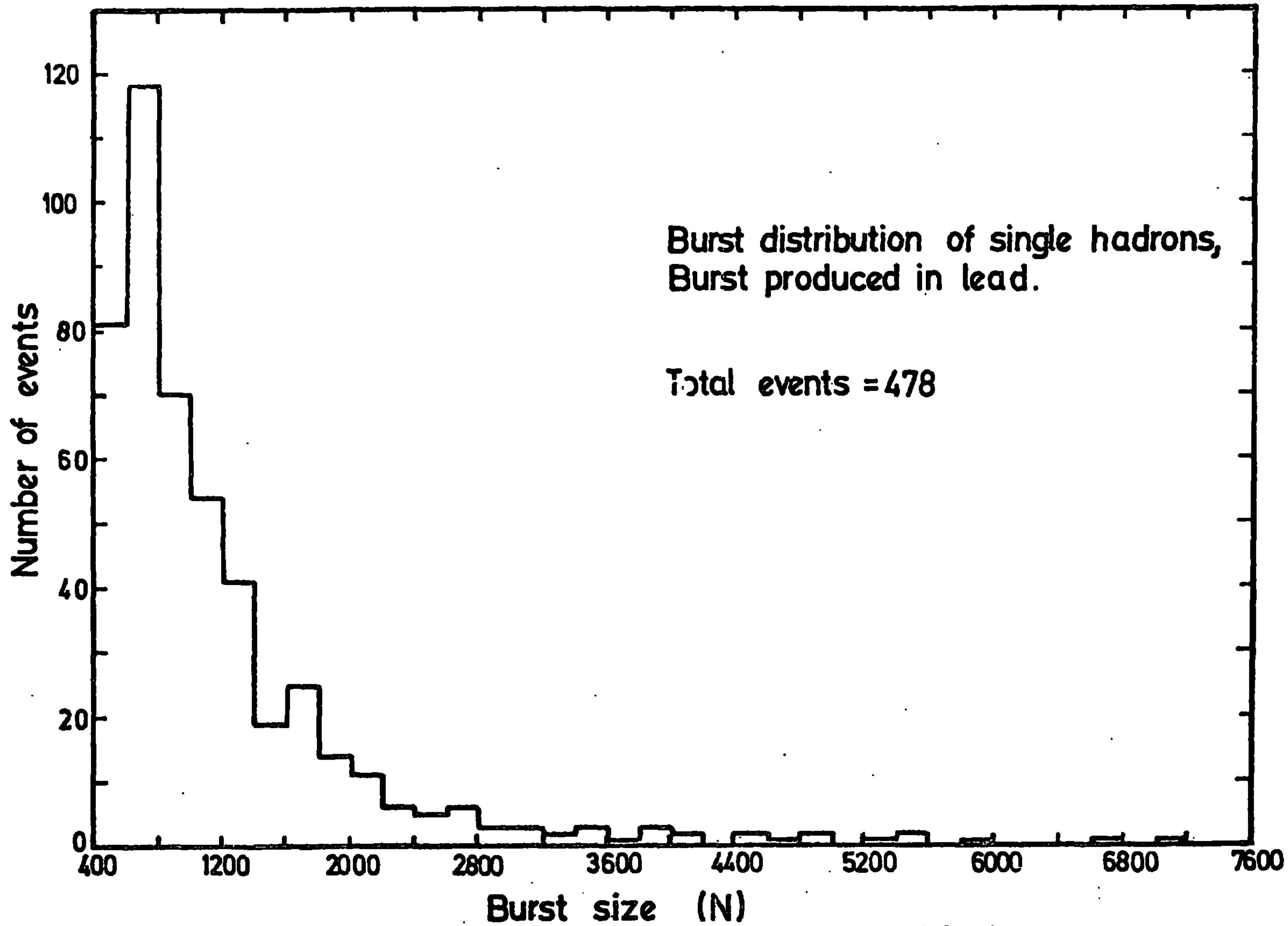

Figure 9.7 The burst size distribution for hadrons interacted in 15cm of lead

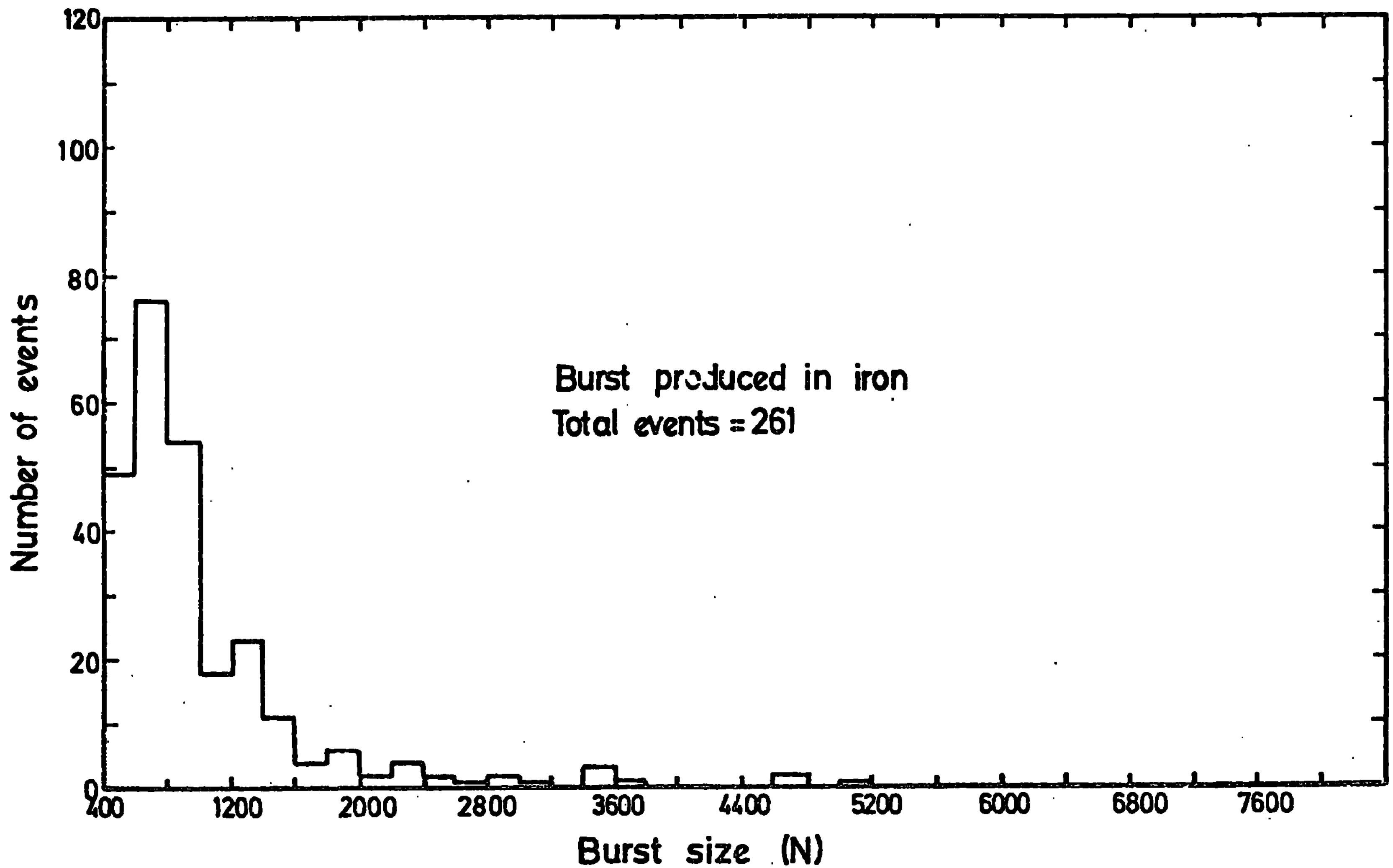

Figure 9.8 The burst size distribution for hadrons interacted in 15cm of iron

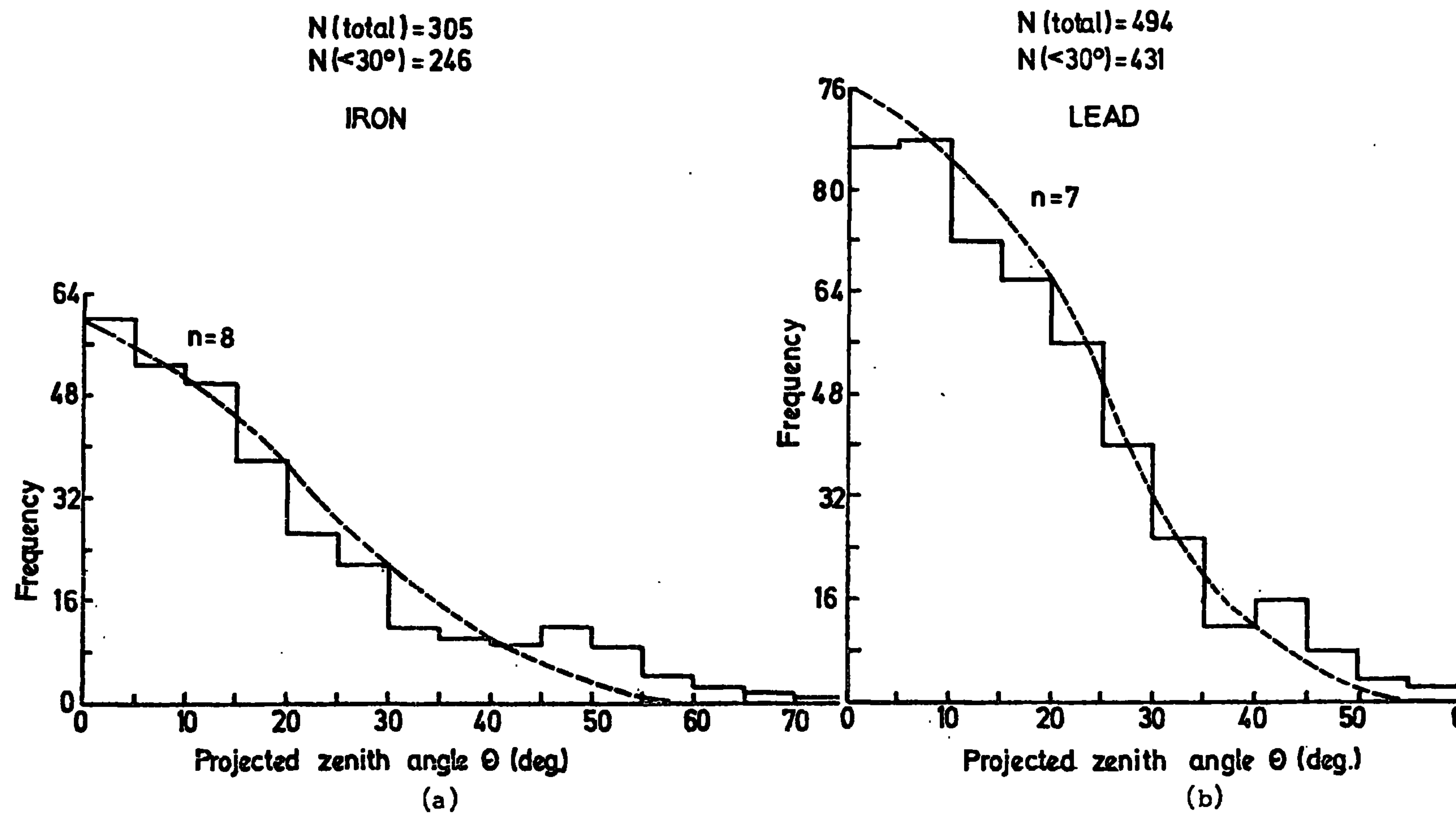

Figure 9.9 The projected zenith angle distribution of bursts observed in iron and lead. The solid distributions are the measured and the dotted are the predicted. The exponent n given by the predicted curves show the best values of n obtained using the minimum - χ^2 fit.

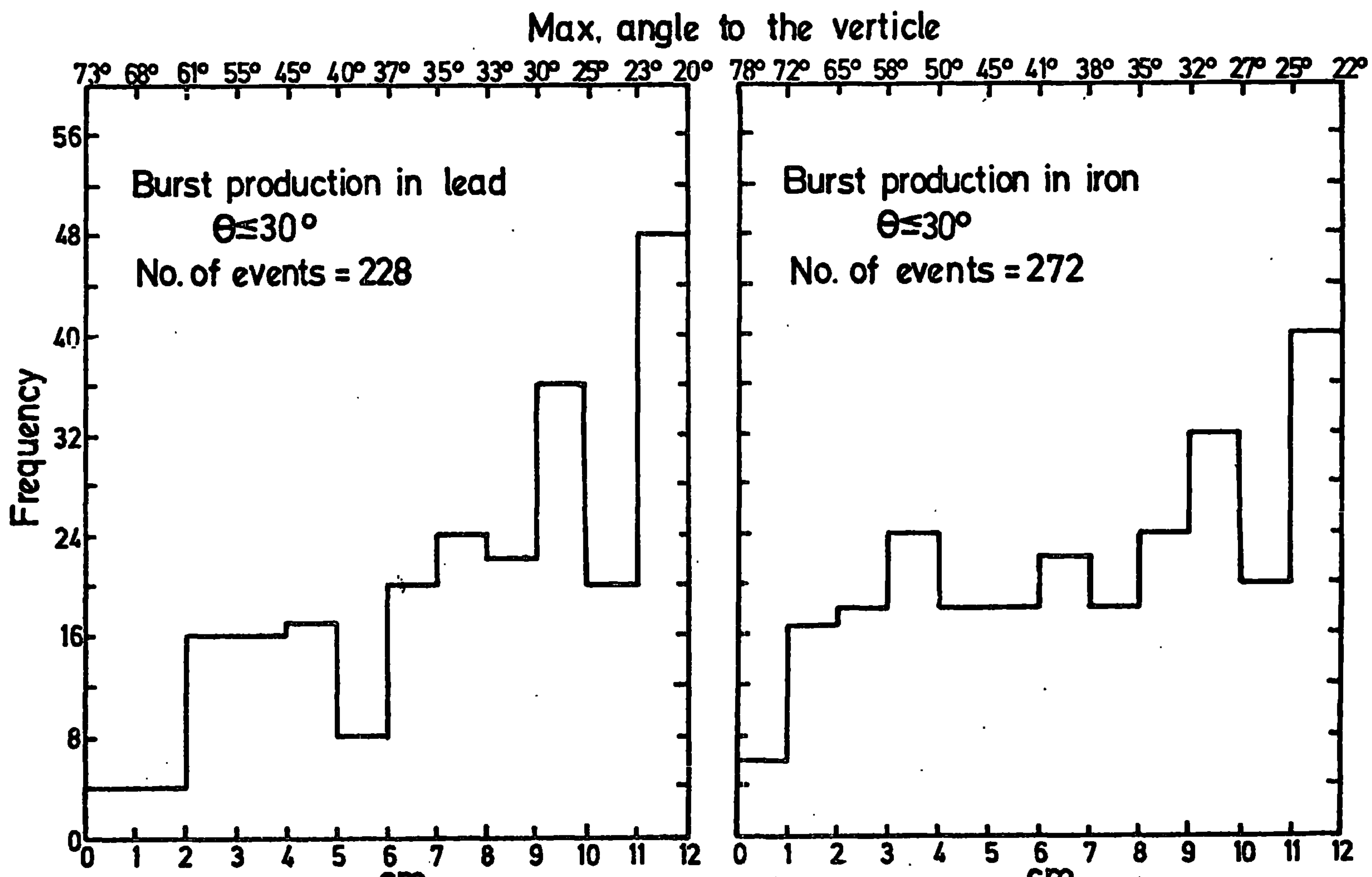

Figure 9.10

Distance from top of F_2 to the point where the burst left the chamber in the front view.

The distribution of the distance from top of F_2 (see figure 6.1) to the point where the burst left the chamber in the front view, for the hadrons with projected zenith angle, $\theta \leq 30^{\circ}$ to the vertical interacted in lead or iron (1 unit = 20 cm)

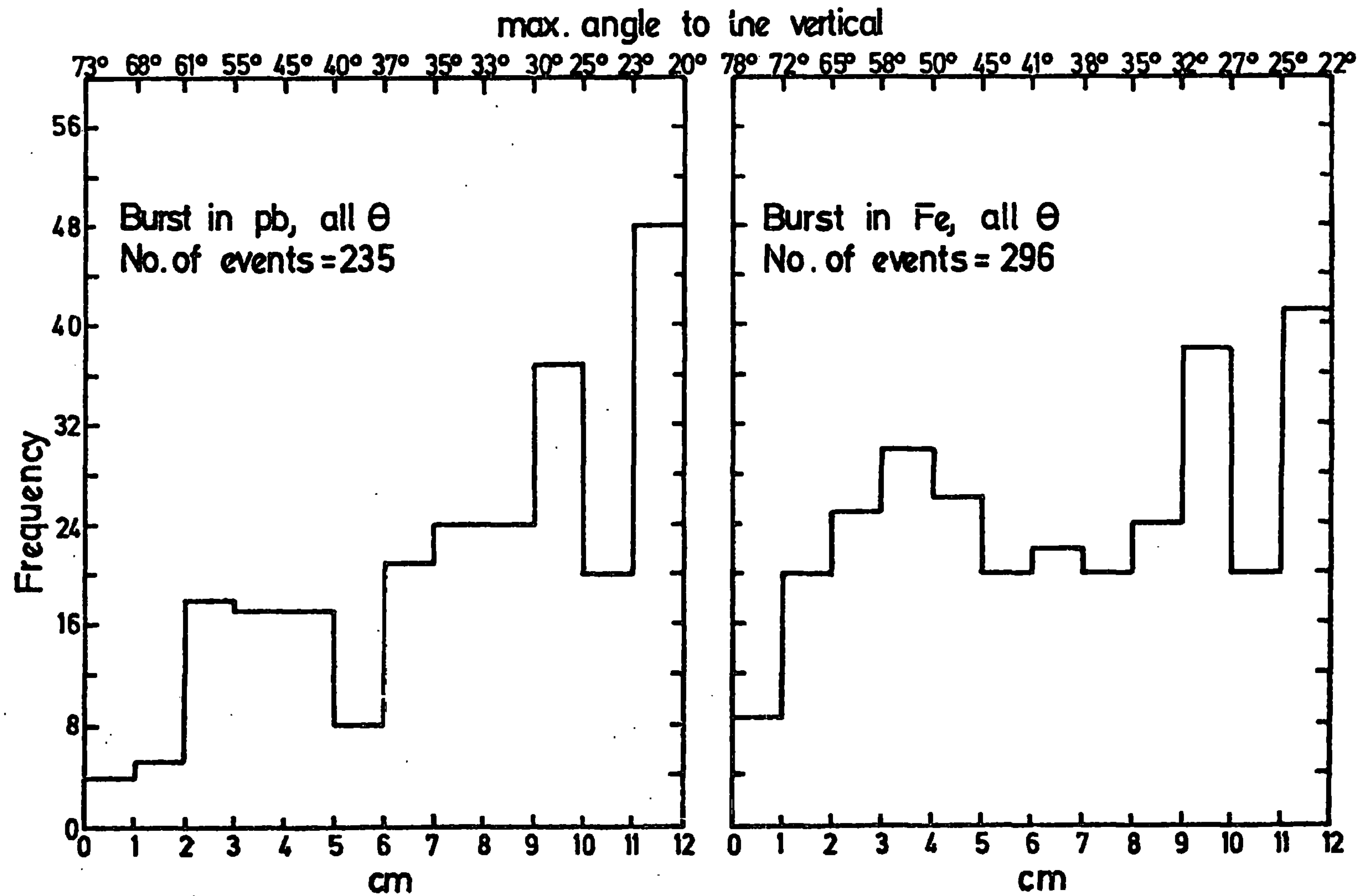

Figure 9.11 Distance from top of F_2 to the point where the burst leaves the chamber in the front view

The distribution of the distance from top of F_2 (see figure 6.1) to the point where the burst left the chamber in the front view, for the hadrons with projected zenith angle, $\theta \geq 0^o$ to the vertical (1 unit = 20 cm)

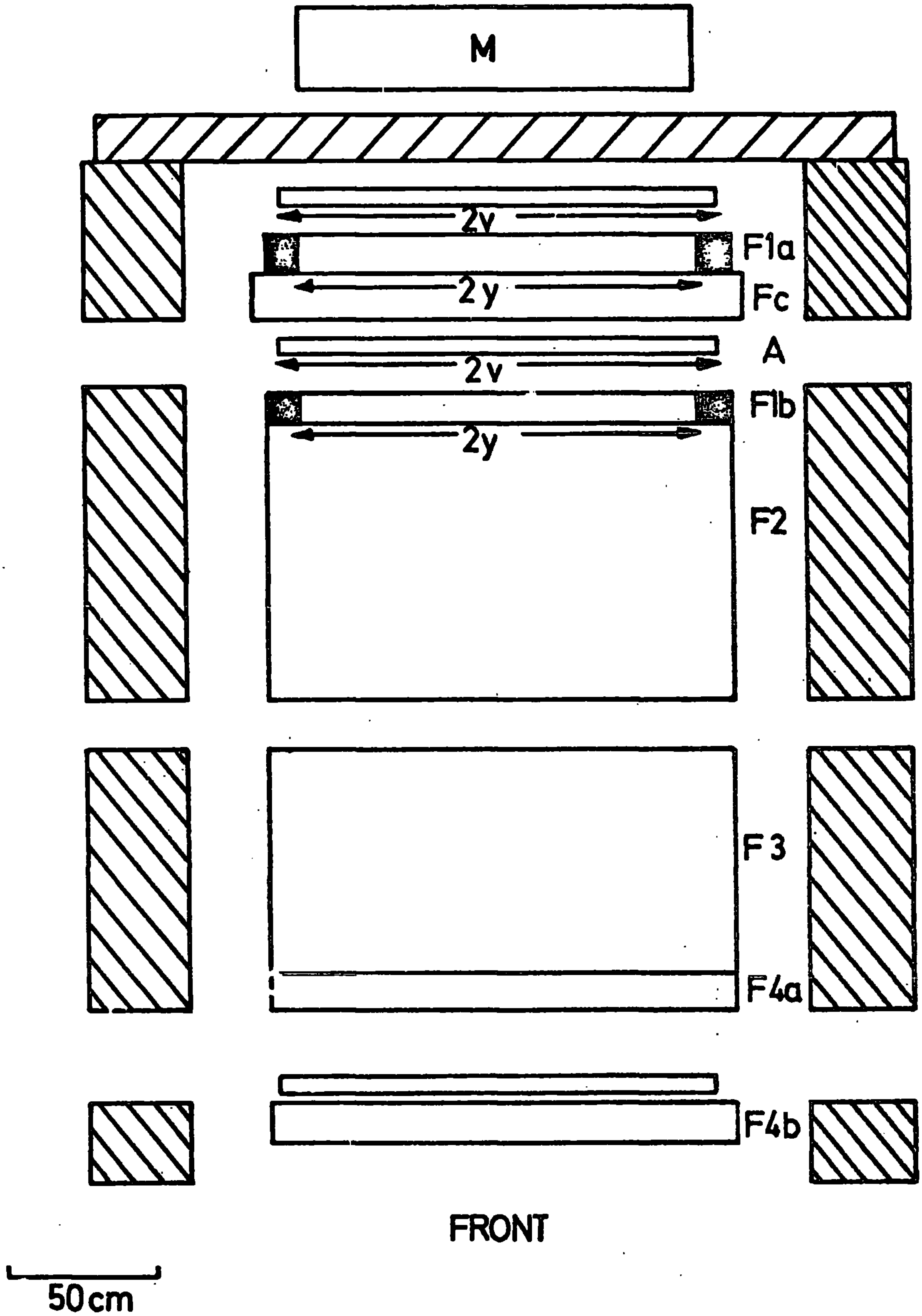

Figure 9.12 Scale diagram of the front of the flash tube chamber showing the restricted acceptance geometry for bursts in lead and iron. To be accepted, the core of the burst must lie between, but not in the dark areas.

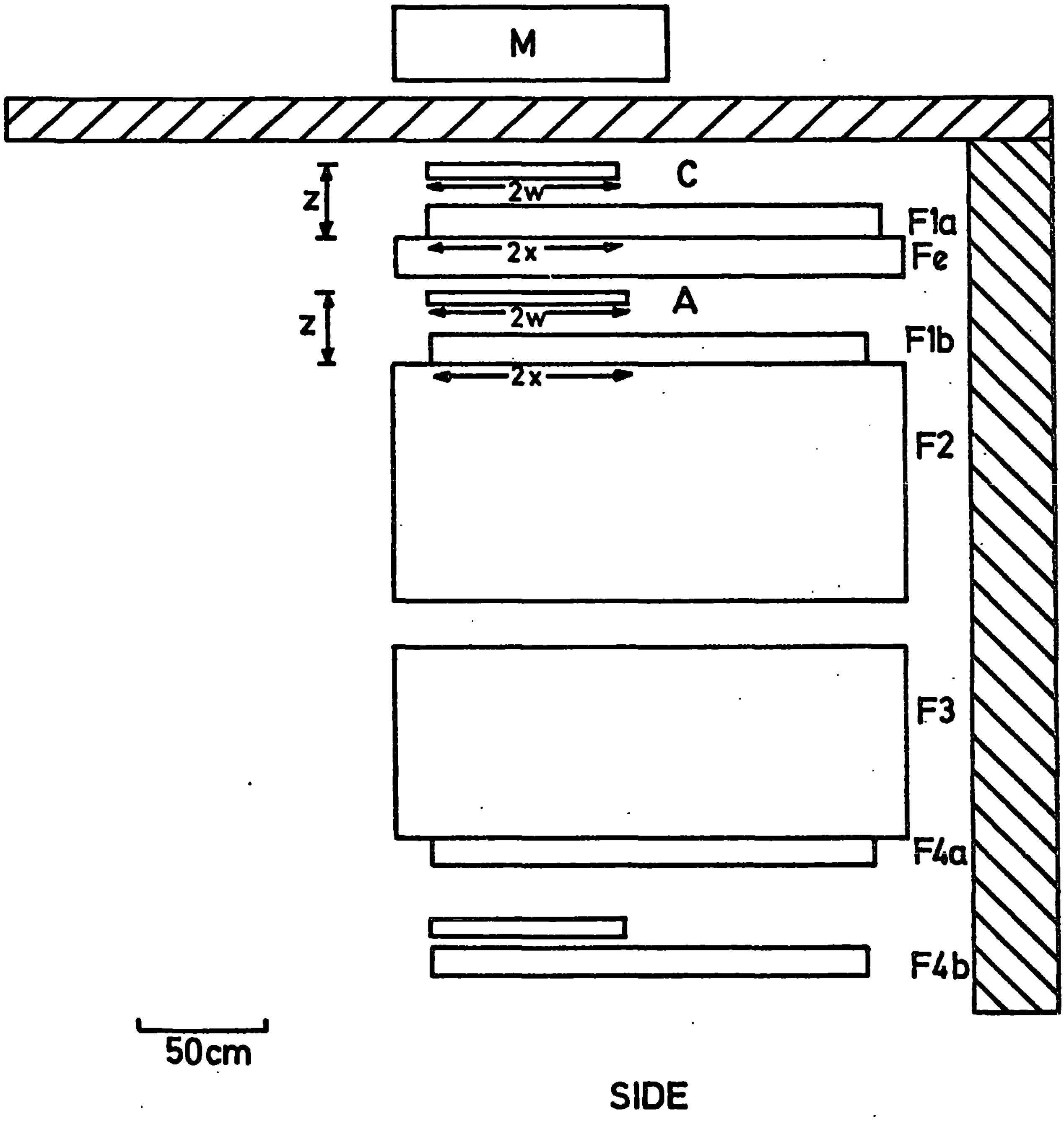

Figure 9.13 Scale diagram of the side of the chamber showing the restricted acceptance geometry for bursts produced in the lead and iron.

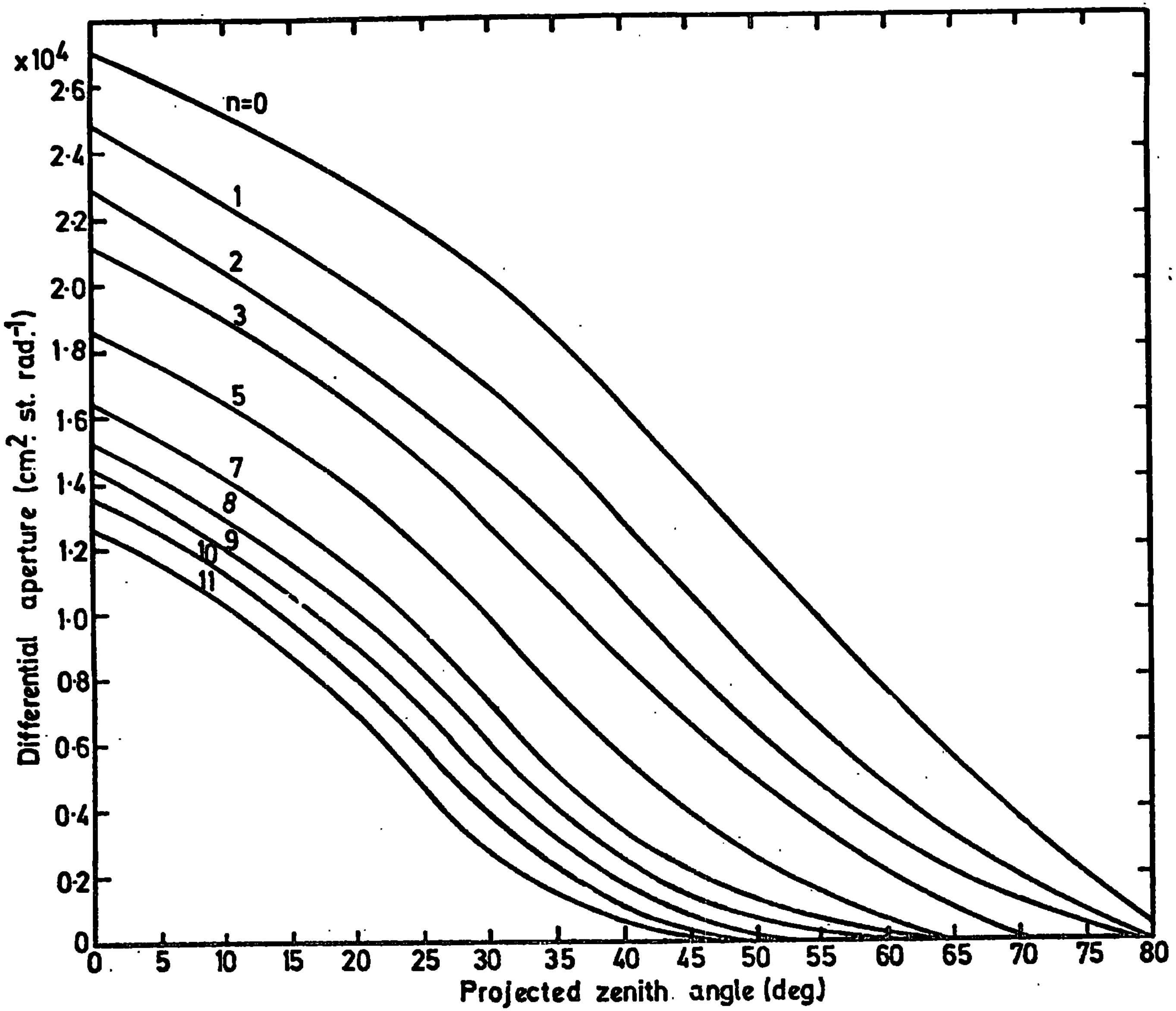

Figure 9.14 The chamber acceptance functions with n as parameter for burst produced in lead. and iron.

exponent, n was determined from the calculated angular distribution and observed projected angular distribution by a minimum chi-square (χ^2) fit. n was found 7.0 ± 2.0 and 8.5 ± 1.5 in lead and iron respectively.

9.6 The measured hadron energy spectrum

Using the measured differential burst spectra detected by the scintillators under the lead and iron in the present experiment and also knowing whether a burst observed under the iron was initiated by a first interaction in the lead or iron, in conjunction with the theoretical relation between burst size and energy, two independent estimates have been made of the vertical differential hadron spectrum. These have been averaged, and the final result has been obtained. In figures 9.15 and 9.16 the integral burst spectrum for bursts initiated in lead and iron is shown. In converting the burst spectrum measurements to an estimate of the incident hadron spectrum, the hadrons have been assumed to be nucleons. If charged pions are assumed the energies should be reduced by 0.75. In figure 9.17 the differential energy spectrum of bursts produced in lead and iron is compared. Figure 9.18 and 9.19 show the incident hadron energy spectrum in lead and iron. Figure 9.20 shows the comparison of figure 9.18 and 9.19. In figure 9.21 the final energy spectrum of hadrons is shown, it is seen that the measurements are consistent with previous work. In table 9.4 the probability of proton and pion interacting in different parts of the chamber is recorded.

particle	Lead	Iron	Glass and aluminium electrode
proton	0.55	0.25	0.12
pion	0.53	0.23	0.12

Table 9.4 The probability of interaction of protons and pions in different parts of the chamber.

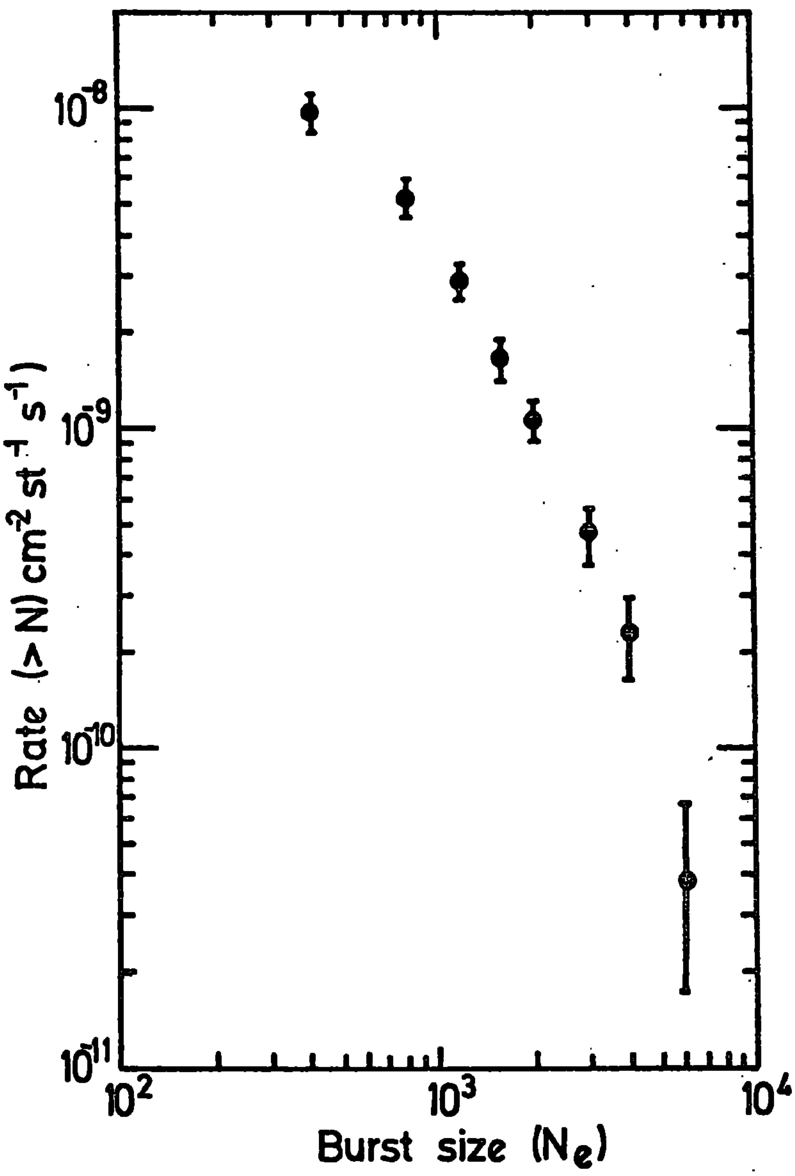

Figure 9.15 The integral burst spectrum of single hadrons interacted in the lead.

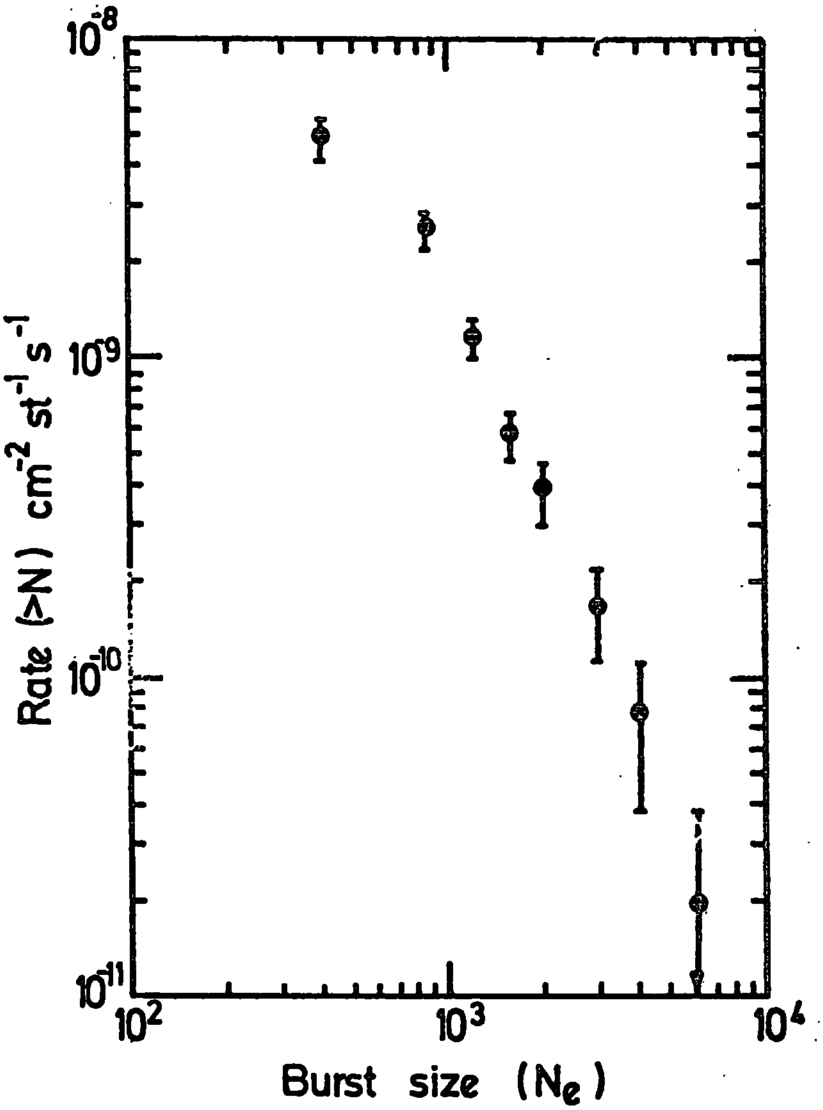

Figure 9.16 The integral burst spectrum of single hadrons interacted in the iron

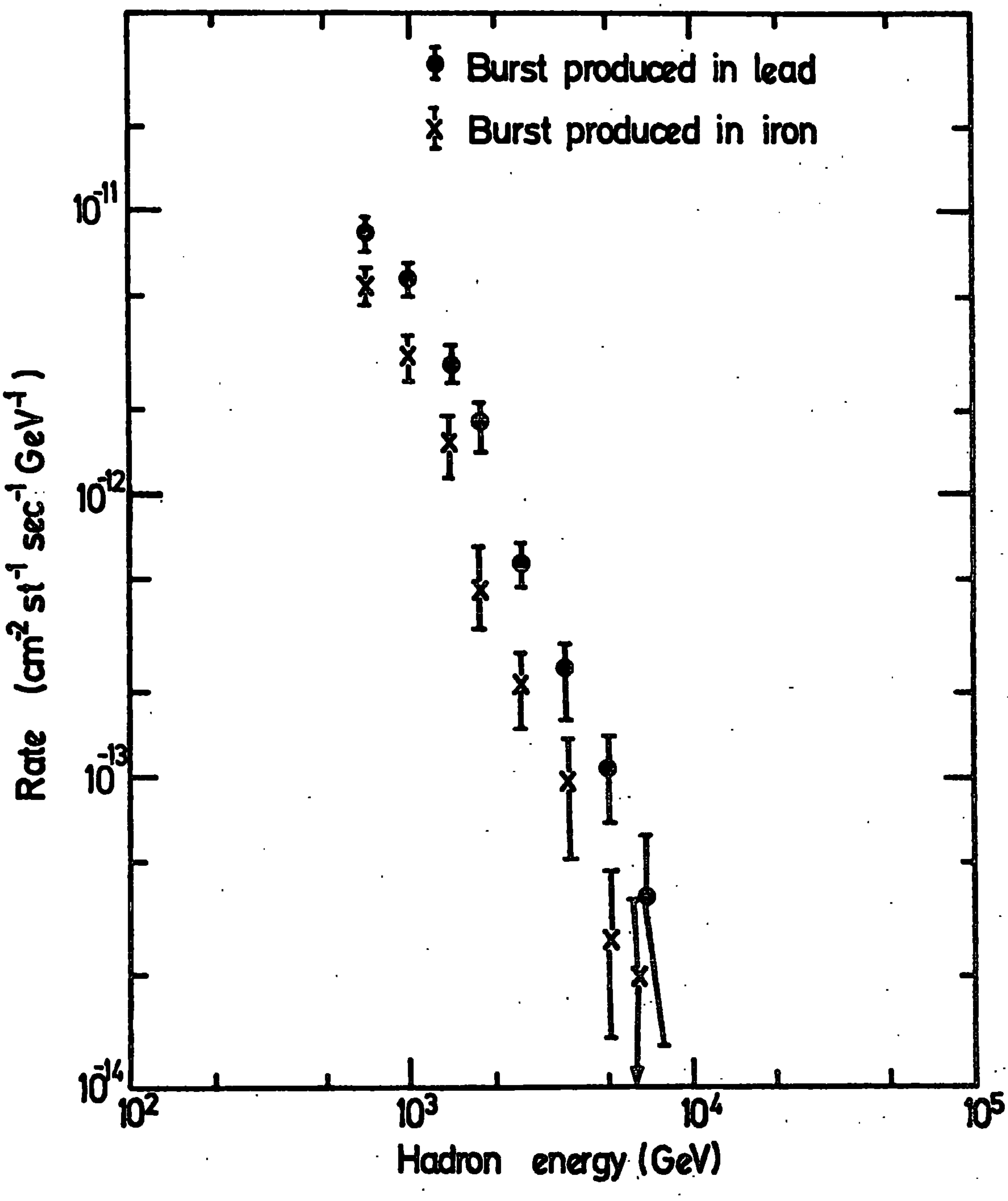

Figure 9.17 The vertical differential energy spectrum of single hadrons interacted in lead (•) and iron (X)

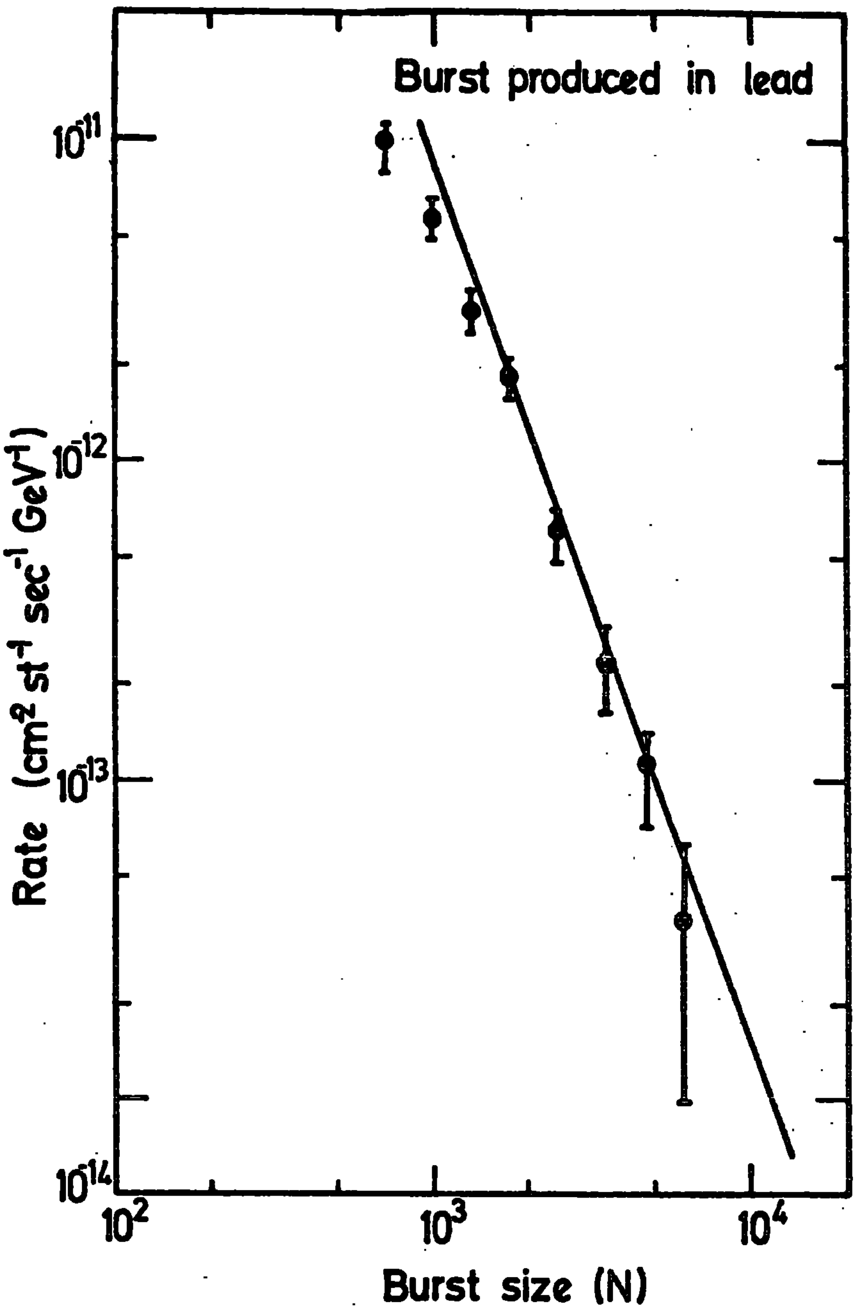

Figure 9.18 The incident differential energy spectrum of hadrons interacted in lead

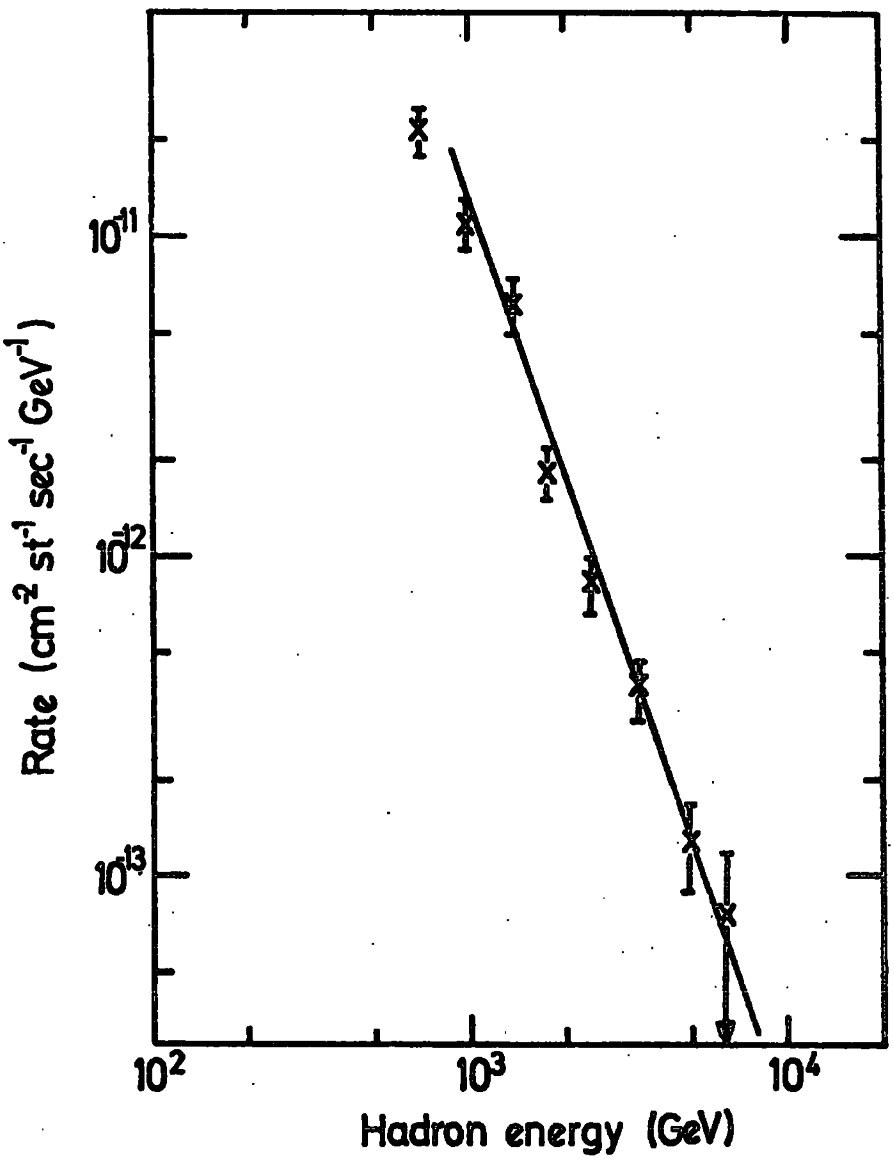

Figure 9.19 The incident hadron energy spectrum of hadrons interacted in the iron

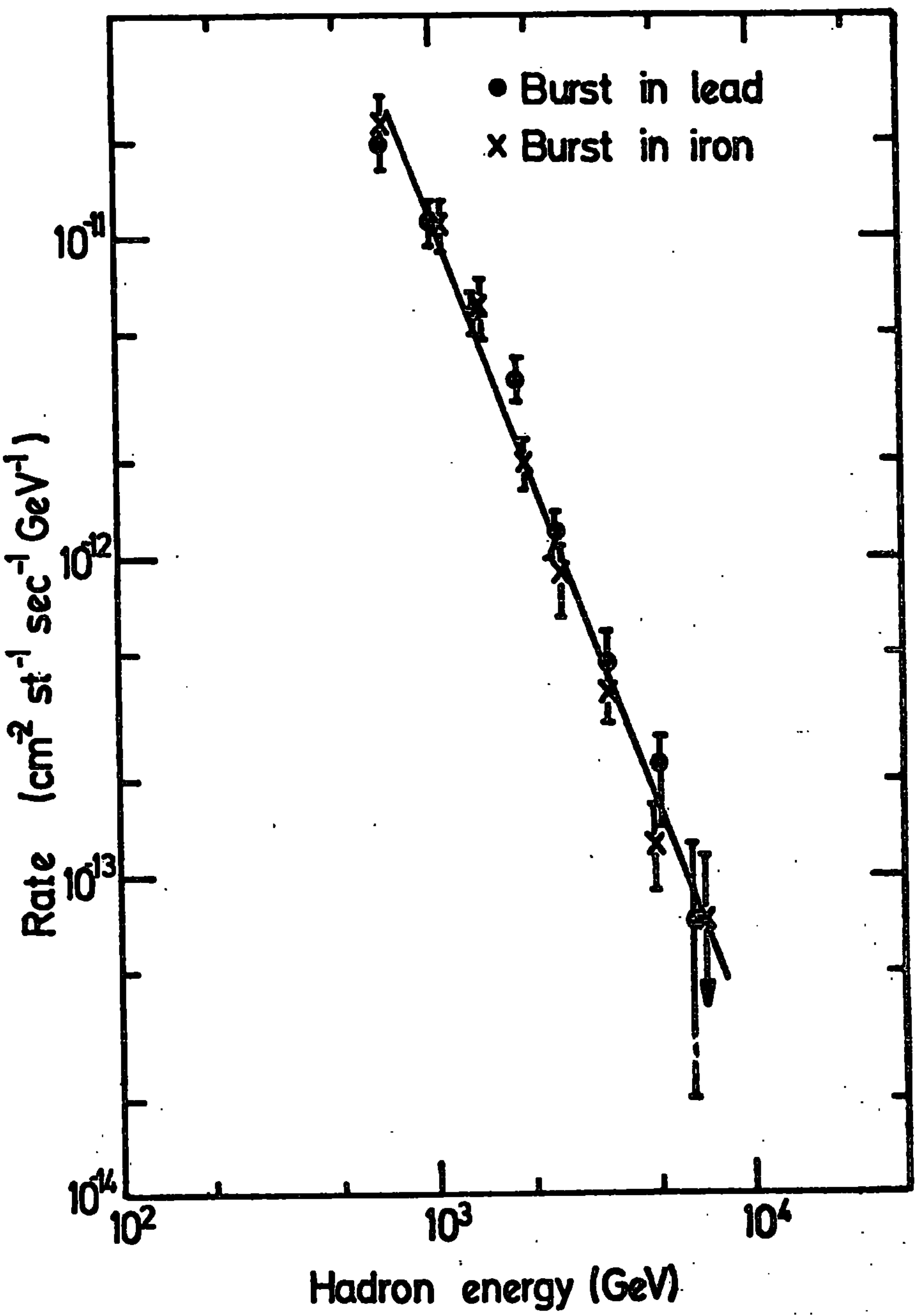

Figure 9.20 The comparison of incident energy spectrum of hadrons interacted in lead (•) and iron (X).

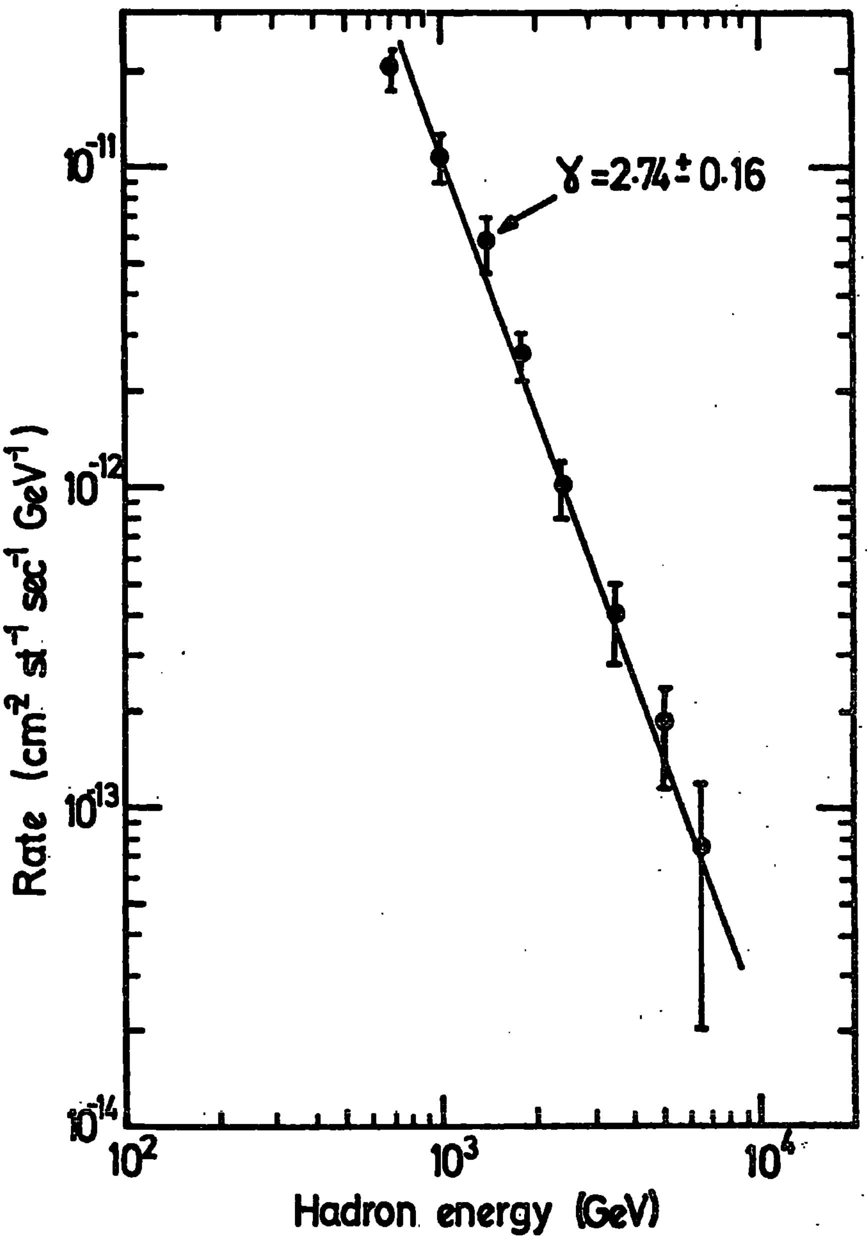

Figure 9.21 The final differential energy spectrum of single hadrons at sea level

9.7 Comparison and conclusion

In figure 9.22 a comparison of the present result with the results of previous experiment (Ashton and Saleh, 1975) and Baruch et al (1975) has been made. It is seen that the hadron energy spectrum is smoothly decreasing in intensity with a slope equal to $2.74 \pm .16$.

It should be noted since the results of Baruch et al reported in Munich Conference claiming a step in the differential energy spectrum between the energy 2 - 8 Tev was withdrawn due to the electronic defect in their experiment the comparison to that result is not made, but it is compared with their recent measurement after eliminating the defect (Baruch et al. v.12 p.4303). The present differential energy spectrum is well represented by: $N(E)dE = A\,E^{-\gamma}\,dE$.
where $\gamma = 2.74 \pm 0.16$ over the whole energy range.

Plates 9.1 and 9.2 show typical hadron interaction in lead and iron.

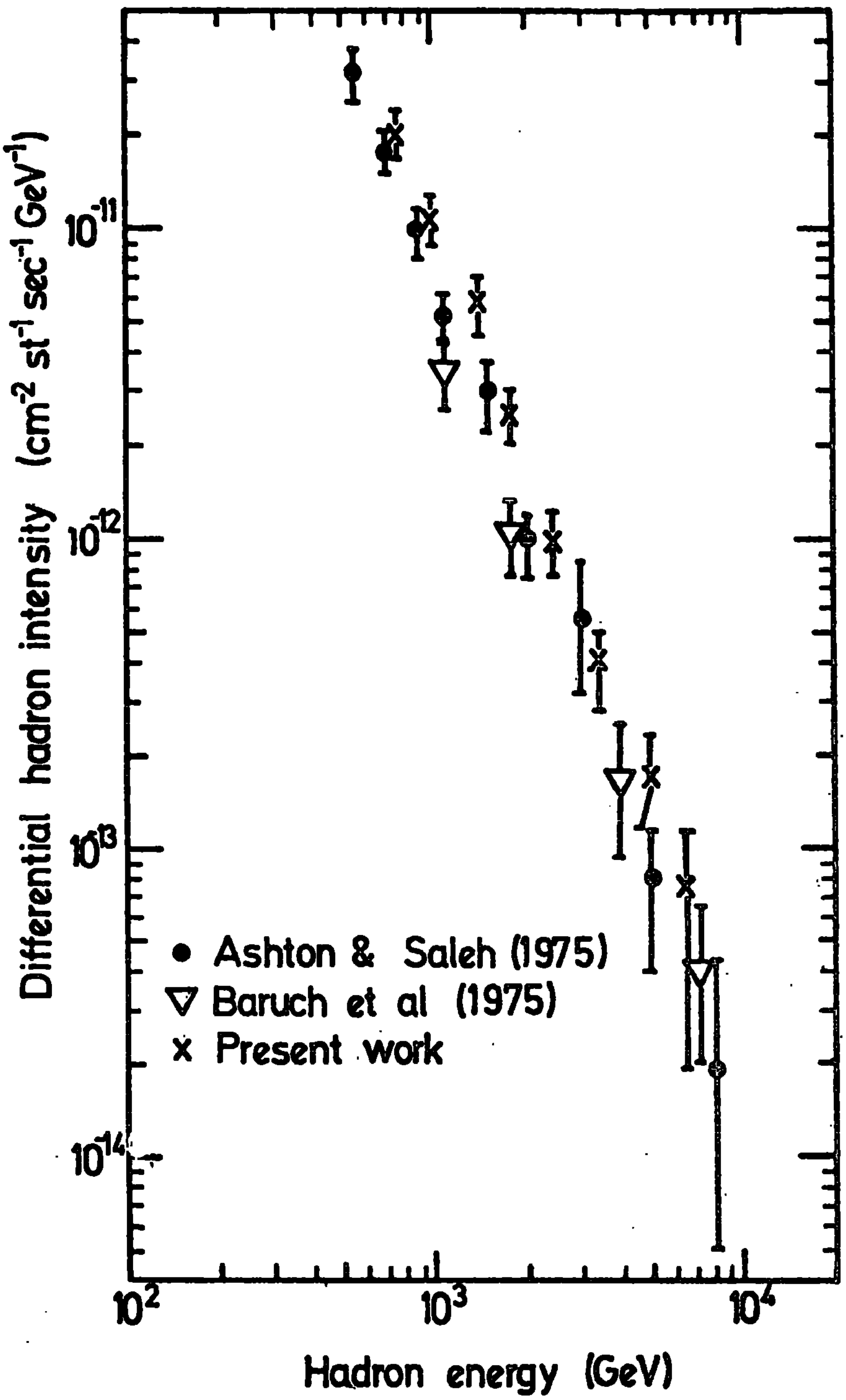

Figure 9.22 The differential energy spectrum of hadrons at sea level, measured by different groups.

PLATE 9.1

Event H115 - 19

A hadron interacted in the lead absorber producing a burst of size 4000 particles. The Track observed in F_2 is either a background muon or a highly ionizing particle initiated the burst observed in F_{1a}

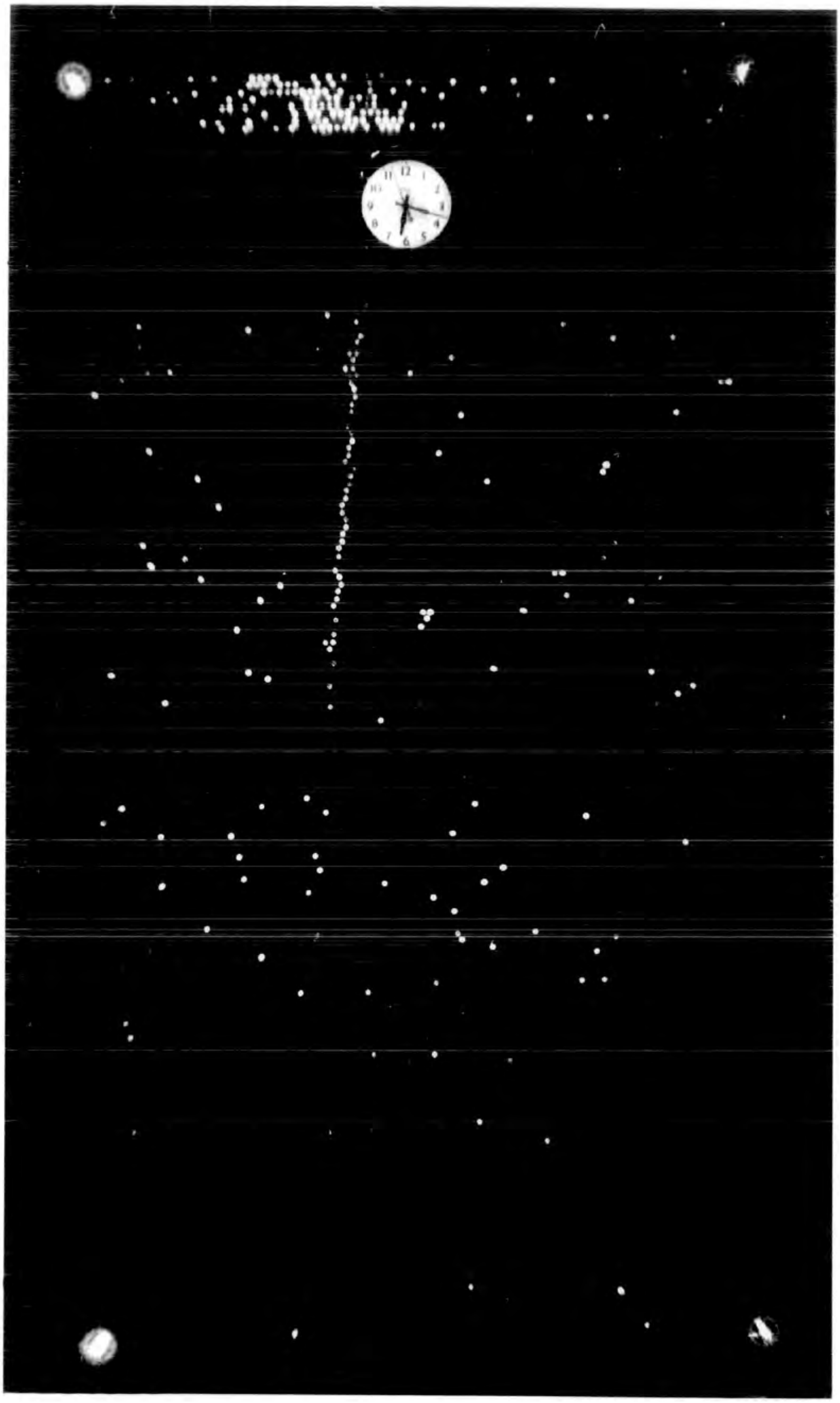

PLATE 9.2

Event H106 - 7

A hadron interacted in iron producing a burst of size = 1707 particles,

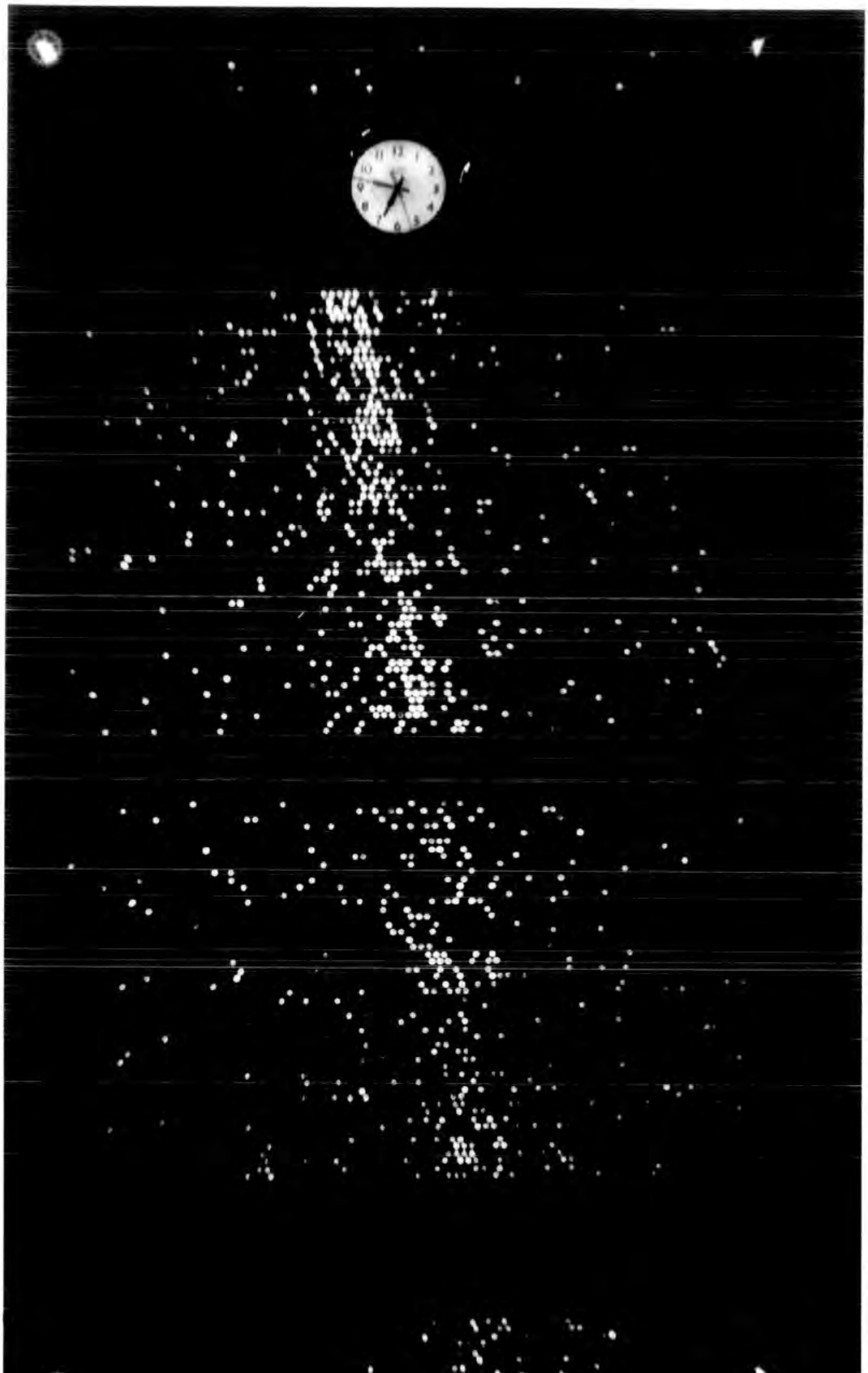

CHAPTER 10

SEARCH FOR MAGNETIC MONOPOLES

10.1 Introduction

The laws of quantum mechanics can explain why electric charge is quantized if the existence of a particle with a single magnetic pole is assumed. This assumption led Dirac in 1931 to predict the existence of a particle known as a magnetic monopole.

Search for magnetic monopoles is importent because this is the only way to explain the quantization of electric charge. Dirac took the fundamental electric charge to be e. He proved that monopoles of fundamental strength, $g = \hbar c/2e$ should exist.

Schwinger in 1966 concluded that the magnetic charge quantum is twice the value predicted by Dirac.

Monopoles produce a high rate of ionisation as they traverse through matter. The rate of energy loss for a relativistic monopole is approximately given by:

$$\frac{dE}{dx} = n^2 . 10 \text{ Gev/gm. cm}^{-2}$$

where $n = 2e.g/hc$. In comparison with the rate of energy loss caused by a particle with electric charge e, the rate for monopoles is approximately 5000 times that of a relativistic e-charged particle ($\frac{dE}{dx} \sim 2$ Mev). This is the main property of monopoles for detection.

The relativistic monopoles could produce tracks similar to those produced by high Z atomic nuclei in visual detectors. The predicted processes that produce monopoles are similar to those producing electron-positron pairs

$$\gamma + P \quad P + g + \bar{g}$$

$$P + P \quad P + P + g + \bar{g}$$

Table 10.1 shows some predicted properties of monopoles.

Author	Fundamental electric charge	Fundamental monopole strength	$^{dE}/_{dx}$ Gev $gm^{-1} cm^{-2}$	Z of nucleus with same dE/dx	Ionization loss in penetrating the atmosphere to sea level
Dirac	e	$^1/_2 \frac{\hbar c}{e}$	9.4	69	$9.4 x 10^{12}$ ev
Dirac	$^e/_3$	$^3/_2 \frac{\hbar c}{e}$	84.6	207	$8.5.10^{13}$ ev
Schwinger	e	$\hbar\, ^c/_e$	36.6	138	$3.8.10^{13}$ ev
Schwinger	$^e/_3$	$3 \frac{\hbar c}{e}$	329.4	414	$3.4.10^{14}$ ev

Table 10.1 Expected properties of magnetic monopoles corresponding to fundamental electric charges e and $^e/_3$.

10.2 Previous searches for magnetic monopoles

Searches for monopoles have been carried out in accelerators. Amaldi et al (1963) and Purcell et al (1963) performed an experiment using a 30 Gev proton beam. They showed that the monopoles mass is greater than 2.8 Gev/c^2 if they exist. Gurevich et al (1972) searched for monopoles using a 70 Gev proton accelerator yeilding the production cross section to be $< 1.4.10^{-43} cm^2$ for Mg$<$ 4.9 Gev/c^2. Giacomelli (1975) searched for monopoles by P - P collision at CERN-ISR. They could detect monopoles of mass, Mg$<$ 30 Gev. They found the upper limit on the production cross-section $< 2.10^{-36}$ cm^2 at 90% confidence level.

Searches for monopoles have been also carried out in cosmic rays by many experimenters. Ashton et al (1969b) performed an experiment at sea level using scintillators and flash tubes, demanding a pulse produced by monopoles of greater than 4,000 times the pulse produced by single muons. They found a flux limit of $< 1.3.10^{-10}$ cm^{-2} sec^{-1} st^{-1} with no candidate. Yock (1975) searched for heavy mass highly charged particles in cosmic rays, no events were observed. An upper limit of 7.10^{-10} cm^{-2} sec^{-1} st^{-1} at sea level under 600 gm/cm^2 concrete was obtained with 90% confidence level.

10.3 Present experiment

10.3.1 Observation of 15 anomolous events

Our experiment triggered basically for the study of hadrons, in E.A.S. producing burst of size ≥ 400 particles either in lead or iron targets. In this experiment the high voltage pulse was applied to the flash tube chamber after a time delay of 330μs after the occurrence of the burst. After this long time delay the track of a particle with charge e producing a burst in iron absorber could not be seen in F_1a, (See scale diagram of the chamber in chapter 6, F_1a consists of 8 layers of flash tubes).

The search for magnetic monopoles was based on the idea that if magnetic monopoles exist and pass through the chamber, its track could be seen in F_1a, due to its highly ionising property and the pulses produced by these particles from detector c, under the lead and detector A, under the iron could be recorded. In the course of experiment 15 unusual events have been observed.

10.4 The efficiency of the chamber for e-charged particles after the application of 330μs time delay

At a time delay of 330μs protons and charged pions interacting in the iron target are expected only to produce an average of 0.35 flashes in the 8 layers of flash tubes in F_1a. Figure 10.1 shows the variation of the internal efficiency η_I with the time delay between the passage of an ionising charge e particle and the application of the high voltage pulse to a single flash tube. Using the Lloyd theory the curve is found to fit the measurements for T_D in the range 1-200μs (Cooper, 1974) and beyond this, the curve is a theoretical extrapolation. In the theory, a, is the tube radius, f_1 is the average probability that a single electron is capable of producing a flash when the high voltage pulse is applied, and Q_1 is the average number of initial electrons produced per unit path length in the neon gas. Figure 10.2 shows a set of curves for variation of η_I as a function of time delay with

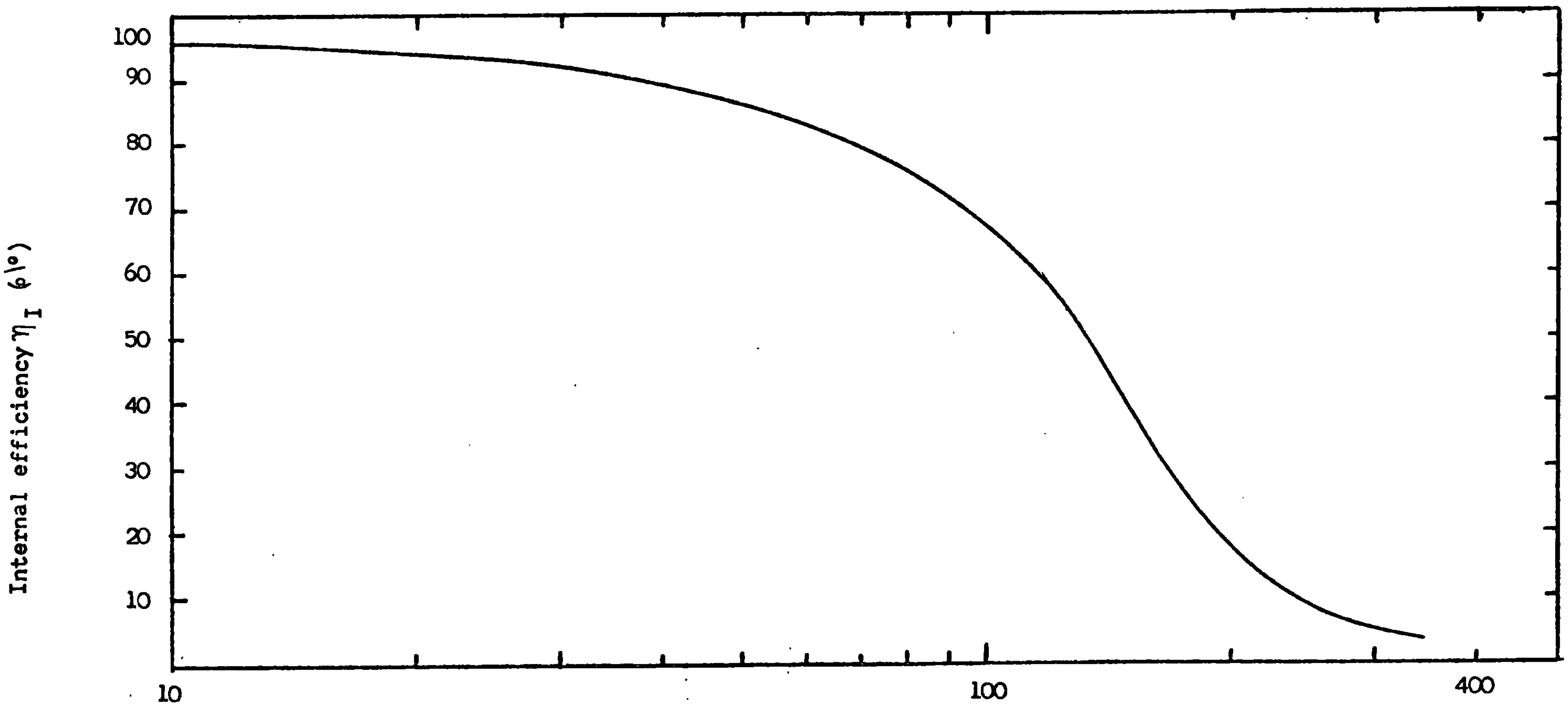

Figure 10.1 Variation of η_I with T_D for the flash tubes used in the present experiment for a $f_1 Q_1 = 9$

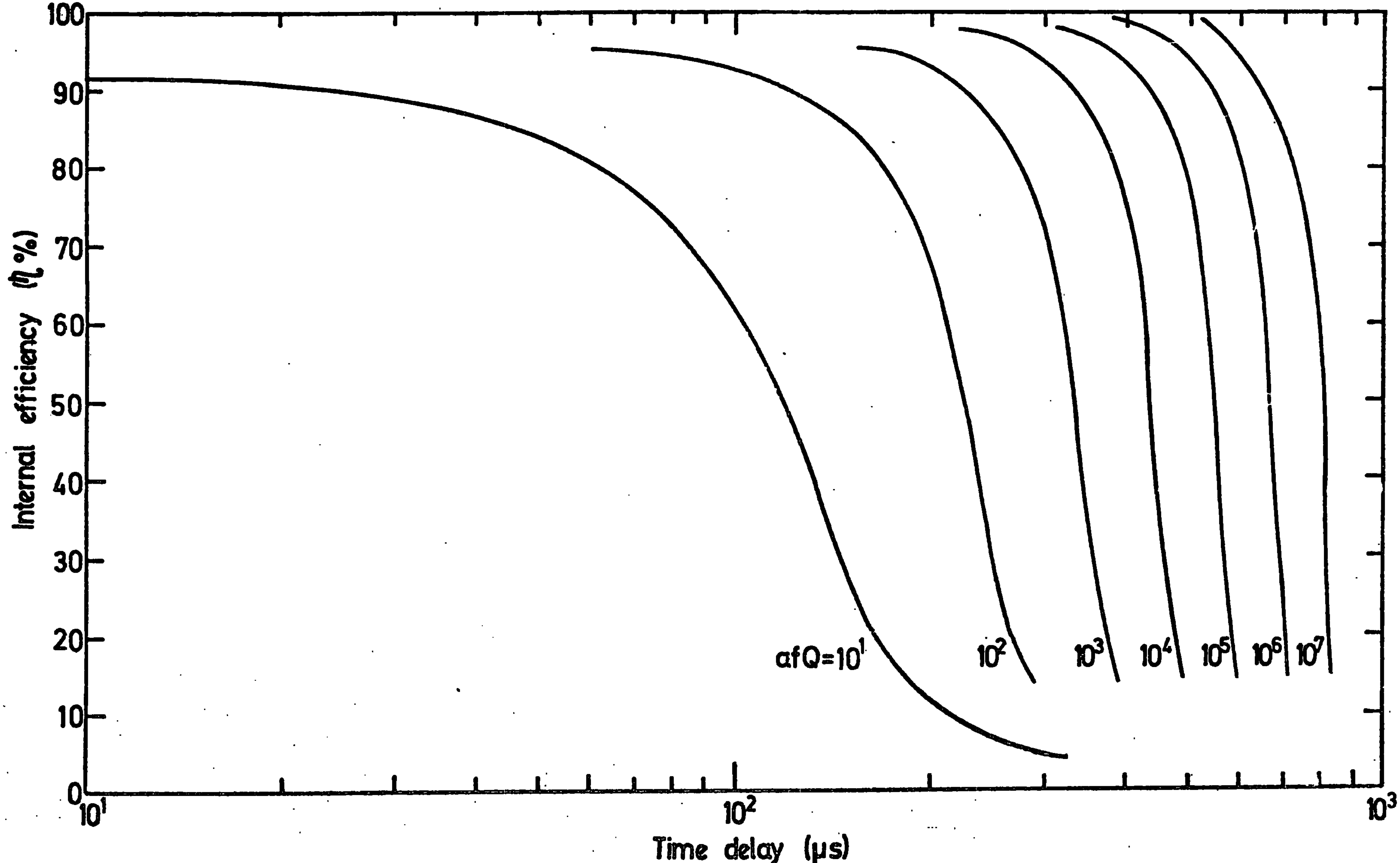

Figure 10.2 Variation of η_I with T_D a f_1Q_1 as a parameter for the flash tubes used in the present experiment

af$_1$$C_1$ as a parameter. The flash tubes used have internal diameter 1.58cm, external diameter 1.78cm and the separation between the centres of adjacent tubes is 1.81cm. It is seen from figure 10.1 that at $T_D = 330\mu s$, $\eta_I = 5\%$. The layer efficiency (probability of a tube flashing per layer) is thus $\frac{1.58}{1.81}.5 = 4.4\%$ and the average number of flashed tubes expected to be observed in the 8 layers of tubes in F_1a between the lead and the iron is 8x0.044 = 0.35. The fluctuations in the number of tubes flashed about the average value are expected to be described by a binomial distribution. If P is the probability of a tube flashing per layer the probability P(r,8) of observing r tubes flashed in 8 layers is:

$$P(r,8) = {}^8C_r\ P^r\ (1-P)^{8-r}$$

$$= \frac{8.7....(8-r+1)}{r!}\ P^r(1-P)^{8-r}$$

10.5 Measured parameters

Figure 10.3 shows the frequency distribution of the observed number of tubes flashed in F_1a laying on the axis of the bursts that were observed to be produced in the iron. Also shown is the expected binomial distribution for P = .044. It is seen that there is an excess of 15 events over expectation for tracks in F_1a with 4-8 flashes on them. The 15 anomalous events are shown in Figure 10.4. Plate 10.1 to 10.11 show the photograph of eleven of the anomalous events. Plate 10.12 is a typical normal event (interaction in lead). Plate 10.13 is a hadron interacted in iron flashing one flash tube out of 8 layers in F_1a. It is clear that some of them are probably produced by hadron interactions near the bottom of the lead so that the resulting electron-photon cascade produced by the γ's from π^o decay is in a very early stage of development and hence highly collimated. The range of distance from the bottom of the lead can be found by solving

$$e^{-\frac{Y}{\lambda}}\ \frac{\Delta Y}{\lambda} = \frac{11}{478}$$

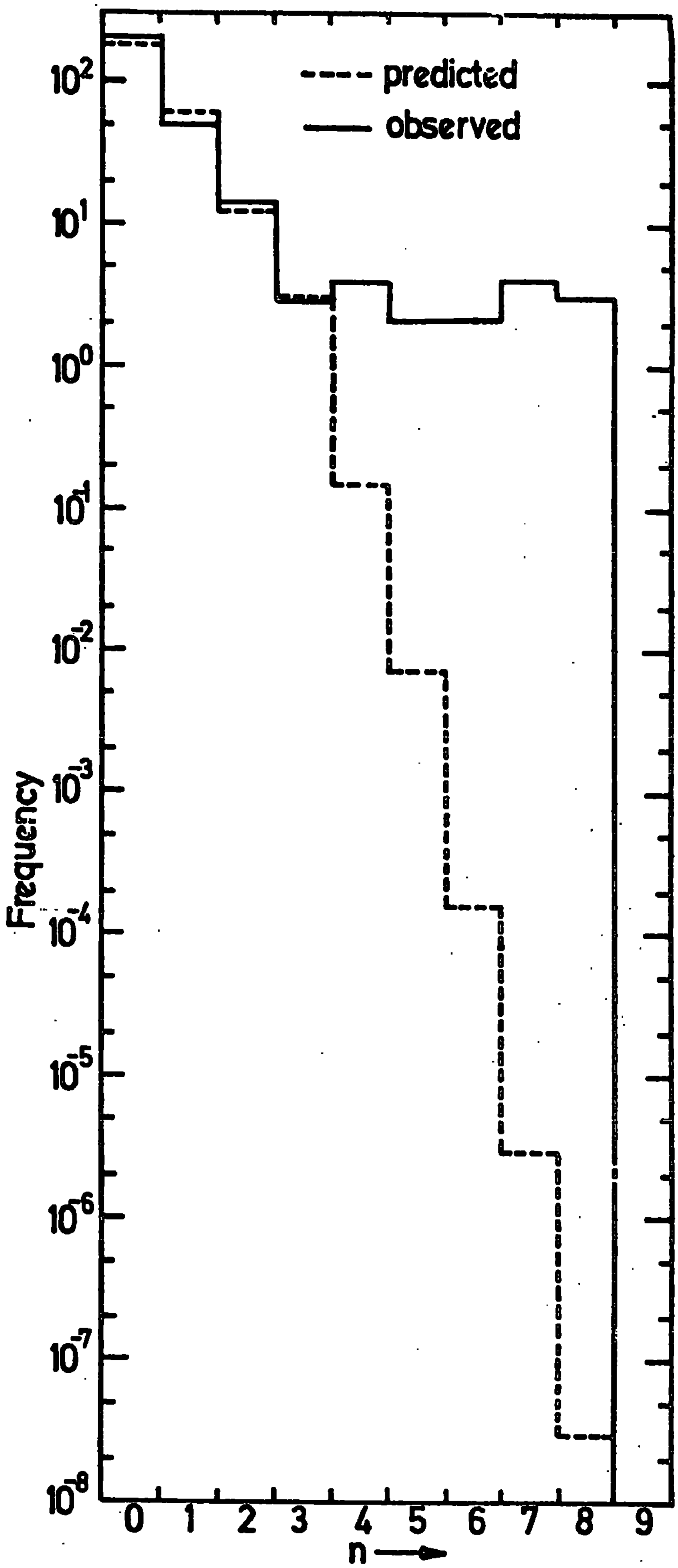

Figure 10.3 Histogram showing the number of tubes flashed in F_{1a} (8 layers of tubes) for the 261 bursts of size ≥ 400 equivalent muons produced by particles which penetrate 15 cm of lead and interact in 15 cm of iron

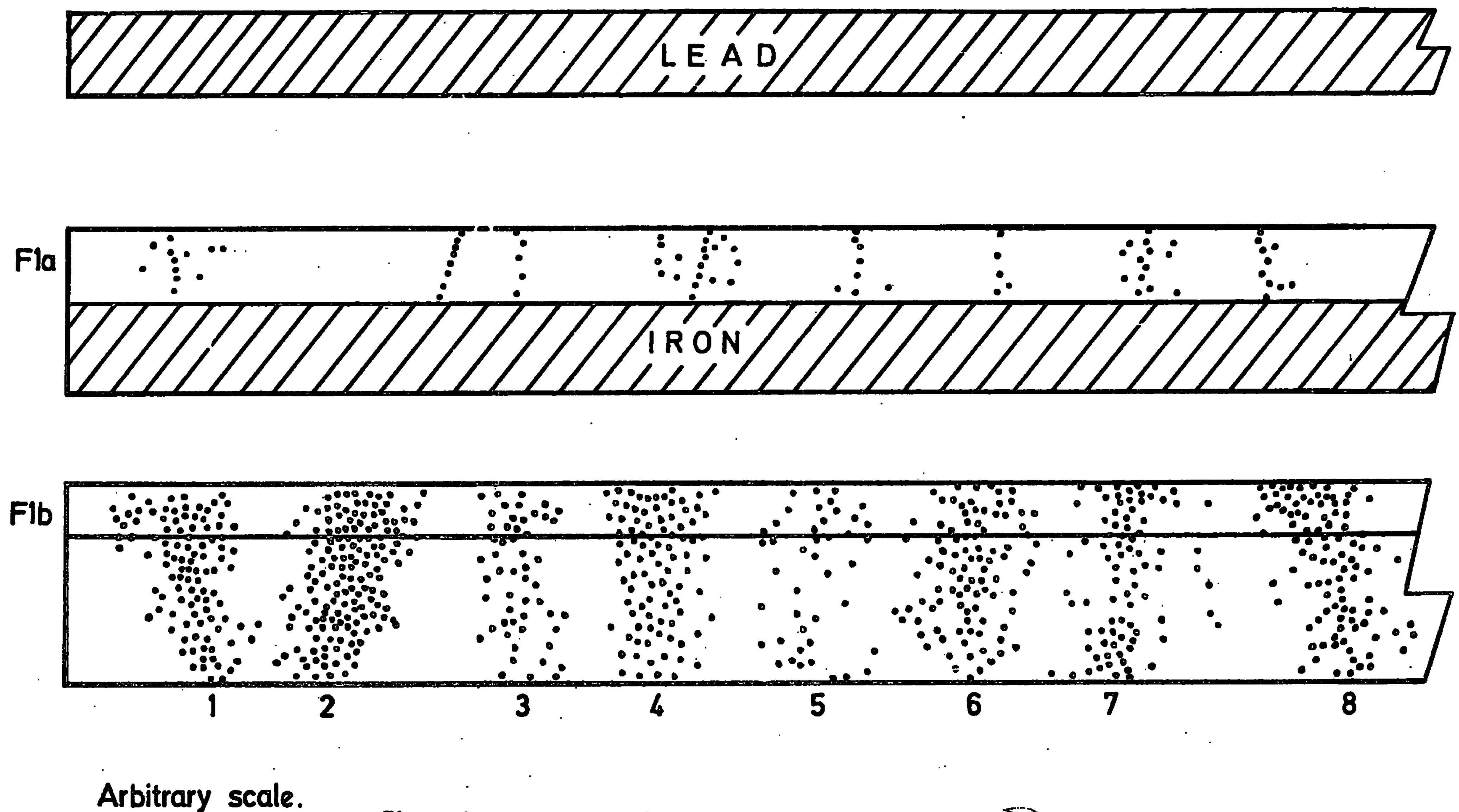

Figure 10.4 The anomalous events

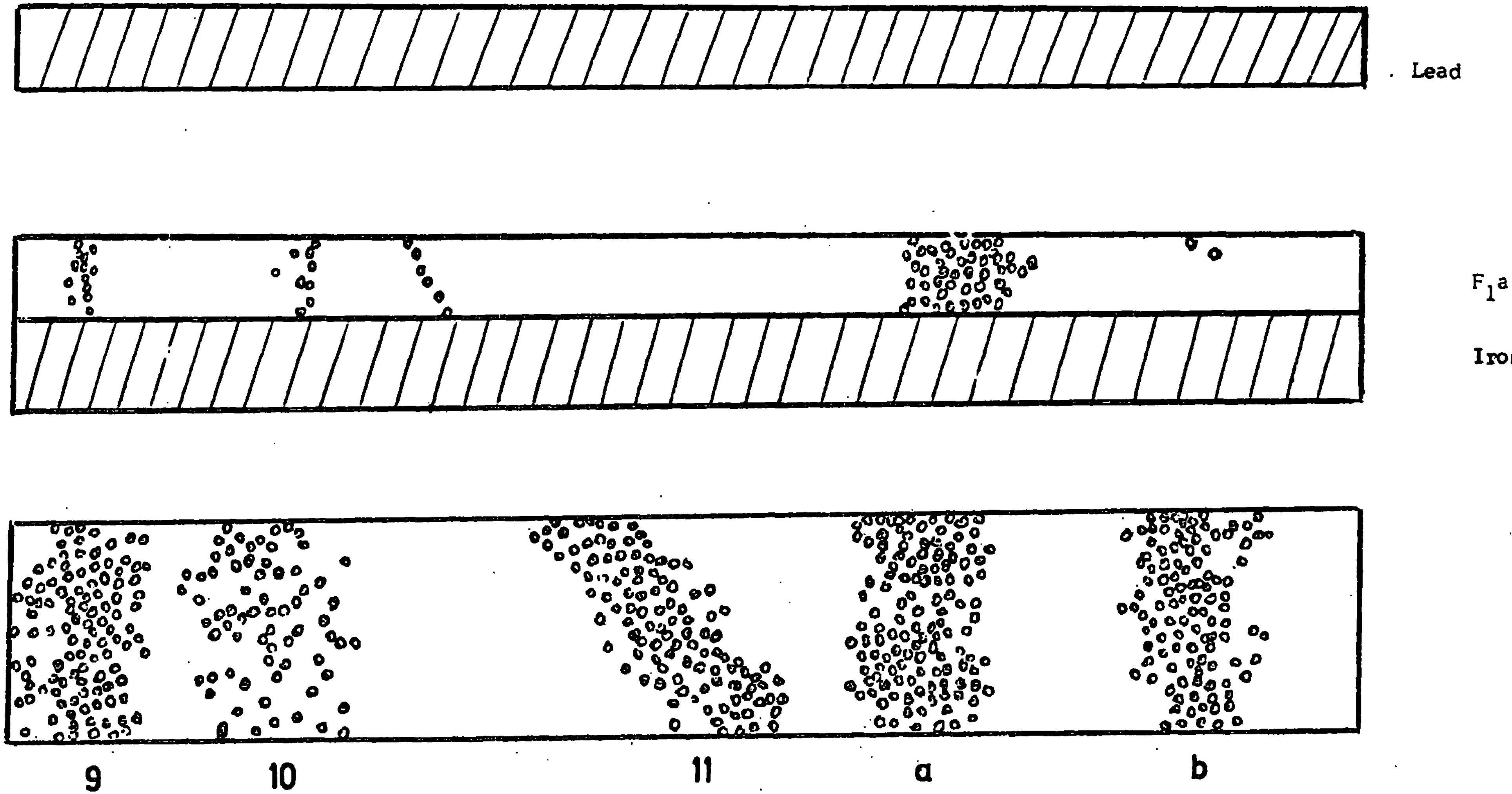

Figure 10.4 cont. 9, 10, 11 unusual events, a - a normal burst produced in lead, b - a hadron passing through lead and interacting in iron one flash tube is flashed in F_1a (the second flash is a background.

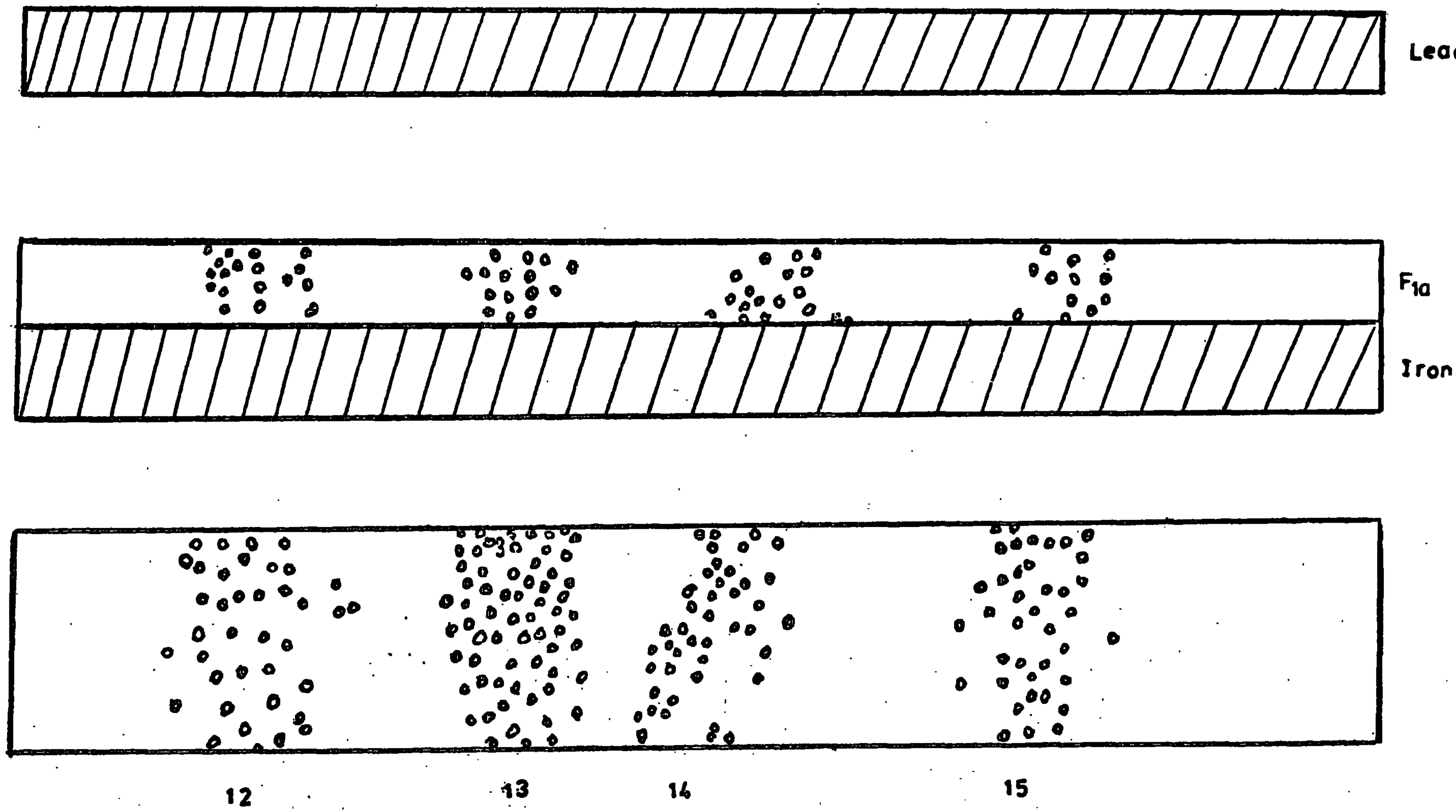

Fig. 10.4 cont.

for Δy where y = 15cm and λ = 19.8cm (The figure 478 is the number of bursts produced in the lead during the experiment). The result is y = 0.97cm.

In order to try to quantitatively separate events which are due to hadron interactions near the bottom of the lead from hadrons which traverse the lead without interacting and then make their first interaction in the iron the ratio R of the number of flashes outside the line of flash tubes lying on the burst axis in F_1a and the line of tubes on either side of it to the number of flashes contained inside the three central tubes width has been used as an estimator. In figure 10.5 R has been plotted as a function of the pulse height (equivalent muons) measured in scintillator C placed under the lead. Figure 10.6 shows a histogram of the data in figure 10.5. The 11 events which occur in the tail of figure 10.3 and are shown in figure 10.4 are marked 1-11. It is seen from figure 10.5 that the 11 events lie in the tail of the R distribution and are not distinctly separated from it by a significant gap. The number of particles contained in the narrow jet that traverses F_1a can be estimated from the measured flash tube efficiency in F_1a as well as from the pulse height from scintillator C. Figure 10.7 shows η_I plotted against $a f_1 \epsilon_1$ ($a f_1 \epsilon_1 = 9$ corresponds to 1 particle, $a f_1 \epsilon_1 = 18$ corresponds to 2 particles etc.) for $T_D = 330 \mu s$. Finally table 10.1 summarises all the available information concerning each individual event. It should be noted that the fit to the data shown in figure 10.3 assumes all bursts produced in the iron are due to charged pions. If a large fraction were produced by nucleons then an excess of events would be observed with zero flashes in F_1a over expectation and this is seen not to be so. This result is consistent with the previous work (Ashton et al, 1975) which suggested that for E > 500 Gev the flux of charged pions becomes greater than that of protons (and hence neutrons) in the vertical cosmic ray beam at sea level.

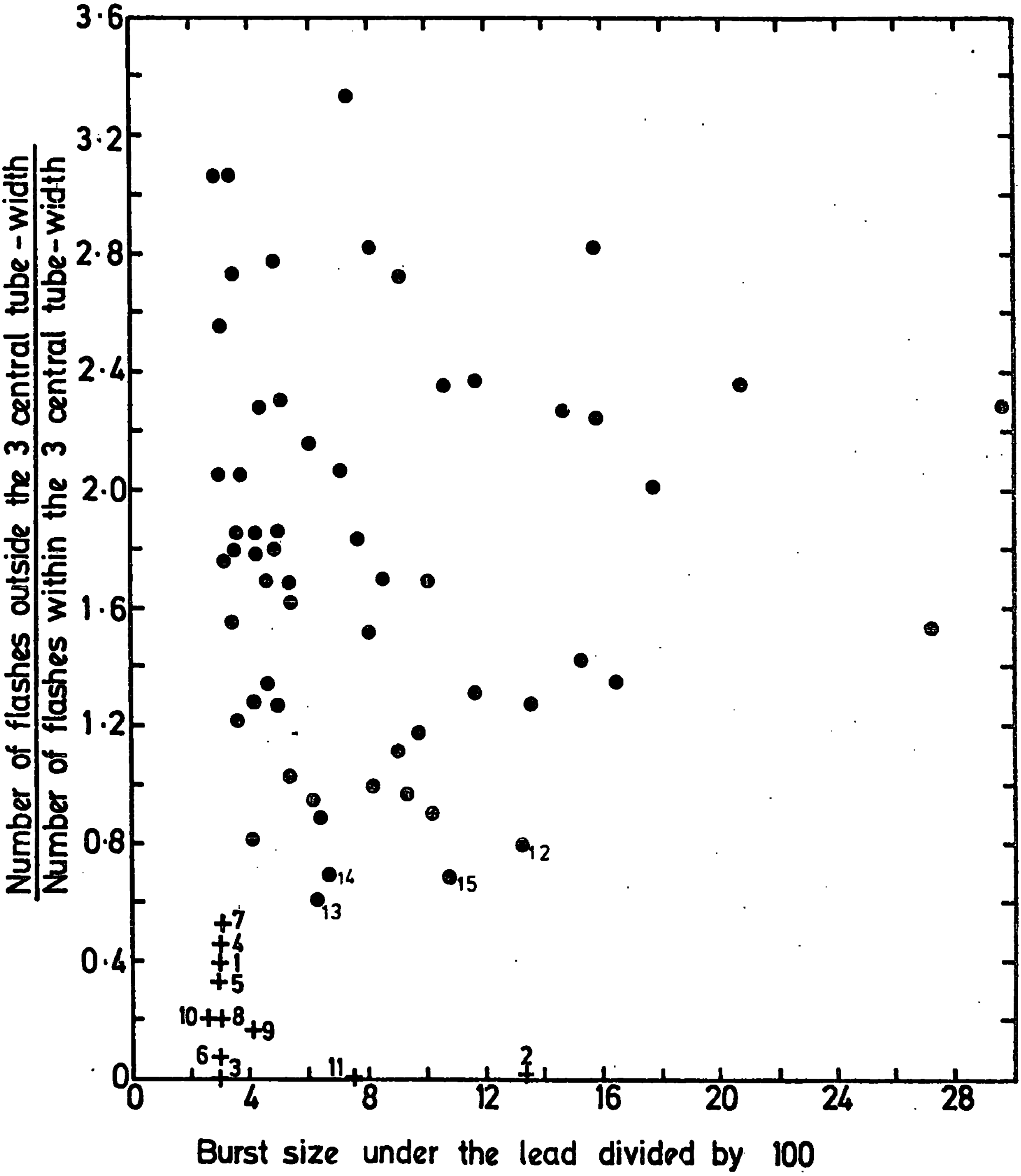

Figure 10.5 Scatter plot of the burst profile observed in Fla R versus the burst size measured in scintillator C

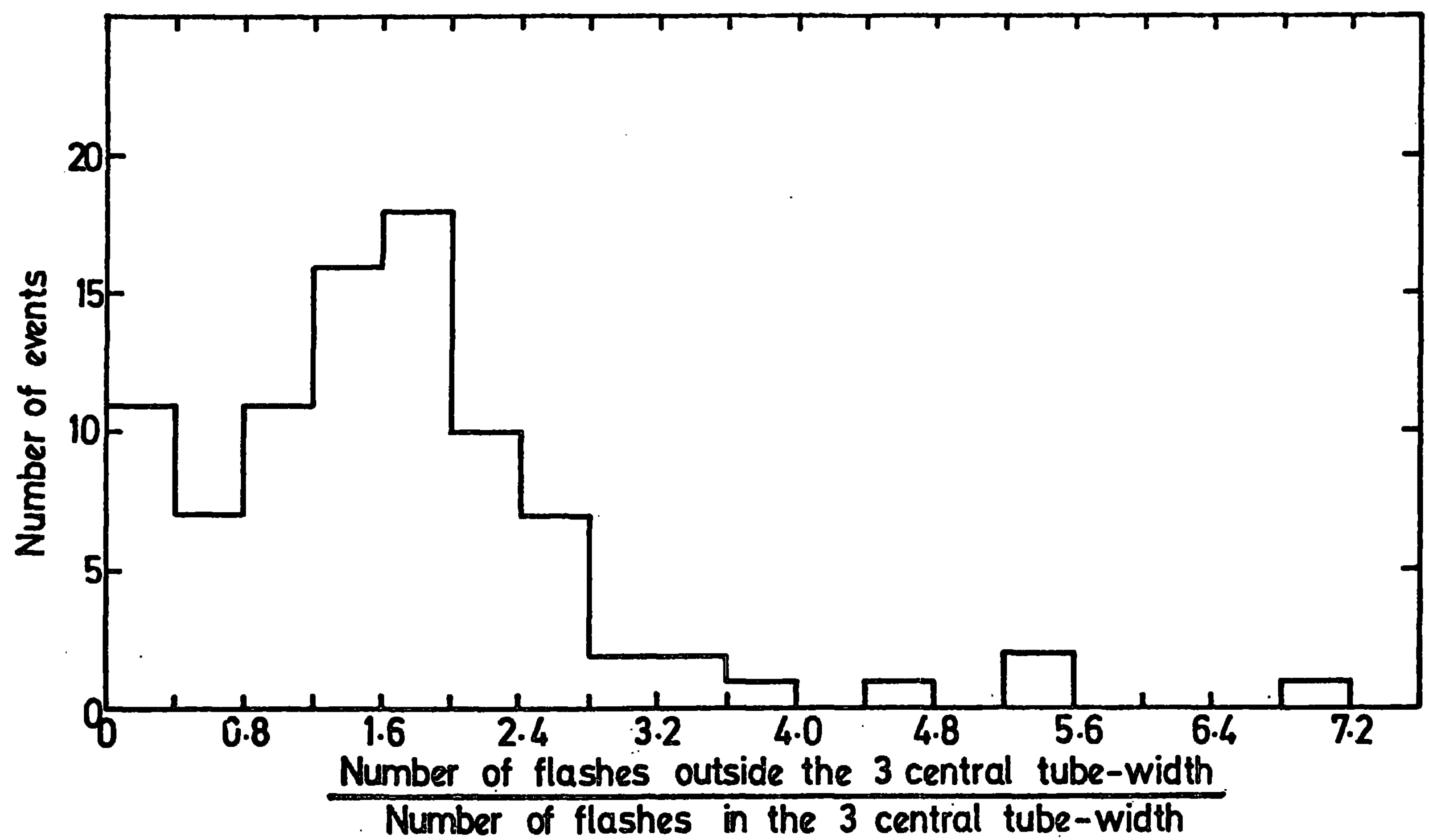

Figure 10.6 The frequency distribution in R, produced from the data in figure 10.5

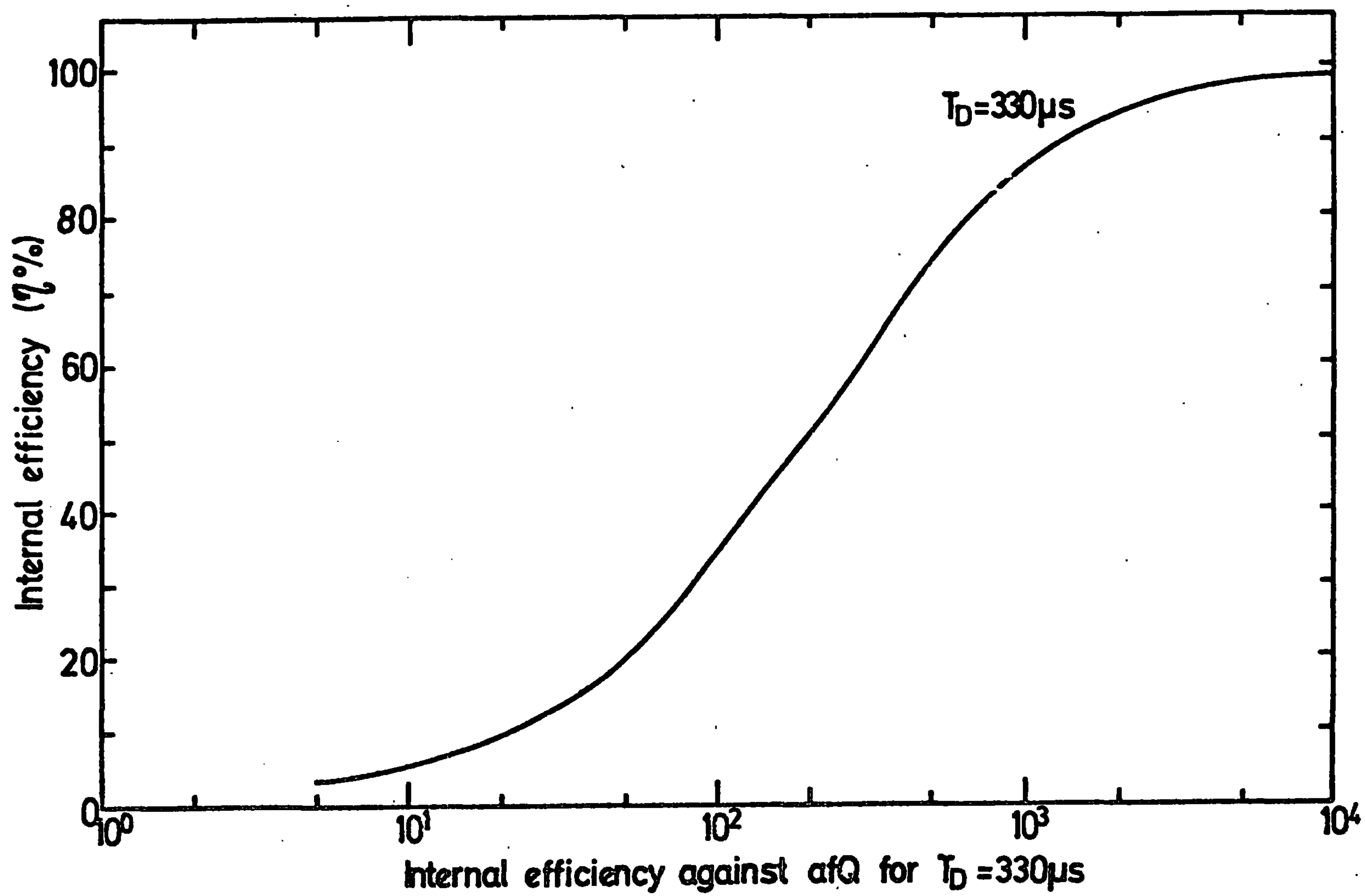

Figure 10.7 Dependence of η_I on a f Q for T_D = 330μs. afQ = radius of tube X probability of an ionizing collision in tube x number of ionizing particles produced per cm. afQ = 9 corresponds to the passage of a single charge e particle.

Ref. no. shown in Fig. 10.4 & Fig. 10.5	No. of layers flashed in Fla out of 8	No. of pts. in jet from scint. C pulse ht.	No. of pts. in jet from flash tube eff. in Fla.	Burst size in scint. A under the Fe	Prim. en. assuming prim. pts. are pions	Accompanying shower size	Density in scint. M of area 1.2 m²		Equivalent Z	
							Measured	Predicted from shower size and core position	Scint. C pulse ht.	Flash tube in Fla
1	7	250	400	1096	1350Gev	$4.1.10^5$	$\geq 80m^{-2}$	$15m^{-2}$	16	20
2	8	1270	900	1350	1000	not measureable	$24.5m^{-2}$	-	-	-
3	5	250	100	655	450	no shower	$3m^{-2}$	-	-	-
4	8	470	900	800	550	not measureable	$27.2m^{-2}$	-	-	-
5	7	250	400	600	470	no shower	$3m^{-2}$	-	-	-
6	5	250	100	1050	1200	no shower	$3m^{-2}$	-	-	-
7	7	250	400	650	450	no shower	$3m^{-2}$	-	-	-
8	7	250	400	950	660	no shower	$3m^{-2}$	-	-	-
9	8	417	900	3448	2800	$4.3.10^5$	$\geq 80m^2$	$129m^{-2}$	20	30
10	6	250	225	827	600	not measureable	$7.2m^{-2}$	-	-	-
11	6	670	225	980	700	no shower	$3m^{-2}$	-	-	-
12	4	1350	50	500	340Gev	not measureable	$11.3m^{-2}$	-	-	-
13	4	650	55	1034	710	no shower	$3m^{-2}$	-	-	-
14	4	620	40	506	400	no shower	$3m^{-2}$	-	-	-
15	4	1100	40	896	600	not measureable	$40.2m^{-2}$	-	-	-

Table 10.1 Details of the 15 anomalous events shown in the tail of figure 10.4 and also in figure 10.5. Only events 1 and 9 can be considered as possible high Z particles as they alone showed large pulse heights in scintillator M. Not measureable means the hadron was accompanied by a shower but it only gave a measureable density ($> 3m^{-2}$) in ≤ 3 detectors. As 4 densities are required for a core to be unambiguously locateable the shower size and core position could not be determined. No shower means the density was not measureable ($< 3m^{-2}$) in any air shower sampling detector.

10.6 Conclusion

From table 10.1 it is seen that only events 1 and 9 produced a large pulse height in scintillator M which would be indicative of a highly ionising particle traversing the lead without interaction and then interacting in the iron. The other events are therefore thought to be produced by hadron interactions near the bottom of the lead such that the electron-photon showers resulting from π^0 decay are in an early stage of development when they traverse F_1a. Events 1 and 9 are probably of the same nature but it cannot be excluded that they are produced by high Z particles ($Z \sim 20$) from the present data. Scintillator M is observed to be saturated but this could be entirely due to the accompanying air shower whose core position and size could be determined for these 2 events. Based on 2 possible events the upper limit to the vertical intensity (assuming a $\cos^8 \theta$ zenith angle distribution) of particles with charge $\gtrsim 2e$ in the cosmic radiation at sea level that can penetrate 15cm of lead and then interact in 15cm iron absorber producing an energy transfer > 400 Gev is $\leq 4.10^{-11}$ cm^{-2} sec^{-1} st^{-1} Highly charged particles of this nature are of considerable interest as according to Yock (1975) they are the true fundamental building blocks of matter rather than quarks carrying fractional electric charge.

PLATE 10.1

An unusual event, 7 layers out of 8 layers of flash tubes in F_1a have flashed. The interaction is in iron.

This event can be a condidate of highly ionising particles with charge $\sim$ 20e.

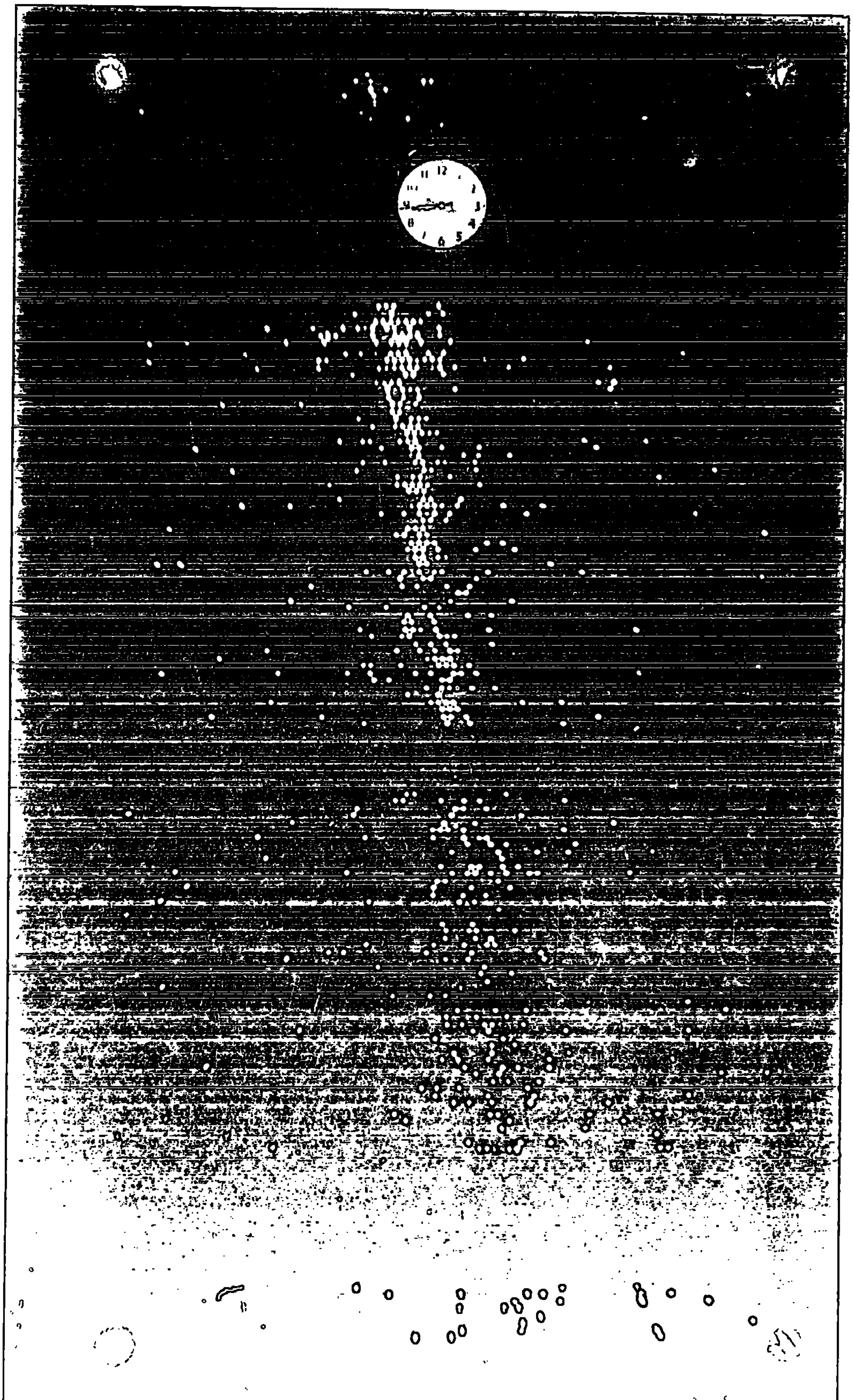

PLATE 10.2

An unusual event, all 8 layers of flash tubes in F_1a have flashed.

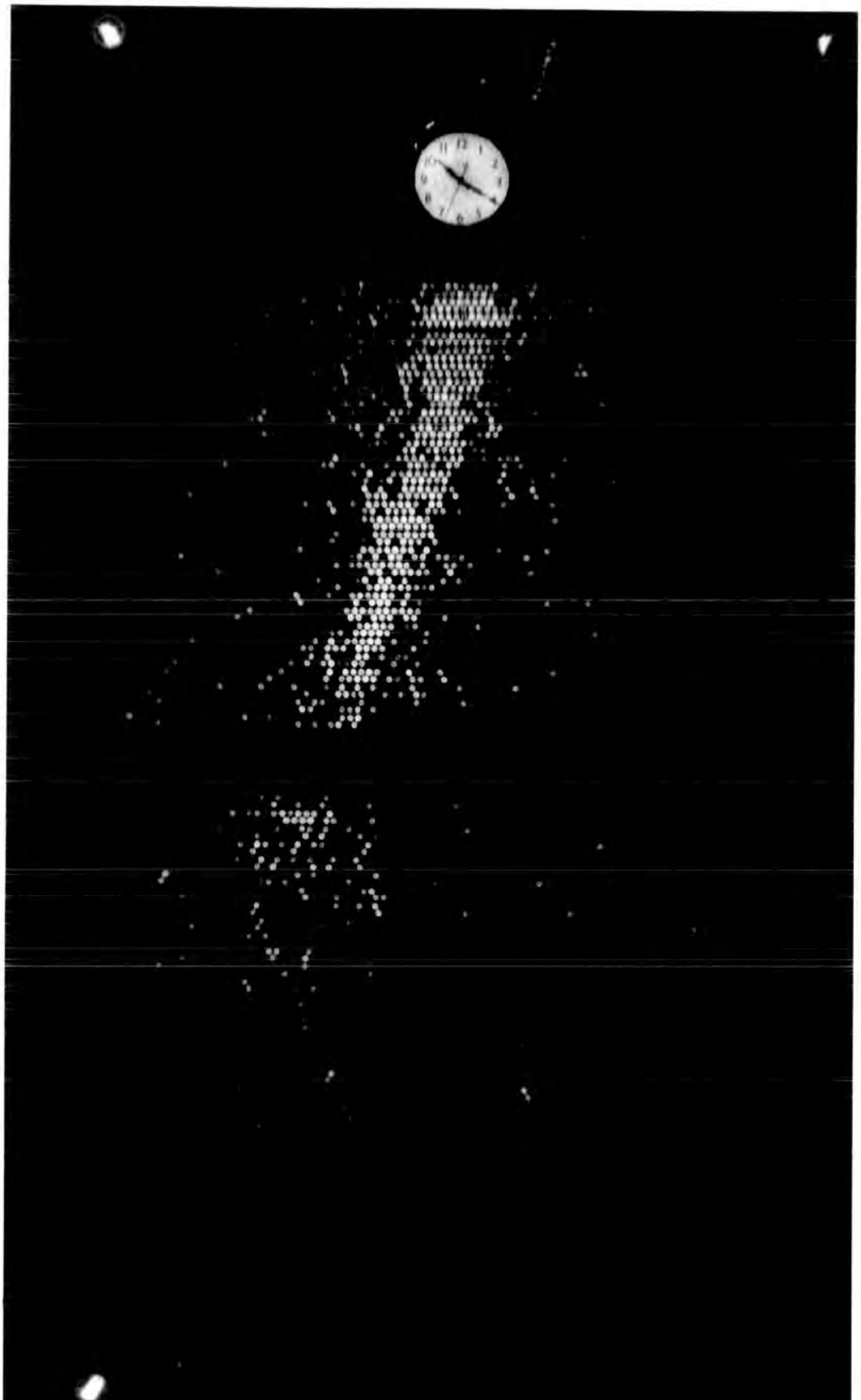

PLATE 10.3

An unusual event

5 layers out of 8 layers of

flash tubes in F_1a flashed

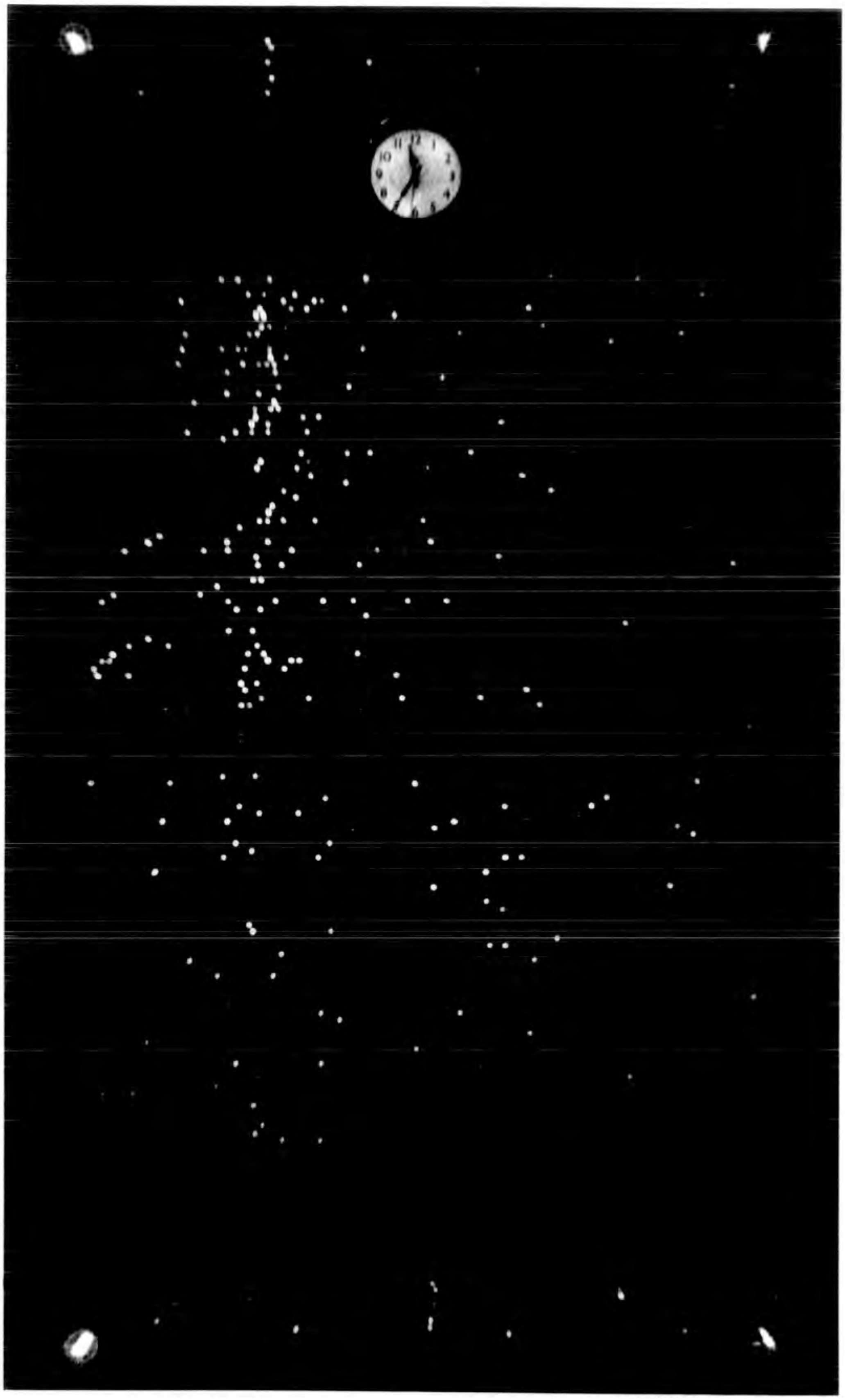

PLATE 10.4

An unusual event, all 8 layers of flash-tubes in F_1a flashed.

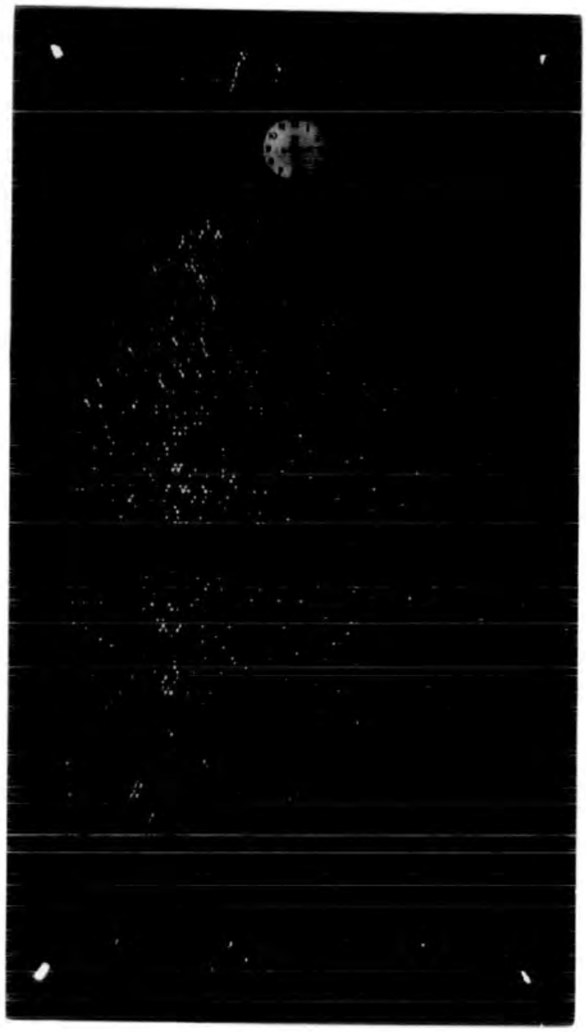

PLATE 10.5

An unusual event, 7 layers out of 8 layers of flash tubes in F_1a flashed.

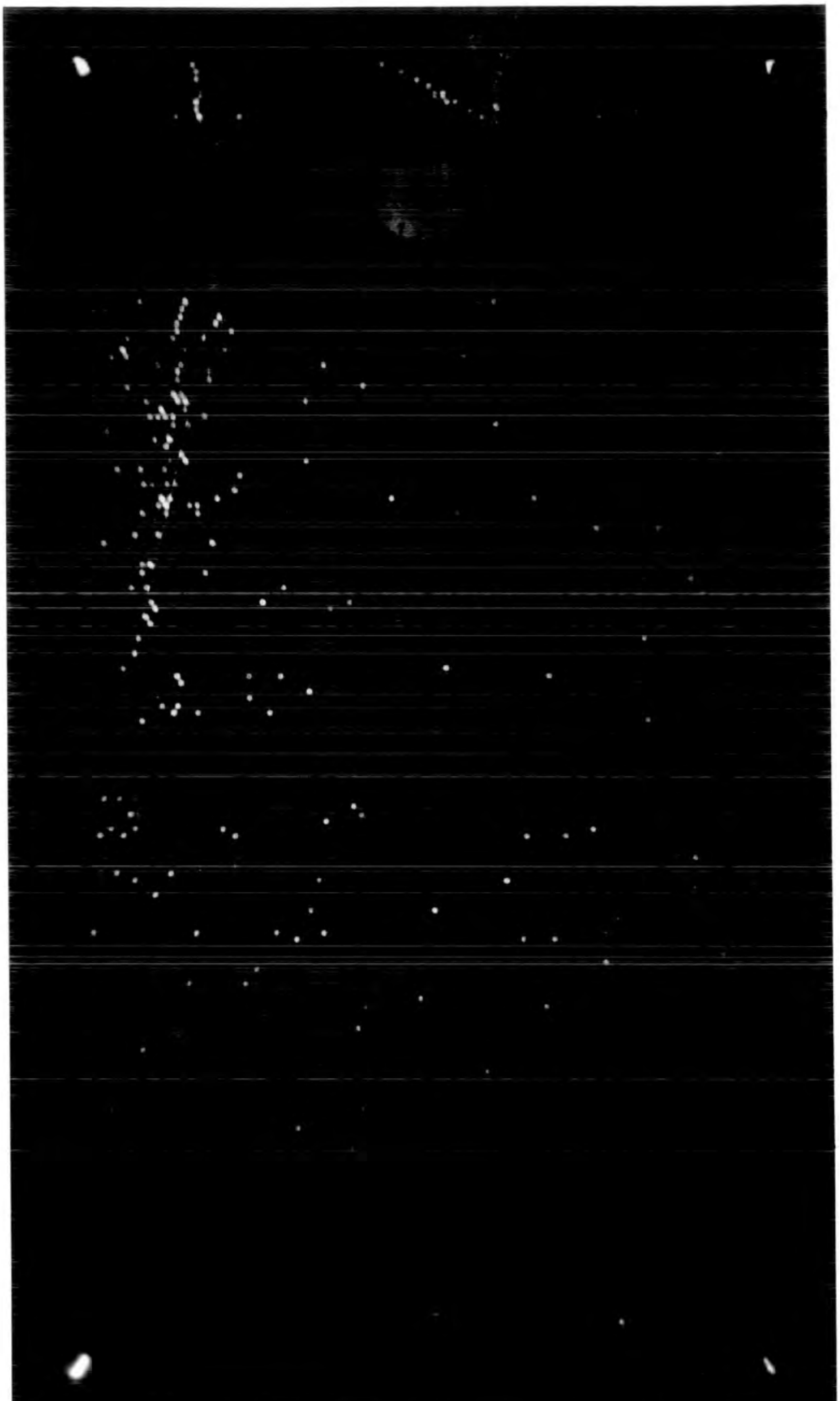

PLATE 10.6

An unusual event, 5 layers out of 8 layers of flash tubes in F_1a have flashed

PLATE 10.7

An unusual event, 7 layers out of 8 layers of flash tubes in F_1a have flashed

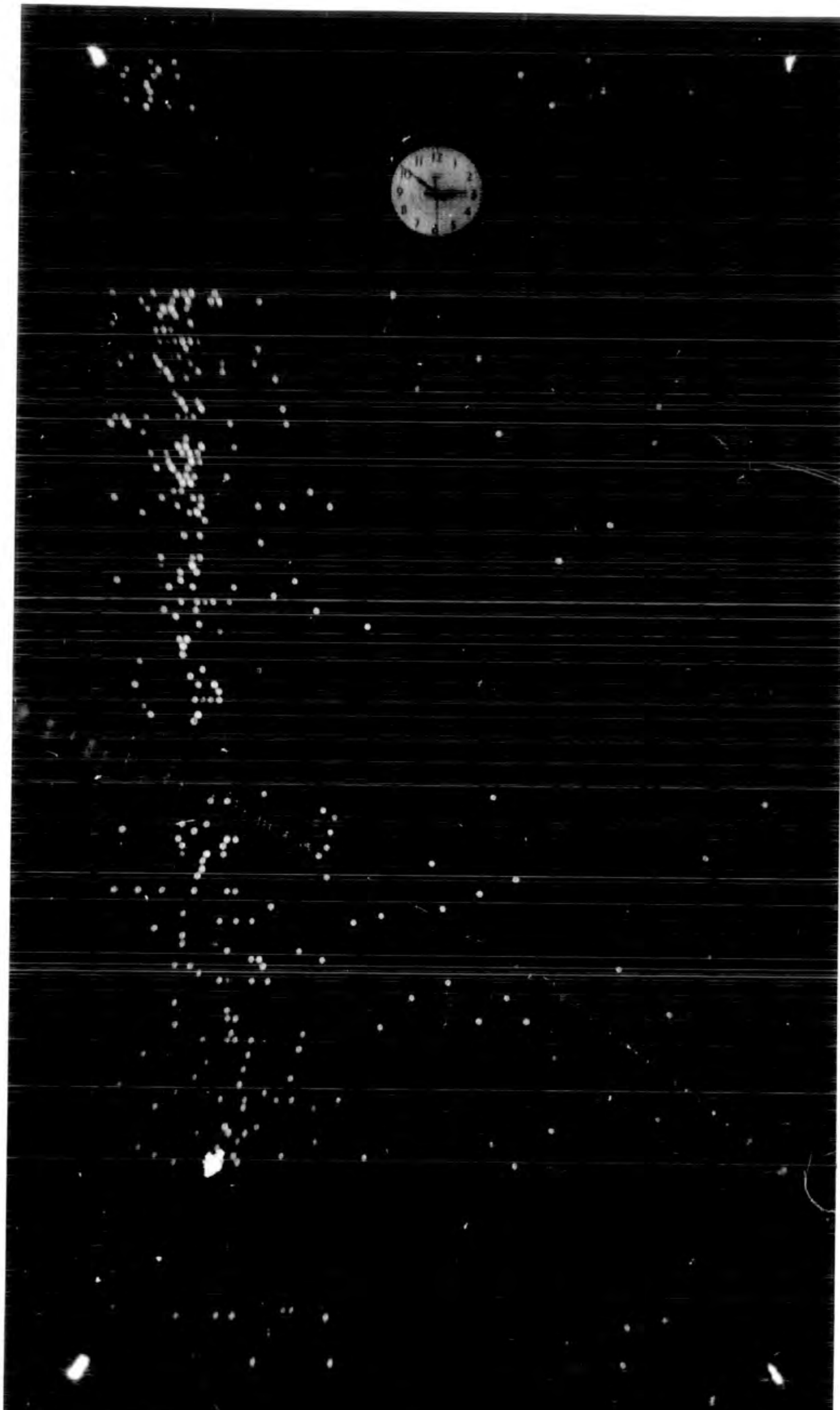

PLATE 10.8

An unusual event, 7 layers out of 8 layers of flash tubes in F_1a have flashed

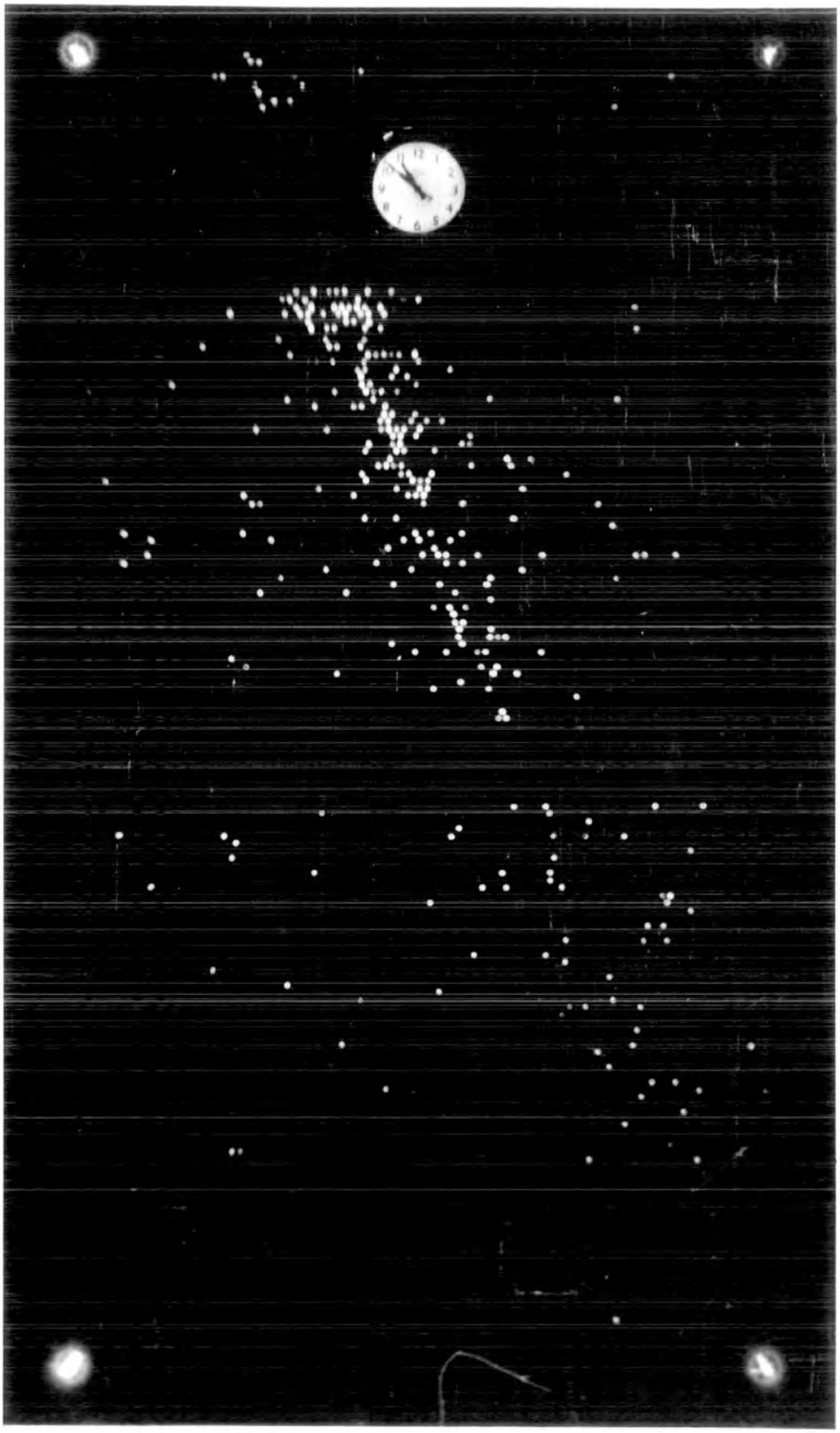

PLATE 10.9

An unusual event all 8 layers of flash tubes in F_1a have flashed. This event can be a candidate of highly ionising particle ($Z > 30$)

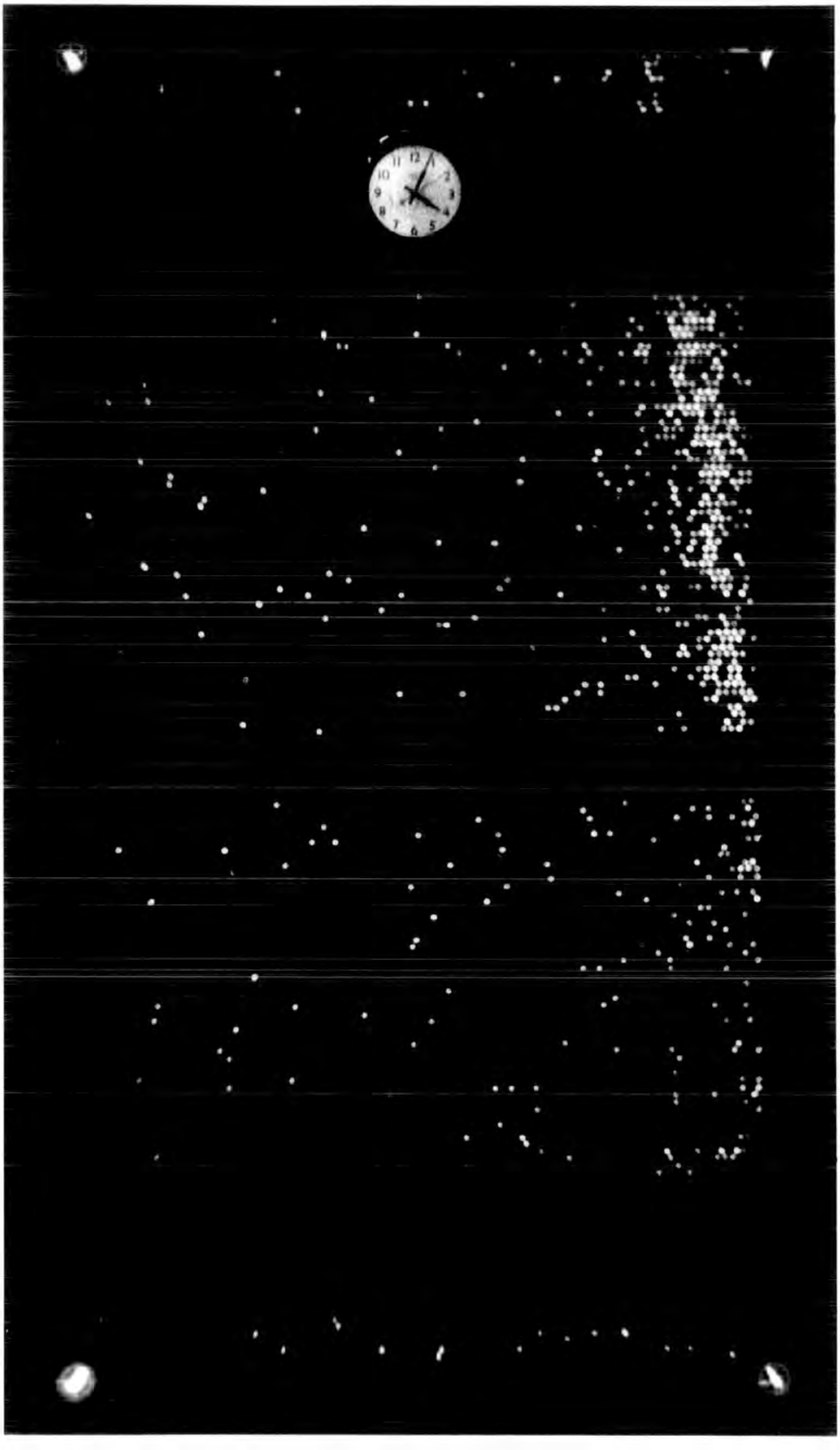

PLATE 10.10

An unusual event, 6 layers out of 8 layers of flash tube in F_1a have flashed

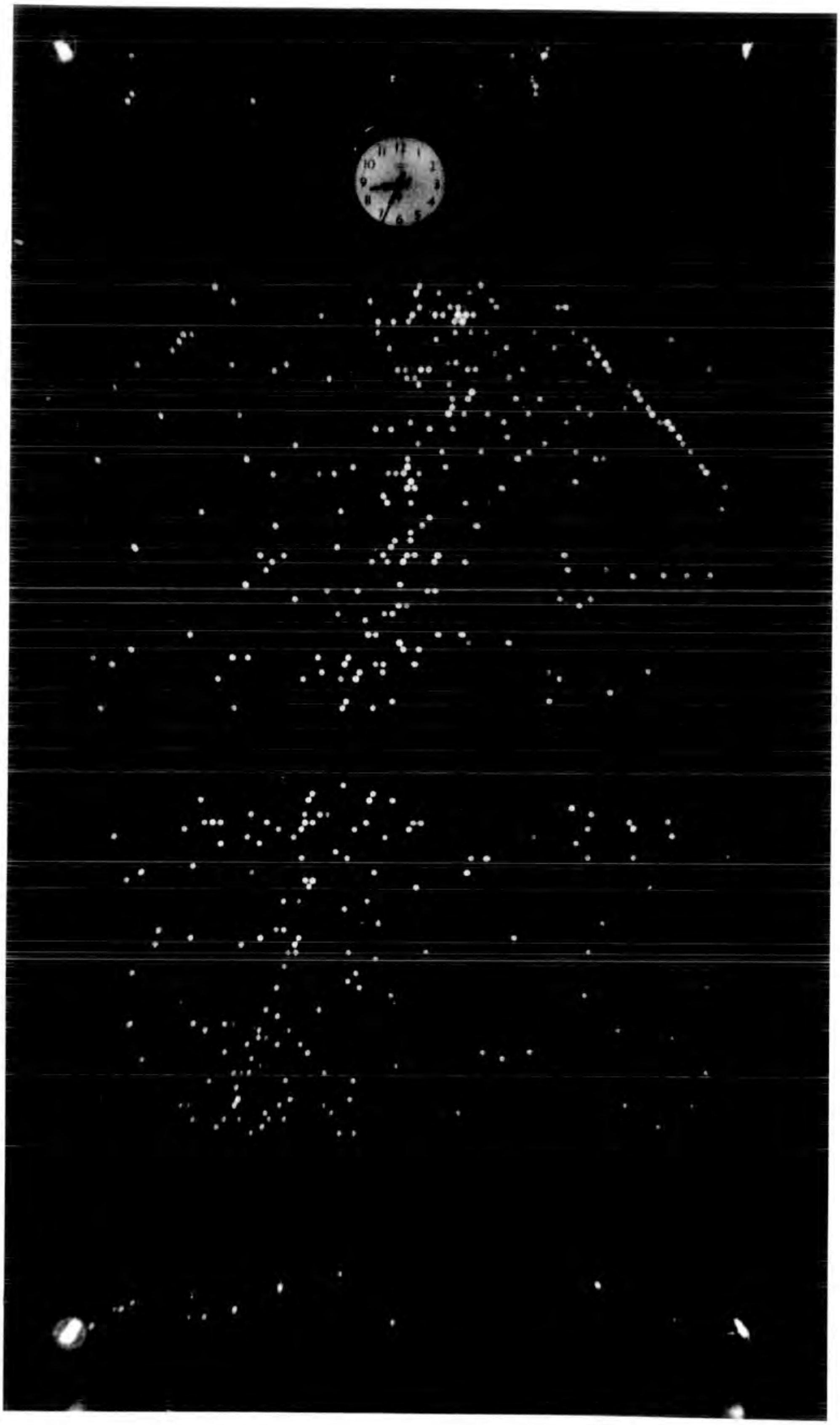

PLATE 10.11

An unusual event, [illegible] layers out of [illegible] layers of flash tubes in F_1a have flashed

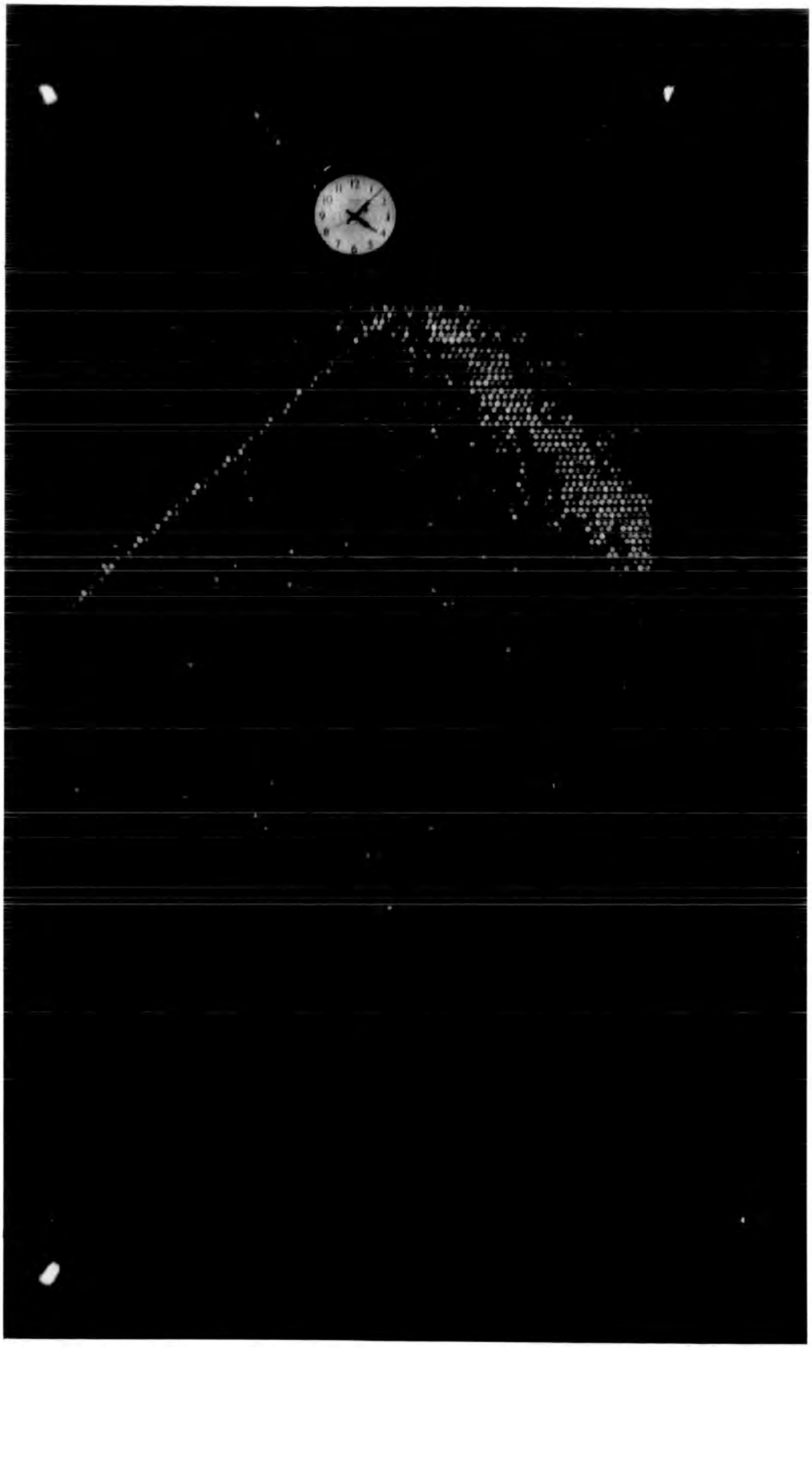

PLATE 10.12

A normal event, burst produced by a hadron in the lead and penetrated in the iron absorber.

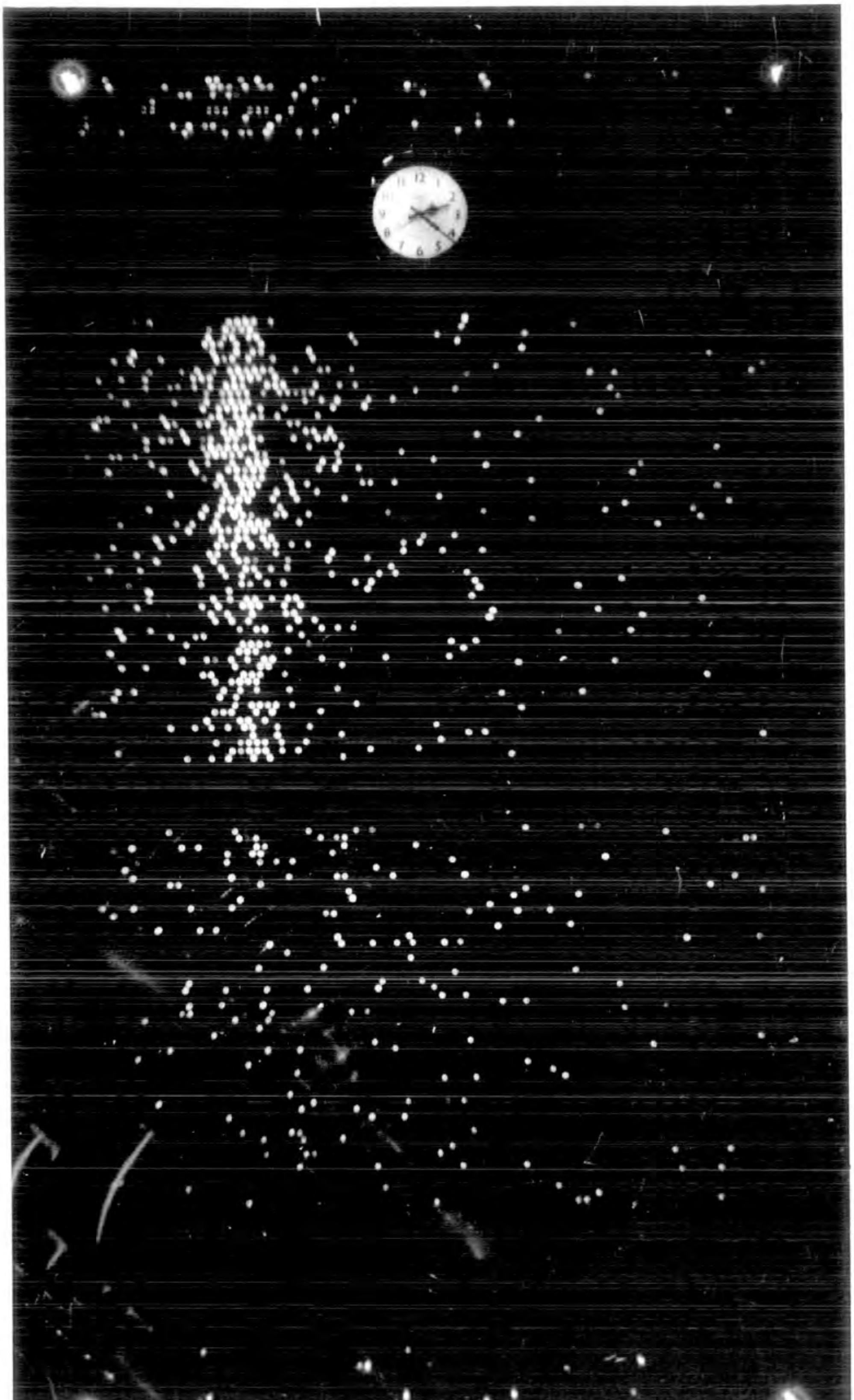

PLATE 10.13

A normal event, a hadron flashing one tube out of 8 layers of flash tubes and interacted in iron.

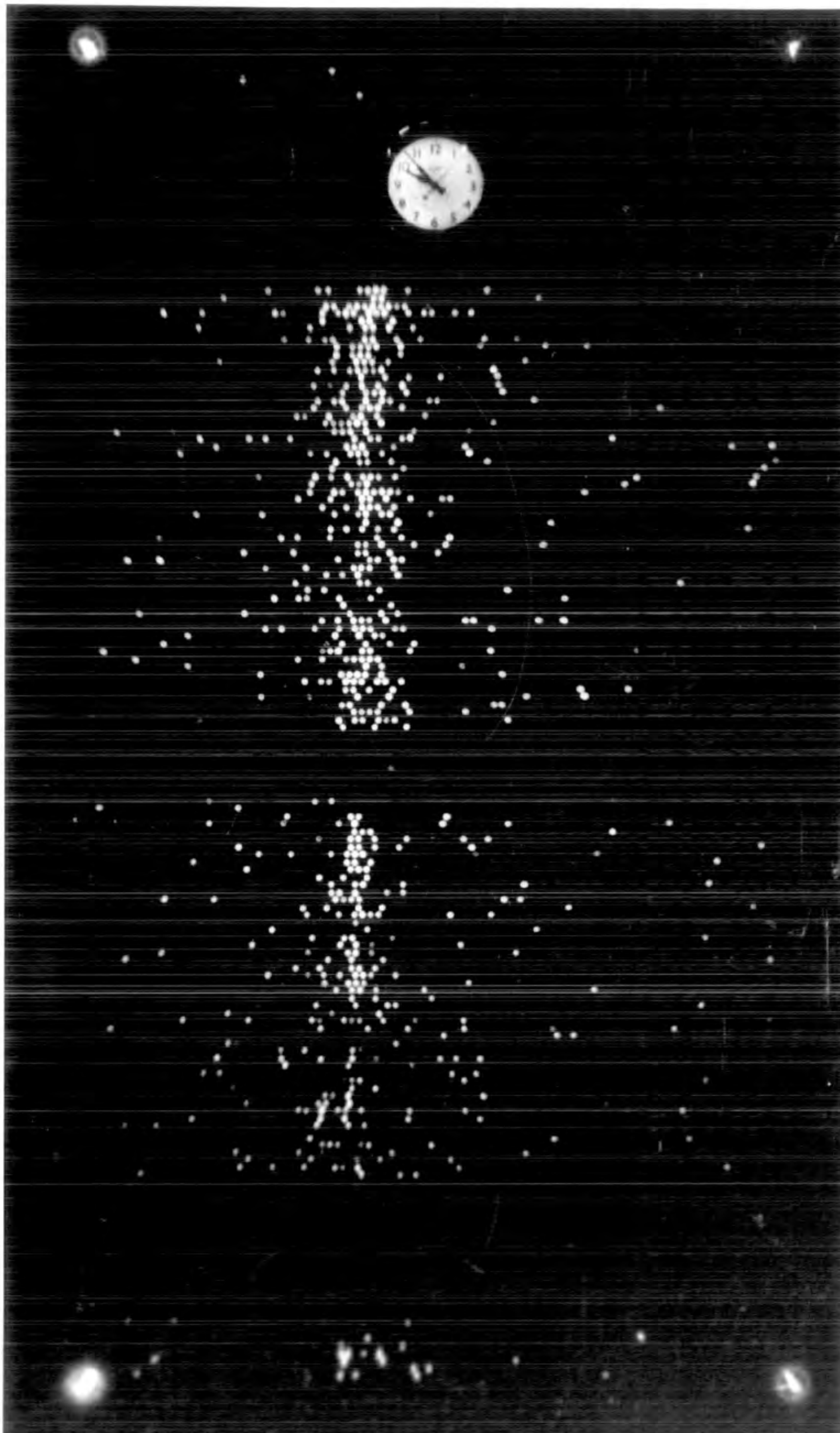

CHAPTER 11

11.1 Summary and current tachyon (faster than light) experiment

The lateral distribution of hadrons of energy $\geq$ 300 Gev in E.A.S. of size 5.10^4 - $1.6.10^6$ has been measured. It is found as the hadron energy increases the lateral distribution steepens. A weak dependence of lateral distribution on shower size has been found.

The energy spectrum of hadrons in E.A.S. steepens as the energy increases.

The dependence of E.r (reflecting the transverse momenta of hadrons) on hadron energy and shower size has been investigated. The results show the mean transverse momentum of hadrons drastically increases beyond the primary energy about 10^4 Gev as the hadron energy and shower size increases. This observation can be either due to a highly inelastic collision or interaction cross-section or both in high energy energy collisions, in other words either the inelasticity or interaction cross-section or both have to increase with energy.

It should be noted that if really the mean transverse momentum drastically increases beyond a primary energy an unknown force could be acting and causing this effect.

The energy spectrum of hadrons in cosmic rays at sea level has been measured over the energy range 400 Gev - 8 Tev. The spectrum is found to be well represented in differential form by $N(E)dE = AE^{-\gamma}\ dE$ Where $\gamma = 2.74 \pm 0.16$ with no suggested anomalous behaviour over the whole energy range.

A study of the ionising power of high energy cosmic ray particles that penetrate 15cm of lead and then interact in a 15 cm thick iron target has yielded 15 unusual events. The unusual events are seen in the 8 layers of flash tubes, operated on a time delay of 330μs between the occurence of the master trigger and the application of the high voltage pulse to the detector between the lead and iron as a highly collimated beam of ionising particles ($\gtrsim$ 100). Visually they look like the flash tube track of a single highly charged particle with $Z \sim 20$.

11.2 Current tachyon experiment

11.2.1 Introduction

The existence of an object travelling faster than light was predicted by relativity theory, both classical and possibly quantistic. In special theory of relativity only the constancy of the speed of light is assumed, it is not supposed to be the highest possible velocity. The total energy relation implies that these faster than light objects (Tachyons) have imaginary rest mass as $E = i\ mc^2/(B^2-1)^{1/2}$.

It is believed that charged tachyons emit Cerenkov light in vacuum without violating energy and momentum conservation, this property has been used to search for tachyons.

After the prediction of these particles experimental work started. Davis et al (1969) searched for tachyon pairs (using the property of emitting Cerenkov light in vacuum), produced in lead by γ-rays from a ^{60}Co radioactive source. The space between two metal plates which was evacuated was used as a detector, an electric field, to accelerate the charged tachyons, of 3 kv cm^{-1} was applied between the plates. The vacuum was viewed by a photomultiplier, the result was observing no pulses to be produced by Cerenkov light.

Search for tachyons has been also carried out in cosmic ray air showers. The idea behind these experiments is that if tachyons are produced in the collision of the cosmic ray particles, either by primaries or secondaries, with atomic air nuclei, they will arrive in a time before the shower front.

The results of the experiments to detect tachyons are negative so far, apart from the results obtained by Clay and Crouch (1974) that has given an apparently positive result. These workers assumed that some tachyons are produced by cosmic ray primaries, with energy of 10^{15}ev or more, when they interact in the atmosphere produce extensive air showers. The majority of the air shower components travel at a speed close to the speed of light (c) on average the first interaction occurs at a height of about 20km , so one can see the shower front about 60μ s after the first interaction at sea level. Second assumption was that at least some of the tachyons survive until they reach to sea level, so tachyons produced at the height of 20km will arrive in an interval of up to, say, 100μs preceding the shower front. The third assumption was that they will interact in some way, that provides an out put from the scintillator, larger than the pulses produced by noise to be separated.

Fegan et al (1975) looked for tachyons over a 400μ sec time interval, at two different energy thresholds. A 200 bit static shift register was used as a delay device. Showers of mean energy 2.10^{15}ev were detected using an array of three plastic scintillators. A 4th scintillator, viewed by a pair of photomultiplier tubes was located at the array centre. At an energy release sensitivity of 0.5 Mev in the scintillator the time distribution of the shaped output pulses from one tube were recorded. No statistically significant deviations have been found. W.E. Hazen (1975) searched for tachyons in extensive air showers under the condition similar to Clay and Crouch, they found no evidence for existence of tachyons. Emery et al (1975) performed a search for tachyons arriving during about 100μ s preceding extensive air showers of primary energy about 10^{15}ev they found no positive evidence.

11.2.2 Experimental arrangement

In the current experiment, tachyons are looked for in extensive air showers of primary energy about 10^{15}ev. The tachyon detector is a flash tube chamber consisted of from top to bottom, 15cm lead, 8 layers of neon flash tubes, 15cm of iron. Below the iron, three 1 m^2 plastic scintillators covering the whole sensitive area of flash tubes are situated. Below the scintillators there is a block of flash tubes called F_1b of 6 layers of flash tubes). The electrodes of this block is short. Below F_1b a block of 94 layers of flash tubes has been put. Under this there exist 8 layers of flash tubes. This 8 layers together with F_1a and F_1b constitute the defining layers. Below the above mentioned 8 layers, there are three more scintillators similar to the top three ones, under these scintillators there are 8 layers of flash tubes.

The pulses produced in top and bottom scintillators, after being added, will be displayed on a 2 beam scope, after going through a delay line giving a delay of 240 μs to the pulses. So the scope shows pulses, produced in top and bottom scintillators in the 240 μs after the arrival of the air showers. A high voltage is applied, 20 μs after the air shower front reachs the scintillators to the flash tube chamber and a photograph is taken from the front view of the chamber. At present this experiment is run by I.A. Ward. Figure 11.1a and 11.1b show the scale diagram of the detector. In figure 11.2 the block diagram of this experiment is shown.

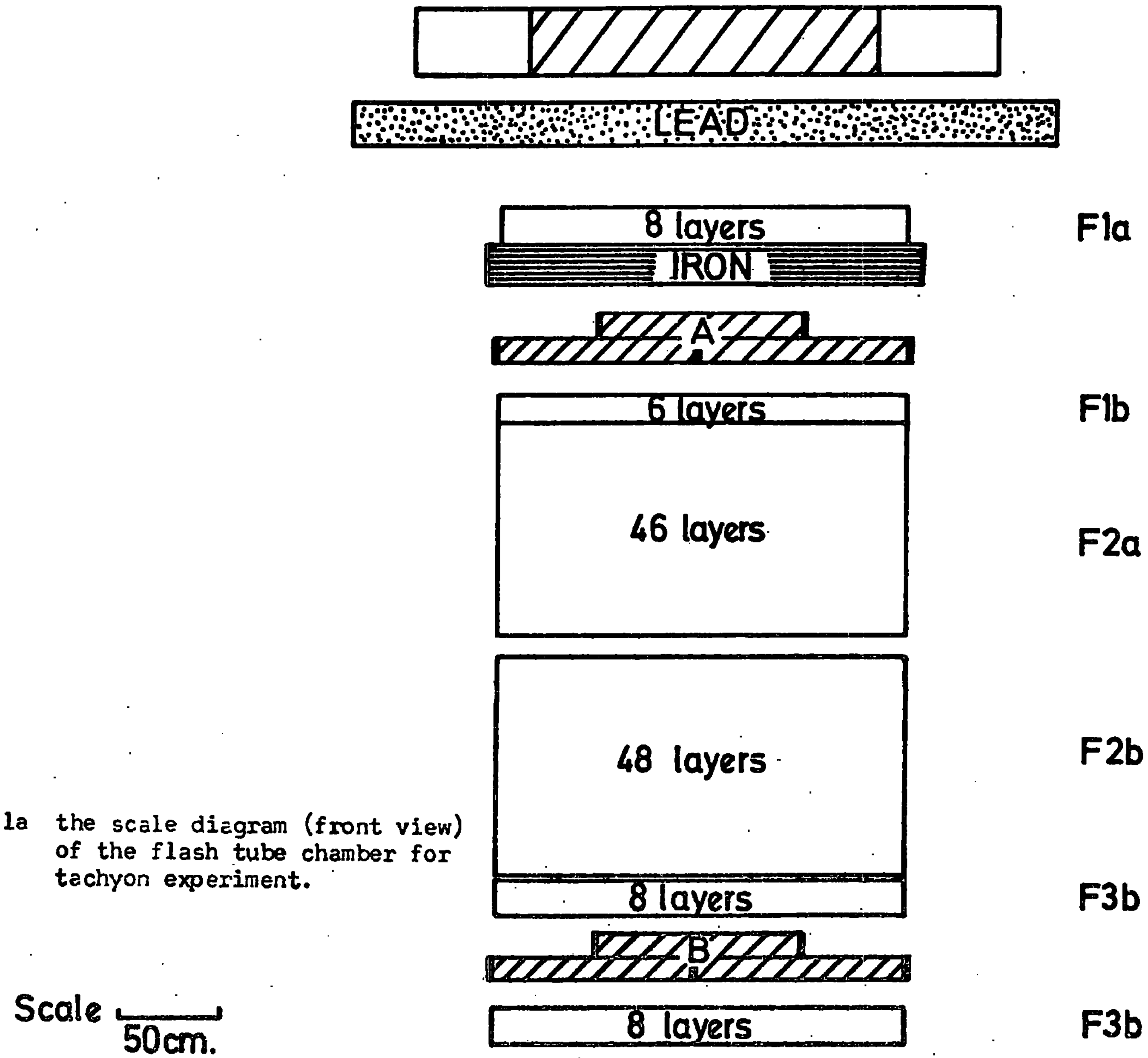

Figure 11.1a the scale diagram (front view) of the flash tube chamber for tachyon experiment.

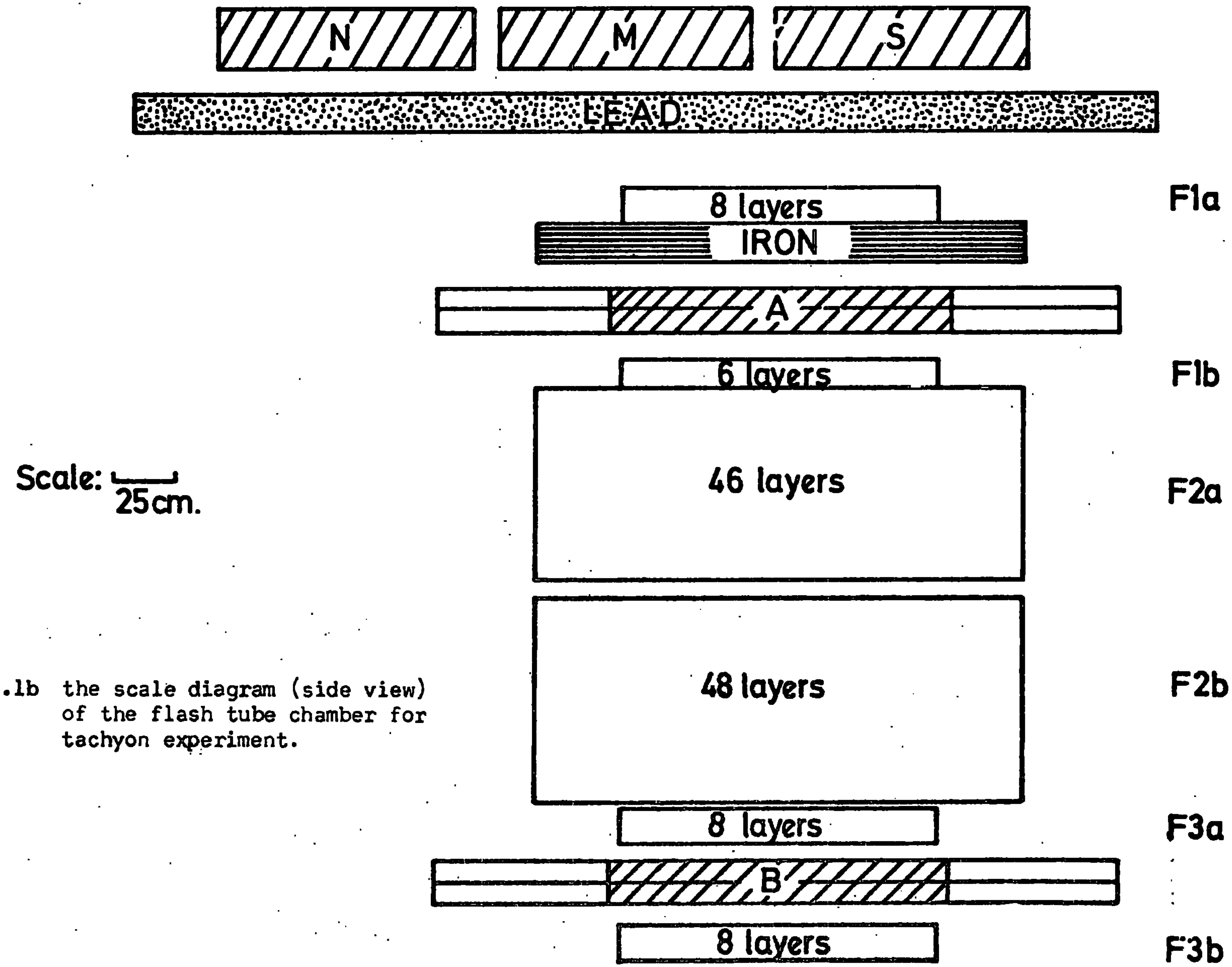

Figure 11.1b the scale diagram (side view) of the flash tube chamber for tachyon experiment.

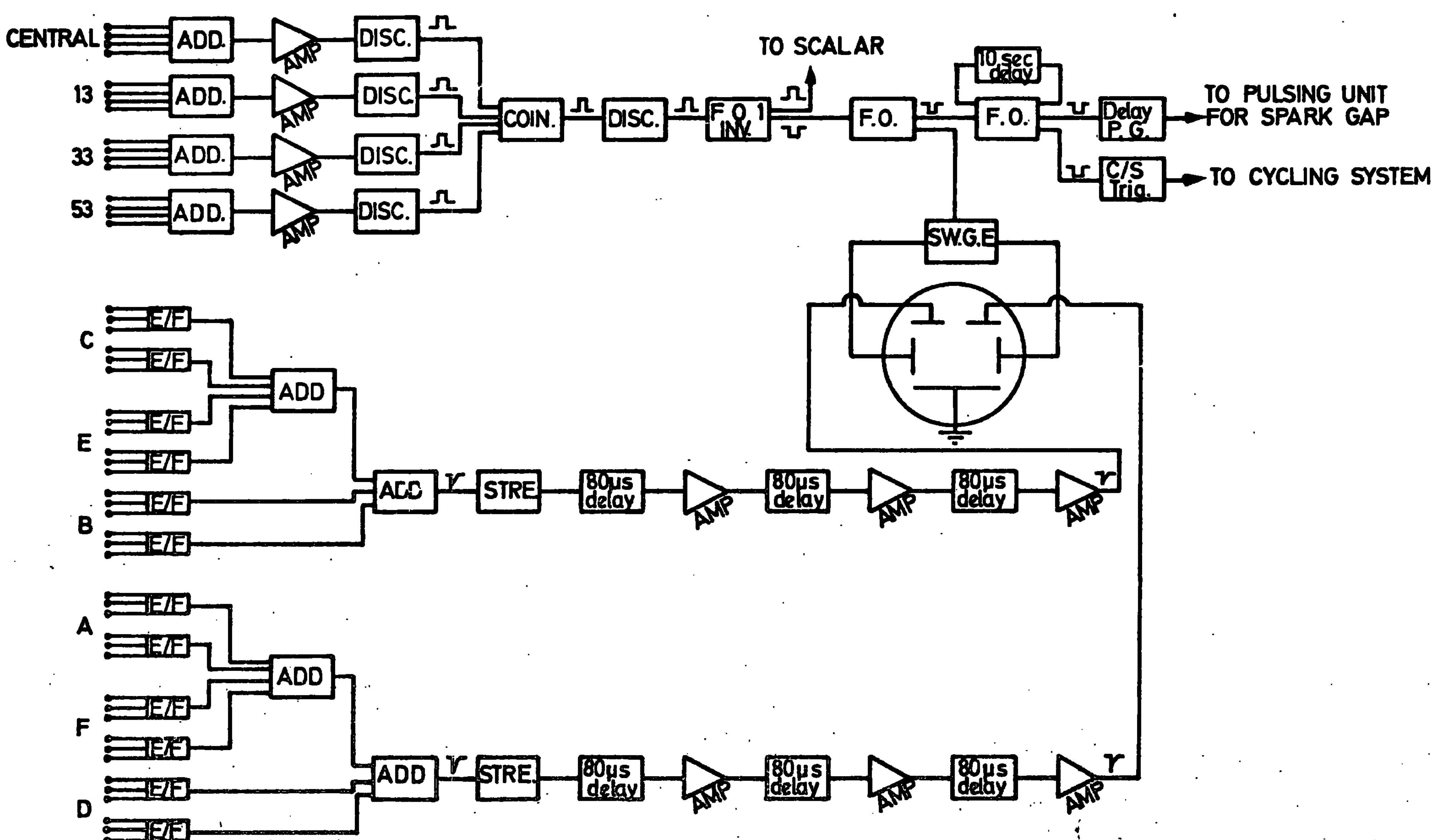

Block diagram for Tachyon experiment.

Figure 11.2

APPENDIX A

A.1 Interactions in the walls of the flash tubes

Before the present experiment, when the chamber was triggered by a local electron density to search for quarks on a 20μs time delay, a significant number of bursts were produced by the interaction of particles in the glass walls of the flash tubes. Plate 1 and 2 give two examples of these interactions.

These events were analysed to obtain evidence against the presence of a large number of muon-induced burst contamination. The interaction length of these particles was determined by measuring the frequency distribution of depth of interactions and using the following relation:

$$F = C\, e^{-\frac{x}{\lambda}}$$

Where F is the frequency and λ the interaction length. The depth of interaction was measured from the top of the flash tube block, F_2 (see figure 6.1 , the scale diagram of the flash tube chamber) to the point of interaction. The total amount of absorber represented by the flash tubes in $F_2 + F_3$ in the vertical direction is 91.5 gm / cm^{-2}. The events that were analysed were those which passed through lead and iron absorbers. Figure A.1 shows the results for charged particles. (the track of charged particles were visible in the flash tubes, F_1a and F_{1b}). The best line through the measured points was drawn and the value for the mean free path of the charged particles was found to be 119 ± 44 g/cm^2. This value is consistant with value of 130 g/cm^2 calculated from the paper of Alexander and Yekutielli (1961), consistant with mean free path of pions. Since muons have a much longer interaction length, do not contribute significantly to the production of burst in the walls of the flash tubes. However, the probability of a muon interacting in matter is approximately proportional to Z^2/A , therefore the contribution of muon-induced bursts in lead and iron is greater than in glass. But because the probability of hadrons passing through lead and iron absorbers and interacting in glass is just 25% so the measurement of the interaction length in the flash tubes is relevant to the consideration of the muon burst contamination in the lead and iron.

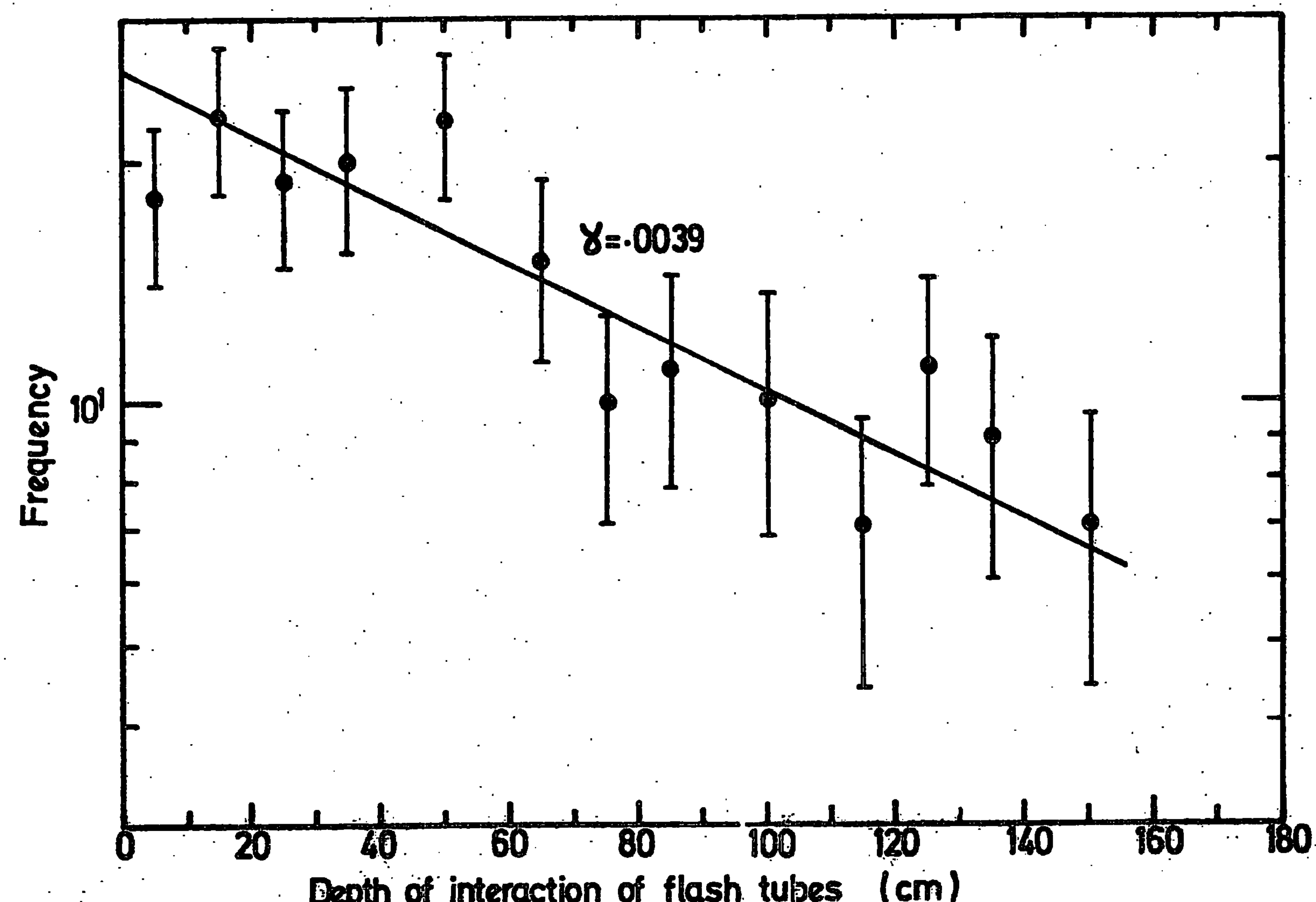

Figure A.1 The relation between the number of bursts observed in F_2 and F_3 as a function of the depth of interaction measured from the top of F_2. From the best line through the experimental points the interaction length of the charged particles can be calculated ($\lambda = 119 \pm 44$ g/cm^2)

PLATE A.1

Event E 35 - 133

The interaction of a charged particle in the walls of the flash tubes

($T_D = 20\,\mu s$)

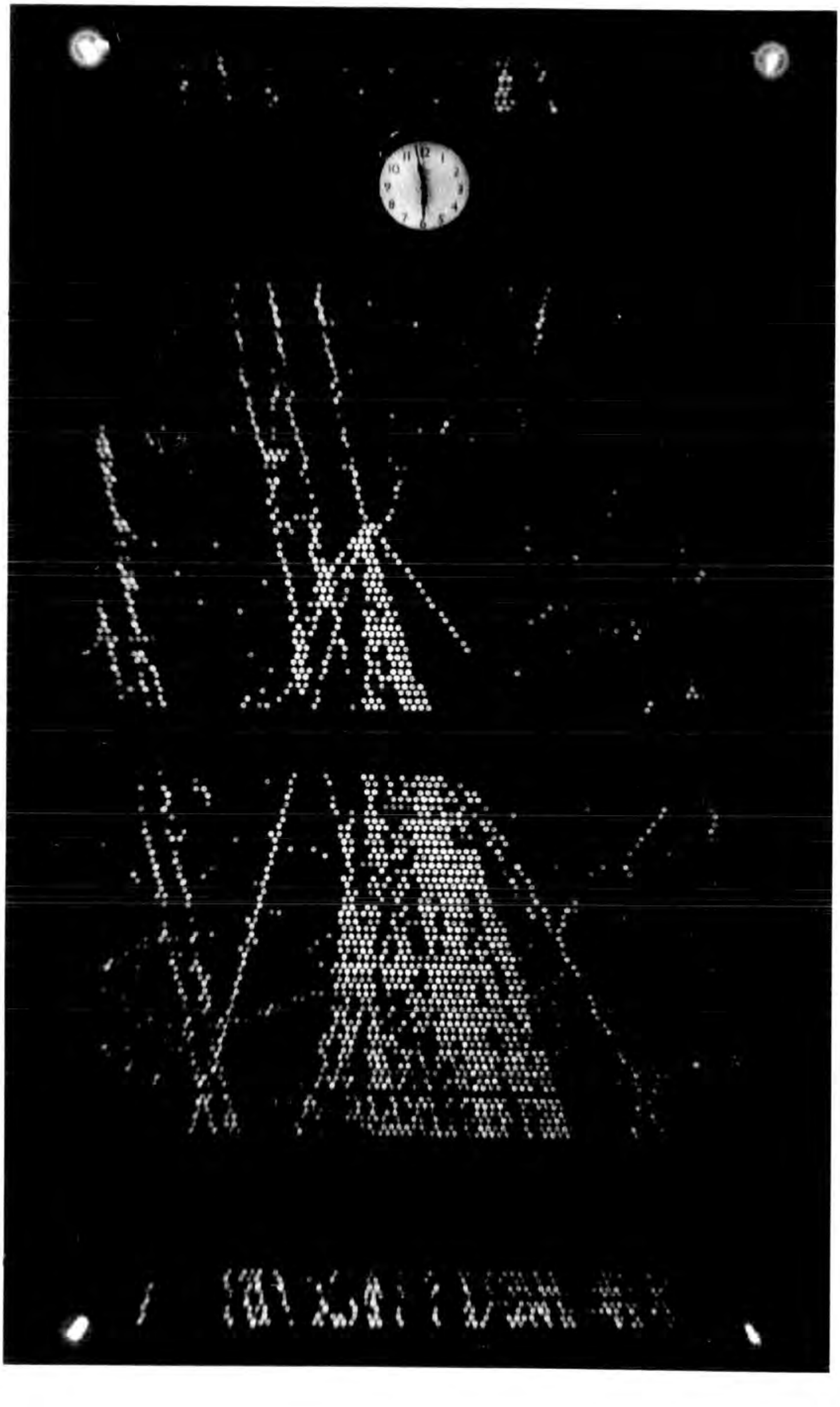

PLATE A.2

Event E 42 - 150

The interaction of a neutral particle in the glass of a flash tube. ($T_D = 20 \mu s$)

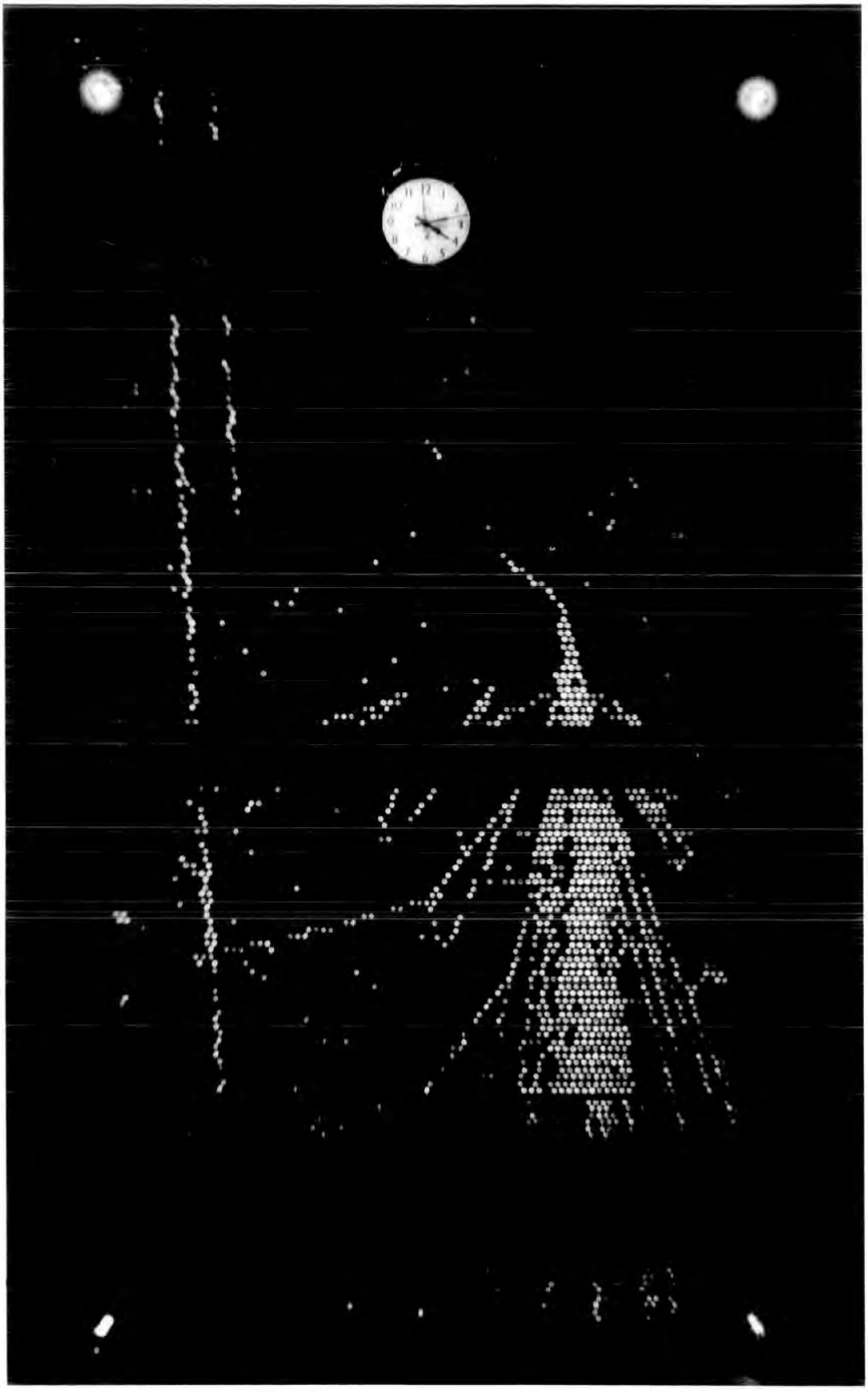

APPENDIX B

B.1 MEASURED PARAMETERS OF EVENTS USED IN THE HADRON ENERGY SPECTRUM MEASUREMENT.

Table B.1 shows the burst size and shower accompaniment information of all events analysed for hadron energy spectrum measurement.

No.	Film no.	Burst size under the lead	Burst size under the iron	Density in M	Density in 61	Density in C	Density in 12	Density in 62
1	H 97-2		1200					
2	H 97-5		3000					
3	H 97-7		3050					
4	H 97-10		1530					
5	H 97-11		1100					
6	H 97-12	800	1500					
7	H 97-13		1110					
	H 98a							
8	H 98b-2	450	850					
9	H 98b-4		2615					
10	H 98c-12		950					
11	H 98c-19	750						
12	H 98c-23	750		> 80				
13	H 99a-3	810						
14	H 99a-7	700						
15	H 99a-8	710						
16	H 99b-6	480						
17	H 99b-7		1040					
18	H 99b-9		705					
19	H 99b-11		3700					
20	H 99b-15		900					
21	H 99b-45		3200					
22	H 99c-2	470	470					
23	H 99c-3		2104					
24	H 99d-1	1550						
25	H 99d-4		2810					
26	H 99d-5	960						
27	H 99d-8		1300					
28	H 99d-10		1360					
29	H 99d-13		1580					
30	H 99e-1	1350						
31	H 99e-5		850					
32	H 99e-7		1300					
33	H 99e-8		1300					
34	H 99e-9	805		> 80				
35	H 99e-14	900						
36	H 99e-15	2600		56				
37	H 99e-17	500						
38	H 99e-18	900						
39	H 96-1		1200					
40	H 96-2		2600					

No.	Film no.	Ne under Pb	Ne under Fe	Δ_M	Δ_{61}	Δ_C	Δ_{12}	Δ_{62}
41	H 96-3	680						
42	H 96-4		710					
43	H 96-17		1300					
44	H 96-18	1350						
45	H 96-24	710						
46	H100-1	650						
47	H100-2		850					
48	H100-4	650						
49	H100-5	410	2610					
50	H100-7	420	1050	15.2		6		
51	H100-11	1502						
52	H100-12		850					
53	H100-13		4006					
54	H100-15		1350	11.3		39.3		
55	H100-17		650					
56	H100-18		655					
57	H100-19		850					
58	H100-20		1351	48.4	37.3	15.5	31	
59	H100-21		1502					
60	H100-23		1354	5.6	9	4.5		
61	H101-1		1125					
62	H101-2		850					
63	H101-3	800						
64	H101-4		925	5.5				
65	H101-5	1906	1104					
66	H101-6	1350	500	11.3				
67	H101-9	650						
68	+H101-10	1707	850	>80	140	21.8	37.3	
69	H101-11		1109					
70	H101-13		1200					
71	H101-14		1100					
72	H101-17		950					
73	H101-20		850					
74	H101-21	1350						
75	H101-22		2000					
76	H101-23		2600					
77	H101-24		950					
78	H101-25		850					
79	H101-26	750		13.5				
80	H101-28		1200	22.6				
81	+H101-30		7500	41.9	15.5	9.3	9.3	
82	H102-3	650						
83	H102-7		1750					
84	H102-8	1050						
85	H102-10	650		10.6				
86	H102-14	1050						
87	H102-19		950					
88	H102-20	800						
89	H102-21		1100					
90	H102-22	900						
91	H102-23		850					
92	H102-24	1900						

No.	Film no.	Ne under Pb	Ne under Fe	Δ_M	Δ_{61}	Δ_C	Δ_{12}	Δ_{62}
93	H102-26		850					
94	H102-27		1100	7.1				
95	H103-2		1100					
96	H103-3		1200					
97	H103-4		1650					
98	H103-6		700	27				
99	H103-7		950					
100	H103-9		1200					
101	H103-10		2710					
102	H103-21		1006					
103	H103-22	1550						
104	H103-24		1300					
105	H103-30		1100					
106	H103-33		3000					
107	H104-1	1250	950					
108	H104-6		1500					
109	H104-14		1650					
110	H104-17		1200					
111	H105-1	1650						
112	H105-2	900						
113	H105-3	4500		17.1				
114	H105-4	1000						
115	H105-6	825	2050	33.9				
116	H105-7	850		18.7				
117	H105-9		854					
118	H105-10		6000					
119	H105-11		1700					
120	H105-12	720						
121	+H105-13		1700	>80	186.6	80.9	102.6	
122	+H105-18	1810	1714	>80	280	217.7	217.7	
123	H106-2	569						
124	H106-3	827						
125	H106-7		1707					
126	H106-8	448						
127	H106-10		1705					
128	H106-12	1480						
	H106-13	620						
129	+H106-14	793		34.3	34.2	12.4	43.5	
130	H106-15		586					
131	H106-16		586					
132	H106-22	900						
133	H106-23	501						
134	H106-25		750					
135	H106-26		950					
136	+H106-27		1004	off	186.6	155	150	
137	H106-29		1200					
138	+H106-30		1700	off	155.5	93.3	118	
139	H106-33		700					
140	+H106-34		600	off	124.4	87	99	
141	H106-36	2758.5						
142	H106-37	2750	1002					

No.	Film no.	Ne under Pb	Ne under Fe	Δ_M	Δ_{61}	Δ_C	Δ_{12}	Δ_{62}
143	H106-38		700					
144	H106-40		570					
145	H106-41		500					
146	H107-2		1500					
147	H107-3		827	60.5				
148	H107-5	1310						
149	H107-6	448						
150	H107-7	931						
151	H107-8	724						
152	H107-9		2000					
	H107-10		758	12.3				
153	+H107-11		655	34	21.8	15.5	6	
154	H107-12		3276					
155	+H107-13	448	1896.5	50	18.6	12.4	18.6	
	H107-14							
156	H108-2	689.6						
157	+H108-3	793	1120.7	>80	217.7	155.5	155.5	
158	+H108-4	620	2344.8	>80	21.7	12.4	18.6	
159	H108-5		517.2					
160	H108-6	448.3	689.6					
161	+H108-7	700		50.8	130.6	124	130.6	
162	+H108-9		741	51	37	18.6	43.5	
163	H108-10		2245					
164	H108-11		724					
165	H108-13	2931	390					
166	H108-16	448						
167	H108-21		586					
168	H108-11 (2nd run)	5772						
169	H108-12	793						
170	H108-14		655					
171	H108-15		896	25.8	42			
172	H108-16		655					
173	H108-17		620					
174	H108-18		655					
175	H108-20		1034					
176	+H109-1	450	827	18	46.6	15.5	18.6	
177	H109-2		727					
178	H109-3		655					
179	H109-4		1034					
180	H109-5		724					
181	H109-6	451						
182	H109-7		965	11	9.3	3.3		
183	H109-8		421					
184	H109-9		421					
185	H109-10		827					
186	H109-13		724					
187	H109-15		655					
188	H109-17		550					
189	H109-21		655					
190	H109-23		896					
191	H109-25		1379					
192	H109-26	517		72	15.2	27.3		

No.	Film no.	Ne under Pb	Ne under Fe	Δ_{M}	Δ_{61}	Δ_{c}	Δ_{12}	Δ_{62}
193	H109-31	448						
194	H109-33	2998						
195	H109-35		655					
196	H109-39		1505					
197	+H109-41	980		39.2	31.1	37.3	25.8	
198	+H109-43	1700	1034	>80	180.6	93.3	164.8	
199	H109-48	517						
200	H109-49		4741					
201	H109-50		1034					
202	H109-53		1206					
203	+H110-1		1138	>80	68.4	31.1	24.9	
204	H110-2	3068	2413	10	15.2			
205	+H110-3	3250	1034	>80	140	108	171	
206	H110-4		1896	16	9.2			
207	H110-10		1430					
208	H110-12	1551						
209	H110-13	517	1224					
210	H110-14		1396					
211	H110-15		827					
212	H110-17		655					
213	H110-19		1034					
214	H110-20	517	465					
215	H110-21		689					
216	H110-23		2758					
217	H110-24		780					
218	H110-25		586					
219	H110-26		827	7.2	21			
220	H110-29	450						
221	H110-30	620						
222	H110-33		758					
223	H110-34		586					
224	H110-38		758	30		21.2		
225	H110-39		586					
226	H110-40	448						
227	H110-41	1600						
228	H110-42		827					
229	H110-43		827					
230	H110-45		793					
231	H110-47	966	2620					
232	H110-48	896						
233	H110-49	966						
234	H110-50		655		18			
235	+H110-51	448	827	18.7	12.4	6.2	3.1	
236	H110-52		689					
237	H110-53		1034					
238	H110-56	620						
239	H110-57	689	1034					
240	H110-58		793					
241	+H110-59	417	3448	>80	146	124	28	
242	H111-2		4741	5.1	15			
243	H111-3		1034		30			
244	H111-28		800					
245	H111-29		1300					
246	H111-36		3500					

No.	Film no.	Ne under Pb	Ne under Fe	Δ_N	Δ_{61}	Δ_c	Δ_{12}	Δ_{62}
247	H111-37		1700					
248	H111-38	1000						
249	+H111-43		6500					
250	H111-45		1200					
251	+H111-46	720			138	61	60	69
252	H111-47		1150					
253	H111-48	2700						
254	H111-51		950					
255	H112-1		1430					
256	H112-2		1401					
257	H112-3		1566					
258	H112-4		1502					
259	+H112-5		827	11.6	35	9.3	6	
260	H112-6		829					
261	H112-8		890					
262	H112-10	410						
263	H112-11		1379	41	21			
264	+H112-13		1034	>80	133.7	155.5	143	15.5
265	H112-15	2500						
266	H112-17		660					
267	H112-18	517						
268	H112-21	1310						
269	H112-23		1465					
270	+H112-26		1172	>80	9.3	3.1	3.1	0
271	H112-27		1420					
272	H 112-28	517		>80				
273	H112-30							
274	H112-31		890					
275	+H112-32		655	10.6	9.3	9.3	6	0
276	H112-33		1420					
277	H114-2	2758	2600	>80	60.6			
278	H114-3		896					
279	H114-5		3820					
280	H114-6		1379					
281	H114-9	517	1034	43.5	9.3	9.4		
282	H114-11		2068					
283	H114-13		896					
284	H114-17		1034					
285	H114-20	1300						
286	H114-22	517		5.5				
287	H114-23	689						
288	H115-1		2830					
289	H115-2		655					
290	H115-3		896					
291	H115-4		710					
292	H115-5	896	1034	12.5	12.3		24.5	
293	H115-6		724					
294	H115-7		465					
295	H115-8		724					
296	H115-9		655	6.5				
297	H115-11		1758					
298	H115-12		896					
299	H115-13		896					
300	H115-14	1172						

No.	Film no.	Ne under Pb	Ne under Fe	Δ_M	Δ_{61}	Δ_C	Δ_{12}	Δ_{62}
301	H115-17		1034					
302	H115-18		1034					
303	H115-19	4000						
304	+H115-20		1750	>80	140	93	59	9
305	H115-21		827					
306	H115-31		1410					
307	H116-1		1041	7.2	12.5	6.2		
308	+H116-2	1034	1086	>80	140	115	149	14
309	H116-4	862	1086	7.2	15.2	6.2		
310	H116-6		1010					
311	H116-7		1379					
312	H116-8		1824					
313	+H116-9		1060	>80	137	93	143	15
314	H116-11	966						
315	H116-12	2700					21.3	
316	H116-13		1964					
317	+H116-16		1896	>80	143	31.1	56	11.5
318	H116-21		2035					
319	H116-22	2035						
320	H116-25		1034					
321	H116-28	1110			9.2	9.2		
322	H116-29		1000					
323	H116-30		2053					
324	H116-31	1000	1041					
325	H116-34	505						
326	H116-35		2071					
327	H116-36		965					
328	+H116-38	5603	724	>80	137	149	146	16
329	H116-40		1778					
330	H116-41		1551					
331	H116-51		1885					
332	H116-55		1428					
333	H116-57		1401					
334	H116-53		1086					
335	H116-58		603					
336	H116-59	966						
337	H116-61		603					
338	H117-4	605						
339	H117-7		586					
340	H117-10	517						
341	H117-11		1431					
342	H117-12	517						
343								
344	H117-14		580					
345	H117-15		1034					
346	H117-18		1600					
347	H117-19		1600					
348	H117-20		1000					
349	+H117-21	1000	584	off	13.3	43.5	84	6.2
350	H117-22	517						
351	H117-23		1571					
352	H117-28		1000					
353	H117-29		827					

No.	Film no.	Ne under Pb	Ne under Fe	Δ_M	Δ_{61}	Δ_c	Δ_{12}	Δ_{62}
354	+H117-32	2655	2586					
355	H117-33	448	603					
356	H117-39		700					
357	H117-42		965					
358	H117-44	517						
359	H117-47		2412					
360	H117-50		586					
361	H117-52		1596					
362	H117-54	1000	1034		15		30.5	
363	H118-2	1724	2844					
364	H118-3	517						
365	+H118-4	517	586	off	25	12.4	9.3	0
366	H118-7		724					
367	H118-8	517						
368	H118-10	512						
369	H118-12		586					
370	H118-16		655					
371	+H118-18		656	off	21.7	6	9.3	0
372	H118-19	620	586					
373	H118-20		896					
374	H118-22	448						
375	H118-23		655					
376	H118-24		1428					
377	+H118-26		724					
378	H118-27	450	465					
379	H118-28		1100					
380	H118-29		655					
381	+H118-30	700	1896	off	168	118	174	17
382	H118-31	650						
383	H118-32		827					
384	H118-34	517	465					
385	H118-37		1034					
386	H118-38	517						
387	H118-39		1241					
388	H118-40	400	586					
389	H118-42		2276					
390	H118-44		2276					
391	H118-46	896						
392	H118-47		750					
393	H118-49		586					
394	H118-50	400	1100					
395	H118-51		827					
396	H118-53	620	655					
397	H118-56		586					
398	H119-4		465					
399	+H119-6	482	603	off	171	62	50	15.5
400	H119-7		586					
401	H119-8		827					
402	+H119-9	517	1060	off	168	140	168	17.7
403	H119-10		1402					
404	H119-11		896					
405	H119-13		1379					

No.	Film no.	Ne under Pb	Ne under Fe	Δ_M	Δ_{61}	Δ_C	Δ_{12}	Δ_{62}
406	H119-17		827					
407	H119-18		465					
408	H119-23		1401					
409	H119-24		655					
410	H119-28	448	1379					
411	H119-30		896					
412	+H119-31	448	1000	off	68	68	53	9.3
413	H119-35		896					
414	+H119-37		480	off	168	59	71	7.7
415	H119-40		724					
416	H119-41		827					
417	H119-46		655					
418	H119-49		586					
419	H120-2	689	2241					
420	H120-3	620						
421	H120-4	3448						
422	H120-6	966						
423	+H120-7		724	off	53	21.7	12.4	6
424	H120-14		724					
425	H120-17	724						
426	H120-20		586					
427	H120-21		827					
428	H120-25	517	1241					
429	H120-29	448						
430	H120-30	1379						
431	H120-31	1551	896					
432	+H120-32	689		off	124.4	25	25	12
433	H120-33	517		off				
434	H120-41	517	655					
435	H120-42	517						
436	H120-47		1034					
437	H120-48	448						
438	H120-49		655					
439	H120-51		586					
440	H120-52	680						
441	+H120-53		586	off	149	31.1	28	6
442	H120-54	448						
443	H120-56		586					
444	H120-59		1896					
445	+H120-63		655	off	177	18.6	15.5	9
446	H120-64		827					
447	H120-67		827	off				
448	H120-68	955	3879					
449	H120-69	1241						
450	H121-5	620						
451	H121-6		3448					
452	H121-7		1962					
453	H121-8		1379					
454	H121-11	1034						
455	H121-12	896	655					

No.	Film No.	Ne under Pb	Ne under Fe	Δ_M	Δ_{61}	Δ_C	Δ_{12}	Δ_{62}
456	H121-15		1379					
457	H121-19		1744					
458	H121-26		2586					
459	H121-28	517						
460	H122-1	450	655					
461	H122-3	793						
462	+H122-4		1034	>80	162	124	171	18
463	H122-5	794		18.5				
464	H122-7		2321					
465	H122-11		896					
466	H122-12	1000	2275	71.3				
467	H122-13		2106					
468	H122-14		1034					
469	H122-15	456	1034					
470	H122-16	517		43				
471	H122-19		827	3.5	30.1	9		
472	H122-22		1034	35.2	9	15		
473	H122-23		1896					
474	H122-25		2321					
475	H122-26		896	3				
476	H122-27	517						
477	H122-34		827					
478	H122-36		896					
479	H122-37	517						
480	H122-39		724					
481	H122-49	450	655					
482	H122-50		1034	25.5				
483	H122-52		896					
484	H122-53	896						
485	+H123-4		1240					
486	H123-6	650	1379					
487	H123-7		896					
488	H123-9	966						
489	H123-11	620	586					
490	H123-13		896					
491	H123-15	3534						
492	H123-18		655					
493	H123-19	517						
494	H123-26		1379	>80				
495	H123-29	1310						
496	H123-31	2700	724					
497	H123-32		5357					
498	+H123-40	1310	960	> 80				
499	H124-7		1700					
500	H124-18		1500					
501	H125-2		586					
502	+H125-3		827	40.3	68.4	62.2	59.1	3.1
503	H125-4		655					

No.	Film no.	Ne under Pb	Ne under Fe	Δ_M	Δ_{61}	Δ_C	Δ_{12}	Δ_{62}
504	H125-5		655					
505	H125-7		655					
506	H125-9		670		21.3			
507	H125-10		586					
508	+H125-12		2413		6	6	3	0
509	H125-16		724					
510	+H125-17		1724	40	171	124	202	16.5
511	+H125-18		1034	>80	6.2	9.3	3.1	0
512	+H125-19		1206	>80	6.2	3	3.1	0
513	H125-20		1034					
514	H126-1		827					
515	+H126-4		2034	>80	12.4	9.3	6.2	2.5
516	H126-18		827					
517	H126-21	1150	1379					
518	H126-22		827	47.4				
519	H126-24		896					
520	+H127-2	2068	6004	>80	137	96	62	7
521	H127-5		827					
522	H127-7		655					
523	H127-8		724					
524	H127-10		655					
525	H127-13		586					
526	H127-21		2500					
527	H127-27		1034					
528	H128-2		655					
529	H128-3		655	5.5	15			
530	H128-4		1379		15.3	3.5		
531	H128-5		655					
532	H128-6	410						9.2
533	H128-8		586					
534	H128-9	448	827	76.4				
535	H128-11		1379		15.3			
536	H128-14		827					
537	H128-15		655					
538	H128-18		724					
539	H128-19	517						
540	H128-21		1034					
541	+H128-22	1310	1896	80.6	68.4	3.1	12.4	0
542	H128-23		586					
543	H128-24	517						
544	H128-27		1034	56				
545	+H128-31		1069	>80	90.2	31	18.7	4.6
546	H128-32		827					
547	H128-34		724					
548	H128-36		1379					
549	H128-37		1034					
550	+H128-40	793	1034	>80	140	62	25	4.5
551	H128-41	1138	1379	>80				
552	H128-43	517						
553	H128-44	1724						

No	Film No.	Ne under Pb	Ne under Fe	Δ_M	Δ_{61}	Δ_C	Δ_{12}	Δ_{62}
554	H128-45		3017					
555	H128-46		2275	>80	18.6			
556	H128-48	689						
557	+H128-49	517	1069	48	22	16		5.6
558	H128-51		724					
559	+H128-53		1379					
560	+H128-56		980	>80	56	34	25	0
561	H128-58		1551					
562	H128-60	448	1241					
563	H128-62		655					
564	+H128-63	793		80.5	65	15.5	18.6	0
565	H129-1		1241					
566	H129=4		827					
568	H129-5	793						
569	H129-6	500						
570	H129-11		896					
571	+H129-14		556	off	143	37.3	46.6	0
572	H129-15	780						
573	H129-16	1300						
574	H129-18	5000	3879					
575	H129-25		724					
576	H129-26		724					
577	H129-27		827					
578	H130-8	620						
579	H130-9	896						
580	H130-16		896					
581	H130-18	1655	1379	14.5				
582	H130-20		724					
583	H130-22		827		30.4			
584	H130-23		3793					
585	H130-24		724					
586	H130-28	448						
587	H130-31	450						
588	H130-32	450	724					
589	H130-34		586					
590	H130-35	620						
591	+H130-36	517		>80	77.7	25	22	0
592	H130-46		550					
593	+H130-50		900					
594	H130-51	720						
595	H130-53		800					
596	H130-							
597	H130-57		640					
598	H130-62		900					
599	H130-66		480					
600	H130-68		540					
601	H130-72	500	660					

No.	Film No.	Ne under Pb	Ne under Fe	Δ_M	Δ_{61}	Δ_C	Δ_{12}	Δ_{62}
602	H131-4		896					
603	H131-6	450						
604	H131-7		1034					
605	H131-9		1379					
606	H131-10	793						
607	H131-11		655	32				
608	H131-13		448					
609	H131-14	3571						
610	H131-18	1100						
611	H131-22	517						
612	H131-23		1241	> 80				
613	H131-24		1379	7.5				
614	H131-25		3392					
615	H131-28		827	3.5				
616	H131-29	2155						
617	H131-30	450						
618	H131-31		1051					
619	H131-33		655					
620	H131-34		586					
621	H131-35	655						
622	H131-39	2069						
623	H132-3	1379						
624	H132-4		1379					
625	+H132-5		1069	> 80	146.2	56	68	5
626	H132-7		1707					
627	H132-9	6000						
628	+H132-12		1034	32.5	46.6	25	9	5
629	H132-15	620						
630	H132-19		896	35	36.3		6.2	
631	H132-21	448						
632	H132-23		586					
633	H132-24		655					
	H132-25		4643					
634	+H132-26	960		> 80	143	99.5	56	6
635	H133-2		827					
636	H133-5	480	900					
637	H133-6		827					
638	+H133-7	620	586	53	146	99.5	56	0
639	+H134-3		620	off	143	81	40	0
640	H134-5		655					
641	+H134-7		724	off	143	46.6	68	0
642	H134-8	420						
643	H135-12		465					
644	H135-13	793	1034	> 80				
645	H135-15		465					
646	H135-17		1034					
647	H135-22		465					
648	H135-23		655					
649	H135-24		463					

No.	Film No.	Ne under Pb	Ne under Fe	Δ_M	Δ_{61}	Δ_c	Δ_{12}	Δ_{62}
650	H150-7		500	off	15.5	9.3	9.3	0
651	+H156-2		1035	80	155	49.7	93	0
652	H136-1		724					
653	H136-6		586					
654	H136-7	5172	1724					
655	H136-9		465					
656	H136-15		462					
657	H137-1		586					
658	H137-2		724	32	9			
659	H137-3		827					
660	H137-7		1551					
661	+H138-1		450	off	74.6	49.8	31.1	0
662	+H138-2		550	off	15.5	12.4	9.3	0
663	+H138-3		450	off	140	62	124	off
664	+H139-1		1379	off	218	93	143	off
665	H139-3		586					
666	H139-4		724					
667	H139-5		1034					
668	+H139-7	820	640	48	143	50	53	9
669	H139-8		1800					
670	H139-11		610					
671	H140-7		724					
672	H140-8		1379					
673	H140-9	1034	896	60				
674	H140-10		655					
675	H140-11		724					
676	H140-13		724					
677	H140-14		827					
678	H141-3		465					
679	H141-7		586					
680	H141-10		655					
681	H142-2		1724					
682	H142-5		655					
683	H142-6		1034					
684	H142-7		586					
685	H142-10		1800					
686	H142-12		586					
687	H142-13		896					
688	+H142-18		896	off	103	34	40	0
689	H142-20		1724					
690	H154-3		2400	off	186.6	93	109	0
691	H143-1		689					
692	H143-2	724	1586					
693	H143-2		1034					
694	+H143-6		1034	off	137	46.6	21.7	0

No.	Film no.	Ne under Pb	Ne under Fe	Δ_M	Δ_{61}	Δ_C	Δ_{12}	Δ_{62}
695	H143-8		400					
696	H154-4	780		off	34.2	12.4	12.4	0
697	H144-1		1379					
698	H144-2		586					
699	H144-6		2500					
700	H144-13		1034					
701	H144-14		655					
702	H144-15		462					
703	H144-17		586					
704	H145-4	2700	2931					
705	+H145-12		3700	off	373	217.7	249	130
706	H145-13		615					
707	H146-1		655					
708	+H146-2		655	off	86	68	49.7	6
709	+H146-3		1480	off	93	62.2	140	9.3
710	H147-2	480	710					
711	H147-4		940					
712	H147-5		680					
713	+H147-6	640		off	31	21.7	12	0
714	H147-7		710					
715	H147-8		940					
716	+H148-1	400	500	off	140	93	131	0
717	H148-2	1050						
718	+H148-3	420	640	off	137	47	31	0
719	+H172-2		723	off	130	63	31	0
720	H149-2		960	off				
721	H149-3		900	off				
722	H149-5		5200	off				
723	H149-6		1700	off				
724	+H149-9		1800	off	133	28	29.9	0
725	H149-12		2000	off				
726	H149-13	900	960	off				
727	H149-14		1300	off				
728	H149-17		960	off				
729	H149-18		1300	off				
730	H149-19		2100	off				
731	+G149-21			off	140	47	62	0
732	+H150-4	440		off	37.3	37.3	31	0
733	+H151-1		586	12	62	49.7	28	0
734	+H152-3	520	760	off	130	46.6	93	0
735	+H152-4		1379	80	155.5	124	15.5	31
736	H$_1$53-1		780	off	12.4	9.3	6.2	0
737	H153-2		780					
738	+H154-2		900	off	18.7	9.3	12.4	0
739	+H154-6		720	off	86	15.5	15.5	0

No.	Film no.	Ne under Pb	Ne under Fe	Δ_M	Δ_{61}	Δ_c	Δ_{12}	Δ_{62}
740	+H158-1	966		off	130	37	40	0
741	H171-4		1100					
742	+H174-4		700	off	143	56	31	0
743	+H174-23		1700	off	137	124	62	0
744	H102-15		3450					
745	H102-1		5000					
746	H101-18		675					
747	H109-32		710					
748	H109-45		658					
749	H109-46		658					
750	H114-5		3500					
751	H114-16		655					
752	H114-19		655					
753	H114-21		724					
754	H114-25		655					
755	H114-26		724					
756	H114-27		724					
757	H115-10		655					
758	H115-15		655					
759	H115-23		695					
760	H115-30		710					
761	H116-47		603					
762	H116-54		603					

ACKNOWLEDGEMENTS

The author wishes to thank Professor A.W. Wolfendale, F.R.S., for the provision of the facilities for this work and for his interest and support.

He is extremely grateful to his supervisor Dr. F. Ashton for his willing guidance, stimulating suggestions and help throughout the work.

The author's special thanks must go to Dr. G. Motamedi, the former Chancellor of Isfahan University, Iran, now the Minister of Science and Higher Education for his continued interest and moral support.

Drs. M.G. Thompson and A.C. Smith are thanked for the help and guidance received from them in the early stage of the work.

Many members of the Cosmic Ray Research Group, Staff and Research Students are thanked for helpful discussions, in particular Dr. D.A. Cooper, Dr. A. Parvaresh and Dr. A.J. Saleh, and Mr. I.A. Ward for their friendly assistance.

The Technical Staff of the Physics Department, Mr. W. Leslie, Mr. M. Lee, Mr. K. Tindle are thanked for their help.

The author is grateful to Mrs. A. Gregory for her invaluable help in drawing many of the diagrams for this thesis.

Mrs. I. Howie is thanked for her careful typing of this thesis.

The author is grateful to his wife, who has been a great source of help.

University of Isfahan is thanked for the leave and financial support throughout this work.

The Government of Iran is thanked for financial support.

REFERENCES

(P.I.C.C.R. = Proceedings of the International Conference on Cosmic Rays)

Adcock, C. et al., J. Phys. A., 2, 574 (1969)

Adair, R.K., et al., Proc. Coral. Gables Conf., 36 (1964)

Adair, R.K., et al., Phys. Rev. Lett., 23, 1355, (1969)

Alexander, G. and Yekutielli, G., Nuovo Cim., 19, 103, (1961)

Alkofer, O.C., Carstensen, K. and Dan, W.D., Prec. Int. Conf. on Cosmic Rays, Hobart, 4, 1314, (1971)

Allaby, J.V., et al. Nuovo Cim., 64A, 75, (1969)

Allan, H.R., et al., Prec. Int. Conf. on Cosmic Rays (Denver) 4, 2407, (1973)

Amineva, T.P., et al., Trudy Fian 46, 157 Izd Nauka Moscow (1970)

Amaldi, E., et al., Nuovo Cim., 28, 733, (1963)

Anderson, C.D., Science, 76, 238, (1932)

Anderson, C.D., and Neddermeyer, S.H., Phys. Rev., 54, 88 (1938)

Antipov, Y.M., et al., Phys. Lett., 30B, 376, (1969)

Appel, J.A., et al., Phys. Rev. Letters, 33, 719, (1974)

Aseikin, V.S. et al., Proc. of 12th Int. Conf. on Cosmic Rays, 6, 2152, (1971)

Aseikin et al., proc. 14th Int. Conf. on Cosmic Rays, 8, 2960, (1975)

Ashton, F., Coats, R.B., et al., Nucl., Inst. and Methods, 37, 181, (1965)

Ashton, F. et al., Canadian Journal of Phys. 46, 1125, (1968a)

Ashton, F., Edwards, H.J. and Kelly, G.M. Phys. Lett., 29B, 249, (1969a)

Ashton, F., Breare, J.M., Holroyd, F.W., Tsuji, K. and Wolfendale, A.W., (1971b), Lett. Nuovo Cim., 2, (14), 707.

Ashton, F., Coats, R.B., Kelly, G.M., Simpson, D.A. Smith, N.J., and Takahashi, T., (1968b), J. Phys. A., 1, 569.

Ashton, F. et al., Izvest Akad. Nauk., 33, 1817, (1969b)

Ashton, F., Cooper, D.A., Nasri, A., Parvaresh, A., and Saleh, A.J., (1975) Prec. 14th Int. Conf. on Cosmic Rays, Munich 8, 2980.

Ashton, F., Smith, N.I., King, J. and Mamidzhanian, E.A., Acta. Phys. Hung., 29, suppl. 3, 25, (1970).

Ashton, F., Edwards, H.J. and Kelly, G.M., (1971a), J. Phys. A. Gen Phys., 4, 352.

Ashton, F., Coats, R.B., King, J., Tsuji, K. and Wolfendale, A.W., (1971c), J. Phys. A., 4, 895.

Ashton, F., 'Cosmic Rays at Ground Level', edited by A.W. Wolfendale, (1973).

Ashton, F., Cooper, D.A., Parvaresh, A. and Saleh, A.J., Proc. of Int. Conf. on Cosmic Rays, Denver, 3, 2096, (1973b)

Ashton, F. et al., J. Phys. A; Gen. Phys., 4, 431, (1971)

Bakich, A.M., et al. Proc. 11th Int. Conf. on Cosmic Rays. Acta Phys. Hung. suppl., 3, 501, (1970)

Babecki, J. et al., Sov. Phys. JETP, 13, 1089, (1961) Bacry, H., et al., Phys. Lett., 9, 279, (1964)

Bagge et al., proc. 9th Int. Conf. on Cosmic Rays, London, 2, 738, (1965).

Bakich, A.M. et al., J. Phys. A, 3, 662 (1970)

Bakich, A.M. et al., Canadian J. Phys. 46, 30, (1968)

Barton, J.C., Proc. Phys. Soc. 90, 87, (1967)

Barton, J.C. and Stockel, C.T., Phys. Lett., 21, 360, (1966)

Baruch, J.E.F. et al. Nature, 242, 6, (1973)

Baruch, J.E.F. et al. to final proc. Int. Conf. on Cosmic Ray

Becklin, E.E. and Earl, J.A., Phys. Rev., 136B, 237, (1964)

Belenkji, S.Z., et al. Nuovo Cim. Suppli, 3, 15, (1956)

Bennett, W.R., Phys. Rev. Lett., 17, 1196, (1966)

Bhabha H.J. Proc. Roy. Soc. 152A, 559, (1935)

Bhabha, H.J. Proc. Roy Soc. 164A, 257, (1938)

Bjorken, J.D., et al. Phys. Lett., 11, 255 (1964)

Blackett, P.M.S. and Occhialini, G.P.S., Nature, 130, 363, (1932)

Böhm, E., et al. Canad. J. Phys. V. 46, p.41, (1968)

Bothe, W. and Kolhörster, W.Z., Phys. 56, 751, (1929)

Bradt, V.H., and Rappaport, S.A., (1967), Phys. Rev., 164, 1567

Braginskii, V.B., Zel'dovish, Yd. B., Martynov, V.K. and Migulin, V.V., Sov. Phys., JETP, 27, 51, (1968)

Bray et al. proc. Int. Conf. on Cosmic Rays, London 2, 668, (1966)

Briatore, L., D'Ettorre Piazzoli, B., Piano, A., Sitte, K., Picchi, P., and Visentin, R., Proc. Int. Conf. on Cosmic Rays, Denver, 3, 2101, (1973)

Briatore, L., Dardo, M., M., D'Ettorre Piazzoli, B., Mannocchi, G., Piochi, P., Sitte, K. and Visentin, R., Proc. Int. Conf. on Cosmic Rays, Munich, 7, 2405 (1975)

Brooke, G. and Wolfendale, A.W., proc. Phys. Soc., 83, 843, (1964)

Brooke, G., Meyer, M.A. and Wolfendale, A.W., proc. Phys. soc. 83, 871, (1964)

Brecher, K., and Burbridge, G.R., Astrophys. J., 174, 253, (1972)

Buja, Z., Acta Phys. pol., 24, 381, (1963)

Cairns, I., et al. Phys. Rev., 186, 1394, (1969)

Chatterjee, B.K., et al., Can. J. Phys., 46, S136 (1968)

Chatterjee, B.K., et al., Can. J. Phys. 46, S131 (1968b)

Chatterjee, B.K., et al., proc. Int. Conf. on Cosmic Rays, London, 2, 802, (1966)

Chin, S., Hanayama, Y. et al. Nuovo Cim., 2A, 419, (1971)

Chukpa, W.A. et al. Phys. Rev. Lett., 17, 60, (1966)

Clark, G., et al., Nuovo Cimento, 8, suppl. 2, Series 10, 623, (1958) Clark, A.F., Ernst, R.D., Finn, H.F., Griffin, G.G., Hansen, N.E., and Smith, D.E., Phys. Rev. Lett., 27, 51, (1971).

Clay, J., Proc. Roy. Acad. Amsterdam, 30, 1115, (1927)

Coats, R.B., Ph.D. Thesis, Durham, unpublished (1967)

Cocconi, G., Koester, L.S. and Perkins, D.H., UCRL High Energy Phys. study seminars, 28, (UCID - 1444), (1961)

Cook, D.D., et al., Phys. Rev., 188, 2092, (1969)

Cowan, E.W. and Matthews, K., Phys. Rev., 4D, 37, (1971)

Crawford, D.F., and Messel, H., Nucl. Phys. 61, 145, (1965)

Crispin, A. and Fowler, G.N., Rev. Mod. Phys., 42, 290, (1970)

Dake, S., et al. proc. Int. Conf. on Cosmic Rays (Hobart), 3, 948, (1971)

Dardo, M., Navarra, G. Pennengo, P. and Silte, K., Nuovo Cim., 9A, 319, (1972)

Diggory, I.S. Hook, J.R., Jenkins, J.A. and Turver, K.E., J. Phys. A, 7, 741 (1974)

Dixon, H.E. and Turver, K.E., proc. Roy. Soc. London, A. 339, 171, (1974)

Dixon, H.E. et al., proc. Int. Conf. on Cosmic Rays (Denver), 4, 2473, (1973)

Dixon, H.E., et al. proc. Roy. Soc. London, A.339, 157, (1974b)

Dirac, P.A.M., proc. Roy. Soc., 133A, 60, (1931)

Dirac, P.A.M., Phys. Rev., 74, 817, (1948)

Dobrotin, N.A. and Salavatinsky, S.A., proc. 10th Ann. (1960)

Earnshaw, J.C., et al. proc. phys. soc., 90, 91 (1967)

Efimov, N.N., et al. proc. Int. Conf. on Cosmic Rays, (Denver), 4, 2378, (1973)

Ellsworth, R.W. Ito, A., Tonwar, S.C., Streitmatter, R.E., Macfall, J.R., Siohan, F. and Yodh, G.B., proc. Int. Conf. on Cosmic Rays, (Munich) 7, 2537, (1975)

Erlykin, A.D. et al., proc. 9th Int. Conf. on Cosmic Rays, London, 2, 731, (1965)

Erlykin, A.D. et al., sov. phys., JETP, 29, 922, (1969)

Evans, G. et al. proc. Roy. soc. Edinburgh (A), 70 , 143, (1971/72)

Fermi, E. and Yang, C.N., Phys. Rev. 76, 1739, (1949)

Feynman, R.P., Phys. Rev. Lett., 23, 1415, (1969)

Fowler, G.N., and Wolfendale, A.W., Handb. Phys., (Berlin; Springer), 46/1, 272, (1961)

Franzini, P. and Shulman, S., Phys. Rev. Lett., 21, 1031, (1968)

Frauenfelder, H., Kruse, U.E. and Sard, R.D., Phys. Rev. Lett., 24, 33, (1970)

Gaisser, T.K., et al., Proc. Int. Conf. on Cosmic Rays (Denver), 4, 2652, (1973)

Galbraith, W. and Jelley, J.V., Nature, 171, 349, (1953)

Galbraith, W., Extensive Air Showers, (Butterworths scientific Publication),(1958)

Galper, A.M., Gomozov, V.A., et al. Sov. J. Nucl. Phys., 10, 193, (1970)

Garraffo, Z., Pignotto, A. and Zgrablich, G., Nucl. Phys. 53B, 419, (1973)

DURHAM UNIVERSITY SCIENCE 31 MAY 1977 SECTION LIBRARY

Giacomelli, G., Rossi, A.M. and Vannini, G., Nuovo Cim., 28A, 21, (1975)

Greider, P.K.F., Inst. Nucl. study, Tokyo, Pub. INS J 125, (1970)

Greider, P.K.F., Nuovo Cim., 7A, 867, (1972)

Greider, P.K.F. proc. 11th Int. Conf. on Cosmic Rays, Budapest, EAS - 43/1 and EAS 43/2, 563 and 569, (1969)

Greider, P.K.F. proc. 13th Int. Conf. on Cosmic Rays, Denver, p.2639, (1973)

Greisen, K., progress in Cosmic Rays Phys., 3, (1956)

Greisen, K., Ann. Rev. Nucl. Sci., 10, 63, (1960)

Grigorov, N.L., et al. proc. 12th Int. Conf. on Cosmic Rays, 5, 1746, (1971)

Grigorov, N.L. Murzin, V.S. and Raport, I.D. Zh. EKSP. Teor. Fiz., 34, 506, Sov. Phys., JETP, 7, 348, (1958)

Grigorov, N.L. et al, Acta Phys. Hung., 29, Supp. 3, 37, (1970)

Hasegawa, H., et al. proc. Int. Conf. on Cosmic Rays, London, 2, 642, (1966)

Hayakawa, S., Cosmic Ray Physics, (Monographs and texts in Phys. and Astro., 467 and 468, (1969)

Hazen, W.E. et.al. proc. Int. Conf. on Cosmic Rays (Munich), 1, 2473, (1975)

Hazen, W.E., Hadson, A.L., Kass, J.R., Green, B.R. and Lloyd, P.G., proc. Int. Conf. on Cosmic Rays, Munich, 7, 2473, (1975)

Hazen, W.E., Phys. Rev. Lett., 26, 582, (1971)

Hebart, et al. proc. 12th Int. Conf. on Low Temp. Phys., 855, (1970)

Hess, V.F., Phys. Z., 13, 1084, (1912)

Hillas, A.M. Acta Phys. Hung., 29, suppl. 3, 355, (1970)

Hillas, A.M., Cosmic Rays, Pergamon Press, (1972)

Hillas, A.M., et al. Phys. Reports (Phys. Lett. C.), 20C, 61, (1975)

Holtrup, G., 4th European Symposium on Cosmic Rays, Lodz, (1974)

Ivanenko, I.P. and Samosudov, B.E., Sov. Phys. JETP, 35, (8), 884, (1959)

Ivanenko, I.P. and Samosudov, B.E., Bull, Acad. Sci. USSR, 30, 1722, (1967a)

Ivanenko, I.P. and Samosudov, B.E., Sov. J. of Nucl. Phys., 5 (3), 442, (1967a)

Jones, L.W. et al. Phys. Rev., 164, 1584, (1967)

Jones, L.W., Bussian, A.E. and Demoester, G.D. et al., Phys. Rev. Lett. 25, 1679 (1970)

Julliusson, E., Proc. Int. Conf. on Cosmic Rays, (Munich), 8, 2689, (1975)

Kamata, K. and Nishimura, progr. theor. Phys. Kyoto, suppl. 6, 93, (1958)

Kameda, T., et al., proc. 9th Int. Conf. on Cosmic Rays, London, 2, pp681-684 (1965)

Kaneko, T. et al. proc. Int. Conf. on Cosmic Rays, Hobart, 7, 2759, (1971)

Kempa, J. Wdowczyk, J., and Wolfendale, A.W., J. Phys. A., 7, 1213, (1974)

Khrimyan, A.V. et al., IZV. ANSSSR Ser. fiz. 28, 1803, (1964)

Khrenov, B.A., IZVEST. AKad. Sci. U.S.S.R., 26, 5, (1962) Khristiansen, G.B., et al., Proc. Int. Conf. on Cosmic Rays, London, 2, 799, (1965b)

Kiraly, P. and Wolfendale, A.W., Phys. Lett., 31B, 410, (1970)

Komori, H., Proc. Int. Conf. on Cosmic Rays, (Munich), 8, 2842, (1975a)

Krisor, K., Nuovo Cim., 27A, 132, (1975)

Lee, T.D., Nuovo Cim., 35, 933, (1965)

Levin, E.M. and Frankfurt, L.L., Sov. Phys. Usp, 2, 106, (1968)

Le Maitre, G. and Vallarta, M.S., Phys. Rev. 43, 87, (1933)

Lloyd, J.L., proc. of the Phys. soc. LXXV, 387 (1960)

Lovati, A., Mura, A., Succi, C. and Tagliaferri, G., Nuovo Cim., (1954), 12, 526

Malos, J., Proc. Int. Conf. on Cosmic Rays (Moscow), 2, 84, (1960)

Matano, T. et al., canad. J. Phys. 46, 556, (1968)

Matano, et al. proc. 11th Int. Conf. on Cosmic Rays, Budapest, 3, pp 463-469, (1969)

Matano, T. et al., Acta Physica Hungaricae, 29, suppl. 3, 463, (1969)

McCusker, C.B.A., and Cairns, I., Phys. Rev. Lett., 23, 658 (1969)

McCusker, C.B.A., Phys. Rev. V. 177, 1902, (1969)

McCusker, C.B.A., et al. Nuovo Cim., 32, 837, (1964)

Miyake, S., et al., Canad. J. Phys., 46, 525, (1968)

Miyake, S., et al., proc. 11th, Int. Conf. on Cosmic Rays, Budapest, 3, pp463-469, (1969)

Miyake, S., et al., Proc. Int. Conf. on Cosmic Rays, 2, 664, (1966)

Murzin, V.S., et al. prog. Elem. part and Cosmic Rays, Amsterdam, pp247-303 (1967)

Mylroi, M.G. and Wilson, J.G., Proc. Phys. Soc. A, 64, 404, (1951)

Murthy, G.T., et al., Can. J. Phys., 46, S153, (1968)

Nesterovd, N.M., et al., proc. of 13th Int. Conf. on Cosmic Rays, 4, 2665, (1973)

Nash, T., et al., Phys. Rev. Lett., 32, (15), 858, (1974)

Nikolsky, S.I., Sov. Phys. JETP, 24, 535, (1967)

Nikolsky, S.I., et al., IZV. AKad. Nauk SSSR 34, 1946, (1970)

Nishimura, J. and Kamata, K., progr. Theor. Phys., 1, 185, (1952)

Nishimura, J. and Kamata, K., see Kamata J., and Nishimura, K., (1958)

Popova, L., Proc. Int. Conf. of Cosmic Rays (Munich), 8, 2819, (1975)

Pinkau, K. and Thompson, K.V., The Rev. of the scientific Inst. 37, 302, (1966)

Price, P.B., Shirk, E.K., Osborne, W.Z. and Pinsky, L.S., Phys. Rev. Lett., 35 (8), 487, (1975)

Rahm, D.C. and Sternheimer, R.M., Brockhaven preprint BNL 14072, (1969)

Rank, D.M., Phys. Rev., 176, 1635, (1968)

Rochester, G.D. and Bulter, C.C., Nature, 160, 855, (1947)

Rossie, B., Phys. Z., 33, 304, (1932)

Rossi, B., High Energy Particles, (1952)

Rossi, B., Proc. of Int. Conf. on Cosmic Rays, (Moscow), 2, 18, (1960)

Saleh, A.J., Ph.D. Thesis, Durham, unpublished, (1975)

Samorski, M., et al., proc. of Int. Conf. on Cosmic Rays, (Hobart), 3, 959, (1971)

Shestoperov, V. Ya., Sov. J. Nuc. Phys., 19, 656, (1974)

Siohan, F., et al., proc. of Int. Conf. on Cosmic Rays, Denver, 3, 2129, (1973a)

Siohan, F., et al., proc. of Int. Conf. on Cosmic Rays, Denver, 3, 2135, (1973b)

Smith, A.C., 1976, Ph.D. Thesis, Univ. of Durham

Stover, R.W. et al., Phys. Rev., 164, 1599, (1967)

Tanahashi, G., proc. Phys. Soc. Japan, 20, 883, (1965)

Tanaka, Y. J. Phys. Soc. Japan, 16, 866, (1961)

Thielheim, K.O. and Beiersodorf, R., Acta Phys., Acta Phys. Acad. Sci. Hung. 29, suppl. 3, 519, (1969)

Turver, K.E., Cosmic Rays at Ground Level, (Ed. Wolfendale, A.W., The Institute of Physics, London), (1973)

Van Staa, R. et al., J. Phys. A., 7, pp 135-149, (1974)

Vatcha, R.H. et al., J. Phys. A., 6, 1050, (1972)

Vatcha, R.H., et al., J. Phys. A. General Phys., 5, 859-876, (1972)

Vatcha, R.H. and Sreekantan, J. Phys. A., 6, pp 1067-1077 (1973)

Wdowczyk, J., Cosmic Rays at Ground Level, (Ed. Wolfendale, A.W., The Institute of Physics, London), (1973)

Wdowczyk, J., and Wolfendale, A.W., J. Phys. A., 6, 148, (1973a)

Wilson, J.G., Nature, 225, 1238, (1970)

Wolfendale, A.W.,'Cosmic Rays at Ground Level', (Ed. by A.W. Wolfendale, published by the Institute of Phys. London), (1973)

Yukawa, H., proc. Phys. Math, Soc. Japan, 17, 48, (1935)

Yock, P.C.M., Nucl. Phys., B76, 175, (1974)

Yock, P.C.M., Nucl. Phys., B86, 216, (1975)

Yodh, G.B., et al., Phys. Rev. Lett., 28, (15), 1005, (1972)